POLYTECHNIQUE MONTRÉAL

affiliée à l'Université de Montréal

Real-Time and Atomic-Level Studies of the Growth, Phase Transformations and Stability of Two-Dimensional Pnictogens

MATTHIEU FORTIN-DESCHÊNES

Département de génie physique

Thèse présentée en vue de l'obtention du diplôme de *Philosophiæ Doctor*

Génie physique

Juillet 2020

POLYTECHNIQUE MONTRÉAL

affiliée à l'Université de Montréal

Cette thèse intitulée :

Real-Time and Atomic-Level Studies of the Growth, Phase Transformations and Stability of Two-Dimensional Pnictogens

présentée par **Matthieu FORTIN-DESCHÊNES**

en vue de l'obtention du diplôme de *Philosophiæ Doctor*

a été dûment acceptée par le jury d'examen constitué de :

Sébastien FRANCOEUR, président

Oussama MOUTANABBIR, membre et directeur de recherche

Joan REDWING, membre externe

Thomas SCHROEDER, membre externe

DEDICATION

To my parents.

ACKNOWLEDGEMENTS

Tout d'abord, je tiens à remercier mon directeur de recherche Oussama Moutanabbir pour son support, ses conseils et pour toutes les opportunités qu'il m'a donné. Je lui suis également très reconnaissant de m'avoir permis d'explorer plusieurs directions de recherche, sans jamais me mettre de pression d'obtenir des résultats.

I am also very grateful to the jury members, Sébastien Francoeur, Thomas Schröder and Joan Redwing for taking the time to read and evaluate my thesis.

Un grand merci à mes collègues du groupe de recherche NHL, notamment Olga Waller, Duy-Tach Phan et Charles-Antoine Deslauriers pour leur aide et leur expertise.

Many thanks to Robert Jacobberger and Michael Arnold for their enthusiasm and thoroughness in all the projects we have collaborated on throughout the years. I also want to thank Andrea Locatelli, Onur Menteş and Francesca Genuzio for their guidance in XPEEM experiments and for their warm welcome in Basovizza. Thanks to Gianluigi Botton, Hannes Zschiesche, Maureen Lagos and Travis Casagrande their great transmission electron microscopy work.

Merci aussi à Richard Martel et Patrick Desjardins pour avoir développé le système à ultra-haut vide dans lequel j'ai effectué la majorité de mes travaux. Merci à Pierre Lévesque pour m'avoir transmis ses énormes connaissances sur la microscopie électronique à faible énergie. Merci aussi à Alain Rochefort, qui m'a généreusement donné son aide et ses conseils à propos des méthodes de calcul de structure électronique. Merci à Joël Bouchard pour son support technique au système à ultra-haut vide. Merci aussi à Christophe Clément pour son aide en salle blanche et à Patricia Moraille pour le support en microscopie à force atomique. Merci également à Josianne Lefebvre pour son aide en microscopie Auger et son expertise en analyse de données XPS.

Merci également au CRSNG et à Hydro-Québec pour le support financier à ce projet, ainsi qu'à Calcul Québec et Calcul Canada pour l'accès aux serveurs de calcul.

Un très grand merci à mes parents pour m'avoir supporté dans tout ce que j'ai entrepris et pour avoir su me transmettre leur intérêt et curiosité pour la science. Merci à mon frère Simon, pour m'avoir encouragé en plus de me fournir un exemple d'excellence. Merci aussi à mes amis, en

particulier Yannick, Pierre-Charles et Tubtim pour avoir entrecoupé cette thèse avec des moment des plus agréables.

Un merci très spécial à ma conjointe Sarah pour son amour pour avoir entrepris ce projet avec moi. Malgré les incertitudes et les difficultés, je n'ai qu'à penser à toi pour savoir que les efforts en vaudront toujours la peine.

RÉSUMÉ

Les pnictogènes, ou éléments du groupe VA sont composés de l'azote (N), du phosphore (P), de l'arsenic (As), de l'antimoine (Sb) et du bismuth (Bi). Grâce à leur configuration électronique de valence (ns^2 np^3), ils adoptent une hybridation sp^3 et forment trois liens covalents en phase solide. Dû à cette configuration électronique unique, les pnictogènes, avec le graphite, sont les seuls matériaux élémentaires à se cristalliser en structures en couches van der Waals (vdW) et quasi-vdW. Typiquement, les éléments légers du groupe VA forment des solides de la phase orthorhombique A17 tandis que les éléments lourds préfèrent la phase rhomboédrique A7. Avec leur structure en couches, les pnictogènes sont des candidats idéaux pour former des matériaux bidimensionnels (2D). En effet, des couches 2D de phosphore noir (A17) ont été obtenues par exfoliation de cristaux massifs en 2014. Le 2D-P a été identifié comme étant un semiconducteur à mobilité élevée ayant des propriétés de transport anisotropes et possédant une bande interdite directe dont l'amplitude augmente graduellement de 0.3 à 2 eV en passant du matériau massif à des couches d'épaisseur atomique. Toutefois, au début de ce projet, la plupart des pnictogènes 2D n'existaient que sous forme de prédictions théoriques. En effet, on prédisait que les matériaux 2D légers du groupe VA seraient des semiconducteurs à large bande interdite, tandis que les pnictogènes lourds subiraient plusieurs transitions de phase électronique et topologique lorsqu'ils approcheraient des épaisseurs atomiques.

Cette thèse vise à développer la synthèse de nouveaux pnictogènes 2D et à élucider les mécanismes gouvernant leur croissance, leur stabilité thermodynamique, ainsi que leurs propriétés physiques de base. La croissance par épitaxie par jets moléculaires (MBE) sur des substrats semiconducteurs et vdW, les transitions de phase et la décomposition thermique de matériaux 2D du groupe VA a été étudiée en temps réels par microscopie électronique à faible énergie (LEEM). De plus, leurs propriétés structurelles, électroniques et thermodynamiques ont été élucidées par la combinaison de calculs *ab initio* avec des mesures de diffraction d'électrons lents (LEED), de microscopie par effet tunnel (STM), de microscopie électronique en transmission à balayage (STEM) et de microscopie de photoélectrons par rayons-X (XPEEM).

Tout d'abord, des substrats potentiels pour la croissance ont été étudiés théoriquement dans le cadre de la théorie de la fonctionnelle de la densité (DFT). La stabilité des pnictogènes 2D et l'effet des

interactions avec plusieurs substrats, dont des métaux de transition (TMs), des semiconducteurs et des semiconducteurs passivés ont été examinés. Il a été déterminé que les TMs interagissent très fortement avec les matériaux 2D du groupe VA. L'interaction entre le Nb(110) et le 2D-P (A17) détruit la structure de ce dernier. D'un autre côté, les propriétés structurales des pnictogènes 2D de la phase A7 sont bien conservées lors de l'interaction avec les TMs. Toutefois une importante hybridation entre les orbitales des couches et du substrat altère les propriétés électroniques des matériaux 2D du groupe VA. En particulier, les monocouches semiconductrices deviennent métalliques sur les TMs (Sc, Zr, Y) et les semiconducteurs (Si, Ge) et perdent donc leurs propriétés intrinsèques. Par contre, la passivation des liens pendants du Si et Ge permet de recouvrer ces propriétés. De plus, l'utilisation de diverses méthodes de passivation est identifiée comme une méthode potentielle pour permettre d'ajuster la structure électronique et le dopage des couches.

Par la suite, des méthodes de croissance de pnictogènes 2D ont été développées. La croissance du 2D-P A17 a été tentée par MBE et par sublimation de substrats de InP recouverts de graphène. Ces méthodes ont toutefois été infructueuses. Cependant, la croissance de 2D-Sb A7 par MBE a été réalisée sur des substrats de Ge(111), Ge(111) passivé et graphène. Des monocouches de 2D-Sb de quelques dizaines de nm ont été identifiées par STM et des îlots multicouches plus larges ont été observés par LEEM, STEM, STM, microscopie à force atomique (AFM) et spectroscopie Raman. Les mesures LEEM et STM indiquent qu'il y a germination homogène et hétérogène de 2D-Sb sur les substrats de Ge, mais seulement germination hétérogène sur graphène. À basse température (<140 °C), la formation de couches et d'îlots amorphes est observée. Les températures plus élevées (140-320 °C) permettent la germination de 2D-Sb cristallin, ainsi que de nanofils. L'étude détaillée de la dynamique de croissance observée par LEEM montre que la croissance latérale de 2D-Sb est alimentée par le Sb_4 déposé directement sur le substrat et que le Sb_4 déposé sur les îlots contribue surtout à la croissance verticale. Deux modes de croissance verticale sont identifiés en fonction des conditions de croissance. À haut taux de déposition et à basse température, il y a germination homogène de multicouches. À faible taux de déposition et à haute température, il y a une transition de mode de croissance résultant en la formation d'îlots triangulaires de type atoll. Par la suite, il est démontré que la co-déposition de As_4 et Sb_4 permet la croissance de 2D-As_xSb_{1-x} sur Si(111) et graphène. La spectroscopie photoélectronique X (XPS), la spectroscopie Raman et les mesures

LEED indiquent qu'il y a formation d'un alliage substitutionnel 2D contenant jusqu'à 15 at. % de As.

Ensuite, la stabilité thermique, environnementale et de phase des pnictogènes 2D est investiguée. La combinaison des mesures LEEM en temps réel avec des calculs *ab initio* et des simulations Monte-Carlo cinétique montre que la décomposition thermique du 2D-P A17 se produit principalement par la formation de trous allongés de profondeur atomique due à la sublimation de P_2 et de P_4 aux bords. Par la suite, l'oxydation du 2D-Sb est élucidée grâce à des mesures XPEEM en synchrotron. Les données montrent qu'il y a germination de Sb_2O_3 aux bords et aux coins des îlots après environ 10 jours. Le Sb_2O_3 croît ensuit vers l'intérieur des îlots pour éventuellement les recouvrir complètement en quelques mois. Finalement, les observations LEEM de la croissance vdW de Sb sur graphène, complémentées par la caractérisation par STEM révèlent la présence de Sb A17 métastable. La phase instable est stabilisée à des épaisseurs quasi-atomiques et transitionne vers le A7 Sb(110) à une épaisseur critique de ~4.5 nm. Cette première observation de la transition de phase montre le charactère unique de la thermodynamique des matériaux vdW sur des substrats interagissant faiblement et procure une avenue potentielle pour stabiliser des matériaux à couches jusqu'à maintenant inconnus.

En somme, les résultats présentés dans cette thèse jettent les bases pour le développement de nouveaux pnictogènes 2D et procurent une compréhension à l'échelle atomique de leur stabilité et de leurs mécanismes de croissance et de transition de phase.

ABSTRACT

Pnictogens, also known as group VA elements, are comprised of nitrogen (N), phosphorus (P), arsenic (As), antimony (Sb) and bismuth (Bi). With their ns^2 np^3 valence electronic configuration, pnictogens tend to adopt a sp^3 hybridization and form three covalent bonds in elemental solids. This unique electronic configuration makes them the only elemental materials, alongside graphite, to crystallize in van der Waals (vdW) and quasi-vdW layered structures. Light group VA elements tend to assemble in the orthorhombic phase (A17) and heavier group VA elements prefer the rhombohedral phase (A7). With their layered structures, pnictogens are ideal candidates to form two-dimensional (2D) materials. In fact, 2D black phosphorus (A17) has been exfoliated from bulk crystals in 2014 and was identified as a high mobility 2D semiconductor with a thickness-dependent direct band gap varying between 0.3-2 eV and displaying interesting anisotropic transport properties. However, by the time this project was initiated, most 2D pnictogens existed only in the realm of theoretical predictions. In fact, it was hypothesized that light group VA 2D materials would be large band gap semiconductors, whereas heavy 2D pnictogens were predicted to exhibit several electronic and topological transitions at near atomic thicknesses.

This thesis aims at developing growth methods for novel 2D pnictogens allotropes and at establishing an atomic-level understanding of the mechanisms governing their growth, thermodynamic stability and basic physical properties. The molecular beam epitaxy (MBE) growth on semiconducting and vdW substrates, the phase transformations and the thermal decomposition of group VA 2D materials was studied in real-time using low-energy electron microscopy (LEEM). Furthermore, their structural, electronic and thermodynamic properties were elucidated by a combination of *ab initio* calculations, low-energy electron diffraction (LEED), scanning tunnelling microscopy (STM), scanning transmission electron microscopy (STEM) and synchrotron-based X-ray photoemission microscopy (XPEEM).

First, potential growth substrates are studied using density functional theory (DFT). The stability and the effect of the substrate-layer interactions is investigated for group VA 2D materials on transition metals (TMs), semiconductors and passivated semiconductors. TMs are found to interact strongly with group VA 2D materials. The interaction with Nb(110) compromises the structural integrity of epitaxial A17 2D-P. On the other hand, the structural parameters of A7 group VA 2D

materials are weakly influenced by the transition metal substrates. However, important orbital hybridization occurs between the substrates and the layers, leading to modifications of the electronic properties. In particular, single layer group VA 2D materials undergo a semiconductor to metal transition on TMs (Sc, Zr, Y) and semiconductor (Si, Ge) surfaces, leading to a loss of the freestanding-like behavior. On the other hand, passivation of the surface dangling bonds reduces the interaction and allows the recovery of the freestanding properties. Moreover, the use of various passivation methods is found to provide an additional degree of freedom to tune the electronic structure and doping of the layer.

Growth methods for group VA 2D materials are then developed. The growth of A17 2D-P was attempted by MBE and by sublimation of graphene capped InP substrates but was not successful. On the other hand, A7 2D-Sb was successfully grown on Ge(111), passivated Ge(111) and graphene substrates by MBE. Nanometric single-layer 2D-Sb flakes were identified by STM and larger multilayer 2D-Sb flakes were observed by LEEM, STEM, STM, atomic force microscopy (AFM) and Raman scattering spectroscopy. LEEM and STM indicate that homogeneous and heterogeneous nucleation of 2D-Sb occur on Ge(111), whereas only heterogeneous nucleation happens on graphene. At low substrate temperature (<140 °C), mostly amorphous dome shaped 3D islands grow, whereas higher temperatures (140-320 °C) allow for the nucleation of 2D-Sb and nanowires. Detailed analysis of the growth dynamics on graphene reveals that the lateral growth of 2D-Sb is driven by Sb_4 species deposited directly on the substrate and that Sb_4 deposited on the 2D islands contributes mostly to vertical growth. Two distinct vertical growth modes are identified by LEEM depending on the growth conditions. Homogeneous multilayer nucleation dominates at high deposition rate and low temperature and a transition to atoll-like growth occurs at low deposition rate and high temperature. Next, the MBE growth of 2D-As_xSb_{1-x} by co-deposition of As_4 and Sb_4 is demonstrated on Si(111) and graphene substrates. LEED, X-ray photoemission spectroscopy (XPS) and Raman spectroscopy show that the grown 2D alloy is substitutional and an As content up to 15 at. % is reached.

The thermal, atmospheric and phase stability of 2D pnictogens is then examined. The LEEM dynamics combined with DFT calculations and kinetic Monte-Carlo simulations show that the formation of monolayer deep anisotropic holes by the sublimation of P_2 and P_4 molecules at edges is the main thermal decomposition pathway of A17 2D-P. Then, the oxidation of 2D-Sb is studied

by XPEEM. The spectromicroscopic data shows that Sb_2O_3 nucleates at the edges and tips of the flakes within 10 days and then grows inward to fully cover the flakes in a matter of months. Finally, real-time LEEM observations of the vdW growth of 2D-Sb on graphene along with STEM characterization of its atomic structure establish the presence of metastable A17 Sb. The unstable bulk allotrope is found to be stabilized at near atomic thicknesses and to undergo a diffusionless phase transformation to the A7 Sb(110) phase when it reaches a thickness of ~4.5 nm. This first observation of the phase transformation highlights the unique thermodynamics of vdW materials on weakly interacting substrates and provides a potential pathway to discover novel layered allotropes and polymorphs.

Overall, these results lay the groundwork for the development of emerging 2D pnictogens and provide an atomic-level understanding of their stability, growth and phase transformation mechanisms.

TABLE OF CONTENTS

LIST OF TABLES

LIST OF FIGURES

LIST OF SYMBOLS AND ABBREVIATIONS

Abbreviations

2D	Two-Dimensional
AFM	Atomic Force Microscopy
ARPES	Angle-Resolved Photoemission Spectroscopy
bcc	body centered cubic
BFGS	Broyden–Fletcher–Goldfarb–Shanno
BL	Bilayer
bP	black Phosphorus
cg	cubic gauche
CMOS	Complementary Metal-Oxide-Semiconductor
CVD	Chemical Vapor Deposition
DFT	Density Functional Theory
DOS	Density Of States
EDX	Energy-Dispersive X-ray spectroscopy
F	Deposition Rate
fcc	face centered cubic
FET	Field-Effect Transistor
FFT	Fast Fourier Transform
FIB	Focused Ion Beam
FOV	Field Of View
FWHM	Full Width Half Maximum
GGA	Generalized-Gradient Approximation

HAADF	High-Angle Annular Dark-Field
hcp	hexagonal close packed
HOPG	Highly Oriented Pyrolytic Graphite
HRTEM	High-Resolution Transmission Electron Microscopy
IPA	Isopropanol
IR	Infrared
KMC	Kinetic Monte Carlo
KS	Kohn-Sham
LDA	Local-Density Approximation
LEED	Low-Energy Electron Diffraction
LEEM	Low-Energy Electron Microscopy
MBE	Molecular Beam Epitaxy
MD	Molecular Dynamics
ML	Monolayer
MOSFET	Metal-Oxide-Semiconductor Field-Effect Transistor
NN	Nearest Neighbor
NW	Nanowire
PDMS	Polydimethylsiloxane
PDOS	Projected Density Of States
PEEM	Photoemission Electron Microscopy
PEG	Polyethylene Glycol
PES	Potential Energy Surface
PL	Photoluminescence
PMMA	Poly(methyl methacrylate)

PP	Pseudopotential
p-sc	pseudo simple cubic
QD	Quantum Dot
QSH	Quantum-Spin Hall
RMSE	Root Mean Square Error
RT	Room temperature
sc	simple cubic
SEM	Scanning Electron Microscopy
SC	Semiconductor
sccm	Standard cubic centimeter per minute
SEM	Scanning Electron Microscopy
SOC	Spin-Orbit Coupling
SS	Subthreshold swing
STEM	Scanning Transmission Electron Microscopy
STM	Scanning Tunneling Microscopy
STS	Scanning Tunneling Spectroscopy
T	Temperature
TEM	Transmission Electron Microscopy
TM	Transition Metal
TMD	Transition Metal Dichalcogenide
UHV	Ultra-High Vacuum
vdW	van der Waals
XPEEM	X-Ray Photoemission Electron Microscopy
XPS	X-Ray Photoemission Spectroscopy

XRD	X-Ray Diffraction

Symbols

A	Area
A_i	Fraction of the surface of layer *i* covered by holes neglecting coalescence
a_0	Bohr radius
a_X	Lattice parameter a of phase X
b_X	Lattice parameter b of phase X
C_6^{ij}	Empirical dispersion coefficient between element *i* and *j*
c_X	Lattice parameter c of phase X
D	Diffusion coefficient
D_0	Pre-exponential diffusion coefficient
d_{X-Y}	Distance between atoms X and Y
e	Elementary charge
E_a	Activation energy
E_D	Desorption activation energy
E_{diff}	Surface diffusion activation energy
E_{disp}	Grimme energy dispersion correction
$E_{\alpha-2D-P}$	Energy of isolated α-2D-P
$E_{P/Nb(110)}$	Total energy of epitaxial α-2D-P on Nb(110)
E_n	Energy of state n
$E_{Nb(110)}$	Energy of the isolated Nb(110) slab
E_{XC}	Exchange-correlation energy
E_{II}	Nuclei repulsion energy

e^-	Electron
ϵ_0	Vacuum permittivity
ϵ_{XC}^{hom}	Exchange-correlation energy of the homogeneous electron gas
F	Deposition rate
$\boldsymbol{F}_I$	Force components on the nuclei
f	Frequency
f_0	Attempt frequency
f_{dmp}	Dispersion damping function
$f_{i\to j}$	Transition rate from state *i* to *j* (KMC)
G	Gibbs free energy
$\boldsymbol{G_{hk}}$	Reciprocal lattice vectors
$\widehat{H}$	Hamiltonian
$H(t-t_0)$	Heaviside function centered at t_0
$\hbar$	Reduced Planck constant
Θ_i	Un-sublimated fraction of layer *i*
θ	Angle
I_t	Tunnelling current
J	Diffusion flux
$\vec{k}$	Wavevector
k_B	Boltzmann constant
L_d	Diffusion length
l_i	Edge length on layer *i* not corrected for hole coalescence
m_e	Electron mass

n_i	Number of holes per unit surface on layer i
$n(\boldsymbol{r})$	Electron density
$n_0(\boldsymbol{r})$	Ground-state electron density
$p_{i\to j}$	Probability of transition from i to j (KMC)
$\boldsymbol{R}_I$	Nuclei positions
R_i^{tot}	Total transition rate (KMC)
r_c	Critical radius
$\mathbf{r_n}$	Position of electron n
ρ_d	Defect density
ρ_s	Atomic density
ρ_v	Vacancy concentration
T	Temperature
T_m	Melting point
T_{mb}	Kinetic energy of many body system
T_s	Single particle kinetic energy
t	Time
t_{sat}	Time to saturation
V_{eff}	Effective potential
V_{ext}	External potential
V_t	Tunnelling voltage
V_{XC}	Exchange-correlation potential
v_L	Hole expansion velocity along the long-axis
v_S	Hole expansion velocity along the short axis

X_i	Correction factor for hole coalescence for layer *i*
γ	Surface energy
ϕ_i	Single particle wavefunctions
ϕ_{sat}	Surface concentration at saturation
ϕ_X	Surface concentration of species *X*
ψ_n	Many-particle wavefunctions

LIST OF APPENDICES

CHAPTER 1 INTRODUCTION

1.1 General context

With the discovery of quantum mechanics 100 years ago, physicists had all the tools to begin understanding the properties of matter. However, to this day, even the simplest elemental materials keep revealing new and exciting fundamental phenomena. One of the biggest breakthroughs of the 21st century in materials science is the isolation of graphene in 2004[1], which provided a novel and versatile platform to study two-dimensional (2D) condensed matter physics. The valence electronic configuration of carbon, along with the hexagonal honeycomb lattice of graphene lead to the emergence of massless Dirac fermions, which dominate the electronic behavior of this atomically thin material. This peculiar electronic structure is at the origin of several impressive features in graphene, such as its extreme electrical conductivity and the emergence of the anomalous quantum Hall effect[2]. On the other hand, the strong in-plane covalent bonds hold the atomic sheet together and ensure its high stability, mechanical strength, flexibility, optical transparency, and surface to volume ratio.

These results quickly motivated the development of a whole new family of materials mimicking the 2D nature of graphene. Over the past 15 years, hundreds of new 2D materials have been experimentally produced[3-5]. Moreover, extensive *ab initio* modelling, supported by machine learning algorithms allowed to predict the existence of thousands of potential 2D materials, based on known van der Waals (vdW) layered crystals[6]. These studies revealed that 2D materials exhibit a wide range of unique physical properties and have the potential to revolutionize several emerging technologies[4]. In fact, reducing the thickness of vdW layered materials leads to a decrease in interlayer interactions and to an increase of the quantum confinement of electrons. For this reason, vdW materials often exhibit electronic transitions at single or few layer thicknesses. For instance, many transition metal dichalcogenides (TMDs) such as MoS2 display an indirect to direct electronic band gap transition, which make them appealing for optoelectronic applications[7]. Moreover, the unique atomic structure of 2D TMDs provides an additional electronic valley degree of freedom to store information in the crystal momentum and process it optically, which might prove useful for quantum computation[8]. On the other hand, 2D semiconductors are particularly interesting for nanoelectronics. In fact, their atomic thickness provides them with an innate

resistance to detrimental short-channel effects in field-effect transistors (FETs), which might allow to preserve their performance in the sub-10 nm range to push further the limits of low-power, high-performance computing[9]. Other metallic materials like graphene, along with insulating materials such as 2D hexagonal boron-nitride (h-BN) could provide all the ingredients needed to design a variety of 2D electronic devices[10]. Perhaps even more powerful is the large surface to volume ratio of 2D materials which makes them highly sensitive to their environment. This allows their use in gas sensors[11, 12], provides the opportunity to tune their properties by surface doping and enable the combination of multiple 2D materials into complex and highly tunable vdW heterostructures[13, 14].

The vast majority of 2D materials are single or few layers stacks of vdW layered materials. These vdW materials are characterized by strong in-plane bonds and weaker vdW interlayer bonds. Quite surprisingly, there are only two classes of elemental vdW materials: graphite[15] and group VA elements (N, P, As, Sb, Bi)[16-18]. Group VA elements have a ns^2 np^3 valence electronic configuration. Besides N, they adopt a sp^3 hybridization leading to the formation of three covalent bonds and an inert doublet. This bonding structure is at the origin of various vdW and quasi-vdW layered allotropes throughout the group. This unique layered allotropy over a full elemental group provides the opportunity to investigate, exploit and fine-tune a wide range of 2D physical phenomena in a simple elemental system. Nevertheless, it took around a decade after the discovery of graphene to recognize the potential of group VA 2D material. In fact, 2D black phosphorus (2D-bP) has been isolated in 2014. This orthorhombic semiconductor has a thickness dependent direct band gap varying from 0.3 eV in bulk to 2.05 eV in single layer[19-21]. Moreover, 2D-bP has a very high hole mobility as well as interesting anisotropic transport behavior. Following 2D-bP discovery and approximatively at the time that this thesis was initiated, the existence of several other 2D group VA allotropes has been theoretically predicted. These include nitrogene[22, 23], blue phosphorene[24], arsenene[25], antimonene[26-28] and bismuthene[29]. In contrast to their semimetallic bulk counterparts, single layer group VA 2D materials are all expected to be high-mobility semiconductors with band gaps decreasing with atomic number from 5.9 eV down to 0.3 eV[22, 30]. Moreover, the increase in spin-orbit coupling (SOC) with atomic number gives rise to multiple topological phases in heavier group VA 2D films[31-34]. For instance, Sb is predicted to exhibit topological semimetal, topological insulator, 2D quantum spin hall and semiconducting phases as its thickness is reduced from 22 bilayers to a single bilayer[34]. Obviously, these properties have

attracted a lot of attention for potential applications in high-performance nano-electronics, photonics and emerging quantum technologies.

Despite their revolutionary potential, 2D materials remain scarcely implemented in emerging technologies. In fact, the lack of scalable synthesis methods prevents the production of high quality 2D materials in a controllable and homogeneous fashion compatible with the device processing standards. High-quality wafer-scale homogeneous synthesis is currently possible only for graphene. The community still heavily relies on exfoliation from bulk crystals yielding 2D flakes with limited lateral dimensions and poor thickness and orientation control. This is even more critical for group VA 2D materials. In fact, at the beginning of this project, most group VA 2D materials existed only in the realm of theoretical predictions. To fully understand and harness the properties of this rich allotropic group of layered materials, it is therefore critical to develop the methods for their epitaxial growth. In order to do so, a deep understanding of their vdW growth mechanisms needs to be established. In fact, the conventional homo- and heteroepitaxy driven by surface dangling bonds and high surface energies does not apply to this class of materials. Moreover, the thermodynamic and environmental stability of materials can be greatly altered at the atomic scale, which can either prevent or facilitate the synthesis and processing of various 2D allotropes. Careful assessment of this stability is therefore essential to the development of this new class of 2D materials.

1.2 Research objectives

This thesis aims at developing group VA 2D materials beyond 2D-bP. Its main objectives are the following:

1- Experimentally establish the existence of 2D allotropes of group VA elements, beyond 2D-bP.

2- Develop synthesis methods for group VA 2D materials and elucidate the underlying growth mechanisms.

3- Determine the thermal, atmospheric and phase stability of group VA 2D materials and identify their key mechanisms.

1.3 Thesis structure

To tackle the research objectives outlined above, this thesis is structured as follows:

Chapter 2 quickly reviews the relevant literature describing the electronic and atomic structure of bulk group VA allotropes. Then, the recent progress on group VA 2D allotropes is presented. In particular, the theoretical predictions of their potential stability and physical properties are reviewed. Moreover, the current state-of-the-art of their synthesis and characterization are described. Finally, *in situ* microscopic characterization of the growth dynamics of 2D materials, which is the main experimental technique used in this thesis, is reviewed.

Chapter 3 gives the basics of the experimental techniques and theoretical approaches used in this thesis and describes the methodology.

Chapter 4 presents a density functional theory study of the stability, substrate-layer interactions and electronic properties of epitaxial group VA 2D materials on potential epitaxial growth substrates. This study aimed at guiding the experimental work, which was carried out in the following chapters. The results presented in this chapter are published (in part) in:

1- Fortin-Deschênes, M.; Moutanabbir, O. “Recovering the semiconductor properties of the epitaxial group V 2D materials antimonene and arsenene.” *The Journal of Physical Chemistry C* 2018, 122, (16) (2018): 9162-9168.[35]

Chapter 5 treats the vdW growth of group VA 2D materials. Attempts at 2D-bP growth are rapidly described. Then, the molecular beam epitaxial (MBE) growth of 2D-Sb on germanium substrates is presented. These results are published in:

2- Fortin-Deschênes, M. et *al*. “Synthesis of Antimonene on Germanium.” *Nano Letters* 2017, 17 (8): 4970-4975.[36]

In the following section, a detailed investigation of the growth dynamics of 2D-Sb on weakly interacting substrates using real-time low-energy electron microscopy (LEEM) is presented. These results are published (in part) in:

3- Fortin-Deschênes, M. et *al*. “Dynamics of antimonene-graphene van der Waals growth.” *Advanced Materials* 2019, 31 (21): 1900569.[37]

Finally, the last section investigates the possibility of incorporating arsenic in 2D-Sb during the MBE growth on semiconductor and graphene substrates. These results are published in:

4- Fortin-Deschênes, M. et *al*. "2D Antimony-Arsenic Alloys." *Small* 2020, 16 (3): 1906540.[38]

Chapter 6 studies the stability of group VA 2D materials under different conditions. First, the thermal stability of 2D-bP and 2D-Sb is studied using real-time LEEM. Moreover, kinetic Monte Carlo simulations of the thermal decomposition of 2D-bP, supported by density functional theory (DFT) calculations are used to interpret the LEEM results and determine the sublimation mechanisms. These results are published in:

5- Fortin-Deschênes, M. et *al*. "Dynamics and Mechanisms of Exfoliated Black Phosphorus Sublimation" *The Journal of Physical Chemistry Letters*, 7, (9) (2016): 1667-1674.[39]

Then, the environmental stability and oxidation of 2D-Sb is studied by LEEM and X-ray photoemission microscopy (XPEEM). Finally, the phase stability and phase transition mechanisms of metastable 2D allotropes of Sb are studied using real-time LEEM, supported by transmission electron microscopy (TEM) measurements and *ab initio* calculations. These results are currently under review in:

6- Fortin-Deschênes et *al*. "Pnictogens Allotropy and Phase Transformation during van der Waals Growth" *Nature* (under review).[40]

Chapter 7 outlines the general conclusion and perspectives of the thesis.

CHAPTER 2 LITERATURE REVIEW

This chapter reviews the background literature allowing to put in context the research carried out in this project. First, the properties and structure of bulk pnictogens (group VA elements) allotropes are summarized. Then, the theoretical and experimental work on the single and few layers form of the vdW layered pnictogens is reviewed, with an emphasis on the development of synthesis methods. Finally, the use of real-time electron microscopy in the study of 2D materials growth is described.

2.1 Allotropy in group VA elements

Most 2D materials are single or few layer thick versions of their bulk counterparts. It is therefore important to understand the crystallography, thermodynamic stability and physical properties of bulk group VA materials in order to design and develop synthesis methods for the 2D phases. Like all groups of the periodic table, group VA elements share similar properties due to their common valence electronic configuration. The ns^2 np^3 electronic configuration is at the origin of the bonding, crystalline configurations as well as the electronic band structure of the materials. Nonetheless, the behavior of group VA elements gradually changes as we go down in the periodic table. The most striking difference is between N and the other elements. In fact, elemental N primarily adopts a sp hybridization, in contrast to sp^3 hybridized heavier elements. However, the additional core electrons induce important differences as we go from P to Bi. The lower ionization energies and decreased overlap of valence electrons forming covalent bonds, associated with the increased core size and screening of nucleus charge, leads to weaker bonds and smaller gap between bonding and antibonding states. As a result, there is a transition from semiconducting to semimetallic allotropes as the atomic number increases. On the other hand, the increase in relativistic effects with atomic mass has important effects on the electronic properties of heavy group VA materials. In fact, the large spin-orbit coupling in Sb and Bi can induce various topological states in bulk and thin films.

This section briefly reviews the bulk group VA allotropes as well as their bonding and resulting electronic properties.

2.1.1 Nitrogen

In ambient conditions, N is in the molecular N_2 gaseous form due to the strong sp bonding. The N_2 molecule has one σ bond, two π bonds and two sp doublets. N_2 liquifies at 77K (1 bar) and solidifies at 63K in the hexagonal close packed β phase composed of disordered N_2 molecules held together by vdW forces[41, 42]. Below 37K, N_2 transitions to the molecular cubic α phase. Several other molecular N_2 phases are also observed at low and moderate pressures (Figure 2.1a), as their stability is ensured by the low energy of the triple bond[43]. Nonetheless, Pauli repulsion prevents further compression of the vdW crystal and denser single-bond phases take over at higher pressures. The first evidence of non-molecular N was obtained in shock-wave experiments at 30 GPa and 6000K[44]. The authors however did not identify the structure of the produced phase. Subsequent studies identified the formation of polymeric threefold-coordinated non-crystalline black N at pressures above 140 GPa and at room temperature (RT)[45, 46]. The first crystalline N phase to be identified is the cubic gauche (cg-N) phase at P > 110 GPa and T > 2000 K (Figure 2.1b)[47]. However, the phase transformation is reversible and cg-N converts to molecular N when the pressure is released[48]. Interestingly, cg-N nanocrystals have been synthesized and stabilized at ambient pressure using plasma enhanced vapor deposition on carbon nanotube substrates with N_2 and sodium-azide precursors[49].

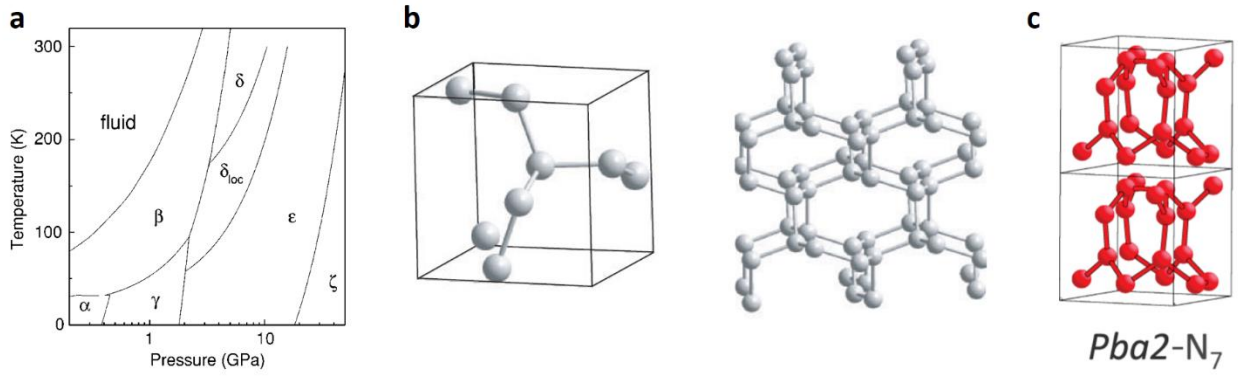

Figure 2.1 a) Low-pressure phase diagram of diatomic nitrogen. Reprinted from [50], with the permission of AIP Publishing. b) Crystal structure of cg-N. Reprinted from [48]. c) Crystal structure of layered polymeric N. Reprinted from [51] (https://doi.org/10.1103/PhysRevLett.113.205502).

Several other atomic N phases have been theoretically predicted, including metallic phases and multiple layered allotropes[43, 52]. The layered phases include A7 and A17 observed in heavier group

VA elements as well as the N_7 layered polymeric phase (Figure 2.1c). The latter has been synthesized at pressures between 120-180 GPa using laser heating at ~3000 K to provide energy for N_2 bond dissociation[51]. Nevertheless, the layered phases are unstable at atmospheric pressure and cannot be used for the isolation of novel 2D allotropes.

2.1.2 Phosphorus

Contrarily to N_2, the sp hybridized P_2 allotrope is not stable under ambient conditions[53]. In fact, the increased core size reduces the stability of the π bonds. In normal conditions, elemental P has a sp^3 hybridization with a tetrahedral bonding structure (Figure 2.2a). Two of its five valence electrons occupy one sp^3 orbital and the three remaining half-filled orbitals are responsible for bonding. This leads to the formation of three covalent bonds per atom, at an angle of ~60-105°. This unique bonding configuration is at the origin of the rich allotropy of P and heavier group VA elements. The simplest sp^3 molecule is tetrahedral P_4, where each atom forms single covalent bonds with all three other atoms of the molecule. P_4 is the main molecular species found in liquid and gaseous P[54]. Like N_2, P_4 can form molecular solids. Solid molecular P_4 is named white phosphorus and adopts the metastable α-P cubic phase in ambient conditions (Figure 2.2) [55]. At 197 K, α-P transitions to β-P, a triclinic molecular solid. Due to the vdW interactions between P_4 molecules, white phosphorus is a low-density soft solid with a relatively low melting point of 317 K.

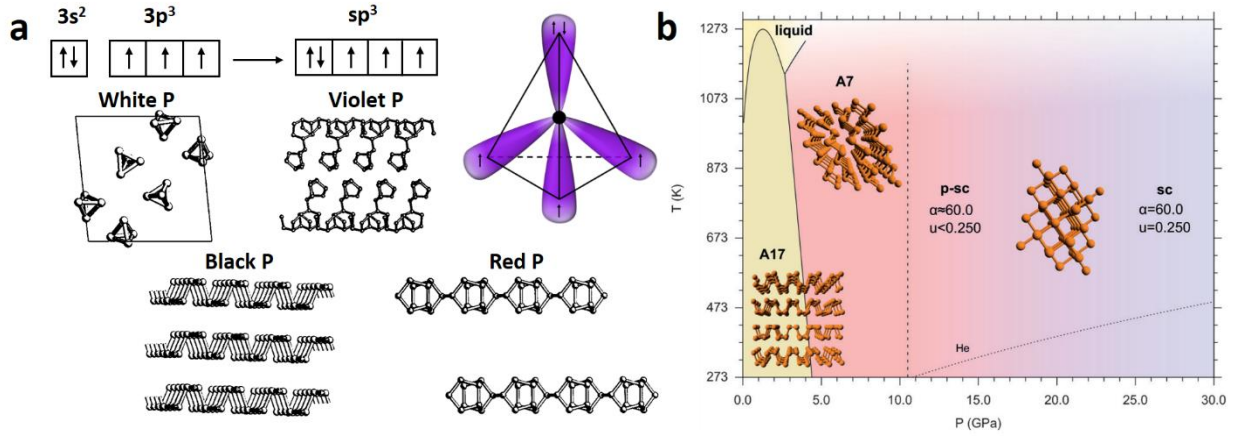

Figure 2.2 a) Valence electronic configuration, sp^3 orbital configuration and low pressure allotropes of P. Structures adapted from [56]. License at https://creativecommons.org/licenses/by/4.0/ b) Phase diagram of P. Reprinted from [57].

The tetrahedral bonding structure of P leads to other more stable 3-fold coordinated covalent solids. These include chain-like structures such as amorphous red P and monoclinic violet P (Figure 2.2a). The threefold coordination of group VA elements is also highly suitable to the formation of planar structures. In fact, the most stable form of P in ambient conditions is layered A17 orthorhombic black P (space group Cmca) (Figure 2.2a). Here "A17" refers to the Strukturbericht designation, which fully identifies the crystal structure, and "A" indicates a single element phase. Similar to graphite, bP is composed of an AB stacking of bilayers with atoms forming three strong covalent in-plane bonds and the layers are held together by vdW interactions. In contrast to graphite, the bP layers are puckered rather than planar due to the ~102° bond angle. Despite its high stability, bP synthesis from the metastable red P requires elevated pressures in the order of 8.5 GPa[58] or the use of catalysts[59].

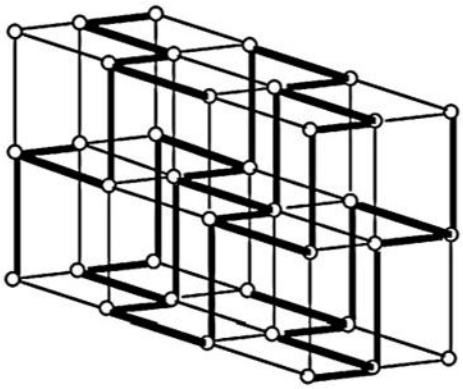

Figure 2.3 Relation between the simple cubic lattice and the A7 lattice. The bold lines indicate P-P bonds in A7 P. Reprinted from [60] (https://doi.org/10.1016/j.crhy.2015.12.009). License at https://creativecommons.org/licenses/by-nc-nd/4.0/

At ~5 GPa, bP transitions to the rhombohedral A7 phase (space group $R\bar{3}m$), which is another layered allotrope. The A7 and A17 phases are very similar, as they both have a bilayer structure of 3-fold coordinated atoms interacting together through vdW forces. The main difference between the two phases is the location of the non-bonding lone pairs. In A7, the doublets of neighboring atoms are on opposite sides of the bilayer. In A17, atoms in zigzag chains have their doublets on the same side of the bilayer, and neighboring chains have their doublet on the opposite side of the bilayer. The A17 → A7 transition is believed to be a diffusionless transformation occurring via a shuffle and shear mechanism [61], even though experimental evidence of this mechanism is lacking.

Reorganization of the covalent bonds and flipping of the doublets occurs during the transition. For this reason, the orientation of the bilayers is not the same after the phase transition. The demonstration of this transition in the Sb system will be presented in Chapter 6.

The A7 phase can be viewed as a distortion of a simple cubic (sc) unit cell along the [111] direction (Figure 2.3). Increasing the pressure in A7 P leads to a larger compression along the [111] out-of-plane direction than along the in-plane directions. This causes a gradual increase of the rhombohedral cell angle from 57.8° to ~60° at 10.5 GPa[57]. At this point, P adopts a pseudo single-cubic (p-sc) phase with three nearest neighbors (NNs) and three second NNs. Further increase in pressure leads to a transition to a true sc phase with six NNs.

Like all group VA materials, phosphorus exhibits a variety of electronic properties depending on its allotropic form. A17 P is a semiconductor since all its valence electrons are either in a strong covalent bond or in an inert doublet. On the other hand, the denser A7 phase does not provide enough space to the lone pair (especially at higher pressures), which increases the energy of the non-bonding doublet and closes the band gap at the Fermi level, making P a semimetal[62]. As pressure is increased further and the A7 phase transforms to the simple cubic phase, the number of atoms per unit cell goes from two to one. With an odd number of electrons per unit cell, P then becomes a true metal.

The phase stability and pressure dependence of heavier crystalline group VA elements is very similar to P but shifted to lower pressure. For this reason, the stability of the A17 phase decreases as we go down in the periodic table.

2.1.3 Arsenic

As is the first group VA element with filled d orbitals. However, the deep-lying As 3d orbitals have very little involvement in chemical bonding[63] and As shares many similarities with P. As vapor is mostly composed of As_4 molecules, with less than 1% As_2 and As[64]. Like P, As can be found in a metastable amorphous allotrope, analogous to red P[65]. Moreover, the yellow arsenic allotrope, composed of As_4 molecules, is very similar to white P, but has a cubic structure[64]. Yellow As slowly decomposes into the thermodynamically stable A7 gray As allotrope, analogous to the high pressure phase of P[17]. Still, the metastable A17 black As phase can also be found in nature[66].

Metastable A17 As can also be obtained by quenching A7 As[67]. Like P, the A17 As phase is semiconducting and the A7 phase is semimetallic[18].

Interestingly, pararsenolamprite, an intermediate phase of As, has been discovered[68, 69]. This phase has a layered structure with vdW interlayer interactions and is composed of alternating A7-like and A17-like atomic arrangements within the unit cell.

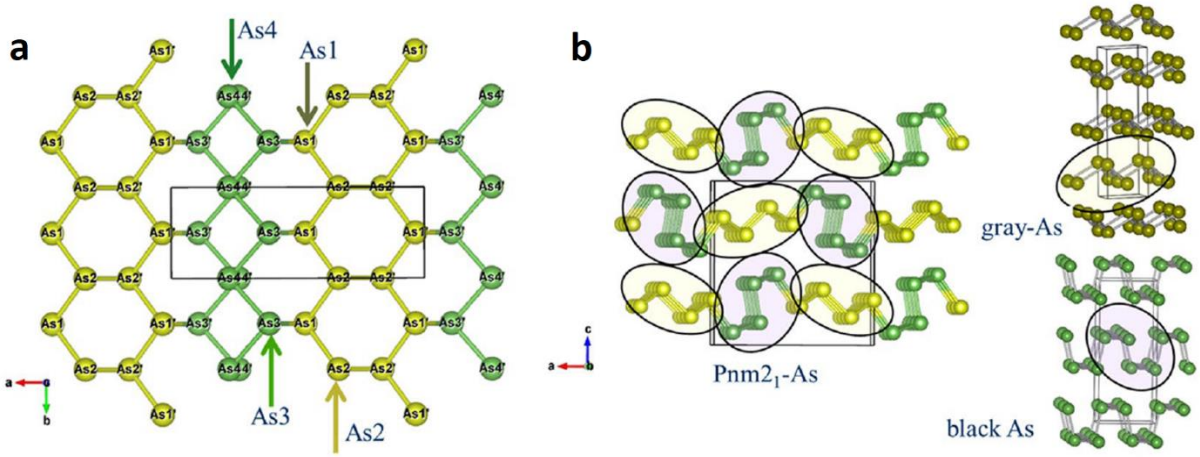

Figure 2.4 Atomic structure of pararsenlolamprite. The layers are composed of alternating A17-like (green) and A7-like (yellow) regions. a) Top view of a single bilayer. b) Side views of the layered As allotropes. Reprinted from [68]. License at https://creativecommons.org/licenses/by/2.0/

Several phase transitions are observed in As at high pressures. Similar to P, As first transitions from A7 to the metallic sc phase at 25 GPa[70] and then to tetragonal and body-centered cubic (bcc) phases at higher pressures[63].

2.1.4 Antimony

Like P and As, Sb vapor is mostly composed of Sb_4 molecules, with Sb_2 and Sb species becoming more important with increasing temperature[71]. Moreover, allotropes analogous to amorphous red-P (black Sb) and molecular white P (yellow Sb) have been observed[65, 72]. Like As, the thermodynamically stable Sb phase under ambient conditions is A7, with 96° bond angles[65]. The lower s-p mixing, and higher nucleus charge screening of heavier atoms leads to more important interlayer interactions, which stabilize the A7 phase. For this reason, the bulk A17 Sb phase has not been observed under any conditions. However, several other Sb phases can be observed at

elevated pressures. Early experiments indicated a transition from A7 to the sc phase at 7 GPa, followed by a transition to the hcp phase at 8.5 GPa[73]. However, it was later shown that A7 Sb only approaches the sc phase by the reduction of the c/a ratio close to the $\sqrt{6}$ value of the sc phase[74]. Nonetheless, the Sb atoms maintain a quasi-layered structure with 3-fold coordination and bond angles above 90°. Further investigation of the high-pressure phases does not mention the presence of the hcp phase. Rather, at P > 8.5 GPa, Sb is thought to transition to the Sb-II phase[75], which is composed of a tetragonal host lattice, with an incommensurate tetragonal guest lattice of Sb chains (Figure 2.5a)[76, 77]. Sb then transitions to a simpler bcc phase at 28 GPa[78]. Like As, the high-pressure phases of Sb are metallic due to their higher coordination and more important s-p mixing[79].

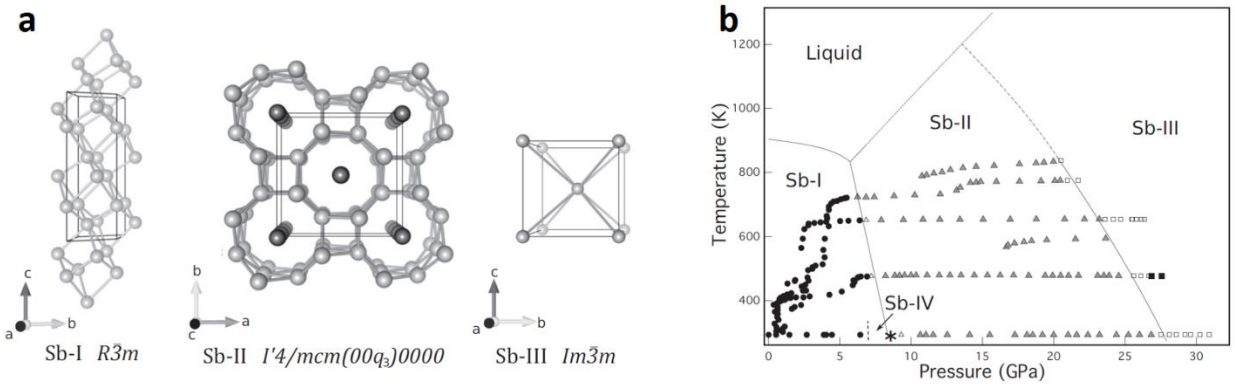

Figure 2.5 a) Equilibrium phases of Sb: Sb-I (A7), Sb-II (tetragonal incommensurate composite structure) and Sb-III (bcc). b) Experimental P-T phase diagram of Sb. Reprinted from [80] (https://doi.org/10.1103/PhysRevB.97.144107).

Even though sc-Sb is not observed at high pressures, experiments have shown its existence in liquid-quenched and vapor-quenched thin films[81, 82]. The authors identified the metastable sc-Sb phase, as well as face centered cubic (fcc), tetragonal and a second rhombohedral phase using transmission electron diffraction[81, 82]. Nonetheless, transition to the equilibrium rhombohedral A7 phase and to the hexagonal close-packed (hcp) phase were observed after heating under electron-beam irradiation.

2.1.5 Bismuth

Bi is the heaviest stable group VA atom and the first to have filled 4f orbitals. Unlike P, As and Sb, Bi vapor is mostly composed of Bi_2 molecules[83]. Moreover, allotropy in Bi is less diverse than

for lighter group VA elements. Amorphous Bi films can be produced at low temperature but are found to convert to the stable crystalline A7 phase as their thickness increases[84, 85]. The Bi and Sb phase diagrams are similar, but with much lower transition pressures in Bi (Figure 2.6). Like for Sb, the layered Bi A17 phase has never been observed. Bi transitions to monoclinic Bi-II at 2.55 GPa[86]. Similar to Sb below 8.5 GPa, Bi-II almost has 6-fold coordination and is analogous to a distorted sc phase[87]. Bi then transitions to tetragonal Bi-III (analogous to Sb-II) and then to bcc Bi-V at 7.7 GPa[88].

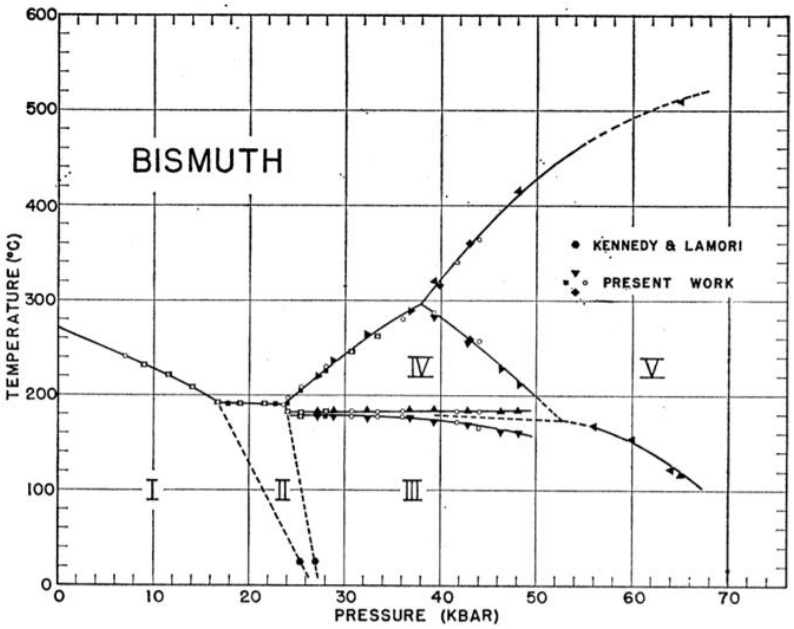

Figure 2.6 Phase diagram of Bi. Bi-I is the A7 phase, Bi-II is a distorted sc phase, Bi-III is tetragonal, Bi-IV is orthorhombic and Bi-V is bcc. Reprinted from [89] (https://doi.org/10.1103/PhysRev.131.632).

2.2 Group VA 2D materials

Reducing the dimensionality of materials has important consequences on their physical properties. The thermodynamic stability of low-dimensional structures is strongly affected by the increasing contribution of surface energy at nanoscale dimensions. For instance, a melting point depression is observed in nanoparticles (0D) of decreasing size[90, 91]. Surface energy contributions can also stabilize unstable bulk phases in nanowires (1D)[92-94]. The stability of vdW layered materials is ensured by their strong in-plane bonds and their self-passivated nature leads to small surface

energies. For this reason, we can assume that given the existence of a stable bulk layered allotrope, the corresponding 2D phase can be isolated. This allows to easily predict the potential existence of novel 2D allotropes and to design synthesis methods for their production.

While the thermodynamics of vdW layered materials is weakly influenced by the reduced dimensions, several other materials properties (electronic, optical, topological, magnetic, etc.) can be greatly altered, mainly due to quantum confinement and reduced interlayer interactions, thus generating a surge of interest in the field of 2D materials.

This section reviews theoretical and experimental studies on group VA 2D materials properties, synthesis, and stability. First, a general introduction to 2D materials synthesis is presented. Then, the experimental and theoretical work on all 2D pnictogen systems is reviewed.

2.2.1 Synthesis methods for 2D materials

There are two main approaches to synthesize 2D materials: exfoliation and growth methods[95]. The various methods are illustrated in Figure 2.7.

The goal of exfoliation methods is to obtain 2D layers from their parent layered crystals. These methods can be easily applied to a wide range of materials and are particularly useful in exploratory research phases to allow for the investigation of the properties of new 2D materials. In fact, systematic DFT investigations have revealed more than 1800 layered compound materials, which are potentially exfoliable to yield 2D materials[6]. The physical properties and potential applications of these materials can be systematically identified by *ab initio* calculations and suitable candidates can then be readily synthesized by exfoliation methods from these bulk crystals.

The two main classes of exfoliation methods are micromechanical exfoliation and liquid phase exfoliation. Micromechanical exfoliation is the most straightforward method and was first used for the exfoliation of graphene from graphite crystals by Novoselov and Geim in their Nobel prize work published in 2004[96]. Since then, the method has been used to produce TMDs[97], 2D h-BN[3], group VA 2D materials[20, 98] and many others. Micromechanical exfoliation was first performed using adhesive tape (Scotch Tape method). However, it is typically achieved using polymers which leave less residues. To obtain the 2D material, a flake of the bulk layered material is first deposited on the adhesive polymer. Another piece of polymer is then used to cleave thinner 2D flakes by

stamping the first flake. The process can be repeated to obtain a higher yield of thinner flakes. Finally, the 2D flakes are transferred to a substrate of interest by stamping the flake covered polymer onto the substrate and slowly peeling it off. 2D flakes of various thicknesses can then be identified by various methods including previously calibrated optical microscopy measurements based on the color and contrast of the flakes as well as by Raman scattering spectroscopy. Direct thickness measurements for flake identification or calibration of optical microscopy/Raman spectroscopy can be done by atomic force microscopy (AFM).

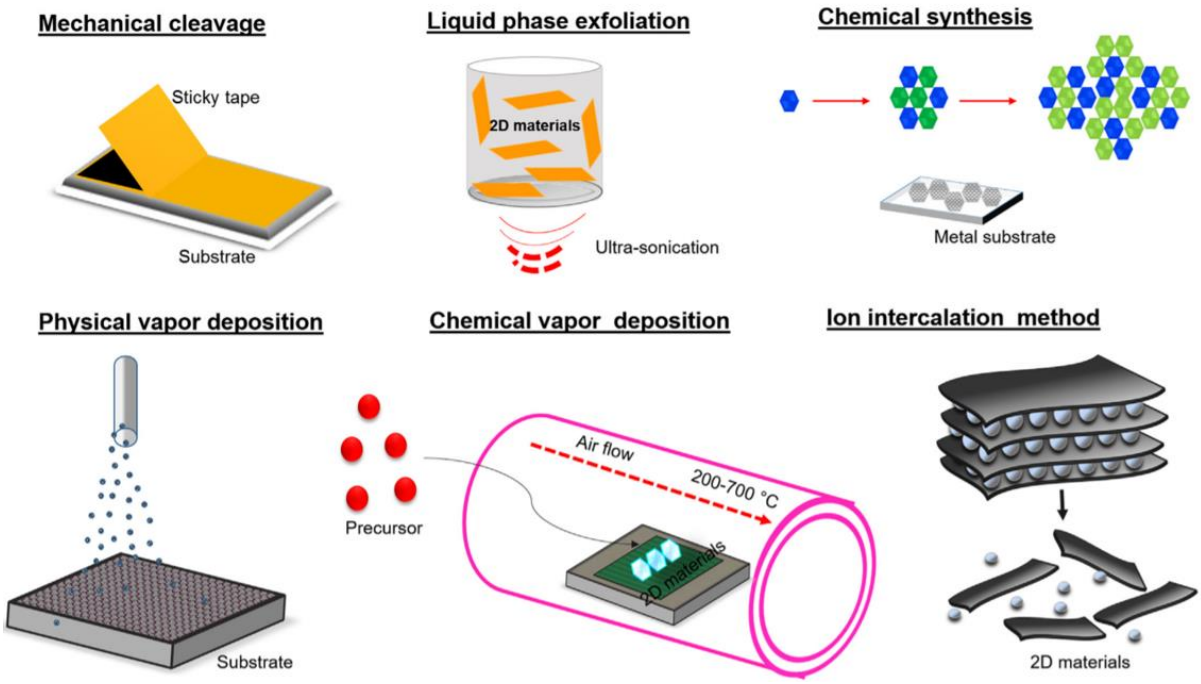

Figure 2.7 Overview of exfoliation (mechanical cleavage, liquid phase exfoliation and ion intercalation) and growth (chemical vapor deposition, physical vapor deposition and chemical synthesis) 2D material synthesis methods. Reprinted from [99], Copyright (2019), with permission from Elsevier.

On the other hand, liquid-phase exfoliation is typically achieved by applying shear force on powdered bulk vdW layered materials in a solvent[100]. The shear force is usually applied using ultrasonication, but can also be obtained by other methods such as ball milling[101]. The liquid exfoliation can also be done by ion or polymer intercalation. After exfoliation, the dispersion is then centrifugated and the supernatant, which contains the thinner flakes, is isolated. Liquid exfoliation generally yields a higher concentration of single and few-layer flakes than

micromechanical exfoliation. Moreover, the solvents can protect air-sensitive 2D materials from oxidation. On the other hand, this method requires more optimization and often leads to 2D flakes with sub-μm lateral dimensions.

Exfoliation methods have important limitations. First, they are limited to 2D materials with available stable parent layered materials. For instance, 2D materials like silicene[102, 103] and germanene[104] have 3D covalently coordinated bulk counterparts. Moreover, exfoliation methods yield materials with limited quality. In fact, exfoliation gives little control over the thickness of the 2D materials, as well as on their lateral dimensions. It is also challenging to produce complete films with these methods. Furthermore, even when films can be produced, there is no control over their crystalline orientation. On the other hand, growth approaches can allow producing high-quality 2D materials and to synthesize 2D materials which do not have bulk parents. The most used growth approaches are chemical vapor deposition (CVD) and physical vapor deposition (MBE). These two methods are based on the deposition of precursor species from a vapor phase onto a suitable substrate. The substrate's role is to support the 2D material and to promote the nucleation and growth of specific allotropes or crystalline orientations. Vapor deposition methods can yield high-quality and uniform films. Nonetheless, they are much more cumbersome to develop and require a more developed infrastructure.

2.2.2 Predictions and synthesis of group VA 2D materials

Known 2D pnictogens are single bilayer or few bilayer thick films of the bulk A7 and A17 layered phases. The 2D form of these allotropes are referred to as β-2D-X and α-2D-X, respectively, where X can be any group VA element. These atomically thin, or few-layer films display strikingly different electronic and topological properties as compared to the bulk phases. The following section reviews the literature on the discovery and on the predictions of the potential existence of group VA 2D allotropes, as well as their emerging physical properties and their thermodynamic and atmospheric stability. The material systems are presented in the order in which they were first experimentally synthesized. We note that the presented literature includes results that were obtain in this project.

2.2.2.1 Bismuthene

Studies of the growth of Bi thin films date back to the 1960s[105]. However, growth of ultrathin Bi films with layered structure began in the early 2000s[106-112], before the discovery of graphene. Nagao et *al*. first grew few-layer thick Bi films on Si(111)-(7×7) by MBE. They deposited Bi at deposition rate (F) 2-3 BL/min on Si(111)-(7×7) at RT. They initially reported the growth of the (111) orientation of the A7 phase, which corresponds to few-layer β-2D-Bi. There was formation of an initial wetting layer, followed by the nucleation of textured 2D nanocrystals. After coalescence of the nanocrystals, a Bi(111) film grew with a 2D step flow growth mode up to ~100 bilayers (BLs). In the next few years, the same group published a series of papers to correct this interpretation[108-110, 112]. They found that Bi initially grow in the (110) orientation up to a thickness of 4 BLs (Figure 2.8). Note that the authors use the trigonal indexing with 3 indices, rather than the rhombohedral indexing. After the growth of 4 BLs, a transition to the (111) orientation is observed by scanning tunneling microscopy (STM) and low-energy electron diffraction (LEED). The authors also carried out *ab initio* calculations to understand the nature of the Bi(110) film. They found that the Bi(110) film rearranges into a layered structure (Figure 2.8).

Ù

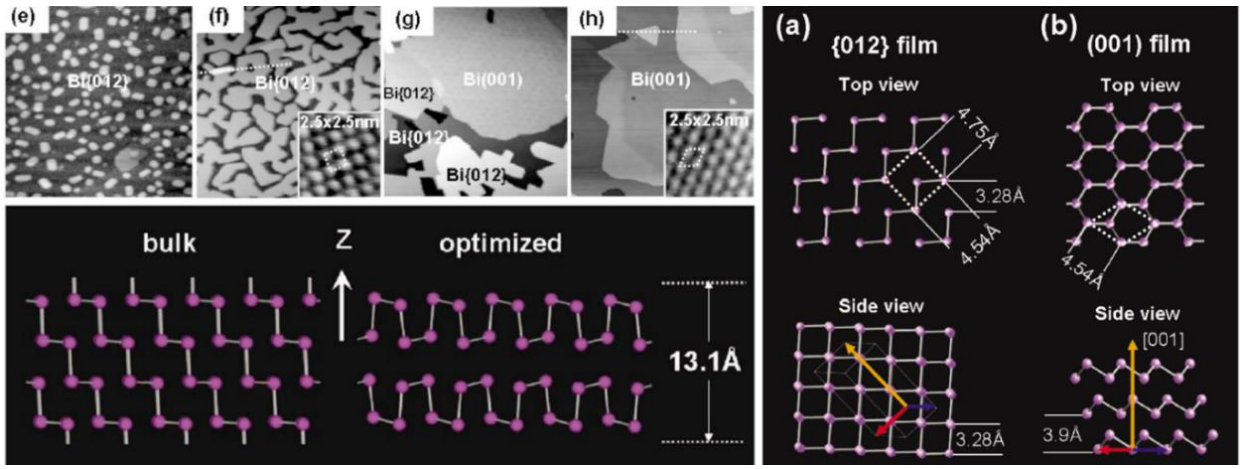

Figure 2.8 Growth of Bi on Si(111)-(7×7). Top-left panel: STM images (160 × 160 nm^2) at increasing deposition (< 2 monolayers (ML), 2-4 ML, 4-6 ML and >6 ML, from left to right). Bottom-left panel: bulk and relaxed (DFT) structures of 4 ML thick Bi(110) films. Right panel: top and side view of Bi(110) (left) and Bi(111) (right) thin films. Reprinted from [109] (https://doi.org/10.1103/PhysRevLett.93.105501).

The authors claim that this structure corresponds to the bP structure (A17 phase). However, even though the puckered BLs are similar to the bP BLs, the structural model presented by the authors does not correspond to the A17 phase. In fact, BLs in the A17 phase are AB stacked with an interlayer displacement vector of [1/2a 0 0] (compared to the proposed [0 0 1/2c]. The authors did not characterize the stacking of the layers and therefore it is impossible to identify the phase as being either A17 Bi, A7 Bi(110) or another stacking order of α-2D-Bi like the one presented by the authors. In fact, to this day, this question has not been treated in the literature for Bi thin films. This question, along with the stability of the A17 phase will be addressed in details in Chapter 6 for the Sb system. In 2005, Scott et *al*. found a similar behavior with a (110) to (111) transition for ultrathin Bi on highly oriented pyrolytic graphite (HOPG)[111]. Hatta et *al*. also observed the same phenomena on Ge(111) substrates a few years later[113].

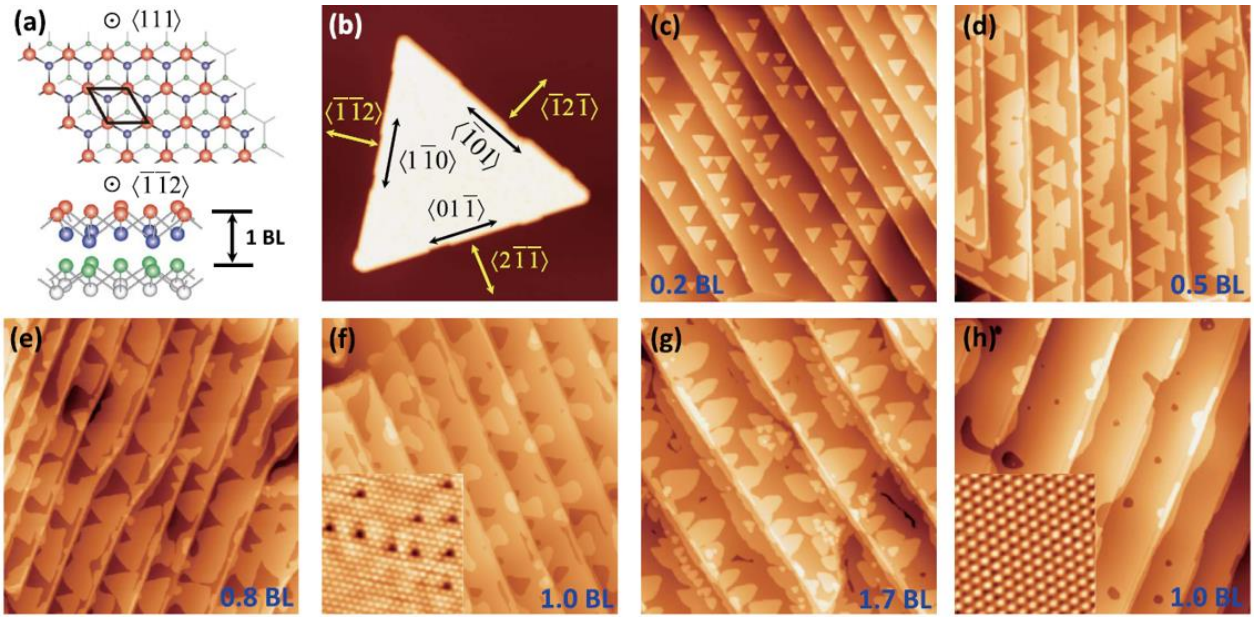

Figure 2.9 (a) Crystal structure of BL Bi(111). (b) STM image a triangular of Bi(111) BL island grown on Bi_2Te_3 (57 × 57 nm^2) c-h) STM of Bi(111) grown on Bi_2Te_3 at increasing coverages (380 × 380 nm^2) Reprinted from [114] with permission from AIP Publishing.

A theoretical paper by Murakami et *al*. in 2006 sparked interest for the 2D-Bi system[31]. They predicted that a previously never observed phase of matter (quantum-spin Hall phase (QSH)) could exist in 1 BL thick Bi(111) films. In 2008 Koroteev et *al*. carried out a more detailed DFT studies of ultrathin Bi(111) and Bi(110) films and predicted an evolution from a semiconducting single-

layer Bi(111) to semimetallic multilayer Bi(111) and Bi(110)[32]. They also found that the large SOC would lead to Rashba spin splitting of the surface states.

Even though Bi growth modes are mainly 2D, the initial growth stage of Bi in the (110) orientation made the testing of these predictions more challenging. In 2011, Hirahara et *al*.[115] demonstrated the MBE growth of BL Bi(111) on Bi_2Te_3. They first grew a few-layer Bi_2Te_3 film on Si(111)-(7×7) to supress the Bi(110) growth. They then deposited a single BL Bi(111) film, which they characterized using ARPES. Based on *ab initio* calculations, they concluded that the ARPES data suggests the presence of the topologically protected edge states of the 2D QSH phase as well as topologically protected surface states. In 2012, Chen et *al*. reproduced the growth and studied its behavior with STM[114]. They first grew Bi_2Te_3 on bilayer graphene on 6 H-SiC(0001) and then deposited Bi at a F=0.1 BL/min at RT and 450 K. Growth at RT resulted in the formation of triangular BL Bi(111) flakes, while growth at 450 K leads to a step-flow growth mode with a smooth surface (Figure 2.9).

In 2016, 2D-Bi started to regain popularity with the discovery of other 2D pnictogens[29]. Since then, many papers have reproduced previous theoretical predictions and investigated 2D-Bi allotropes. Moreover, a few attempts at synthesizing 2D-Bi using exfoliation[116, 117] and hot pressing[118] have been made. In 2017, Reis et *al*. demonstrated the growth of single-layer flat (graphene-like) 2D-Bi on 4H-SiC(0001). They deposited Bi at ~500 °C, which led to reconstructed $(\sqrt{3} \times \sqrt{3})$-Bi-SiC(0001). Post-growth annealing at ~400 °C was then done to improve the Bi film order. The resulting flat 2D-Bi is stabilized by bonding with the surface Si atoms. Using angle-resolved photoemission spectroscopy (ARPES) and STM, the authors determined that the Bi/SiC is wide-gap quantum spin Hall insulator. By scanning-tunneling spectroscopy (STS), they found a 0.8 eV bulk band gap and conductive edges states. The authors mention the potential of this material for high T dissipationless spin current devices.

2.2.2.2 Phosphorene

The electronic structure and band gap opening in single layer bP were first predicted in 1981 by Takao et *al*. using a tight-binding approach[119]. Nonetheless, phosphorene was first synthesized by exfoliation from bP crystals only in 2014[20, 120, 121]. In these first studies, the authors fabricated FETs with few nm thick bP films and demonstrated high hole mobilities up to ~1000 $cm^2V^{-1}s^{-1}$. The

authors observed a strong conductance anisotropy, which originates from the anisotropic rectangular unit cell. By means of DFT calculations, the authors also found that 2D-bP has a thickness dependent direct band gap which increases with decreasing thickness from 0.3 eV in bulk to 1.0 eV in single layers. More accurate calculations based on hybrid functionals[21, 122, 123] found higher band gap values in the order of 1.5 to 2 eV, and STS measurements confirmed a band gap of 2.05 eV for single layer bP[124]. The *ab initio* calculations also indicated that the hole mobility could reach 10 000 $cm^2V^{-1}s^{-1}$ in single layer bP. Moreover, the authors found significant exciton binding energies (~800 meV) in single layer bP. The crystal structure of 2D-bP also leads to anisotropic optical properties such as linear dichroism[21] and anisotropic Raman responses[125, 126].

Due to its thickness-dependent direct band gap, high charge carrier mobility and anisotropic properties, 2D-bP quickly attracted a lot of attention for electronic and optoelectronic applications[20, 120-122, 127-133]. These include bP as a channel material for high-performance FETs with ultrashort channels, as well as tunable infrared (IR) to visible photodetectors and light sources. However, two main obstacles to the integration of 2D-bP in novel technologies quickly emerged. The first is the rapid oxidation of 2D-bP in ambient conditions. In fact, Favron et *al*. have shown an increased oxidation rate with decreasing thickness due to a higher photoassisted oxidation rate when the conduction band energy shifts closer to oxygen acceptor states[134]. Nonetheless, bP oxidation can be avoided or slowed down by capping[135] or chemical passivation[136]. The second obstacle however remains highly problematic to this day. In fact, there are currently no growth method to produce 2D-bP films with reasonable quality and homogeneity. There have been a few attempts at growing 2D-bP films (Figure 2.10). Xu et *al*. used MBE with a white P source and cracker cell at 900°C to deposit P species on Si(111) and Si(100) substrates at RT. The authors claim to have obtained few-layer 2D-bP quantum dots (QDs) with average radii of 27.5 nm and heights of 3.1 nm, based on AFM, Raman spectroscopy and XPS measurements (Figure 2.10). We however note that the resolution of the presented AFM data might lead to overestimation of the radius of the dots. Moreover, complementary characterization such as high-resolution TEM (HRTEM) would be necessary to confirm the nature of the QDs. In fact, it is rather surprising that P would condense in the bP phase at RT without any catalyst. Smith et *al*. used a different method to obtain 2D-bP flakes on a Si substrate[137]. They first deposited an amorphous red P film by evaporation of either bP or red P in a tube furnace. The red P film was then annealed in a pressure

vessel containing Sn and SnI_4 at 27.2 atm. The exact temperature inside the vessel in unknown, but the authors report an external temperature of 950°C, which is then reduced gradually to 600°C within a few hours then cooled down. This method yielded various 2D flakes with thicknesses going from 4 bilayers up to hundreds of nm. Li et *al*. used a relatively similar method to obtain high quality flakes with domain sizes going up to 70 µm[138]. They first deposited an amorphous red P film on a sapphire substrate in a tube furnace. Then, they transferred a 2D h-BN flake on the red P film. The substrate was then introduced into an end-loaded Boyd-England piston cylinder and the red P film was converted to bP at 1.5 GPa and 700°C. Figure 2.10 shows cross-sectional TEM of the synthesized film. The bP is well oriented on the substrate and has an atomically sharp interface with h-BN. Nonetheless, the minimum film thickness is in the order of 50 nm.

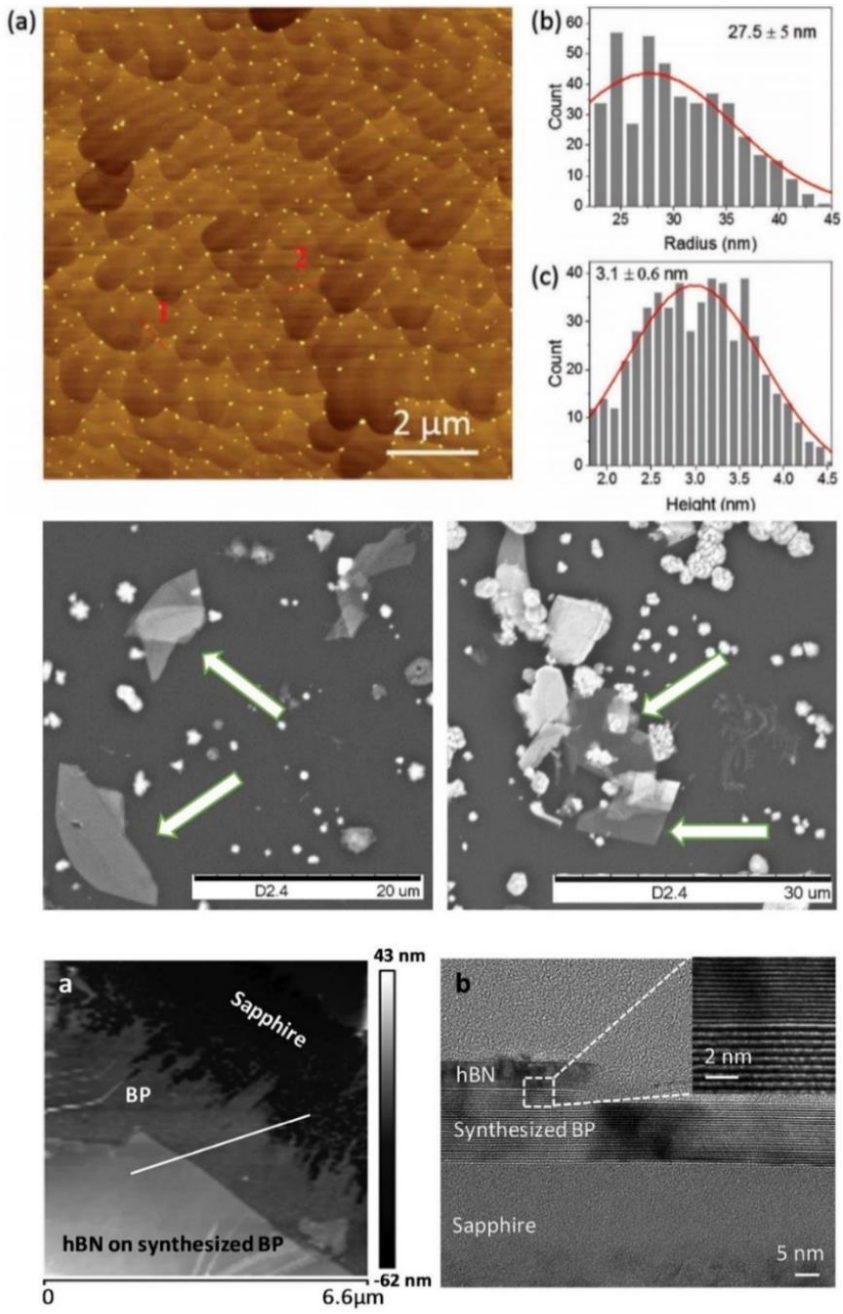

Figure 2.10 Direct synthesis of 2D-bP. Top: MBE grown α-2D-P "quantum dots". Reprinted from[139]. Middle: α-2D-P flakes obtained by the conversion of an amorphous red P film using Sn and SnI_4 at 27.2 atm. Reprinted with permission from[137]. © 2016 IOP Publishing Ltd. Bottom: α-2D-P flake obtained by the high-pressure conversion of a red P film capped by a 2D h-BN layer. Reprinted from[138] .

A few months after the exfoliation of 2D-bP, Zhu and Tománek published a DFT study of a new layered allotrope of P and its related β-2D-P phase[24]. The authors named the bulk allotrope blue phosphorus. Blue P is very similar to the high-pressure A7 phase of P and is an AB stack of buckled honeycomb bilayers. By comparison, A7 P is an ABC stack of buckled bilayers. Unlike the high pressure A7 phase, blue P and A7 P at 0 Pa are semiconductors with band gaps of 1.3 eV and 1.1 eV, respectively. The authors also calculated the band structure of single layer blue P and found it to be an indirect semiconductor with a ~3.0 eV band gap. Contrarily to α-2D-P, β-2D-P cannot be obtained by exfoliation since the A7 P phase reverts to the A17 phase at ambient pressure[57].

Nonetheless, Zhang et *al*. reported the synthesis of single layer blue P by MBE in 2016. They used bulk bP as a source of P_4 molecules which were deposited on an Au(111) substrate at 230°C. They characterized the atomic structure and electronic properties using STM, STS and DFT (Figure 2.11). They found that the P overlayer rearranges into a superstructure with a supercell formed of two triangular groups of six P atoms and a lattice constant of 14.7 Å. The 6 dots seen in STM are however most likely the top atoms since the calculated lattice constant of blue P is 3.28 Å, which means that the supercell should contain about 40 atoms. The authors also found using STS that the P layer is semiconducting with a 1.10 eV bandgap. It is rather obvious from the STM images and the simulated structure that the P overlayer does not have the single layer β-2D-P structure. In fact, the overlayer forms ~1 nm triangular domains with β-2D-P-like structure. The buckling orientation changes at the intersection of each triangle (neighboring atoms are both on the bottom of the bilayer at the intersection). Considering the 2.40 Å distance between P and the substrate, it is probable that there is a strong covalent interaction between Au and P. Nonetheless, the authors find a relatively weak substrate-layer interaction of -270 meV/atom using DFT. However, since P-P bonds are missing on the edges of the unit cell, we can safely assume that strong P-Au bonds are compensating for the missing P-P bonds to give the -270 meV/atom interaction energy. In fact, Gu et *al*. addressed the issue of Au-P interactions by passivating the Au(111) substrate with a Te overlayer prior to growth[140]. While the authors claim to have a quasi-free-standing blue P layer on Te/Au, the triangular supercell is still visible in their STM images. It is therefore plausible that strong Au-P interactions are required to stabilize the 2D blue P structure or at least to catalyse its growth. In fact, no multilayer blue P are observed in either study, which highlights the importance

of the Au substrate in blue P growth. The effects of substrate-layer interactions will be discussed in detail in Chapter 4.

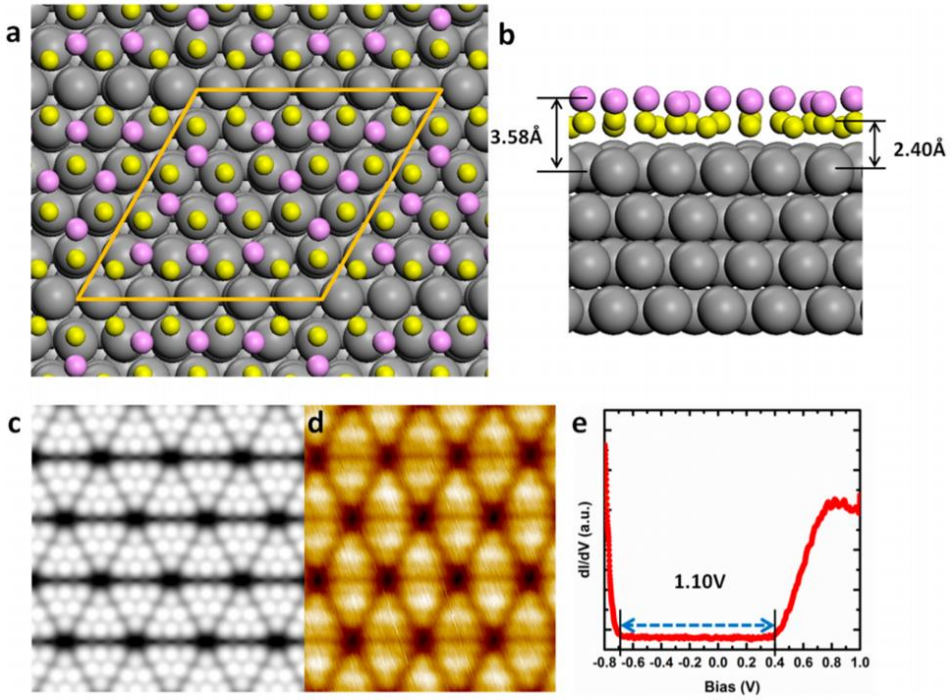

Figure 2.11 Growth of blue phosphorus on Au(111). a, b) Structural model of single-layer β-2D-P on Au(111). c, d) Simulated and measured STM image of the structure in (a, b). e) dI/dV STS curve measured on the β-2D-P layer, suggesting the presence of a 1.10 eV band gap. Reprinted with permission from *Zhang, J. L. et al., Nano Letters 2016, 16, (8), 4903-4908*. Copyright (2016) American Chemical Society [141].

2.2.2.3 Antimonene

Like many other 2D materials, 2D-Sb has been studied in other contexts before the rise of the field of 2D materials. The research on Sb(111) thin films began in 2004 and focused mainly on the topological properties of thin Sb(111) films using ARPES measurements and *ab initio* calculations[34, 142-145]. Theoretical investigations revealed that Sb(111) undergoes several topological transitions as its thickness is reduced. Zhang et *al*. determined that Sb transitions from a topological semimetal to a topological insulator at a thickness of 22 bilayers, then to a quantum spin Hall phase at 8 bilayers and finally to a trivial semiconductor at 3 bilayers[34]. However, the early experimental studies did not investigate the growth behavior or morphology.

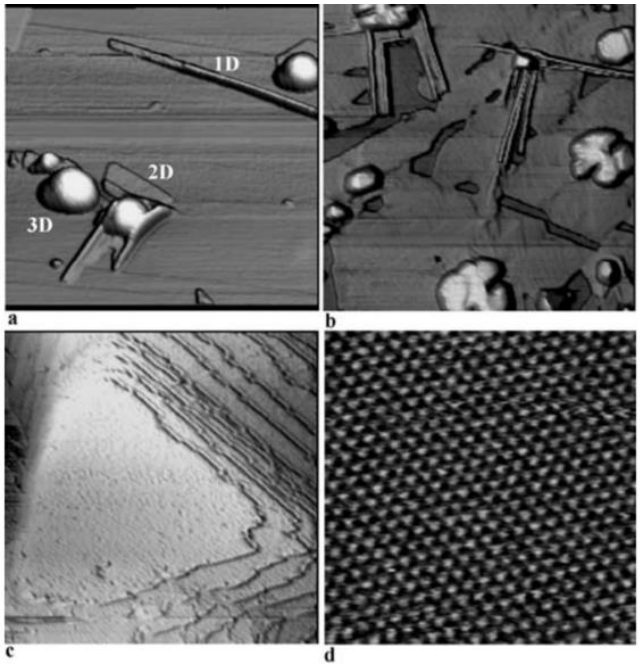

Figure 2.12 STM images of Sb deposited on graphite. a) After 1.2 nm deposition at RT. b) After 4 nm deposition at RT. c-d) Zoom-in images from a facetted 3D island. Image area: (a) 1 × 1 μm^2, (b) 2 × 2 μm^2, (c) 60 × 60 nm^2 and (d) 8 × 8 nm^2. Reprinted by permission from Springer Nature Customer Service Centre GmbH: Springer Nature, Applied Physics A: Materials Science & Processing [146], Copyright 2007.

On the other hand, Wang et *al*. studied in detail the MBE growth of Sb on HOPG[146, 147]. They varied the substrate temperature between RT and 100°C and found that 1D, 2D and 3D structures can grow simultaneously (Figure 2.12). At RT, only 3D structures grow and at higher temperatures, mostly 2D and 1D structures grow. The 2D and 3D structures were found to be A7 Sb(111). The authors also suggested that the nanowires (NWs) initially nucleate in the sc phase and transition to a compressed A7 Sb(110) phase.

In 2015, Zhang et *al*. published a paper which sparked the interest for antimonene[28]. They determined the electronic properties and stability of single and few-layer β-2D-Sb and β-2D-As using *ab initio* calculations. β-2D-Sb was predicted to be stable and potentially exfoliable from bulk A7 Sb. Using the HSE06 hybrid functional, the authors determined that β-2D-Sb should be a semiconductor with a 2.28 eV indirect band gap. They also predicted that single-layer β-2D-Sb would transition to a direct band gap (1.96 eV) semiconductor at 7% biaxial tensile strain. Aktürk

et *al*. later published detailed DFT calculations of 2D-Sb allotropes, which included spin-orbit coupling[26]. The strong SOC, reduces the band gap to 1.55 eV for monolayer β-2D-Sb. Soon after, Wang et *al*. studied multiple other theoretical 2D-Sb allotropes[27]. Only β-2D-Sb and α-2D-Sb were found to be stable, whereas other allotropes have imaginary phonon modes. Unlike β-2D-Sb, α-2D-Sb is predicted to be a direct band gap semiconductor with a narrow gap of 0.34 eV[26].

Further theoretical studies explored the physical properties of β-2D-Sb. Pizzi et *al*. carried out detailed multiscale simulations of β-2D-Sb metal-oxide-semiconductor FETs (MOSFETs) and found high performances even at ultrashort channel lengths[148]. They determined electron and hole mobilities of 630 $cm^2V^{-1}s^{-1}$ and 1737 $cm^2V^{-1}s^{-1}$, respectively. They also found that the subthreshold swings are at the minimal achievable value of 60 mV dec^{-1} at channel lengths down to 7 nm. Other studies examined the potential tunability of the physical properties of β-2D-Sb. For instance, Wang et *al*. have shown that the magnitude and nature (direct or indirect) of the band gap of β-2D-Sb nanoribbons can be tuned by controlling the width of the ribbon and the orientation of its edges[149]. Aktürk et *al*. demonstrated the tunability of the magnetic properties of β-2D-Sb by the adsorption of various adatoms[150]. Zhang et *al*. explored different methods to induce topological phase transition in 2D-Sb such as biaxial strain[151] and controlled oxidation[152]. In fact, depending on the stoichiometry, antimonene oxides were found to be 2D topological insulators with band gaps of up to 177 meV.

Synthesis efforts for 2D-Sb mainly focused on the β phase since the bulk A17 Sb phase was never observed. β-2D-Sb was first produced by micromechanical exfoliation[98]. Thin Sb flakes were peeled off from a freshly cleaved A7 Sb crystal using an adhesive tape and then transferred to a viscoelastic polymer. The viscoelastic polymer was used to transfer the flakes onto a 300 nm SiO_2/Si substrate. The authors obtained few-layer flakes as well as single layer regions (Figure 2.13). They confirmed the atomic thickness and mechanical stability of the flake by folding it over itself using the AFM tip (Figure 2.13 (c,d)). The resulting ~0.4 nm step height corresponds to one β-2D-Sb BL. Soon after, few-layer β-2D-Sb was produced by liquid phase exfoliation by the same group[153]. The dispersion was made in 4:1 isopropanol/water using a standard sonication and centrifugation method. One of the most important conclusions of these two papers was that contrary to α-2D-P, β-2D-Sb is highly stable in ambient conditions. In fact, the buckled honeycomb lattice of a few-layer β-2D-Sb flake was still resolvable by AFM after exposure to atmospheric conditions

for two months. However, the authors do not describe the oxidation of single layer flakes. The early oxidation stages of β-2D-Sb will be discussed in Chapter 6 based on LEEM and XPEEM measurements.

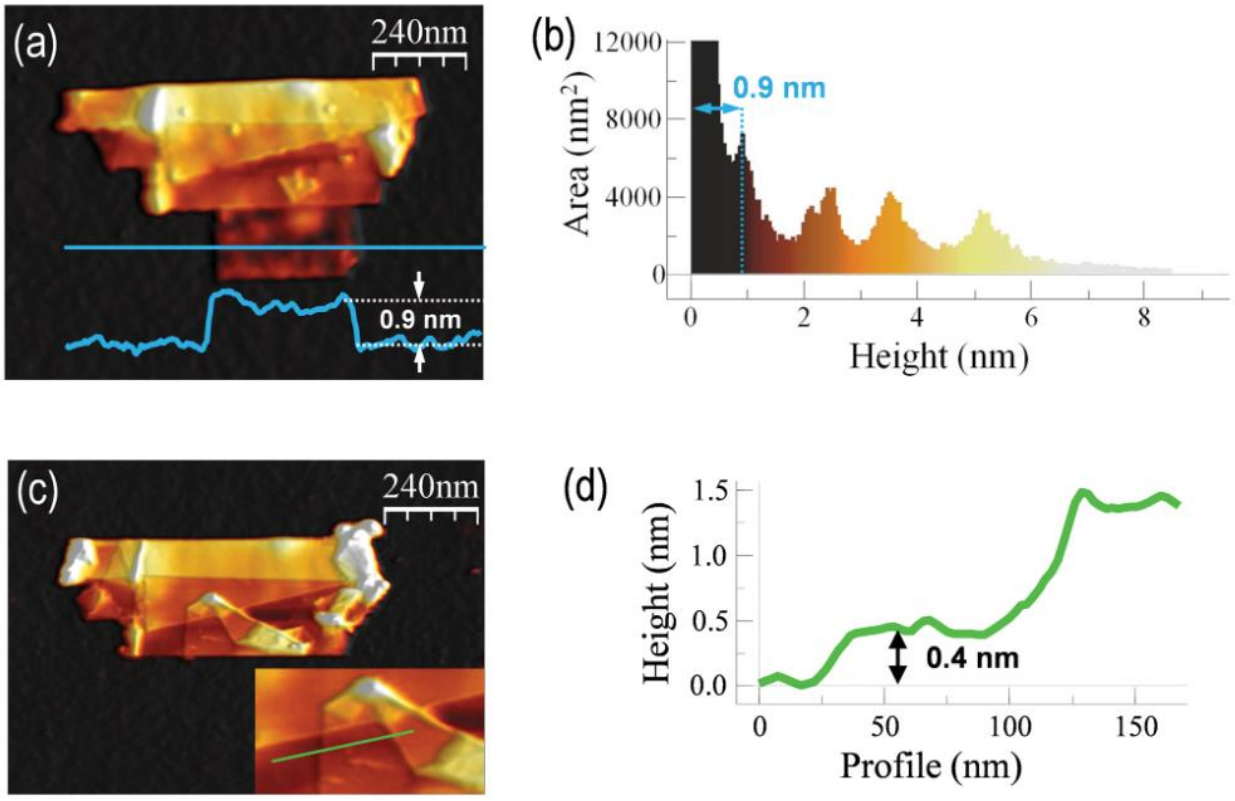

Figure 2.13 AFM of micromechanically exfoliated β-2D-Sb. a) AFM image of a β-2D-Sb flake. b) Histogram of the flake in (a). c) Same flake as in (a) but after a nanomanipulation process. The lower terrace was folded over itself using the AFM tip. d) Profile along the green line in the inset in (c). The 0.4 nm step height indicates that the bottom terrace is single layer thick. Reprinted from[98].

Soon after, the direct growth of β-2D-Sb was developed by three groups in parallel. The first study by Ji et *al*. came out at the end of 2016[154]. The growth was done by vdW epitaxy on fluorophlogopite mica (001) substrates ($KMg_3(AlSi_3O_{10})F_2$). A two-zone tube furnace along with Sb powder precursor were used (Figure 2.14). The first zone (Sb powder) was heated at 660 °C and the second zone was heated at 380 °C. The Sb vapor was carried by Ar+H_2 carrier gases (30% H_2). With this method, the authors obtained few-layer β-2D-Sb flakes, as well as thicker β-2D-Sb islands. The authors report thicknesses from 1 nm to 50 nm and lateral dimensions of 5-10 µm.

The grown flakes (4-50 nm) have polygonal shapes originating from the A7 crystal structure (triangular, hexagonal, etc.). The crystal structure is confirmed by HRTEM and the authors carried out various characterization. They found that the E_g and A_{1g} Raman modes shift from 111 cm^{-1} and 150 cm^{-1} in bulk A7 Sb to 139 cm^{-1} and 166 cm^{-1}. However, we note that in their work, the signal to noise ratio of the E_g peak in flakes below 8 nm was most likely too low to properly determine the peak position. The authors also determined relatively high optical transmittance (between 75-85%) in the λ=400-700 nm range for flake thicknesses between 4 and 18 nm. Finally, the authors measured the electric properties of flakes with thicknesses >30 nm. The flakes are found to have conductivities up to 10^4 S m^{-1} and no effect of the gate voltage is observed.

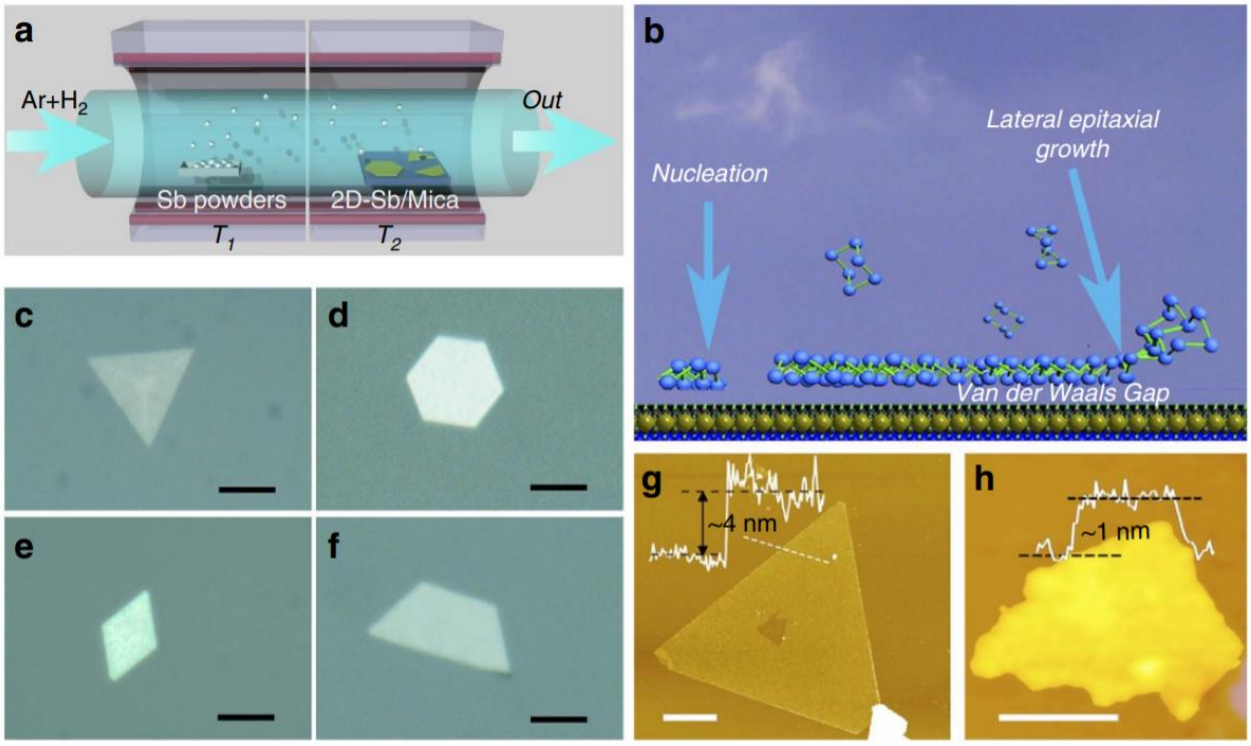

Figure 2.14 Multilayer β-2D-Sb grown by vdW epitaxy. a, b) Schematics of the experimental growth setup and vdW growth process. c-f) Optical microscopy images of β-2D-Sb flakes. g, h) AFM images of single flakes. Scale bars in g) and h) are 1 μm and 50 nm, respectively. Reprinted from[154]. License at https://creativecommons.org/licenses/by/4.0/

The second study was published soon after by Wu et *al*.[155] The authors used MBE with a source of Sb crystals to grow single-layer β-2D-Sb on $PdTe_2$ at a substrate T of 400 K and characterized the samples with STM. Single-layer β-2D-Sb flakes with dimensions of ~30 nm, as well as a

continuous single-layer region of 100 nm are observed. The grown β-2D-Sb has a lattice constant of 4.13 Å in relatively good agreement with DFT calculations for single layers. The authors also present a LEED pattern, which shows only one set of diffraction spots. From this result, the authors claim that the β-2D-Sb is epitaxial, and lattice matched with the substrate. Another more plausible interpretation is that only the $PdTe_2$ LEED spots are visible. In fact, the weak substrate-layer interaction should allow the β-2D-Sb lattice to be randomly oriented on the vdW substrate, as will be discussed in Chapter 5. The authors measured the X-ray photoemission spectroscopy (XPS) spectra of the grown β-2D-Sb and find two components for the Sb $4d_{3/2}$ (33.60 eV and 33.30 eV) and Sb $4d_{5/2}$ (32.35 eV and 32.05 eV) peaks. They attribute the main components (33.60 eV and 32.35 eV) to β-2D-Sb and the smaller components to Sb atoms not yet formed into antimonene. This interpretation is highly questionable for two main reasons. First, Sb evaporates into Sb_4 molecules rather than Sb atoms and the weakly interacting vdW substrate should not catalyse the dissociation of Sb_4. Second, the desorption (and surface diffusion) of Sb_4 is very fast on vdW substrates. For instance, the surface diffusion energy barrier of Sb_4 on graphite is only 60 meV[156]. The second set of components might therefore be associated to Sb_4 aggregates or possibly to weak Sb-substrate bonds. Wu et *al*. also studied the air stability of the β-2D-Sb single layers. They exposed grown β-2D-Sb to air in the loadlock of the ultra-high vacuum (UHV) system for 20 minutes and did not find any degradation in their STM measurements. The long-term stability of the single layers was not investigated.

Before the publication of the aforementioned two growth studies, the author of thesis demonstrated the MBE growth of single and few-layer β-2D-Sb on Ge substrates. These results were published a few months later in ref. [36] and are discussed in details in Chapter 5.

Following these three initial studies, many groups demonstrated the growth of β-2D-Sb on various substrates including Cu[157], Cu_3O_2[158], graphene[37, 159], as well as flat graphene-like β-2D-Sb on Ag(111)[160, 161]. This flat β-2D-Sb allotrope is stabilized by the bonds with the Ag substrate.

Considering the instability of the A17 phase, it is not surprising that the growth of α-2D-Sb took much longer to be reported. The first report came by Märkl et *al*.[162] The authors first deposited Bi on MoS_2, then evaporated Sb on the Bi flakes by MBE. The grown flakes were characterized by STM (Figure 2.15) and were found to be polycrystalline and containing different allotropes of 2D-Sb and 2D-Bi. 2 BL thick α-2D-Sb, 1 BL thick β-2D-Sb and Bi allotropes were observed. Using

STS, the authors determined that all allotropes are semimetallic. This behavior is expected considering that multilayer Sb and Bi are semimetallic and that Sb and Bi should interact strongly due to their chemical and crystallographic similarities.

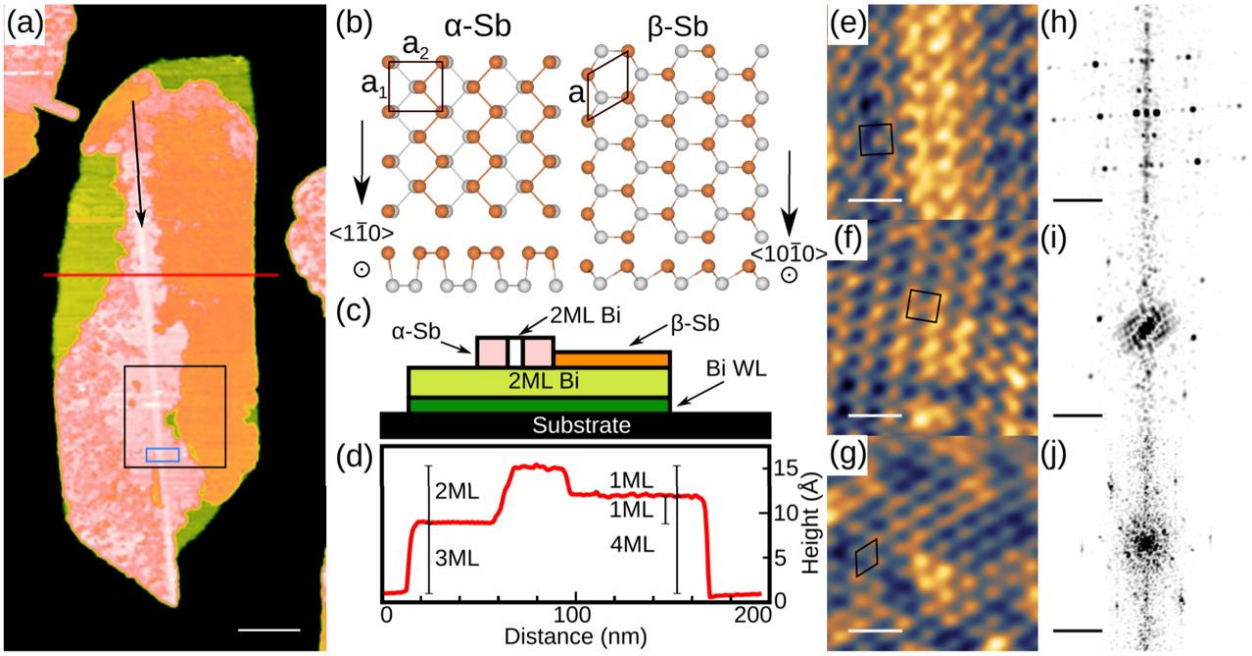

Figure 2.15 STM images of 2D-Sb on 2D-Bi. a) Large-scale STM image of a vdW heterostructure comprising an α-2D-Bi base (light green), 2 BL α-2D-Sb (pink) and 1 BL β-2D-Sb (orange). b) Atomic structure of α and β 2D phases. c) Schematic of the phases in the flake in (a). d) Profile along the red line in (a). e-g) Atomic-resolution STM of α-2D-Bi, α-2D-Sb and β-2D-Sb, respectively. h-j) Corresponding FFT of (e-g) Reprinted from [162]. License at https://creativecommons.org/licenses/by/3.0/

A year after the report by Märkl et *al*., another study reported the growth of α-2D-Sb[163]. They deposited Sb by MBE on T_d-WTe_2 at 400 K and ~0.3 ML/minute. Both single layer and few-layer flakes with dimensions of a few hundreds of nm were observed (Figure 2.16a). The number of layers was determined with the step height. The step height of BL α-2D-Sb was ~7.8 Å and higher terraces had steps heights of ~6.4 Å, close to DFT predictions. We however note that STM topography measurements are not accurate when measuring step heights between different materials. In fact, constant current measurements are highly dependent on the density of states (DOS) of the probed materials. The nature of the grown allotrope was determined by atomic

resolution STM (Figure 2.16 (b-d)). The surface structure corresponds to α-2D-Sb, with lattice parameters of ~4.4 Å and ~4.8 Å. The STS indicates that flakes of different thicknesses are all metallic (Figure 2.16f). Nonetheless, the first unoccupied peak was found to shift closer to the Fermi level, as the number of layers increases (Figure 2.16f). The authors measured the Raman spectra of flakes between 3 and 20 layers thick. They identified two peaks, which they attribute to A_1^3 (147 cm^{-1}) and A_1^2 (131 cm^{-1}) vibration modes (Figure 2.16g). This labelling is based on DFT predictions[27] and is highly questionable. If fact, an important question emerges from these Raman spectra. The authors observe a shift of the peaks to 150 cm^{-1} and 118 cm^{-1} as the thickness increases. These wavenumbers actually correspond to the Raman spectrum of β-2D-Sb[36, 154]. In fact, A17 Sb should display three Raman modes when excited with in-plane polarised light, as was observed for A17 P[19].

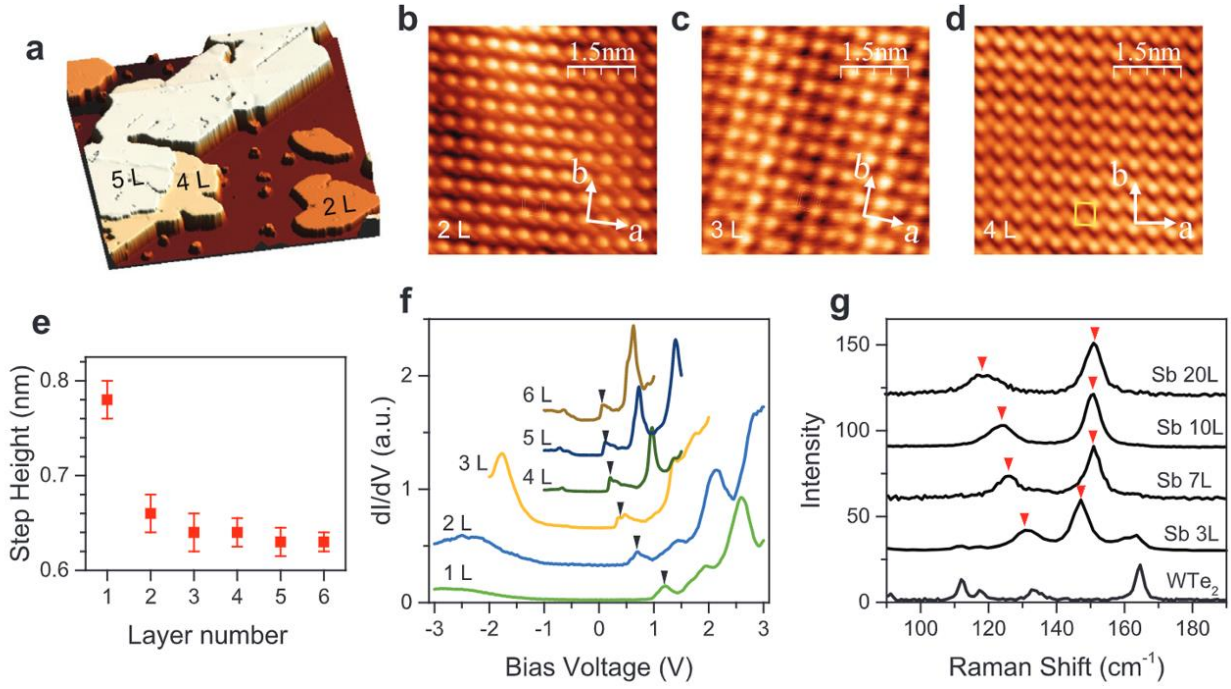

Figure 2.16 a) STM image of α-2D-Sb grown on WTe_2. b-d) Atomic resolution STM of 2-4 BL thick α-2D-Sb on WTe_2. e) Measured step height for the first six terraces. f) STS of 1-6 BL thick α-2D-Sb on WTe_2. g) Raman spectra of α-2D-Sb on WTe_2 .Reprinted from [163].

There is no doubt that the surface structure observed by STM corresponds to α-2D-Sb. However, in general, surface characterization is not enough to determine the crystal structure. This is especially true since A17 is known to be an unstable phase of Sb. In fact, the surface structures of

A7 Sb(110) and A17 Sb (010) (α-2D-Sb) are identical. This will be discussed in detail in Chapter 6 and is the topic of one of the papers published in the course of this thesis[40].

2.2.2.4 Arsenene

Possibly due to its known toxicity, 2D-As has been studied experimentally much less than antimonene or phosphorene. However, its theoretical investigation came hand in hand with the research on antimonene. Single-layer α- and β-2D-As were first predicted to be stable by Kamal and Ezawa[25] and a few weeks later by Zhang et *al*. [28]

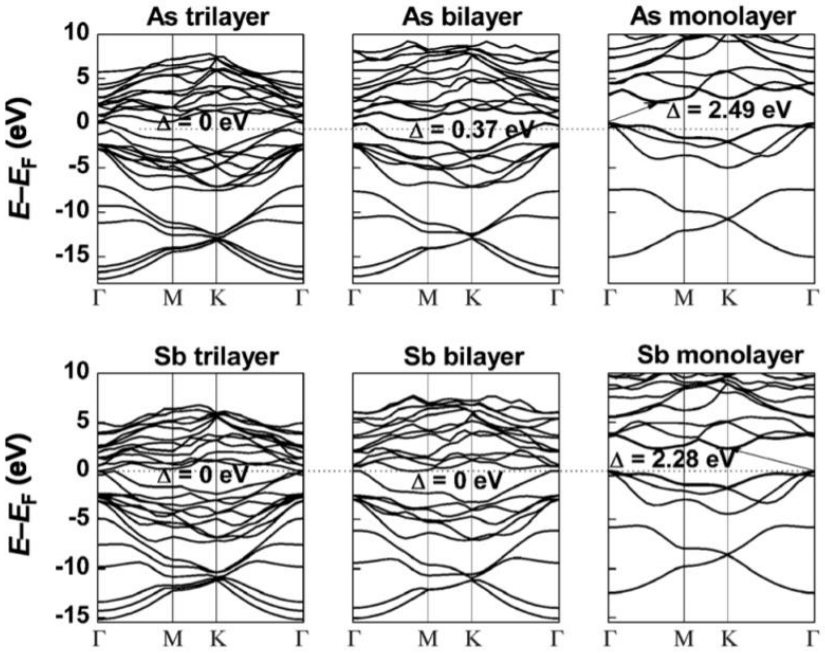

Figure 2.17 Band structure of β-2D-As and β-2D-Sb monolayer, bilayer and trilayer calculated at the HSE06 level of theory. Reprinted from [28].

Like antimonene, β-2D-As is expected to transition from a semimetal to a semiconductor when its thickness decreases (Figure 2.17). At 2 BLs thickness, β-2D-As becomes an indirect semiconductor with a 0.37 eV band gap (HSE06). Single-layer β-2D-As has an indirect band gap of 2.49 eV and becomes a direct band gap semiconductor a 4% biaxial strain (Γ point). DFT investigations have also predicted that under larger strain (~11.5%), β-2D-As could become quantum spin Hall insulator exhibiting topologically protected helical edge states and a bulk band gap of 696 meV[164, 165]. Like antimonene, β-2D-As has attracted a lot of attention due to its promising electronic

properties. Pizzi et *al*. predicted electron and hole mobilities of 635 and 1700 $cm^2V^{-1}s^{-1}$, respectively. Like β-2D-Sb, β-2D-As is a potential candidate for ultra-short channel FETs, with its calculated 64 mV dec^{-1} SS in 7 nm channel dual-gate MOSFETs.

The first claim of β-2D-As synthesis was made by Tsai et *al*. in 2016[166]. They used a N_2 plasma treatment of an InAs substrate, followed by annealing at 450 °C. The N reacted with the In atoms of the substrate to form an InN layer (~14 nm), leaving an As rich surface. During the annealing process, the As recrystallized to form a ~14 nm layer on top of InN. The crystallinity of As is confirmed by TEM and Raman spectroscopy. However, the surface orientation is the $(01\bar{1})$ plane of A7 As, which does not correspond to β-2D-As. The authors also claim that the As is semiconducting with a 2.3 eV band gap, based on photoluminescence (PL) measurements. They note that the PL cannot originate from the InN or InAs due to their band gaps of 0.65 and 0.354 eV. Nonetheless, a careful assessment of quantum confinement in the 14 nm InN layer should be taken into consideration before making claims regarding the semiconducting nature of the top As layer. The same group also reported similar results for Sb on InSb obtained by the same method[167]. In 2017 Gusmão reported on the synthesis of As, Sb and Bi nanosheets by shear exfoliation using kitchen blenders[116]. The authors however did not demonstrate the 2D nature of the produced flakes (i.e. thickness measurements).

More convincing attempts at synthesizing β-2D-As were published in 2019[168, 169]. Hu et *al*.[168] synthesized few-layer β-2D-As using a method similar to that used by Ji et *al*. to first grow β-2D-Sb[154]. They used a two-zone tube furnace and a source of As powder. For the sublimation of As, the T of the first zone was first set at 325 °C, then increased to 425 °C over 20 min and then kept at this T for 20 min. This leads to the sublimation of As_4 molecules. The second zone was kept at 325 °C for the growth of As on a mica substrate. They used a H_2 carrier gas at a flow of 20 sccm. The growth resulted in flat hexagonal and half-hexagonal (trapezoidal) flakes with lateral dimensions of a few μm to ~25 μm. The flake thickness increases with the lateral dimensions and thicknesses between 4 nm (~11 layers) and 48 nm (~140 layers) were observed. Like β-2D-Sb, a blue shift of the A_{1g} and E_g Raman modes was observed as the thickness of the layers went from 48 nm to 4 nm (from 253.2 cm^{-1} to 257 cm^{-1} for A_{1g} and from 194.2 cm^{-1} to 200.0 cm^{-1} for E_g). Interestingly, the authors observed that the ambient stability of β-2D-As is much lower than that of β-2D-Sb (Figure 2.18). They exposed the flakes to air and observed the oxidation process using

optical microscopy. Degradation occurs in a timescale of minutes to hours and was associated to oxidation. The oxide nucleates on the edges and on various spots on the surface of the flakes. The authors measured the Raman spectra after the oxidation and found the presence of As_2O_3 modes. XRD measurements indicate that the As_2O_3 is cubic arsenolite. The authors also demonstrated that the β-2D-As can be protected from oxidation by passivation using various polymers. The best passivation was obtained with polyethylene glycol (PEG), with the first signs of oxidation appearing after 51 days. Measurements of the electrical properties expectedly indicated a metallic behavior, which changed into a semiconducting behavior with oxidation.

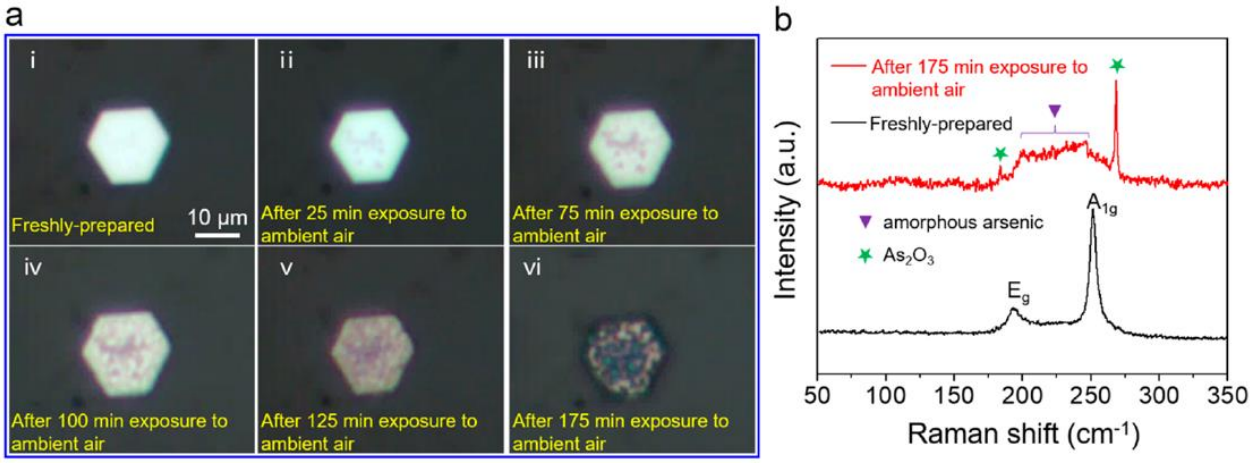

Figure 2.18 a) Optical microscopy images of the oxidation of β-2D-As under atmospheric conditions. b) Raman spectra of freshly prepared and oxidized β-2D-As flakes. Reprinted with permission from *Hu, Y. et al., Chemistry of Materials 2019, 31, (12), 4524-4535*. Copyright (2019) American Chemical Society[168].

On the other hand, Shah et *al*. used MBE to deposit As on Ag(111)[169]. They used solid source As to deposit As_4 at a vapor pressure of 2×10^{-7} Torr in the growth chamber at a substrate at T of 250-350 °C. The authors claim to have obtained single-layer β-2D-As based on LEED, STM and ARPES measurements. While the STM and ARPES data are in relatively good agreement with a β-2D-As structure, the presented LEED data seems to indicate a p(5×1) superstructure on Ag(111), rather than an epitaxial β-2D-As structure. Post-growth annealing of the substrate to 400 °C led to a transition to a $(\sqrt{3} \times 14)$ structure as observed with LEED and STM. This seems to indicate a strong interaction between the As overlayer and the Ag(111) substrate.

The metastability of A17 As in normal conditions allowed to study α-2D-As more easily than α-2D-Sb. Chen et *al*. first isolated α-2D-As in 2018 by micromechanical exfoliation from natural mineral samples[18]. They obtained few-layer thick flakes and demonstrated the highly anisotropic properties of α-2D-As (Figure 2.19). They determined a conductance ratio of 6.4 between the armchair and zigzag directions, as well as a mobility ratio of 28 and a thermal conductivity ratio of 0.6. The anisotropy of several transport properties is found to be higher than for other 2D materials such as α-2D-P.

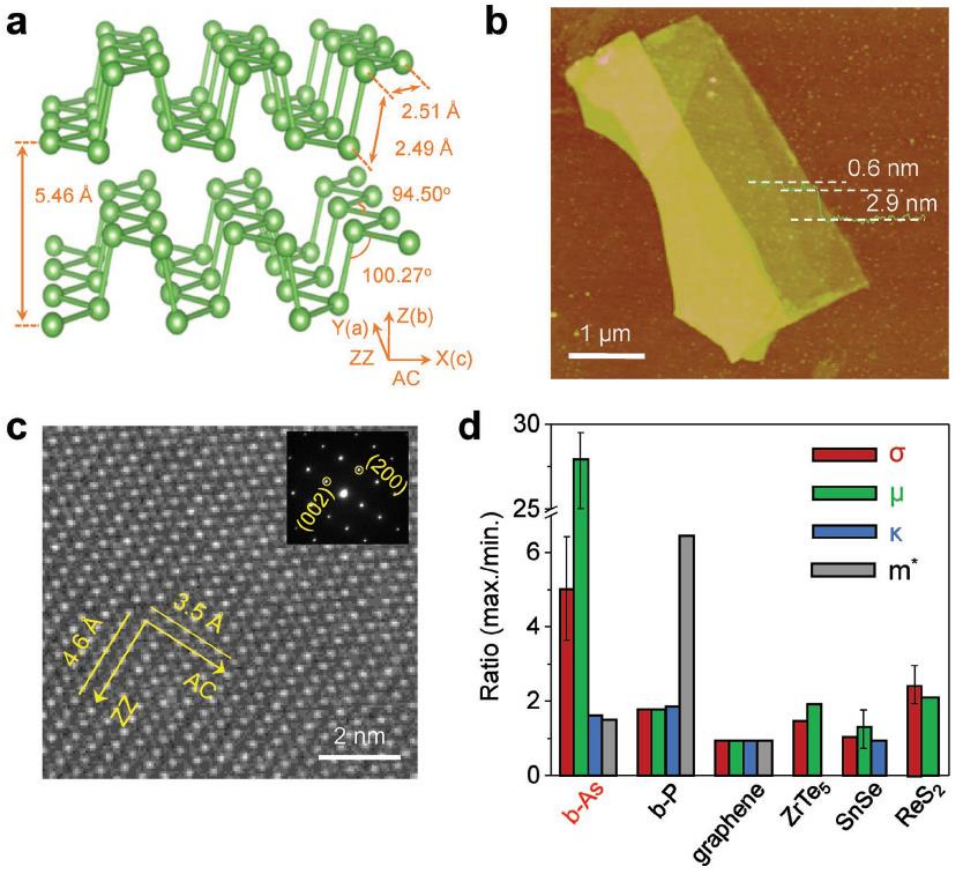

Figure 2.19 a) Atomic structure of α-2D-As. b) AFM image of an exfoliated α-2D-As flake. c) STEM image of α-2D-As. d) Comparison of the anisotropy (max/min ratio) of the transport properties of α-2D-As and other 2D materials (electrical conductivity (σ), mobility (μ), thermal conductivity (κ) and effective mass (m*)). Reprinted from [18].

Zheng et *al*. later exfoliated α-2D-As form natural minerals and obtained single layers as well as bilayer, trilayers and quadrilayers[170]. An increase in mobility with decreasing thickness up to values

of ~60 $cm^2V^{-1}s^{-1}$ in few-layer flakes (5.7 nm) was observed. A small decrease in the mobility was found below this thickness. The relatively low mobility is likely associated to defects since the flakes are obtained from natural mineral samples. The authors studied the oxidation by STEM-energy-dispersive X-ray spectroscopy (EDX) and a relatively slow oxidation rate resulting in ~10 wt% O was observed after 36 hours. The authors note that thinner regions oxidize more rapidly, but do not mention the thickness of the flakes. The authors also conclude that α-2D-As oxidizes more slowly than α-2D-P.

2.2.2.5 Nitrogene

Even though layered N has been synthesized at high pressure and temperature[51, 171], no attempts to stabilize the phase in ambient conditions or to directly grow 2D-N has been published. Nonetheless, the existence and potential metastability of 2D-N allotropes has been recently predicted[22, 23, 172-175]. Özçelik et *al*. first predicted the metastability of single-layer and multilayer β-2D-N. ML 2D-N was found to have a cohesive energy of 3.67 eV/atom with DFT. This means that it is much less stable than the N_2 molecule which have a triple bond energy of 4.88 eV/atom. Nonetheless, the authors carried out MD simulations to assess the stability of β-2D-N. The structure was found to be stable over the 6 ps simulation period at 850 K, but to decompose into N_2 molecules at 1000 K. The authors concluded that β-2D-N is at least stable at RT. They found that ML β-2D-N should be a wide band gap semiconductor/insulator with a gap between 5.96 eV and 7.26 eV depending on the functional used.

Ersan et *al*. predicted the existence of another group VA 2D allotrope consisting of buckled square and octagon rings[172]. However, there is no consensus on its theoretical stability[23, 172].

2.2.2.6 Group VA 2D alloys

Due to their chemical proximity, pnictogens are known to naturally form alloys of the A7 and A17 phases, often with perfect miscibility[176-178]. Alloying between group VA elements could therefore be a powerful paradigm to finely tune the properties of group VA 2D materials. Most binary combinations of group VA 2D materials have been predicted to be stable[179-182]. Theoretical studies have mainly focused on the electronic properties of substitutional alloys. Studies found that the magnitude of the electronic band gap of group VA binary alloys can be tuned by changing the

composition[182]. It was also found that the band gap of monolayers can be changed from indirect to direct at some compositions. For instance, Zhao et *al*. determined that β-2D-As_xSb_{1-x} can be a direct band gap semiconductor at x=0.31-0.38[183].

The synthesis of group VA 2D alloys is currently limited to a short list of binary materials. The growth of relatively thin Bi_xSb_{1-x} films has been realized by MBE on GaAs(111) substrates[184]. On the other hand, α-2D-AsP has been isolated by micromechanical exfoliation and used in tunable photodetectors[178]. Moreover, the growth of β-2D-As_xSb_{1-x} by MBE has been realized in the course of this thesis and will be presented in Chapter 5[38].

2.3 *in situ* monitoring of 2D materials growth dynamics

As mentioned above, 2D materials can be synthesized by exfoliation and growth methods. This thesis focuses on growth approaches, due to their potential scalability the higher quality of the synthesized materials. Controlling the growth of novel 2D materials requires a deep and detailed understanding of their nucleation and growth mechanisms. The complexity of the involved atomic processes and their sensitivity to experimental parameters rules out guesswork and detailed modelling approaches as reliable sources of information on these complex processes. While *ex situ* characterization of grown samples may allow to untangle a part of these mechanisms, *in situ* real-time observations of the growth provides unmatched detailed information about the involved processes and growth dynamics.

The growth dynamics can be monitored by a variety of techniques, including spectroscopic, diffraction and microscopic methods. Each of these methods has its advantages and limitations. Spectroscopic methods give precise information on the chemistry but lack spatial and/or temporal resolution. Diffraction methods inform us about the crystallography of the growing materials but also lack spatial and/or temporal resolution. On the other hand, microscopic methods have a good spatial resolution. Their temporal resolution can be as low as a few femtoseconds when using pump-probe techniques, and continuous imaging with atomic to a few nm resolution can be routinely achieved with sub-second time resolution in electronic microscopes. While microscopy does not necessarily provide spectroscopic or diffraction capabilities, most electron microscopes allow for some level of spectroscopic analysis or diffraction characterization. Moreover, at atomic resolution, microscopic measurements give the same information as diffraction, but with an

additional morphological component. For these reasons, we will focus our review on *in situ* microscopic methods.

Several microscopy methods have been used to image crystal growth. These include x-ray tomography, TEM, scanning electron microscopy (SEM), STM, LEEM and PEEM. It is however important to consider the compatibility of the characterization method with the studied growth process. In fact, epitaxial growth is done in highly controlled conditions (pressure, temperature, and chemical species), under which the characterization equipment needs to be operational. For instance, CVD is typically done at relatively high pressure ($>10^{-3}$ mbar), which hinders the operation of most electron microscopes. On the other hand, MBE can be carried out under ultra-high vacuum. We note that environmental TEM and SEM as well as liquid cell microscopy have been developed to circumvent these issues. Another important aspect to consider is the imaging geometry. In fact, epitaxial growth is done on relatively thick substrates. Even though atomic-resolution TEM has been used to image the epitaxial growth of metals and semiconductors on suspended 2D materials[185], it is not currently used for the study of 2D materials growth due to the challenges related to the preparation of electron-transparent growth substrates. On the other hand, surface microscopy allows to study realistic experimental conditions for 2D materials on growth substrates.

This section reviews the literature on the real-time imaging of the growth of 2D materials by surface microscopy.

2.3.1 Real-time surface electron microscopy of 2D materials growth

Surface electron microscopy methods include SEM, PEEM and LEEM. The working principles of LEEM and SEM are similar. In both cases, an electron beam is directed to the surface. In SEM, the highly focused beam scans the surface and the secondary electron emission rate as a function of the e-beam position is used to recreate an image of the surface. In LEEM, a collimated e-beam is sent to the surface, reflected, and directed through a set of magnetic lenses to create an image of the surface on a phosphorescent detector[186] (details in Chapter 3). The low kinetic energy (0-100 eV) ensures that only the first few monolayers of the surface are imaged, making it a particularly well-suited imaging technique for 2D materials growth. On the other hand, the large kinetic energy of SEM (keV range) provides weaker contrast on atomically thin materials. PEEM is also highly

surface sensitive. In PEEM, the surface is excited by UV or X-ray photons and the ejected photoelectrons are used to form an image. This provides chemical sensitivity to the PEEM. In fact, energy filtering of the photoelectrons can be done to image specific core electrons or features in the valence band. However, this requires a high-intensity X-ray source only available in synchrotron facilities. Moreover, one must be cautious of the potential effects of the high-intensity X-ray on chemical reactions.

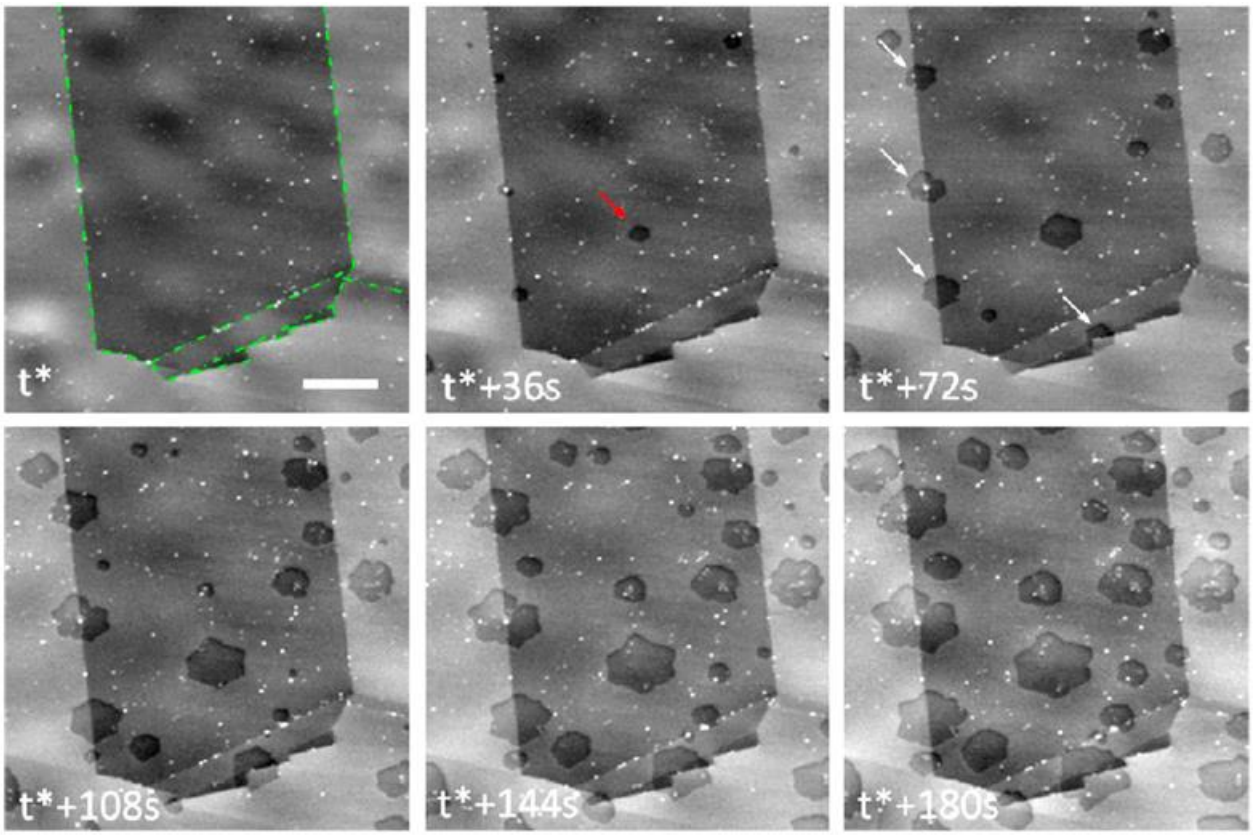

Figure 2.20 *in situ* SEM observations of graphene growth on Cu foil. A Cu grain boundary is highlighted by the green dashed line. Nucleation at grain boundaries is indicated by white arrows. The scale bar is 20 μm. Reprinted with permission from *Wang, Z.-J. et al., ACS Nano 2015, 9, (2), 1506-1519*. Copyright (2015) American Chemical Society[187].

There has been very few *in situ* SEM studies of the growth of 2D materials[187, 188]. The most notable study was carried out by Wang et *al*.[187] Using environmental SEM, they studied the low-pressure CVD growth of graphene from C_2H_4 on copper substrates (Figure 2.20). Interestingly, the contrast between Cu and monolayer graphene is sufficient for rapid imaging in high-pressure conditions.

The real-time observations allowed to determine the nucleation rate and induction time (time before nucleation). Moreover, using electron backscatter diffraction, the authors identified the effect of the crystallographic orientation of Cu grains on surface pre-melting and graphene nucleation rate. The direct measurement of the growth dynamics of single graphene islands revealed three successive growth phases: (1) attachment limited growth (2) diffusion limited growth and (3) equilibrium between etching and growth.

Real-time PEEM studies of 2D materials growth are even more scarce than SEM studies[189]. Cui et *al*. studied graphene growth on Ru(0001) by CVD and surface segregation using UV-PEEM. The authors carried out basic characterization of the growth dynamics. Moreover, they studied the dynamics of O_2 etching of graphene edges. By measuring the etching rate at temperature between 600 K and 1000 K, they determined that the etching process is reaction limited with an activation energy of 27 kJ/mol. Their results are a proof of concept that PEEM can be used to image 2D materials growth. Considering its chemical sensitivity, PEEM could be a very powerful tool to investigate the growth dynamics of compound 2D materials such as TMDs, group VA 2D alloys or h-BN.

LEEM is by far the most used microscopic technique to study the growth dynamics of 2D materials[190-202]. The group of Kevin F. McCarty at Sandia National Laboratories made particularly interesting contributions to this field[191, 192, 196]. They observed the growth of graphene on transition metals (Ru(0001) and Ir(111)) by C_2H_4 deposition and C sublimation. They used these highly reflective metals as model systems to directly image the C adatom concentration. Using controlled deposition, they measured the LEEM I-V curves as a function of C adatom coverage (Figure 2.21a). A significant reduction of the LEEM reflected intensity can be observed with C coverages as low as 0.03 ML (Figure 2.21a). This allowed the authors to spatially resolve the adatom surface concentration in real-time, while measuring the growth dynamics. Both C and C_2H_4 deposition led to an initial linear increase of the adatom concentration until the threshold concentration for nucleation c^{nucl} was reached (Figure 2.21b). After nucleation, the adatom concentration decreases since graphene islands capture the diffusing atoms. After stopping the deposition, an equilibrium concentration is eventually reached. The spatial distribution of C adatoms can be seen in Figure 2.21c. The C concentration is homogeneous on the Ru(0001) surface. This led the authors to suggest that graphene growth is not limited by surface diffusion of C monomers since no

concentration gradient is observed at the edges of the islands. Based on their observations of the velocity of the growing fronts under different conditions (T and deposition rate) and their fitted kinetic model, the authors proposed that the growth is limited by the attachment of clusters of 5 C atoms. Nonetheless, it is important to note that the relatively high signal to noise ratio, as well as the lensing effect at graphene edges might not allow to see concentration gradients, especially when the diffusion length is relatively short.

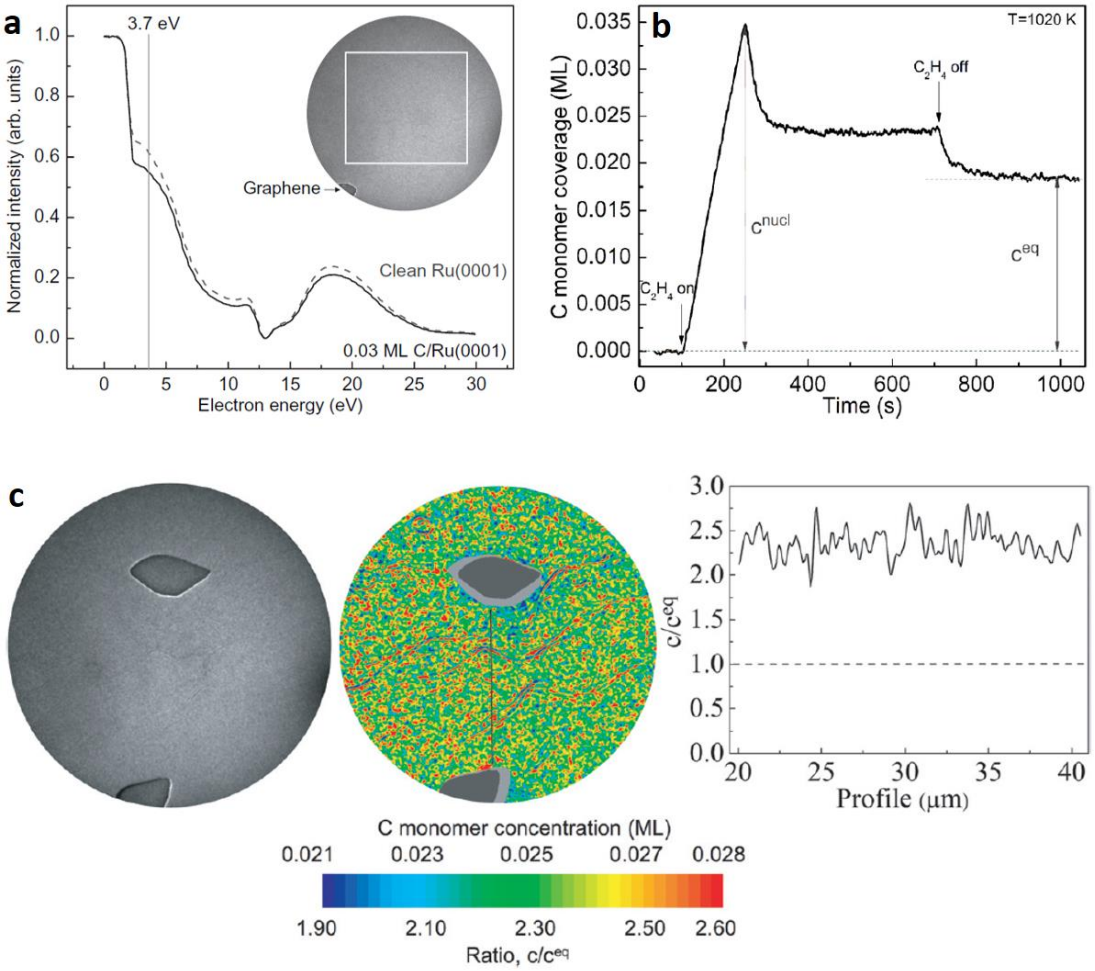

Figure 2.21 (a) LEEM reflectivity (I-V) curves for clean Ru(0001) (dashed line) and 0.03 ML C on Ru(0001) (solid line). Reprinted from [191]. (b) LEEM measured C adatom concentration on Ru(0001) as a function of time during C_2H_4 deposition. Reprinted from [192]. (c) LEEM image and corresponding C monomer concentration during C deposition on Ru(0001) at t=403 seconds and 980 K. Reprinted from [191]. License at https://creativecommons.org/licenses/by/3.0/

The real-time study of graphene growth on Cu(111) by Nie et *al*. highlights other powerful features of LEEM[199]. They observed two types of nucleation events. In a first step, nucleation occurs mainly at defects on the Cu(111) surface. In fact, LEEM provides high contrast at atomic step edges and step bunches, as explained in Chapter 3. Graphene nuclei are mostly observed at step bunches and impurity defects (Figure 2.22a). The authors then solved the steady-state surface diffusion equation for C adatoms by assuming that graphene nuclei act as perfect sinks for C adatoms (c=0) (Figure 2.22b).

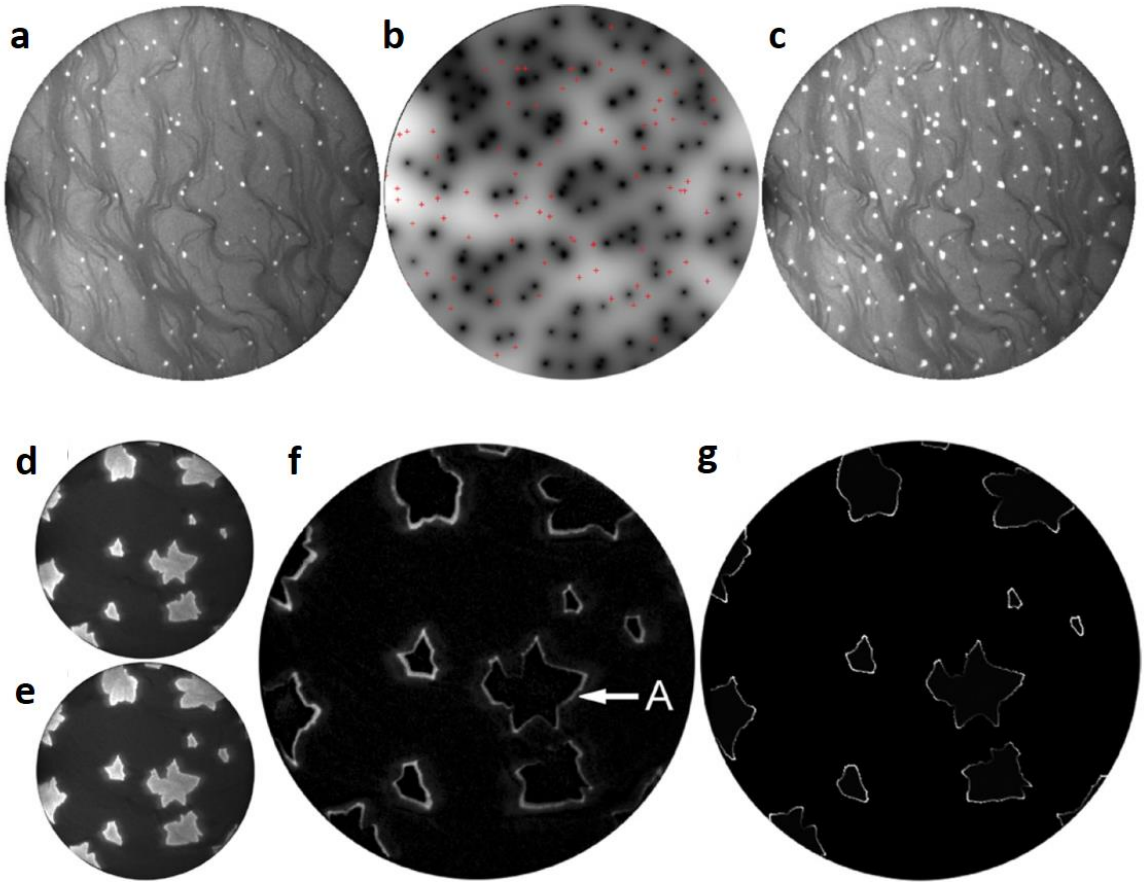

Figure 2.22 (a) LEEM image showing graphene islands nucleating at Cu(111) defects (46 μm field of view and T=894 °C). (b) Surface C concentration calculated by solving the surface diffusion equation. Red crosses indicate secondary nucleation sites. (c) LEEM image after secondary nucleation following an increase in the C flux. (d, e) LEEM images separated by 61 s during growth at 893 °C (20 μm field of view). (f) Difference between (e) and (d) images. (g) Flux at graphene edges calculated by solving the diffusion equation. The grayscale intensity is proportional to the flux at the edges. Reprinted from [199] (https://doi.org/10.1103/PhysRevB.84.155425).

In a second stage, the authors increased the deposition rate, leading to secondary nucleation. The secondary nucleation sites (marked by red crosses in Figure 2.22b) are located in regions with high C concentration, suggesting that the growth on Cu(111) is diffusion limited, in contrast to the growth on Ru(0001) and Ir(111). Furthermore, the authors recorded the LEED patterns of the two type of graphene nuclei (not shown here). The islands which nucleated at defects displayed a polycrystalline LEED pattern, whereas the secondary nuclei were mostly single crystals. This indicates different nucleation mechanisms and highlights the importance of surface preparation for high-quality growths. To better visualize the diffusion limited growth, the authors presented a comparison of the measured growth rate with the diffusion limited calculated growth rate (Figure 2.22 (d-g)). By subtracting two LEEM images recorded at different times during graphene growth, bright bands appear at the edges of the islands. The thickness of the band is proportional to the growth rate (Figure 2.22f) and can be compared to the calculated concentration gradient at the edges of the islands, which is proportional to the growth rate (Figure 2.22g).

The methods elaborated by the group of Kevin McCarty have been used by other groups to provide important intuitions on the growth mechanisms of graphene on various substrates such as Pt(111)[194] and Ni(111)[195, 197]. More recently, *in situ* LEEM has been used to study the growth dynamics of h-BN[201, 202]. These results demonstrate that *in situ* LEEM can be highly beneficial to understand the growth mechanisms of novel 2D materials. This can be increasingly useful for systems which have never been synthesized, such as emerging group VA 2D materials.

CHAPTER 3 METHODOLOGY

This chapter presents the methodology in the following way. First, the choice of synthesis methods for group VA 2D materials is explained based on the properties of each system. Then, the experimental setup used for growth and *in situ* characterization is presented. The basic working principles of LEEM/LEED and PEEM are explained. Then, technical details on the experimental characterization techniques used in the thesis are given. Finally, the theoretical modelling methods are described, and a brief review of the theory is given. More details on the methodology used for specific experiments are provided before each experimental section throughout the thesis.

3.1 Choice of synthesis methods for group VA 2D materials

Even though group VA 2D materials share similar valence electronic configurations and allotropes, their chemical and phase stability differs importantly throughout the group and individualized synthesis methods need to be developed. Below is the rationale behind the choice of the synthesis methods.

3.1.1 Nitrogene

Nitrogene remains the most challenging group VA 2D material to synthesize. In fact, the instability of solid polymeric phases at pressures below hundreds of GPa and the extreme stability of the N_2 triple bond rules out the use of vdW epitaxy. The two main issues are the recombination of precursors into gaseous N_2 and the fact that neither of the A7 and A17 bulk phases have been observed. A possible solution would be to combine high-pressure to destabilize molecular N_2, along with a highly interacting lattice-matched hexagonal transition metal or ionic substrate to promote the stability of the single layer β-2D-N phase. The A7 and A17 phases are expected to be ~1.55-1.83 eV/atom more energetic than molecular N in normal conditions[43]. The substrate-layer interaction energy cannot reach these values (for instance, even the interaction energy of 4-fold coordinated sp^3 silicene on Ag(111) is ~0.7 eV/atom). β-2D-N would therefore be metastable once the pressure is released.

Due to the challenges outlined above and the limited available time, nitrogene synthesis has not been attempted in this thesis. Efforts have been directed at the synthesis of heavier group VA 2D materials, which also have attractive properties but present more realistic technical difficulties.

3.1.2 Phosphorene

Due to the lower stability of P_2 as compared to A17 and A7 P, the direct synthesis of 2D-P should be feasible. Only the more stable A17 phase will be studied. Bulk A17 P can be synthesized either at high pressure or using catalysts. For this reason, two synthesis methods were explored:

1- Conventional epitaxy on a lattice matched transition metal substrate.

2- Thermal decomposition of a III-V semiconductor surface capped by a graphene layer.

The first method is rather self-explanatory. The use of a lattice matched strongly interacting substrate should increase the stability of epitaxial α-2D-P. Moreover, the surface dangling bonds can catalyse the decomposition of precursor species. The preparation of the transition metal surface and the epitaxial growth could be done by MBE or CVD. However, since α-2D-P is known to oxidize rapidly in ambient conditions, the growth is attempted by MBE. In fact, the UHV cluster used for the synthesis is equipped with *in situ* characterization tools, as described in section 3.2.

The second method is an attempt to achieve high phosphorus pressure in a confined 2D space to promote the growth of α-2D-P. In fact, annealing III-V semiconductors leads to the separation of the III (liquid) and V (gas) elements. Trapping the gas between a graphene layer and the surface might lead to high pressure and temperature conditions favorable to α-2D-P. For instance, Algara-Siller et *al*. demonstrated the formation of 2D square ice by trapping water between two graphene sheets to induce high pressure conditions[203]. Nonetheless, we note that the III-V recombination might limit the maximal pressure achievable. Still, phase separation might create high pressure regions where recombination is not possible.

3.1.3 Arsenene and antimonene

Since heavier group VA elements directly crystallize in the layered vdW phases, conventional epitaxial growth methods can be used. As for phosphorus, MBE will be prioritized over CVD. In fact, real-time LEEM observation of the growth is possible using MBE, which will provide highly valuable information about the vdW growth mechanisms. As detailed in Chapter 4, group IV semiconductors with (111) surface orientations are almost lattice matched to β-2D-As and β-2D-Sb. Moreover, these substrates are highly advantageous for future technological applications since they are the main platform for the current complementary metal-oxide-semiconductor (CMOS)

technology. Since the single layer α-2D phases of As and Sb are expected to be slightly more thermodynamically stable than the β-2D phases, growth of both allotropes may be achievable. The deposition on surfaces with rectangular symmetry or weakly interacting substrates might allow to observe α-2D-As and α-2D-Sb.

The synthesis of arsenene has been challenging in the MBE/LEEM system due to the high As_4 pressure. For this reason, arsenene synthesis will not be discussed in this thesis. Nonetheless, the synthesis of 2D-As_xSb_{1-x} alloys will be presented.

3.1.4 Bismuthene

The synthesis of 2D-Bi has already been demonstrated in literature. Although many questions remains unanswered, they were not investigated in this thesis.

3.2 Group VA 2D materials growth setup

The growth and *in situ* characterization of group VA 2D materials is carried out in UHV cluster illustrated in Figure 3.1. The cluster is composed of a STM, an XPS and a LEEM, which are connected by a transfer tube. The base pressure everywhere in the cluster is generally maintained below 10^{-9} mbar to prevent contamination or oxidation of the samples.

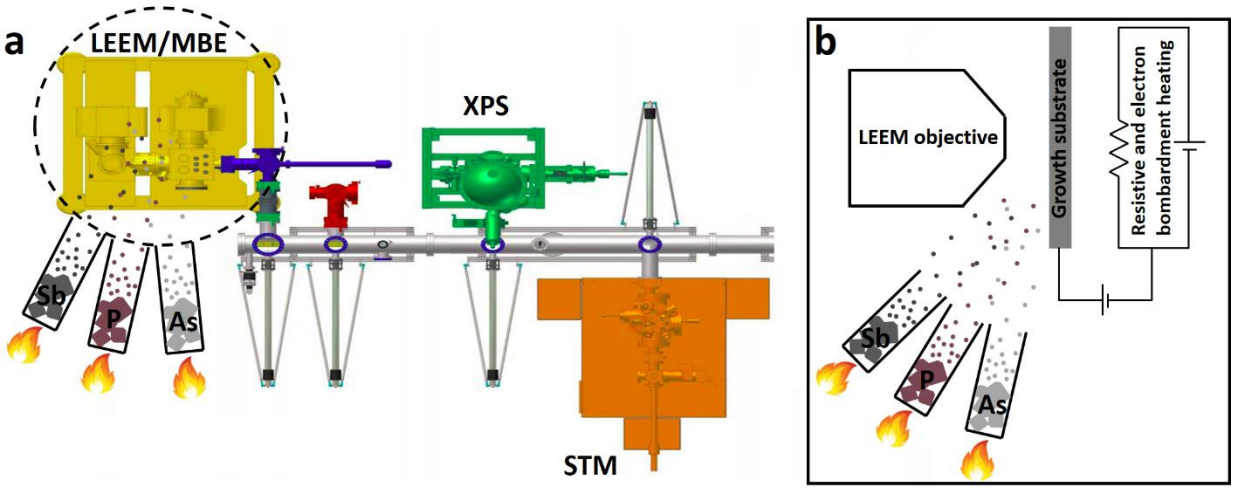

Figure 3.1 a) UHV cluster used for group VA 2D materials synthesis. The LEEM/MBE, XPS and STM are connected by a UHV transfer tube. Knudsen cells used for the evaporation of. b) Schematics of the LEEM/MBE chamber.

Surface cleaning and conditioning can be done in the XPS chamber using an Ar^+ sputter gun, which allows to send energetic Ar^+ ions (up to 3 keV for singly ionized ions) for the controlled removal of surface atomic layers. High-T annealing can be done in the STM or LEEM chamber by radiative and/or electron bombardment heating using a resistively heated tungsten filament located at ~3 mm from the back surface of the samples and a bias up to 1 kV (see Figure 3.1b for instance). The samples are fixed in molybdenum sample holders and temperatures of ~1500 °C can be reached (although temperatures above 1000°C can be safely maintained only for a short duration).

Deposition of group VA elements is done by solid source MBE using Knudsen cells located directly in the LEEM main chamber to allow for real-time observations during growth (Figure 3.1b). Two Knudsen cells can be loaded and operated simultaneously. The SFC cells from CreaTec Fischer & Co. GmbH allow the evaporation and sublimation of precursor materials from pyrolytic boron nitride crucibles up to 800 °C. Red phosphorus is used for P_4 deposition, whereas As powder and Sb crystals are used for As_4 and Sb_4 deposition.

3.3 Characterization techniques

3.3.1 LEEM/LEED and PEEM

Most of the characterization was done using LEEM/LEED and PEEM. *in situ* and real-time growth characterization was carried out at Polytechnique Montreal using the FE-LEEM/PEEM P90 from SPECS GmbH. On the other hand, *ex situ* XPEEM characterization was done at the Nanospectroscopy beamline of the Elettra Sincrotrone Trieste[204, 205]. The basic principles of LEEM/LEED an PEEM are explained below. A monochromatic and collimated beam of electron is produced in the illumination column by field emission or thermionic emission (Figure 3.2a (1)). The electrons are accelerated to ~15 keV and directed to the sample by a set of magnetic lenses, electrostatic deflectors and a magnetic prism (2). After passing through the objective lens (3), located a few mm away from the sample, the electrons are slowed down to around 0-100 eV and interact with the sample. The reflected electrons are then redirected by the magnetic prism (2) to the imaging column (4), which allows the formation of an image on a microchannel plate detector imaged by a CCD camera (8).

The interaction of low-energy electrons with the surface gives a rich contrast. Contrarily to high-energy electrons (like SEM), the contrast is not governed by the atomic mass of the surface atoms[186]. In fact, the energy dependent reflected intensity depends on the scattering of electrons from individual atoms, but also on the electronic band structure and crystal structure. Generally, electrons with energies matching band gaps in the electronic structure of the surface will be reflected, whereas electrons matching states in the band structure will be transmitted through the crystal (Figure 3.2b). On the other hand, interference between electrons reflected from different crystal planes (Bragg reflections) can provide reflection minima or maxima. Moreover, interference of electrons reflected from two atomic terraces leads to high contrast at atomic steps.

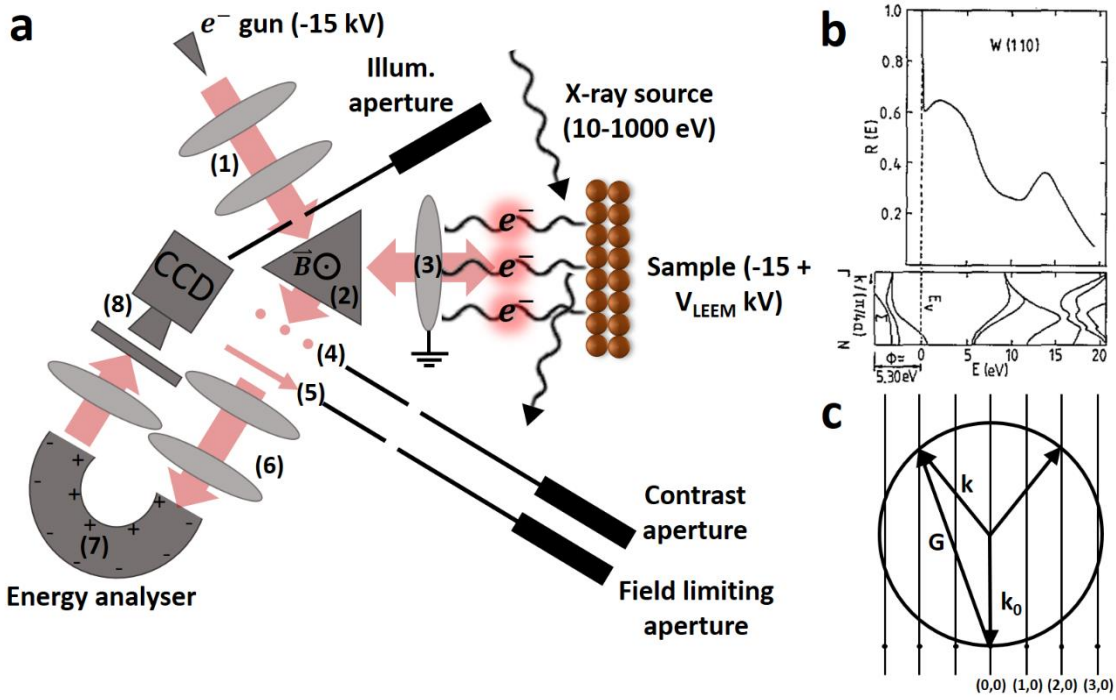

Figure 3.2 a) Schematics of a LEEM/LEED/PEEM system. The main elements are: (1) electron illumination column, (2) magnetic prism, (3) objective lens, (4) objective back focal (LEED) plane, (5) objective image (LEEM) plane, (6) imaging optics, (7) energy analyser and (8) electron detector. b) LEEM reflectivity as a function of sample voltage for the W(110) surface and corresponding electronic band structure . Reprinted from [186]. © IOP Publishing. c) Ewald construction for LEED.

Since the low-energy electrons have a small penetration depth, constructive and destructive interference is only partial. Surface diffraction (LEED) still occurs and is given by the 2D Laue

condition: $\boldsymbol{k}^{||} - \boldsymbol{k}_{\boldsymbol{0}}^{||} = \boldsymbol{G}_{\boldsymbol{hk}}$, where $\boldsymbol{k}^{||}$ and $\boldsymbol{k}_{\boldsymbol{0}}^{||}$ are the reflected and incident electron wavevectors parallel to the surface and $\boldsymbol{G}_{\boldsymbol{hk}}$ are the surface reciprocal lattice vectors. This condition is illustrated in Figure 3.2c in the Ewald construction. Since the 2D lattice does not have vertical periodicity, the reciprocal lattice points are rods in the 3rd direction (perpendicular to the sample). The radius of the Ewald sphere is $|\boldsymbol{k}_{\boldsymbol{0}}|$ (diffraction at 90°) and the allowed diffractions spots are the intersection of the Ewald sphere with the $\boldsymbol{G}_{\boldsymbol{hk}}$. Since the rods always intersect the Ewald sphere if the energy is high enough, LEED spots are visible at any energy above their threshold ($|\boldsymbol{k}_{\boldsymbol{0}}| = |\boldsymbol{G}_{\boldsymbol{hk}}|$). In the back-focal plane (4), the distance of the electrons from the optical axis is proportional to $\left|\boldsymbol{k}^{||}\right|$ and hence the 2D reciprocal space is directly visible (LEED pattern). The projector lenses in the imaging column can be used to image either the back-focal plane (4) or the image plane (5) of the objective lens (LEED and LEEM modes). Plates with apertures can be inserted in each of those planes (Figure 3.2a) to either select a LEED spot or region on the surface of the sample. This allows for dark-field LEEM (LEEM imaging of a specific crystal orientation or surface reconstruction) or for μ-LEED (LEED from a specific region). μ-LEED can be done with a better spatial resolution by reducing the size of the incident beam using an illumination aperture.

For PEEM, the electron source is replaced by a photon source, which can either be a UV light/laser or X-ray/UV synchrotron radiation. The use of an X-ray source allows for spectroscopic imaging. In fact, the photoelectron kinetic energy can be selected using the energy analyser (7). This can be used to image specific features in the valence band or core levels. Varying the electron kinetic energy (changing the sample voltage at fixed analyser pass energy) provides a hyperspectral image. On the other hand, if the back focal plane of the objective lens is imaged, angle-resolved photoemission spectroscopy (ARPES) can be done. Selecting specific areas of the sample with the field-limiting aperture (5) gives the opportunity to measure μ-ARPES, with a lateral resolution of ~3 μm.

3.3.2 Other characterization techniques

A variety of characterization techniques have been used. Their working principles are well-known and will not be discussed here. However, specific details about their use in this thesis are given below.

3.3.2.1 Scanning-tunneling microscopy (STM)

STM characterization was performed to determine the atomic structure and phase of the grown group VA 2D materials, as well as their nucleation behavior using the Aarhus 150 from SPECS GmbH in the UHV cluster shown in Figure 3.1. After deposition, samples are directly transferred to the STM through the transfer tube under UHV. The surface is imaged in constant current mode using a tungsten tip. The samples are kept at or above RT during imaging. Scanning-tunneling spectroscopy (STS) was employed to determine the electronic structure of the grown materials. The Aarhus 150 measures the STS by turning off the STM feedback loop (to keep the sample/tip distance constant) and sweeping the tunneling voltage. dI/dV curves are acquired using the same procedure by numerically differentiating the I(V) curve. Nonetheless, the relatively high temperature (RT) along with the numerical differentiation technique yield a poor energy resolution and only the global behavior can be determined.

3.3.2.2 X-ray photoemission spectroscopy (XPS) and XPEEM

The chemical characterization was done by XPS both *in situ* in the UHV cluster and *ex situ* in the Laboratoire pour l'analyse de la surface des matériaux (LASM) in Polytechnique. These systems provide a spatial resolution of the order of 1 mm and an energy resolution of the order of 1 eV. More detailed XPS was also obtained by XPEEM in the Nanospectroscopy beamline in Elettra Sincrotrone Trieste using the SPELEEM III, from Elmitec GmbH. The spectral imaging energy resolution of the XPEEM system is 300 meV and the spatial resolution is 30 nm. Extraction of accurate XPS spectra from the XPEEM data is obtained with a lateral resolution of ~100 nm.

3.3.2.3 Atomic force microscopy (AFM)

The morphology and topography of the grown samples was characterized by AFM. AFM images were acquired in the Laboratoire de caractérisation des matériaux (Université de Montréal) using a Veeco Dimension 3100 microscope equipped with a silicon probe in tapping mode. WsXM was used for AFM and STM data analysis and image processing[206].

3.3.2.4 Raman scattering spectroscopy

Raman scattering spectra were acquired using a Renishaw inVia system with 633 nm laser excitation in the Laboratoire de caractérisation des matériaux (Université de Montréal). The ~1 μm lateral resolution allow to probe the vibrational properties of individual group VA 2D islands and to distinguish between different grown allotropes.

3.3.2.5 Scanning transmission electron microscopy (STEM)

Accurate atomic structure characterization and details about the substrate-layer interface were obtained by STEM, which was carried out at the Canadian Center for Electron Microscopy. Group VA 2D materials flakes are prepared for STEM observation by a cross-section lift out and thinning to electron transparency using a focused ion beam (Zeiss NVision 40 FIB). STEM imaging was done with a FEI Titan 80-300 Cubed TEM, equipped with hexapole-based aberration correctors for both the probe-forming lens and the image lens. STEM measurements were performed at 200 kV with a semi-convergence angle of 19 mrad. The signal was acquired on a high angle annular dark field (HAADF) detector with an inner acceptance semi-angle of 64 mrad.

3.4 Theoretical modelling

3.4.1 Density functional theory

In order to guide the experimental work, interpret the results and understand the properties of the synthesized materials, we must be able to determine the quantum mechanical state of the studied systems. The presence of substrate-layer interactions and finite dimensions make this a highly complex task. Thankfully, modern density functional theory (DFT) can give surprisingly accurate approximations of the solutions of the many-body Schrödinger equation for relatively large systems at a reasonable computational cost.

Starting from the Born-Oppenheimer approximation, the non-relativistic many-body problem in materials science consists of solving the Schrödinger equation for electrons in the potential of the nuclei:

$$\hat{H}\psi_{\mathrm{n}}(\mathbf{r_1}, \mathbf{r_2}, \ldots, \mathbf{r_N}) = E_n\psi_{\mathrm{n}}(\mathbf{r_1}, \mathbf{r_2}, \ldots, \mathbf{r_N}) \tag{3.1}$$

with the Hamiltonian:

$$\widehat{H} = -\frac{\hbar^2}{2m_e}\sum_i \nabla_i^2 + \sum_i V_{ext}(\boldsymbol{r_i}) + \frac{e^2}{4\pi\epsilon_0}\sum_{i\neq j}\frac{1}{\left|\boldsymbol{r_i} - \boldsymbol{r_j}\right|^2} \tag{3.2}$$

where the summations are on all electrons of the system and the external potential V_{ext} accounts for the effect of the nuclei. The Hohenberg-Kohn (HK) theorems allow to reframe this problem based on the electron density $n(\boldsymbol{r})$ rather the wavefunctions. They state:

Theorem 1: The external potential $V_{ext}(\boldsymbol{r})$ of any system of interacting particles is uniquely determined up to a constant by the ground state particle density $n_0(\boldsymbol{r})$.

Theorem 2: A universal energy functional of the particle density $E[n(\boldsymbol{r})]$, valid for any $V_{ext}(\boldsymbol{r})$ can be defined. This functional is minimized by the ground state density of the system $n_0(\boldsymbol{r})$.

Theorem 1 tells us that the Hamiltonian, and therefore the many body wavefunction and physical properties of the system are fully determined by the ground state density. On the other hand, theorem 2 tells us that if we knew the energy functional $E[n(\boldsymbol{r})]$, we could minimize it to determine all these properties.

The practical application of DFT requires an additional reformulation of the problem, known as the Kohn-Sham (KS) approach. The KS approach replaces the complex many body system by a fictitious auxiliary independent particles system which has the same ground state density as the real system. All the differences between the real and auxiliary systems are then accounted by the exchange-correlation energy E_{XC}, which can be approximated at different levels of accuracy. The single particle density is given by:

$$n(\boldsymbol{r}) = \sum_i |\phi_i(\boldsymbol{r})|^2 \tag{3.3}$$

where $\phi_i(\boldsymbol{r})$ are the single particle wavefunctions. The energy functional of the auxiliary system is given by:

$$E_{KS}[n] = T_s[n] + \int V_{ext}(\boldsymbol{r})n(\boldsymbol{r})d^3r + \frac{e^2}{4\pi\epsilon_0}\int \frac{n(\boldsymbol{r})n(\boldsymbol{r'})}{|\boldsymbol{r} - \boldsymbol{r'}|}d^3r d^3r' + E_{XC}[n] \tag{3.4}$$

with the single particle kinetic energy:

$$T_s[n] = \sum_i -\frac{\hbar^2}{2m_e}\nabla^2\phi_i(\boldsymbol{r}) \tag{3.5}$$

The exchange-correlation energy can be understood as the difference between the real and independent particle energy:

$$E_{XC} = (T_{mb} - T_s) + \left(E_{int} - \frac{e^2}{4\pi\epsilon_0}\int \frac{n(\boldsymbol{r})n(\boldsymbol{r}')}{|\boldsymbol{r}-\boldsymbol{r}'|}d^3r d^3r'\right) \tag{3.6}$$

where T_{mb} and E_{int} are the kinetic energy and electron interaction energies of the many body system. It can be shown that minimization of the KS energy is equivalent to solving the Kohn-Sham equations:

$$\left(-\frac{\hbar^2}{2m_e}\nabla^2 + V_{eff}(\boldsymbol{r})\right)\phi_i(\boldsymbol{r}) = E_i\phi_i(\boldsymbol{r}) \tag{3.7}$$

where the effective potential is given by:

$$V_{eff}(\boldsymbol{r}) = V_{ext}(\boldsymbol{r}) + \frac{e^2}{4\pi\epsilon_0}\int \frac{n(\boldsymbol{r}')}{|\boldsymbol{r}-\boldsymbol{r}'|}d^3r' + \frac{\delta E_{XC}[n]}{\delta n(\boldsymbol{r})} \tag{3.8}$$

and $V_{XC} = \frac{\delta E_{XC}[n]}{\delta n(\boldsymbol{r})}$ is the exchange-correlation potential.

In practice, minimisation of the ground-state energy is done self-consistently according to the procedure illustrated in Figure 3.3. An initial guess for the density is first made and used to compute V_{eff}. The single particle Hamiltonian is then diagonalized in a relevant basis set (often a plane-wave basis set) and the single particle solutions are used to compute a new density. This density is then inputted (often mixed with the density from previous iterations) to compute V_{eff} again for multiple self-consistent loops until convergence of the ground state energy is achieved. After convergence, quantities of interest can be computed from the single electron wavefunctions.

Several approximations of the exchange-correlation energy exist. The most widely used classes of approximations are the local-density approximation (LDA), based on the homogeneous electron gas, and the generalized-gradient approximation (GGA), which takes into account the non-uniformity of the electron density[207]. The LDA exchange-correlation energy functional is given by:

$$E_{XC}^{LDA}[n] = \int n(\boldsymbol{r})\epsilon_{XC}^{hom}\big(n(\boldsymbol{r})\big)d^3r \tag{3.9}$$

whereas the GGA energy also depends on the gradient of the density:

$$E_{XC}^{GGA}[n] = \int n(\boldsymbol{r})\epsilon_{XC}(n(\boldsymbol{r}), |\nabla \mathrm{n}(\boldsymbol{r})|)d^3r \tag{3.10}$$

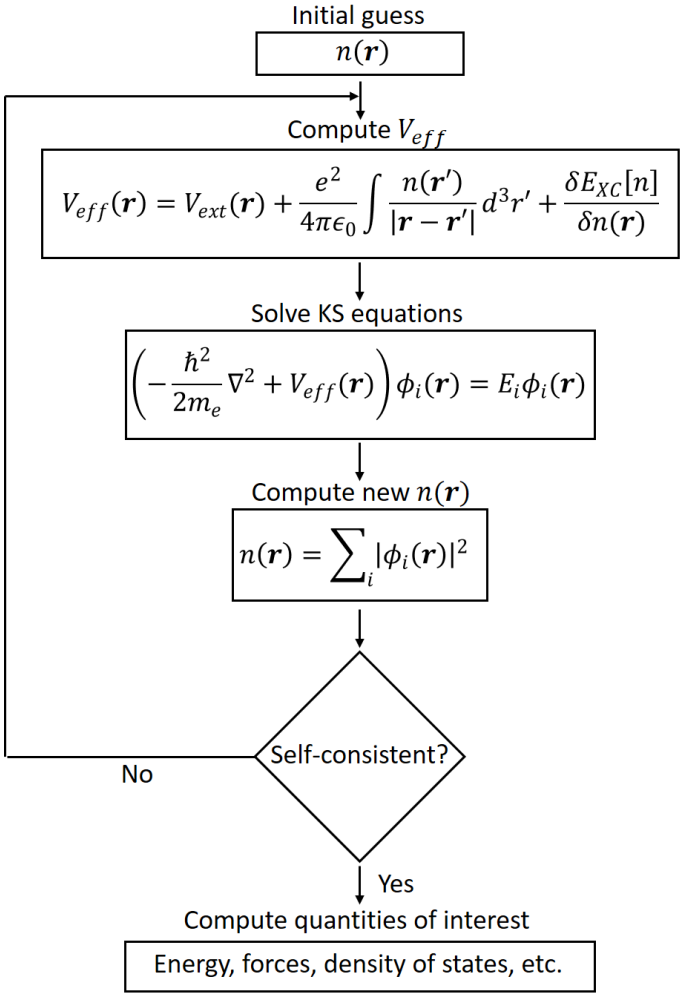

Figure 3.3 Schematic representation of the self-consistent loop for the solution of KS equations. Adapted from [208].

The specific form of the exchange-correlation energy ϵ_{XC} generally contains both exact and parametrized terms. Nonetheless, in all cases, the functional is strictly local, which is problematic when considering vdW layered systems. In fact, vdW interactions are non-local in nature and are not well reproduced by LDA or GGA[209]. In this thesis, two different methods will be used to treat

the vdW interactions. First, the PBE (GGA) functional[210] with the DFT-D2 method from Grimme[211], which is an empirical correction added to the energy to account for dispersion forces:

$$E_{disp} = -s_6 \sum_{i=1}^{N_{at}-1} \sum_{j=i+1}^{N_{at}} \frac{C_6^{ij}}{R_{ij}^6} f_{dmp}(R_{ij}) \tag{3.11}$$

where s_6 is a scaling factor dependent on the exchange-correlation functional, C_6^{ij} is an empirical coefficient for the atomic pair ij, R_{ij} is the interatomic distance, f_{dmp} is a damping function and the summations are for all atomic pairs. The second method is the optB86b-vdW non-local functional[212-214].

All DFT calculations were carried out with Quantum Espresso code[215, 216], which uses a plane-wave basis set and pseudopotentials (PPs). PPs are effective ionic potentials constructed in way such that valence electrons are described by pseudo-wavefunctions, which are equal to the real the real Kohn-Sham wavefunctions outside a cut-off radius and have the same energy eigenvalues. Nonetheless, in contrast to the real wavefunctions, the pseudo-wavefunctions do not have nodes close to the nuclei. This allows to truncate the plane-wave expansion at much smaller Fourier frequencies and reduce the computational cost by several orders of magnitude. Since core electrons are confined near the nuclei and are not involved in chemical interactions, they are not explicitly treated in DFT calculations and are included in the PP.

Even though the electronic structure can be approximated quite accurately with KS DFT, the equilibrium positions of the nuclei need to be known in order to extract information from the system. This is even more important when studying new materials or complex systems (epitaxial 2D materials for instance), for which the atomic structure is unknown. Structural relaxation of the system is facilitated by the Hellmann-Feynman theorem, which states that if the Hamiltonian depends on a parameter λ, the derivative of the energy of the eigenstates with respect to this parameter is given by the expectation value of the derivative of the Hamiltonian. The theorem can be applied to the nuclei positions to give the components of the force on the ions:

$$\boldsymbol{F}_I = -\int n(\boldsymbol{r}) \frac{\partial V_{ext}(\boldsymbol{r})}{\partial \boldsymbol{R}_I} d^3r - \frac{\partial E_{II}}{\partial \boldsymbol{R}_I} \tag{3.12}$$

where $\boldsymbol{R}_I$ are the nuclei positions and E_{II} are the nuclei repulsion energies.

3.4.2 Kinetic Monte Carlo

Atomistic simulations of kinetic processes such as growth and thermal decomposition can provide significant insight into the mechanisms governing these phenomena. This can be done with unmatched accuracy by molecular dynamics (MD) simulations. However, MD simulations suffer from two important limitations. First, forces need to be calculated accurately, which can be extremely computationally expensive with *ab initio* approaches. On the other hand, semi-empirical models to compute the forces rapidly are usually limited to very specific systems. The second issue is the time scales involved. To reproduce atomic vibrations, MD requires time steps of the order of 10^{-15} seconds[217]. However, relevant kinetic processes with significant energy barriers can occur in timescales of seconds or even more. Kinetic Monte Carlo (KMC) avoids these problems by considering only the transitions for state to state, such as diffusion or desorption. According to transition state theory, the rate a transition is given by $f = f_0 \exp(-E_a/k_B T)$, where f_0 is the attempt frequency, E_a is the activation energy of the transition and k_B is the Boltzmann constant. The E_a can be estimated from *ab initio* calculations and the f_0 are usually set based on physical intuition, since their accuracy is not critical as compared to the exponential term. This approach however requires making hypotheses about the involved transitions. For this reason, KMC can allow to test models but has a weak predictive power.

KMC is used in Chapter 6 to simulate the sublimation of α-2D-P. The simulations are carried out on Matlab using a rejection-free KMC algorithm implemented as follows. The α-2D-P atomic lattice is represented by a matrix and the different sublimation events are considered based on the atomic environment of the atoms. First, an initial configuration i is set at $t = 0$ and multiple KMC iterations are carried out. A single iteration contains the following step. All the possible sublimation events in the matrix are identified and attributed a rate $f_{i\to j}$. Then, the total transition rate is calculated with $R_i^{tot} = \sum_j f_{i\to j}$ and the probability of each transition is set as $p_{i\to j} = f_{i\to j}/R_i^{tot}$. A transition to the state j is randomly chosen according to $p_{i\to j}$ using a binary search and the system is updated to the state j, with the time updated to $t = t + \ln(1/u)/R_i^{tot}$, where u is a random number between]0,1]. Then multiple iterations can be done starting from the new states j. This procedure allows to simulate the sublimation of one α-2D-P layer. To obtain accurate rates, thousands of such simulations are averaged.

CHAPTER 4 THEORETICAL ANALYSIS OF POTENTIAL GROWTH SUBSTRATES

To guide the experimental work on the synthesis of group VA 2D materials, this chapter presents a DFT investigation of epitaxial 2D pnictogens on several potential substrates. The main goal of the study is to understand the stability, substrate-layer interactions and electronic properties of epitaxial group VA 2D materials in order to establish potential experimental conditions to achieve their large-scale growth. A part of the results presented in this chapter have been published in the following paper [35]:

Fortin-Deschênes, M.; Moutanabbir, O. "Recovering the semiconductor properties of the epitaxial group V 2D materials antimonene and arsenene." *The Journal of Physical Chemistry C* 2018, 122, (16) (2018): 9162-9168.

4.1 Epitaxial group VA 2D materials on transition metals

As mentioned above, the growth of light group VA 2D materials needs to be done under high pressure or with the use of a catalyst. Highly reactive substrates such as transition metals are particularly effective catalysts and can be exploited for the growth of the 2D material. While their use also imposes restrictions on the substrate's symmetry, they can facilitate the nucleation of specific phases. In principle, because of their weak interaction, 2D materials are less sensitive to substrate symmetry than 3D materials which typically bond with the substrate under well-defined crystalline orientations. However, as the reactivity of the substrate and the epitaxial 2D material increases, the minimization of the surface and interface energies becomes a determining factor for the nucleation and stability particular phases. This is especially important for group VA elements which may grow in various allotropic forms depending on surface symmetry, lattice parameter and surface reactivity. For these reasons, lattice matched metallic substrates, which have a potential to promote the growth of several allotropes will be considered for α-2D-P and β-2D-P. In fact, both these materials are expected to require catalytic growth. With these basic considerations, potential substrates can be easily identified. We note that the ~1.39 in-plane lattice parameters ratio of α-2D-P (Table 4.1) is close to $\sqrt{2}$. This makes cubic (110) oriented surfaces good candidates for α-2D-P epitaxy. With lattice constants of 3.30 Å and 3.31 Å, Nb(110) and Ta(110) are lattice matched to α-2D-P. On the other hand, the 3-fold rotational symmetry of β-2D-P makes hexagonal (0001)

and cubic (111) substrates well-suited for epitaxial growth. For cubic (111), the surface lattice constant is $\sqrt{2}$a in bcc and $\sqrt{2}/2$a in fcc. However, there are no cubic (111) transition metal lattice matched to β-2D-P. Nevertheless, hcp Zr(0001) and Sc(0001) are lattice matched to β-2D-P.

Since heavier elements are known to crystallize in the A7 phase under normal conditions, the use of reactive substrate becomes less critical as the atomic number increases. Moreover, the dependence of the interfacial energy on the epitaxial orientation should weaken with decreasing substrate reactivity. It is therefore instructive to examine the properties of epitaxial group VA elements as a function of the substrate's reactivity. Y(0001) and Si(111) will be studied as substrates for the growth of β-2D-As growth and Ge(111) for the growth of β-2D-Sb. Si and Ge are particularly relevant due to their widespread use in the semiconductor industry. While Si has been the main platform for CMOS technology, Ge can be easily grown on Si to form what is commonly known as Ge virtual substrates. The direct growth of group VA 2D materials on these group IV semiconductors is highly desirable for the integration of this new class of materials in emerging nanoscale technologies compatible with the current semiconductor manufacturing.

Table 4.1 Lattice parameters of group VA single layers. See reference [172] for lattice parameters.

	a_β (Å)	a_α (Å)	b_α (Å)	Substrates
2D-N	2.27			Not studied in this thesis
β-2D-P	3.28			Sc(0001), Zr(0001)
α-2D-P		3.31	4.55-4.62	Nb(110), Ta(110)
β-2D-As	3.67			Y(0001), Si(111)
α-2D-As		3.67	4.72-4.77	
β-2D-Sb	4.04-4.12			Ge(111)
α-2D-As		4.27-4.36	4.74-4.78	
β-2D-Bi	4.19-4.33			Not studied in this thesis
α-2D-Bi		4.44-4.55	4.87-4.94	

At the other extreme of surface reactivity are vdW substrates. These weakly interacting substrates may be particularly useful for the growth of heavier group VA 2D materials such as Sb and Bi which readily crystallize in the A7 phase. Studying 2D materials epitaxy on weakly interacting substrates is of great importance to the development of vdW heterostructures and to allow the conservation of the freestanding properties of the layers. Section 4.2 is dedicated to this subject. The lattice parameters of group VA 2D materials and the corresponding potential substrates considered in this chapter are shown in Table 4.1.

4.1.1 α-2D-P

First, the behavior of α-2D-P on Nb(110) is examined. Nb(110) substrates are modelled with supercell slab geometries consisting of 9 atomic layers with the three bottom layers fixed at bulk position. The lattice parameter used in the supercell calculation is 3.308 Å, as determined by relaxation of bulk bcc Nb using the Broyden–Fletcher–Goldfarb–Shanno (BFGS) algorithm and the PBE functional with Grimme vdW corrections (DFT-D2). At least 15 Å of vacuum are added in the out-of-plane direction to avoid interactions between periodic images. For adsorption calculations, monolayer α-2D-P is strained to be lattice matched on Nb(110). The relaxed α-2D-P lattice parameters are a=3.306 Å and b=4.569Å, leading to a compressive strain of 0.06% in the *a* direction and a tensile strain of 2.4% in the *b* direction.

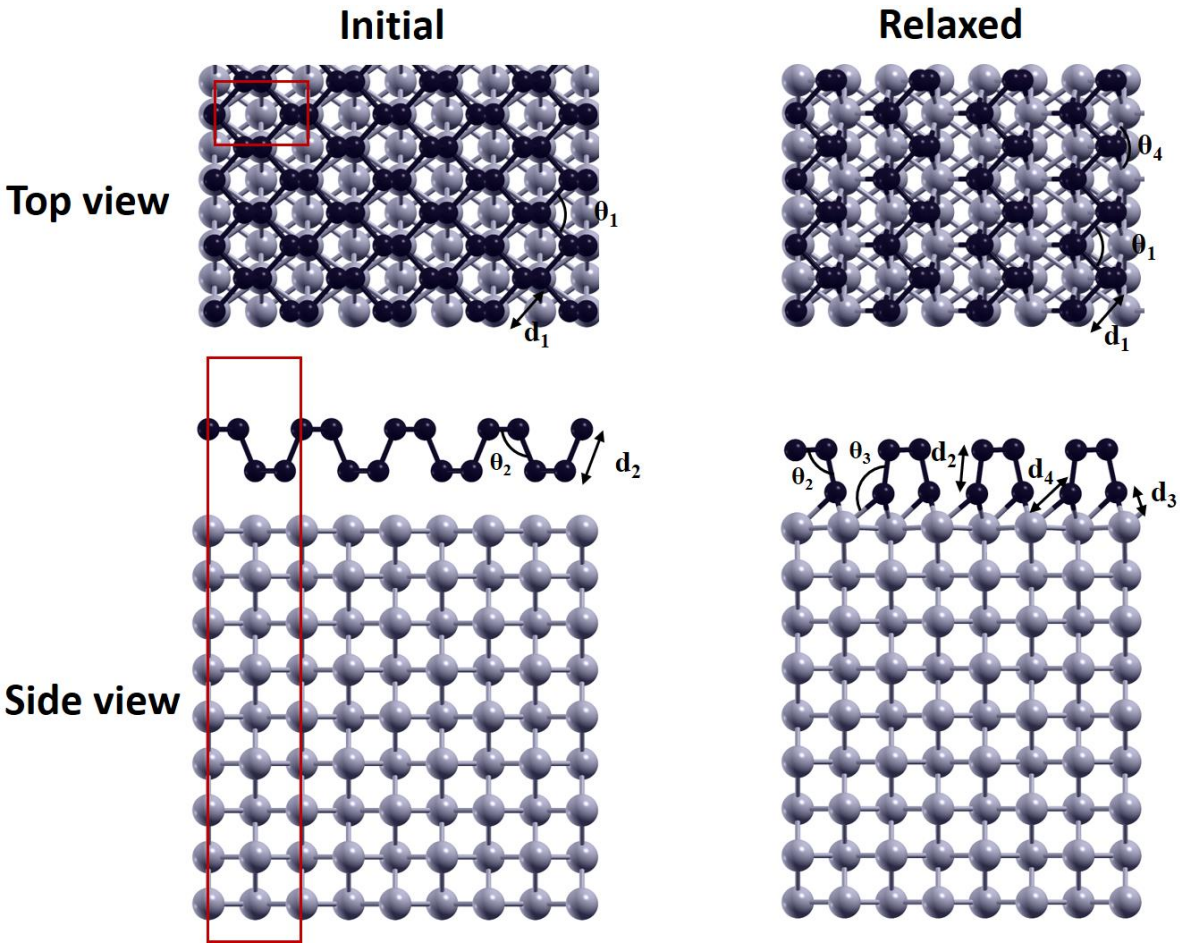

Figure 4.1 Initial and relaxed geometries for epitaxial α-2D-P on Nb(110).

The initial and relaxed supercell geometries are shown in (Figure 4.1). To determine possible local minima in the potential energy surface, four initial configurations are taken into account. The first configuration is shown in Figure 4.1 and the three others are obtained by translations of (a/2 0 0), (0 b/2 0) and (a/2 b/2 0) of the bP lattice of the first. All considered initial configurations were found to lead to the same relaxed geometry. The adsorption energy E_{ads} of α-2D-P on Nb(110) is determined by:

$$E_{ads} = (E_{\mathrm{P/Nb(110)}} - (E_{\alpha-\mathrm{2D-P}} + E_{Nb(110)}))/N_{atoms} \quad (4.1)$$

where $E_{\mathrm{P/Nb(110)}}$ is the total energy of epitaxial α-2D-P on Nb(110), $E_{\alpha-\mathrm{2D-P}}$, the energy of freestanding α-2D-P and $E_{Nb(110)}$ the energy of the isolated Nb(110) supercell. A value of $E_{ads} = -801\ \mathrm{meV/atom}$ is found. This strong interaction is also associated with important structural modifications of the P overlayer. In fact, the α-2D-P layer is not stable on Nb(110) and forms parallel chains on the substrate, similar to the Seiwatz chains that form on Ge(111)[218]. However, contrarily to Seiwatz chains, the P chains on Nb(110) have four atoms per unit cell and non-equivalent top and bottom atoms. Here, the chains are formed by breaking the in-plane P-P bonds on the bottom of the BL and by forming additional bonds with the Nb surface atoms. The structural parameters of the P chains are shown in Table 4.2 (See Figure 4.1 for definitions). The atomic structure of the top atoms is similar to the zigzag chains in α-2D-P, with a noticeable contraction of d_2 and a reduction of the θ_2 bond angle. Obviously, the structure of the bottom atoms is different from α-2D-P since the P atoms only have one P neighbor. The bottom P atoms have two equivalent Nb neighbors at a distance of d_3=2.429 Å, hinting to possible P-Nb chemical bonds. The P-P-Nb and Nb-P-Nb bond angles are θ_3=133.79° and θ_4=69.85°, departing significantly from the typical sp^3 behavior of allotropic P. A third Nb neighbor can also be seen. However, the P-Nb distance is d_4=2.596 Å, indicating a weaker interaction.

Table 4.2 DFT calculated structural parameters for P chains on Nb(110) and freestanding monolayer α-2D-P.

P chains on Nb(110)								α-2D-P			
d_1 (Å)	d_2 (Å)	d_3 (Å)	d_4 (Å)	θ_1 (°)	θ_2 (°)	θ_3 (°)	θ_4 (°)	d_1 (Å)	d_2 (Å)	θ_1 (°)	θ_2 (°)
2.261	2.205	2.429	2.596	94.03	95.97	133.79	69.85	2.220	2.254	96.27	103.78

The interaction between the P overlayer and the Nb substrate can be better understood by looking at the charge density and the projected DOS (PDOS). The charge density of the P overlayer minus the superposition of isolated atoms charge densities is shown in Figure 4.2a. The isosurface is plotted at a density of 0.01 e^-/a_0^3. Only bonds involving P atoms are visible at this density due to the delocalized nature of the metallic Nb-Nb bonds. As expected from the calculated interatomic distances, the increased charge density between P atoms within chains indicates the formation of covalent bonds. Moreover, the large distance between chains breaks the P-P bonds of the bottom zigzag chains of α-2D-P. The charge density between the bottom P atoms and their two closest Nb neighbors is of the same magnitude than in P-P bonds, meaning that two of the three P-P bonds of the bottom P atoms were replaced by P-Nb bonds. In fact, the latter are stronger since the adsorption energy of α-2D-P on Nb(110) is largely negative.

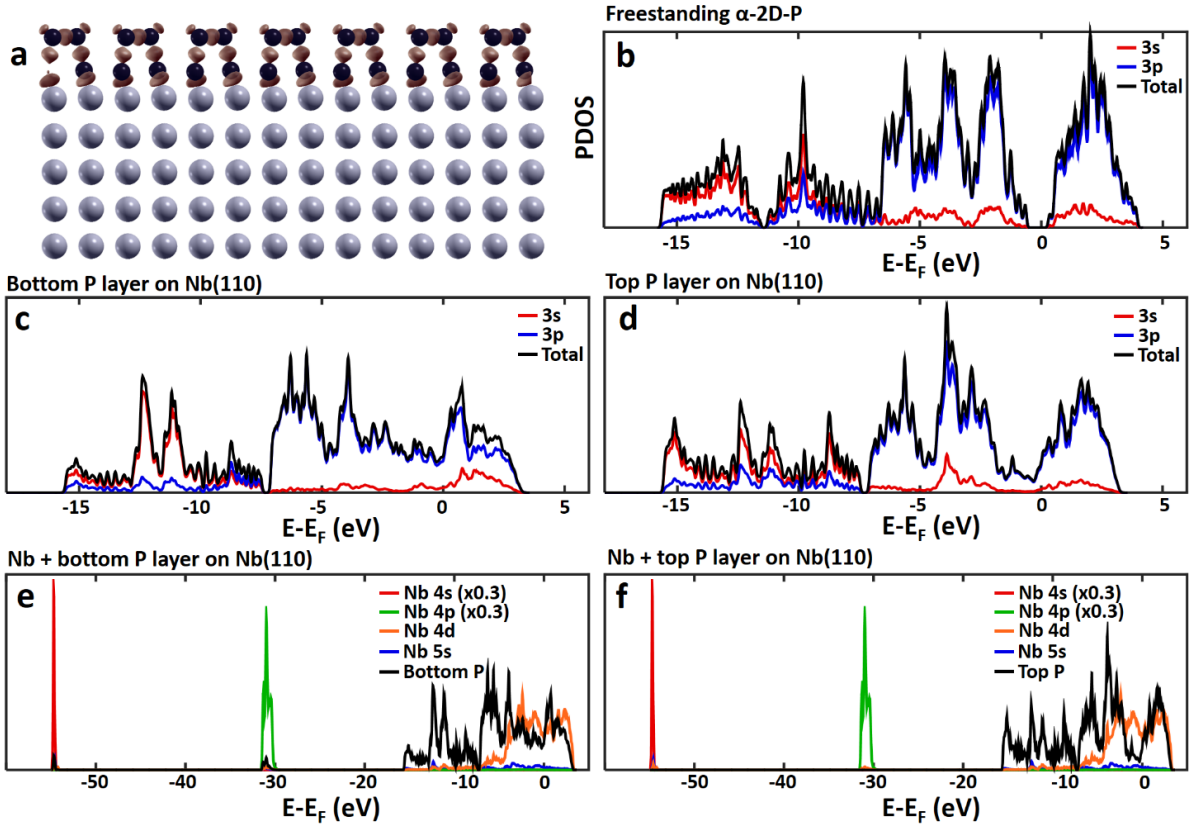

Figure 4.2 a) Charge density minus superposition of atomic charge densities isosurface for α-2D-P relaxed on Nb(110). Isosurface at 0.01 e^-/a_0^3. b) PDOS of freestanding α-2D-P. c) PDOS of the bottom P layer on Nb(110). d) PDOS of the top P layer on Nb(110). e) PDOS of the top Nb atoms and bottom P. f) PDOS of the top Nb atoms and top P.

The PDOS of freestanding α-2D-P can be seen in Figure 4.2b. The results are similar to previously published PDOS[219]. Left and right of -11.5 eV are the bonding and antibonding 3s states. Similarly, immediately left and right of the Fermi level are the bonding and antibonding 3p states. Nonetheless, there is a relatively significant overlap in 3s and 3p PDOS indicate due to the sp^3-like hybridization. The band gap is ~0.8 eV, slightly smaller than previously published PBE values, most likely due to the small strain induced by the vdW correction.

The PDOS of the top and bottom atoms of the P overlayer on Nb (110) can be seen in Figure 4.2c and Figure 4.2d, respectively. The PDOS of α-2D-P is strongly affected by the interaction with the Nb substrates. The 3p orbitals are the most perturbed by this interaction. In fact, the bonding and antibonding 3s states are still clearly visible in both the top and the bottom P atoms. However, we can notice that a small ~0.3 eV band gap has opened between the 3s and 3p states at -7.3 eV and that there is no more gap at the Fermi level. Overall, the system has transitioned from a semiconductor to a metal, as most clearly seen for the bottom P atoms. An important decrease in the PDOS of the top P atoms at the Fermi level is nonetheless still present. Moreover, we can notice a decrease in the overlap between the 3s PDOS and the 3p PDOS for the bottom P atoms. However, the overlap for the top P atoms is conserved. This indicates that the top P atoms are still sp^3 hybridized. It is noteworthy that the bottom P layer shows weak s-p hybridization, as expected from the bond angles.

The PDOS of the bottom and top P atoms, as well as the PDOS of the top Nb layer can be seen in Figure 4.2 (e, f). A small but noticeable overlap between the 4s and 4p Nb PDOS and the bottom P PDOS is observed. Since these states are only weakly involved in bonding, the small overlap is another clear sign of the Nb-P bond. On the other hand, the top P layer does not show any hybridization with the Nb 4s and 4p orbitals. The most significant Nb-P interaction is between P 3p and Nb 4d states, as seen in the PDOS close to the Fermi level. Moreover, this hybridization with the Nb 4d states at the Fermi level leads to a transition from semiconductor to metal in α-2D-P on Nb(110). In fact, a clear peak in the Nb 4d and bottom P 3p PDOS is seen at the Fermi level. For the top P atoms, this peak is not present.

The results presented above agree with the assumption that reactive TM substrates are useful at catalysing chemical reactions for 2D-P synthesis. However, the reaction of α-2D-P with the highly energetic Nb(110) surface leads to the formation of P chains, which passivate the Nb surface

dangling bonds. The Nb(11) surface is therefore unlikely to lead to the epitaxial growth of α-2D-P epitaxy. In fact, Nb(110) will lose its catalytic potential after the deposition of the first P layer.

4.1.2 Epitaxial β-2D-P and β-2D-As

The following subsection discusses epitaxial β-2D-P and β-2D-As on hcp transition metals. The methodology is the same as for α-2D-P on Nb(110). Similarly to α-2D-P on Nb(110), there are many possible ways to stack the β phase of group VA 2D materials on hcp substrates, as described below. At equal surface lattice parameters, the atomic density of group VA β-2D materials is twice the surface atomic density of the hcp surfaces. Here, only the most stable adsorption sites on the hcp surfaces are considered (hcp, fcc, atop and bridges sites). The only combinations of sites which can host the two atoms of the β-2D unit cell are (atop, hcp), (atop, fcc) and (fcc, hcp). Since the β-2D lattice is buckled, it is possible to place the bottom (or top) atom on either of these sites, leading to six possible stacking of β-2D group VA 2D materials on hcp surfaces. For instance, (atop, hcp) indicates that the bottom β-2D group VA atom is in the atop site and the top atom is in the hcp site, whereas (hcp, atop) indicates that the bottom atom is in the hcp site and the top atom is in the atop site.

The relaxed geometries of the different stackings are shown in Figure 4.3 and the calculated E_{ads} and structural parameters for β-2D-P and β-2D-As on hcp (0001) TM surfaces are shown in Table 4.3. We notice that the structure of β-2D-P and β-2D-As on metal surfaces is well conserved, in contrast to α-2D-P on Nb(110). In fact, the P-P/As-As bond angles θ and P-P/As-As interatomic distance $d_{V\text{-}V}$ vary by less and 0.7° and 0.013 Å for β-2D-P on Sc(0001), with respect to freestanding β-2D-P. The variations are < 2.2° and < 0.021 Å for β-2D-P on Zr(0001) and < 2.1° and < 0.016 Å for β-2D-As on Y(0001). These slightly larger variations on Zr(0001) and Y(0001) might be caused by the larger lattice mismatch on these substrates (-0.98% and -1.49%, as compared to 0.05% on Sc(0001)). However, the E_{ads} of β-2D-P on metals (between -455 meV/atom and -817 meV/atom) are still relatively large and comparable with the -801 meV/atom of α-2D-P on Nb(110). The E_{ads} of β-2D-As are about 12% smaller (in absolute values) than those β-2D-P, as expected from the weaker bond strength with increasing atomic number.

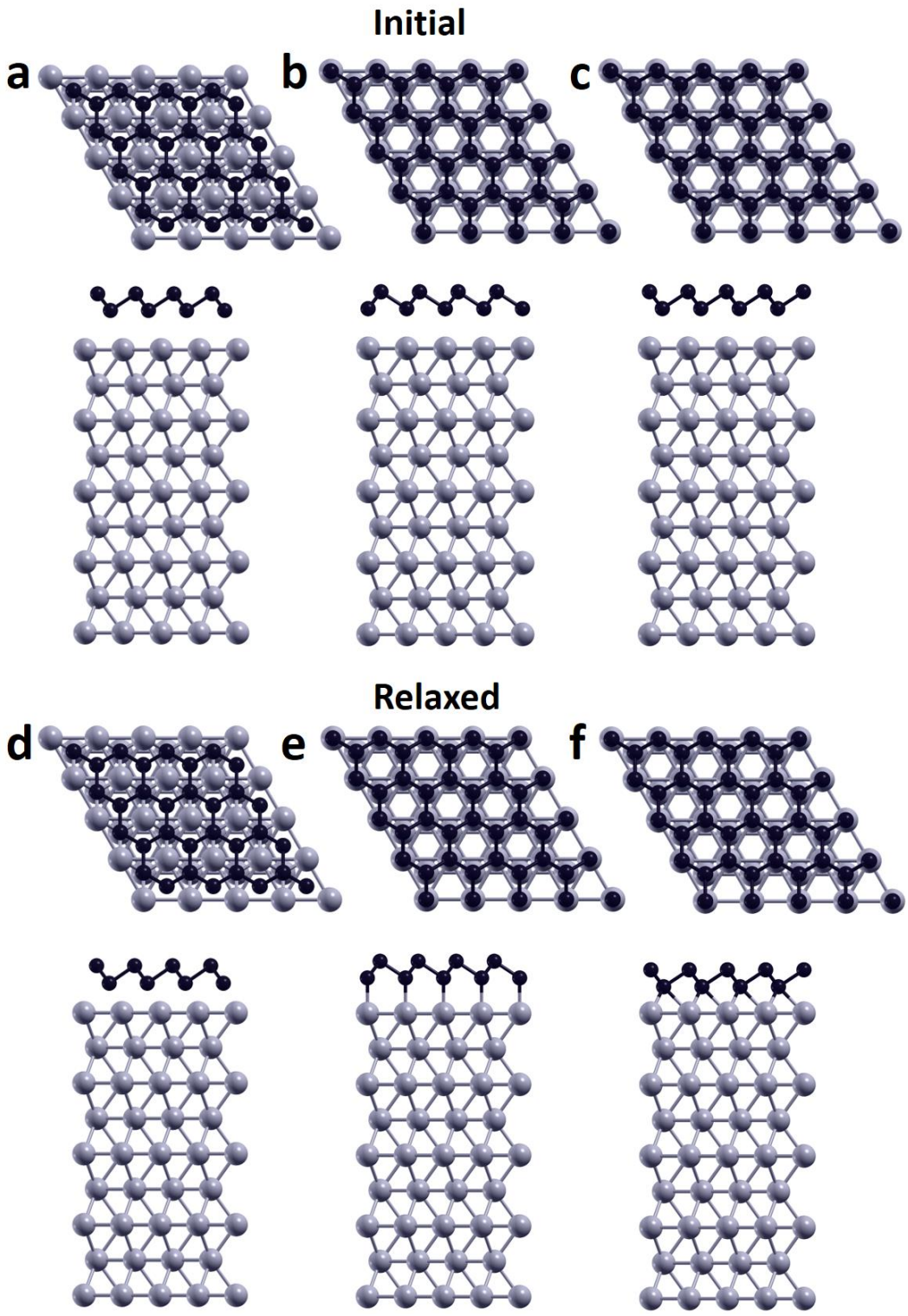

Figure 4.3 Stick and balls models of the atomic structure of group VA β-2D materials on hcp TM substrates used in DFT calculations. a, d) (hcp, fcc). b, e) (atop, hcp). c, f) (hcp, atop)

Table 4.3 Adsorption energies and structural parameters of freestanding and epitaxial β-2D-P and β-2D-As on transition metals.

	Strain (%)	E_{ads} (meV/atom)	d_{V-V} (Å)	d_{V-M} (Å)	θ_{V-V} (°)
Freestanding β-2D-P	0	-------	2.262	-------	93.1
β-2D-P/Sc (hcp-fcc)	0.05	-517	2.275	2.948	92.5
β-2D-P/Sc (fcc-hcp)	0.05	-498	2.281	2.954	92.2
β-2D-P/Sc (atop-fcc)	0.05	-455	2.261	2.657	93.3
β-2D-P/Sc (atop-hcp)	0.05	-472	2.261	2.639	93.3
β-2D-P/Sc (fcc-atop)	0.05	-799	2.263	2.689	93.1
β-2D-P/Sc (hcp-atop)	0.05	-797	2.267	2.693	92.9
β-2D-P/Zr (hcp-fcc)	-0.98	-538	2.283	2.881	90.9
β-2D-P/Zr (fcc-hcp)	-0.98	-538	2.289	2.917	90.6
β-2D-P/Zr (atop-fcc)	-0.98	-567	2.252	2.634	92.4
β-2D-P/Zr (atop-hcp)	-0.98	-558	2.249	2.637	92.6
β-2D-P/Zr (fcc-atop)	-0.98	-817	2.253	2.694	92.4
β-2D-P/Zr (hcp-atop)	-0.98	-804	2.251	2.701	92.5
Freestanding β-2D-As	0	-------	2.503	-------	92.0
β-2D-As/Y(hcp-fcc)	-1.49	-522	2.519	3.250	89.6
β-2D-As/Y (fcc-hcp)	-1.49	-499	2.516	3.256	89.7
β-2D-As/Y (atop-fcc)	-1.49	-404	2.489	2.938	91.0
β-2D-As/Y (atop-hcp)	-1.49	-428	2.489	2.913	90.9
β-2D-As/Y (fcc-atop)	-1.49	-684	2.515	2.995	89.8
β-2D-As/Y (hcp-atop)	-1.49	-703	2.513	2.997	89.9

Regardless of the TM substrate or epitaxial group VA 2D material, the most stable adsorption stacking is (fcc-atop) or (hcp-atop), with ~ -800 meV/atom for β-2D-P and ~ -700 meV/atom for β-2D-As. The four other stackings have E_{ads} of ~200-300 meV larger. We can also notice that interchanging the fcc-hcp sites does not affect significantly E_{ads} nor the structural parameters. In fact, the fcc and hcp sites are equivalent with respect to the hcp substrate top layer. Further analysis will therefore be restricted to (hcp-fcc), (atop-hcp) and (hcp-atop). Moreover, the trends of the structural parameters and E_{ads} as a function of the stacking are almost independent of the TM or the group VA 2D material (they depend mostly on the stacking). This is expected considering the chemical similarity between these systems. Interestingly, the (atop-hcp) stacking is not the most stable configuration, even though it has the shortest d_{V-M}. In fact, it is the least stable stacking for β-2D-P on Sc(0001) and for β-2D-As on Y(0001) (excluding the quasi-indentical (atop-fcc)) and a close second to (fcc-hcp) for β-2D-P on Zr(0001).

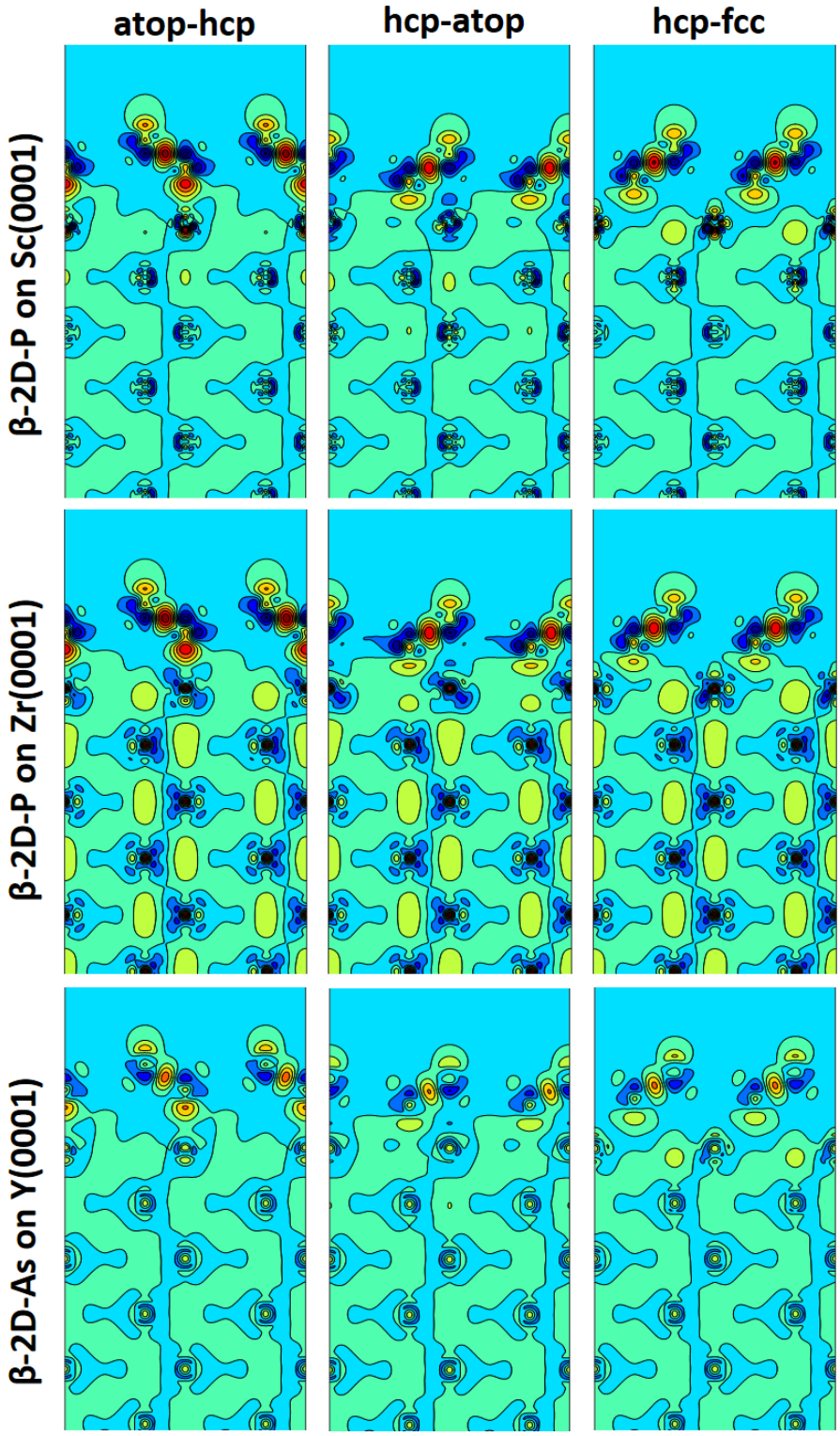

Figure 4.4 Charge density minus superposition of atomic charge densities for β-2D-P and β-2D-As on transition metals for three stackings ((atop, hcp), (hcp, atop) and (hcp, fcc)).

Moreover, the substrate-layer interaction energy of the (hcp-fcc) stacking is about 30% weaker than the (hcp-atop) configuration (and $d_{V\text{-}M}$ is about 0.2-0.25 Å larger), even though the bottom atoms are in the same adsorption site. This behavior is unexpected considering the natural stacking of A7 group VA materials. In fact, in bulk A7 pnictogens, the weak interlayer bonds are rotated by 180° from the strong in-plane bonds around the normal of the layer (the 180° rotation refers to the projection of these bonds in the plane of the layer). For the (hcp-fcc) stacking, the bonds between the group VA atoms and the TM atoms are in this configuration. However, for the (hcp-atop), the substrate-layer bonds are directly aligned with the in-plane covalent bonds.

To better understand the substrate-layer interactions and their dependence on the stacking configuration, we look at the charge densities and PDOS. The charge densities minus superposition of atomic charge densities for β-2D-P on Sc(0001)/Zr(0001) and for β-2D-As on Y(0001) for the three main stackings are shown in Figure 4.4. Similar to the structural parameters and E_{ads}, the charge densities are almost independent of the TM substrate and group VA layer. However, the behavior depends strongly on the stacking. The charge density re-localization between to top TM atom and bottom VA atom in the (atop-hcp) configuration is very large, possibly indicating a strong chemical bond. In fact, there is an important increase in charge density at the location of the doublet of the bottom atom, as compared to the top atom's doublet. However, it is not clear that the increased charge is shared by the bottom layer atoms and top TM atoms. In fact, the charge is mostly localized close to the group VA atoms, which may explain the relatively small interaction energy. Nonetheless, the charge re-localization is positive everywhere between the top substrate and bottom layer atoms.

For the (hcp-atop) configuration, the charge re-localization is negative between the bottom group VA atom and its nearest TM atom neighbor. We note that this is also the case for the interlayer bonding between TM atoms within the substrate. We can nonetheless notice a continuous positive charge re-localization region going from the bottom group VA atom to the TM substrate. We note that this weak charge localization occurs in the three equivalent bonding directions, leading to a more significant interaction. Since the structural parameters of the group VA layer are almost conserved with respect to the freestanding materials, an important charge re-localization is not expected. Still, a decrease of the charge density in the VA-VA bonds is observed for the (hcp-atop) configuration, as compared to (hcp-fcc) and (atop-hcp). This indicates that some of the charge has

been re-localized upon adsorption to form the bonds with the TM substrate, which are at the origin of the strong substrate-layer interaction.

In agreement with the calculated structural parameters and E_{ads}, no sign of group VA-TM molecular orbitals is observed for the (hcp-fcc) stacking. In fact, a small negative charge re-localization surrounds the doublet of the bottom group VA atom for β-2D-P on Sc(0001) and β-2D-As on Y (0001). Moreover, a relatively important repulsion is observed between the doublet and the substrate charge, as indicated by the local maxima surrounding the negative re-localization region. This repulsive behavior is at the origin of the relatively weak E_{ads}, as compared to the (hcp-atop stacking). Moreover, Löwdin charge analysis reveal a charge transfer from the Sc substrate to β-2D-P of 0.14 e^-/unit cell, mostly concentrated on the bottom P atom (0.09 e^-/unit cell for (atop-hcp) and 0.11 e^-/unit cell for (hcp-atop)). This indicates the slight ionic character of the substrate-layer bond, in agreement with the ~0.9 electronegativity difference between the group VA and TM atoms.

The PDOS of freestanding β-2D-P and epitaxial β-2D-P on Sc(0001) are shown in Figure 4.5. The PDOS of β-2D-P on Zr(0001) and β-2D-As on Y(0001) are very similar to β-2D-P on Sc(0001) and are not shown here. The PDOS of freestanding β-2D-P shares many features with the PDOS of α-2D-P. The bonding and antibonding 3s states are similar to α-2D-P and are located left and right from -11 eV. The band gap at the Fermi level is ~1.5 eV, significantly larger than for α-2D-P. Moreover, s-p hybridization is also present as evidenced by the features shared by the 3s and 3p PDOS. Important modifications of the PDOS occur upon interaction with the TM substrate (Figure 4.5 (b-h)). β-2D-P transitions from a semiconductor to a metal, as indicated by the large PDOS at the Fermi level. We notice that there is still an important decrease in the PDOS in the region separating the bonding and antibonding 3p states. However, the Fermi level has shifted above the band gap, meaning that the layer is fully metallic. The Fermi level shift to higher energies is due to the ~0.1 e^- charge transfer from the substrate to the layer. We also notice that the substrate-layer orbital hybridization is not as pronounced as for α-2D-P on Nb(110). This is expected considering the structural integrity of epitaxial β-2D-P. Like α-2D-P, the 3s states are not as affected as the 3p states by the interaction with the substrate. Moreover, it appears that the $3p_z$ states are more affected than the $3p_x$ and $3p_y$ states. According to Shao et *al*., group VA β 2D materials have sp^2 states partially hybridized with p_z states (three σ bonds) and p_z dominated states (π bonds or doublets)[161].

As seen in the PDOS (Figure 4.5 (c-h)), the most affected orbitals are the p_z states of the bottom atoms, indicating the doublets are responsible for the interaction with the substrate.

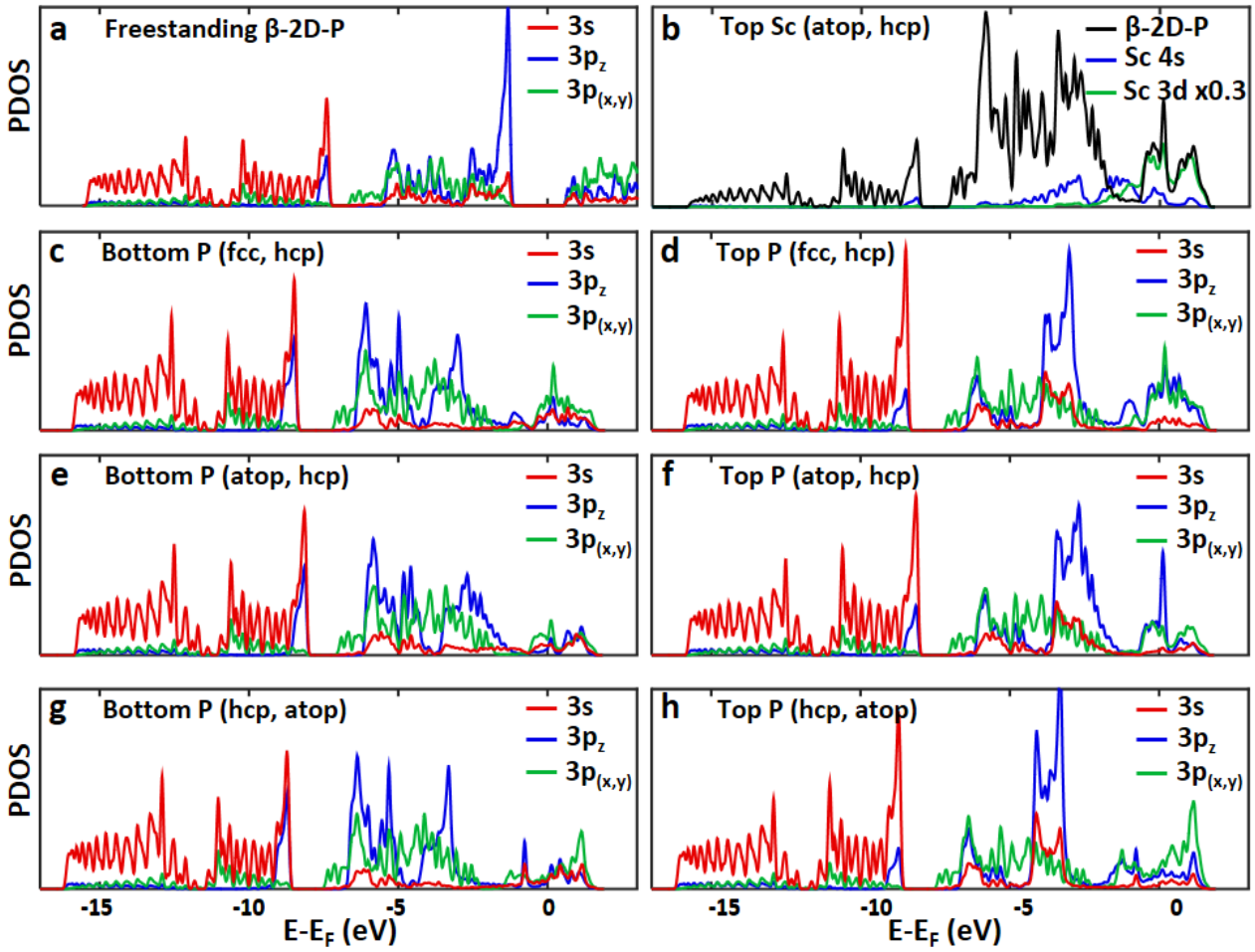

Figure 4.5 PDOS of freestanding and epitaxial β-2D-P on Sc(0001). (a) Freestanding β-2D-P. (b) Epitaxial (hcp, atop) β-2D-P on Sc(0001) showing PDOS of β-2D-P and the top Sc atom. (c, d) Top and bottom P atom (fcc, hcp). (e, f) Top and bottom P atom (atop, hcp). (g, h) Top and bottom P atom (atop, hcp). The PDOS of $3p_x$ and $3p_y$ is identical and only one is shown.

In summary, TM substrates interact strongly with group VA 2D materials. In all cases, the E_{ads} of the most stable configurations are in the order of 700-800 meV/atom. For α-2D-P on Nb(110), the interaction is strong enough to compromise the structural integrity of the epitaxial layer. The structure of α-2D-P and α-2D-As on hcp (0001) TM surfaces is conserved. While these substrates may be useful to demonstrate the existence of novel group VA 2D materials, the interaction is

strong enough to modify the electronic structure beyond recognition. In fact, group VA 2D materials on TM surfaces should be considered as 2D overlayers rather than 2D materials in their own right. Undoubtedly, most measurements of their physical properties other than structural would be dominated by substrate effects due to the strong modification of the electronic structure, especially around the Fermi level.

4.2 Group VA 2D materials on weakly interacting substrates

Considering that TM substrates strongly alter the properties of group VA 2D materials, weakly interacting surface are interesting candidates as growth substrates. While light group VA 2D allotropes may require catalytic surfaces for their growth, heavier group VA elements (As, Sb, Bi) crystallize more readily in their stable A7 phase. Weakly interacting substrates may therefore be suited for their growth. As mentioned above, group IV semiconductors are particularly appealing due to their widespread use as substrates for CMOS technologies. Even with their relatively high surface energies, these semiconductors can be expected to interact less than TM substrates with self-passivated materials. In fact, the directionality of their covalent bonds increases the energetic cost of bonding with materials with different coordination. Nonetheless, the surface dangling bonds of semiconductor surfaces might interact with the 2D layers and should not be neglected. Various dangling bond passivation methods will be considered in this section. Growth on passivated semiconductor substrate (vdW epitaxy) is a method which was initially proposed by Koma to reduce the substrate-layer interactions to relax the lattice-matching condition in heteroepitaxy[220]. The method has since been used to heteroepitaxially grow multiple materials, mainly on Si(111)-H[221-226]. Here, the goal is not to relax the lattice-matching condition, but rather to better preserve the properties of the layer by minimizing the interfacial interactions.

(111) oriented of diamond cubic group IV semiconductors are composed of an ABC stacking of covalently bonded bilayers. These bilayers have the same structure as the β-2D bilayers, making the (111) diamond cubic surface ideal for the epitaxial growth of group VA β-2D materials. Interestingly, with a surface lattice parameter of 4.00 Å, Ge(111) is almost lattice matched to β-2D-Sb (predicted lattice constant of 4.04-4.12 Å). The focus of this section will therefore be the behavior of β-2D-Sb on Ge(111) and passivated Ge(111) surfaces. Furthermore, to better understand the group trends and compare weakly interacting substrates to TM substrates, β-2D-As

and β-2D-AsSb on Si(111) will also be considered. Monolayer β-2D-AsSb is latticed matched to Si(111), according to DFT calculations. β-2D-As has a 6.7% lattice mismatch on Si(111). A (4×4) β-2D-As supercell on $\left(\sqrt{13} \times \sqrt{13}\right)$ R13.9° Si(111) will therefore be considered to produce results comparable to those on TM substrates.

To be as realistic as possible and to explore experimentally achievable conditions, this section will study passivated substrates which can be practically produced with high quality. The Si(111) and Ge(111) surfaces have one dangling bond per unit cell. This dangling bond can be passivated in many ways. The simplest method is by surface reconstruction. The stable reconstructions in the expected growth conditions (RT - 400°C) are Si(111) (7×7) and Ge(111)-c(2×8). These reconstructions are however known to be unstable upon deposition of virtually any species. Another method to passivate the dangling bonds is by growth or transfer of a 2D material. For instance, monolayer graphene can be grown on Ge(111) as well as on Ge(100) and Ge(110)[227]. This can provide a way to integrate group VA 2D materials on any orientation of Si or Ge since Ge virtual substrates can be easily grown on Si. Nonetheless, the 2D passivating layer is expected to screen the interaction between the group VA 2D material and the substrate, leading to a loss of the epitaxial relationship. The dangling bonds can also be passivated by bonding with atoms or molecules (Figure 4.6). The most obvious way to passivate the dangling bonds is by forming one bond per unit cell with a monovalent atom. In the case of Ge(111), this can be achieved by using H or halogens. Like Si(111)-H, Ge(111)-H can be obtained by an HF dip[228, 229]. This however leads to a rough surface[230]. High-quality Ge(111)-H can nonetheless be obtained by annealing in H_2 atmosphere[230] or by reaction of clean Ge(111) surfaces with atomic H under UHV[231, 232]. The stability of the Ge(111)-H surface is relatively high, as evidenced by the slow regrowth (timescale of weeks) of native oxide in ambient conditions[228].

Unlike HF, wet HCl and HBr passivate the Ge(111) dangling bond with the halogen[233, 234]. However, the resulting Ge(111)-Cl and Ge(111)-Br less stable than Ge(111)-H, but can still prevent oxide regrowth for an hour in ambient conditions[233, 234]. The oxidation requires the presence of both O_2 and water[233] and the halogen passivated surfaces may be stable during group VA 2D materials epitaxy. The Ge(111)-I passivation can be achieved by exposition to I vapor under UHV[235]. Wong et *al*. have shown that methyl passivation (Figure 4.6b) also yields a (1×1) surface. CH_3 and H react similarly with the Ge(111) dangling bond and the C atom completes its octet by

forming a fourth bond with Ge. Ge(111)-CH_3 can be obtained by reaction of $(CH_3)_2Mg$ with Ge(111)-Br. The resulting surface is atomically flat and more stable than Ge(111)-H in ambient conditions. The methyl passivation is stable up to 400 °C in UHV.

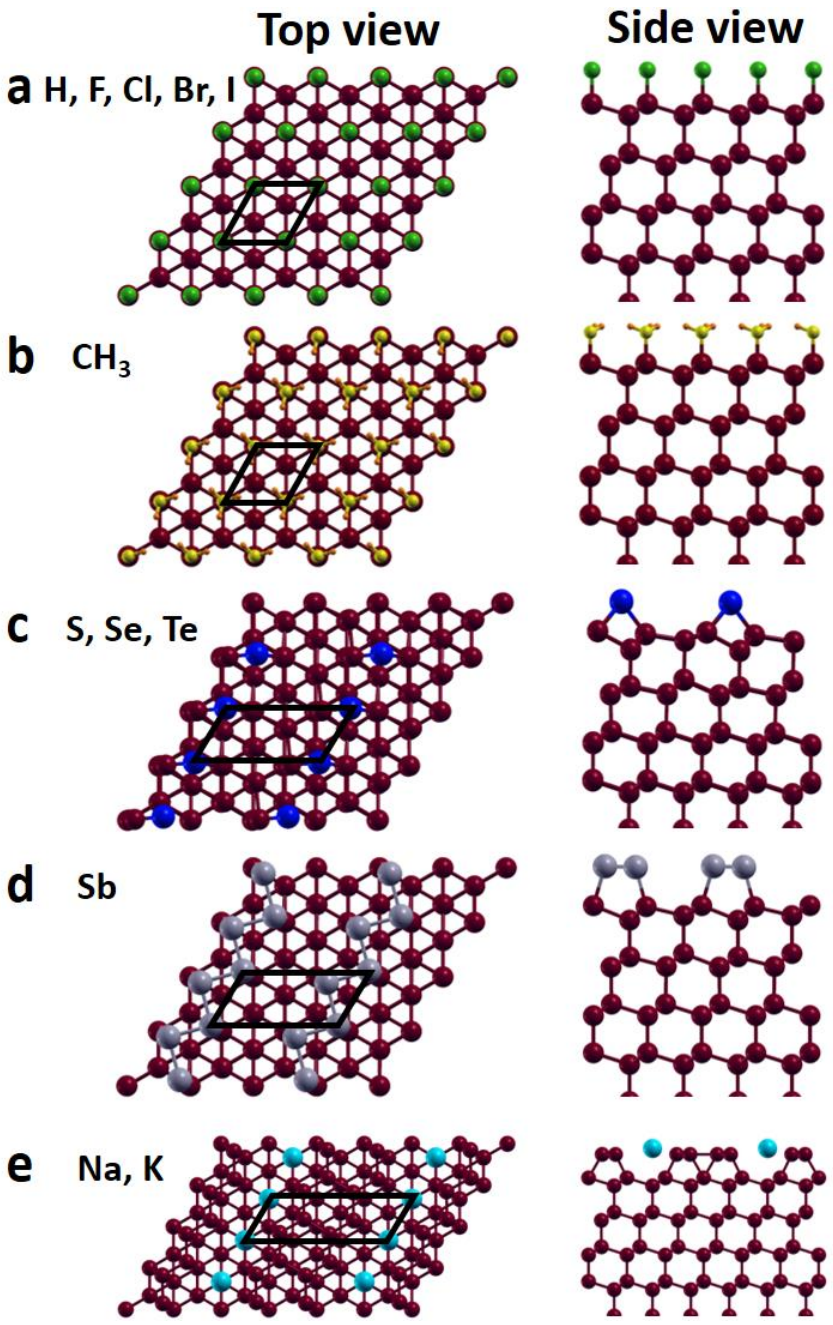

Figure 4.6 Ge(111) passivation by atoms and molecules. Adapted with permission from *Fortin-Deschênes, M; Moutanabbir, O., J. Phys. Chem. C 2018, 122, 9162-9168* [35]. Copyright (2018) American Chemical Society.

Chalcogens (O, S, Se, Te, At) have a valency of -2, meaning that they tend to form two bonds. They can therefore passivate the Ge(111) surface by bonding with two surface atoms and forming a (2×1) superstructure (Figure 4.6c). The passivation is only possible with S, Se and Te. O will react by forming an oxide layer on the surface and At passivation has not been discussed in literature. Ge(111)-S can be obtained by immersion in $(NH_4)_2S$ at 70 °C or by adsorption of H_2S followed by annealing in UHV[229, 236, 237]. The resulting surfaces are stable for months in ambient conditions. Similarly, Ge(111)-Se and Ge(111)-Te are obtained by adsorption of H_2Se or Te vapor on clean Ge at RT followed by annealing at 300-400 °C[238, 239].

Interestingly, Ge(111) can be passivated by Sb. The passivation is achieved by the deposition of Sb_4 on freshly cleaved Ge(111)-(2×1) or sputter-annealed Ge(111)-c-(2×8) at RT in UHV followed by annealing at 650 °C[218, 240, 241]. This results in the formation of Seiwatz chains, which are a (2×1) superstructure on Ge(111). The Sb atoms form zigzag chains where every atom bonds with its two Sb neighbors and forms a third bond which passivates the Ge surface dangling bond (Figure 4.6d). Since the Seiwatz chains are obtained at 650 °C, above the Sb melting point, the Sb passivated surface is highly stable and should not be disturbed by the group VA 2D material growth. It is also important to note that the growth of crystalline Sb was not observed in the Sb passivation studies[218, 240, 241].

Even though alkali metals are monovalent, they form metallic bonds in ambient conditions. It is therefore not surprising that they do not produce a (1×1) passivated Ge(111) surface. Li, Na and K adsorption on Ge(111) followed by annealing at 300 °C leads to a (3×1) superstructure described as an honeycomb chain-channel structure[242, 243] (Figure 4.6). The passivation occurs mostly by Ge-Ge surface bonds similar to a surface reconstruction. The lack of covalent bonds leads to a poor surface passivation[244]. It is still interesting to study alkali metal passivation since their electropositivity might allow for the electron doping of the epitaxial 2D layer. On the other hand, the high electronegativity of halogens might lead to hole doping.

The methodology used to study 2D pnictogens on semiconductor and passivated semiconductor surfaces is the same as that employed in the previous section for group VA 2D materials on TMs. However, the weakly interacting surfaces increases the importance of considering vdW interactions. For this reason, several methods were compared: GGA (PBE), PBE with Grimme

corrections (DFT-D2) and a vdW functional (optB86b-vdW[212, 214, 245]). We also note that the bottom substrate atoms (backside of the slab) are passivated with H for all calculations.

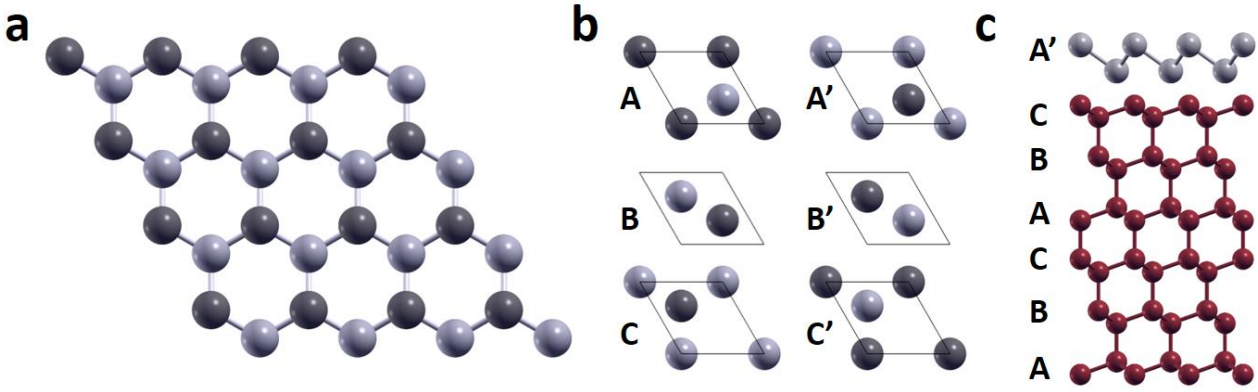

Figure 4.7 (a) Structure of monolayer β-2D materials. Darker atoms are on the bottom of the buckled bilayer and lighter atoms are on the top. (b) Unit cells for the various considered stacking. (c) Example of the ABC-A' stacking of β-2D-Sb on Ge(111). Adapted with permission from *Fortin-Deschênes et al., Nano Letters 2017, 17, 4970-4975.* [36]. Copyright (2017) American Chemical Society.

As for TM substrates, there are several ways to stack group VA 2D materials on diamond cubic (111) surfaces (Figure 4.7). The ABC stacking of the (111) substrate is used as a reference to identify the stacking of the epitaxial layer and ABC-X and ABC-X' configurations are considered (X being A, B or C). The X' indicates that the vertical position of the top and bottom atoms are interchanged. For example, in the ABC-A' stacking (Figure 4.7c), the atoms of the layer have the same (x,y) coordinates as A layer of Ge, but with inverted z coordinates. The six stackings are analysed for β-2D-Sb on Ge(111) and Ge(111)-H. For the other systems, ABC-A and ABC-B' are taken as representative stackings for 'aligned' configurations, where the bottom group VA atom is aligned with the top substrate atom and 'misaligned', where it is not.

The E_{ads} as a function of the substrate-layer distance as well as the charge densities minus superposition of atomic charge densities for β-2D-Sb on Ge(111) and Ge(111)-H can be seen in Figure 4.8. The relaxed structural parameters are presented in Table 4.4. First, we notice that the adsorption energies on semiconductor surfaces are much smaller than on TM substrates (268-431 meV/atom with optB86b-vdW and 306-484 meV/atom with DFT-D2. DFT-D2 and optB86b-vdW give qualitatively and quantitatively similar results, but DFT-D2 systematically yields E_{ads} ~30-50

meV/atom larger. On the other hand, PBE significantly underestimates the interaction (E_{ads} between 116-259 meV/atom). For conciseness, only optB86b-vdW values will be mentioned unless specified otherwise. The most stable stacking is ABC-B. This is not surprising considering that the natural stacking of A7 Sb is ACB.

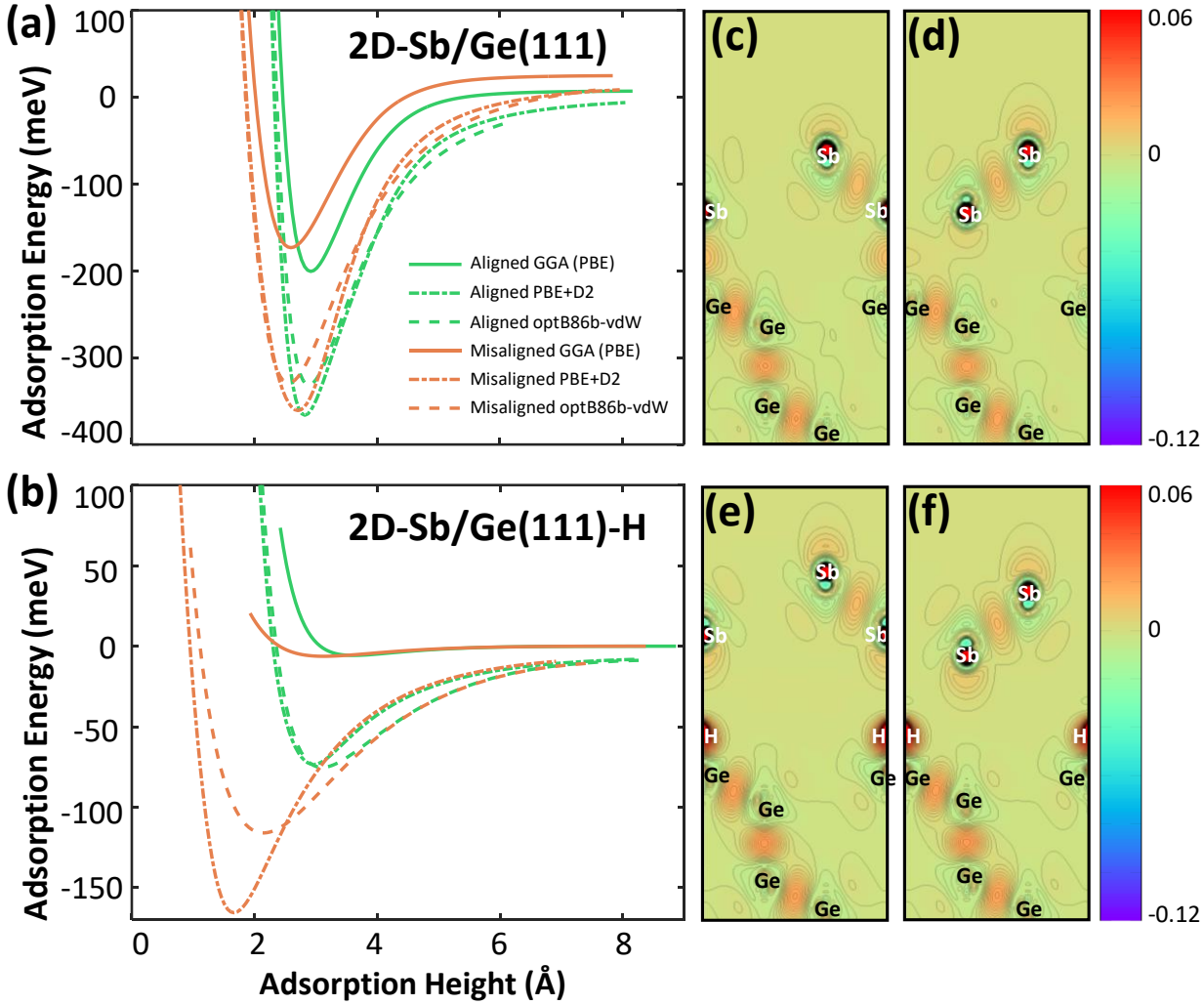

Figure 4.8 (a, b) Adsorption energy as a function of adsorption height for epitaxial 2D-Sb on (a) Ge(111) and (b) Ge(111)-H. (c-f) Charge density minus superposition of isolated atom charge density on the Ge(112) plane for (c) 2D-Sb/Ge(111) aligned, (d) 2D-Sb/Ge(111) misaligned, (e) 2D-Sb/Ge(111)-H aligned and (f) 2D-Sb/Ge(111)-H misaligned. Color scale is in $e^{-}\times a_0^{-3}$. Reprinted with permission from *Fortin-Deschênes, M; Moutanabbir, O., J. Phys. Chem. C 2018, 122, 9162-9168* [35]. Copyright (2018) American Chemical Society.

The structural parameters vary weakly upon adsorption, indicating that the nature of the epitaxial layer is preserved. A small but systematic increase in d_{Sb-Sb} of 0.02 Å is observed upon adsorption. The same effect can be seen on the bond angle. However, since the lattice parameter is fixed, the two parameters represent only one degree of freedom. The increase in bond length is consistent with weak bonding with Ge. In fact, the additional Sb-Ge bonds slightly weaken the Sb-Sb bonds. The calculated d_{Sb-Ge} also indicate weak Sb-Ge bonding. As a reference, the Ge-Ge bond length is 2.46 Å and the interlayer Sb-Sb distance in bulk A7 Sb is 3.30 Å. The d_{Sb-Ge} is ~2.91 Å for the aligned stackings and varies from 3.28 Å to 3.65 Å as E_{ads} decreases for the misaligned stackings.

Table 4.4 Adsorption energies and structural parameters of freestanding and epitaxial β-2D-Sb on Ge and H passivated Ge substrates. Adapted with permission from *Fortin-Deschênes, M; Moutanabbir, O., J. Phys. Chem. C 2018, 122, 9162-9168* [35]. Copyright (2018) American Chemical Society.

		E_{ads} (meV/atom)	d_{Sb-Sb} (Å)	d_{Sb-Ge} / d_{Sb-H} (Å)	θ (°)
Freestanding β-2D-Sb		-------	2.884	-------	90.3
Aligned	Sb/Ge ABC-A	331	2.907	2.895	89.4
	Sb/Ge ABC-C’	328	2.904	2.901	89.5
Misaligned	Sb/Ge ABC-A’	325	2.908	3.492	89.4
	Sb/Ge ABC-B	431	2.904	3.278	89.5
	Sb/Ge ABC-B’	329	2.901	3.484	89.7
	Sb/Ge ABC-C	268	2.905	3.647	89.5
Aligned	Sb/Ge-H ABC-A	75	2.885	3.111	90.3
	Sb/Ge-H ABC-C’	75	2.885	3.111	90.3
Misaligned	Sb/Ge-H ABC-A’	123	2.884	3.140	90.3
	Sb/Ge-H ABC-B	115	2.882	3.176	90.4
	Sb/Ge-H ABC-B’	116	2.883	3.198	90.4
	Sb/Ge-H ABC-C	121	2.885	3.195	90.3

The charge densities indicate that significant interaction still occurs (Figure 4.8 (c, d)). In fact, clear Sb-Ge bonds are present, especially in the aligned configurations. The magnitude of the charge reorganization in the Sb-Ge and Sb-Sb bonds are comparable in the aligned stackings, but a weaker Sb-Ge bond is seen in the misaligned stacking. We note however that there are three equivalent bonds in the misaligned stackings and only one in the aligned stackings. We can also see an overall decrease in the Sb charge density, even in the top Sb doublet since that the displaced charge contributes to Sb-Ge bonding. This charge reorganization is even more obvious in the bottom doublet of the misaligned stacking (~50% decrease).

H passivation significantly reduces the substrate-layer interactions. After passivation, E_{ads} drops down to 75-123 meV/atom. Moreover, PBE yields extremely weak bonding (Figure 4.8b) in the order of 6-8 meV/atom. This indicates that the substrate-layer interaction is almost purely vdW. The structural parameters of epitaxial β-2D-Sb on Ge(111)-H are almost identical to the freestanding ones (± 0.002 Å for d_{Sb-Sb} and ± 0.1° for θ). There is a reduction of the adsorption height for the misaligned stackings and a slight increase for the aligned stackings, as compared to Sb/Ge(111). Overall, d_{Sb-H} is almost independent of the stacking and close to the expected sum of the vdW radii of H and Sb. The larger E_{ads} in misaligned stackings can be attributed to the larger coordination (vdW) of the H atom. Similarly, the charge densities (Figure 4.8 (e, f)) confirm the efficient surface passivation. A strong Ge-H bond is formed, and no Sb-Ge nor Sb-H bonds are observed. Moreover, the charge densities of the top and bottom Sb atoms are more symmetric than on the Ge substrate, indicating a quasi-freestanding behavior.

The PDOS of freestanding β-2D-Sb, β-2D-Sb on Ge(111) and β-2D-Sb on Ge(111)-H are shown in Figure 4.9. The PDOS of freestanding β-2D-Sb (Figure 4.9a) is very similar to β-2D-P, but with a ~1.05 eV band gap. The PDOS of epitaxial β-2D-Sb on Ge(111) preserves most features of freestanding β-2D-Sb (black curve in Figure 4.9b (ABC-B')). However, the PDOS in the band gap is not zero anymore and the Fermi level shifts below the band gap. The PDOS of the top Ge atom can also be seen in Figure 4.9b. Even though Ge is semiconducting, there is a large peak in the Ge $4p_z$ PDOS. This peak is associated with the Ge(111) surface dangling bond and makes the Ge surface metallic. We notice some hybridization of the Sb states with the Ge(111) surface band (Figure 4.9 (c,d)). This hybridization transforms semiconducting β-2D-Sb into a metal. For the aligned stackings, the hybridization is mostly with the Sb $5p_z$ states, whereas the Sb 5s and Sb $5p_{(x,y)}$ of the misalign stackings are more involved in the substrate-layer bond, as expected from the relative positions of the Sb and Ge atoms.

The PDOS of β-2D-Sb on Ge(111)-H is shown in Figure 4.9 (g-j). H efficiently passivates the Ge dangling bond. In fact, Ge recovers its semiconducting nature due to the saturation of the dangling bond. A narrow peak at -4.1 eV in the PDOS of H 1s and Ge $4p_z$ (not shown) confirms the passivation and indicate that the saturated dangling bonds interact weakly with each other. The PDOS of β-2D-Sb on Ge(111)-H is quasi-identical to the PDOS of freestanding β-2D-Sb and the semiconducting behavior is conserved upon adsorption. The stacking has little influence on the

PDOS. As expected, the PDOS of the more strongly interacting misaligned stackings is slightly more affected by the interaction with the substrate. Moreover, the PDOS of the top and bottom atoms do not have important differences.

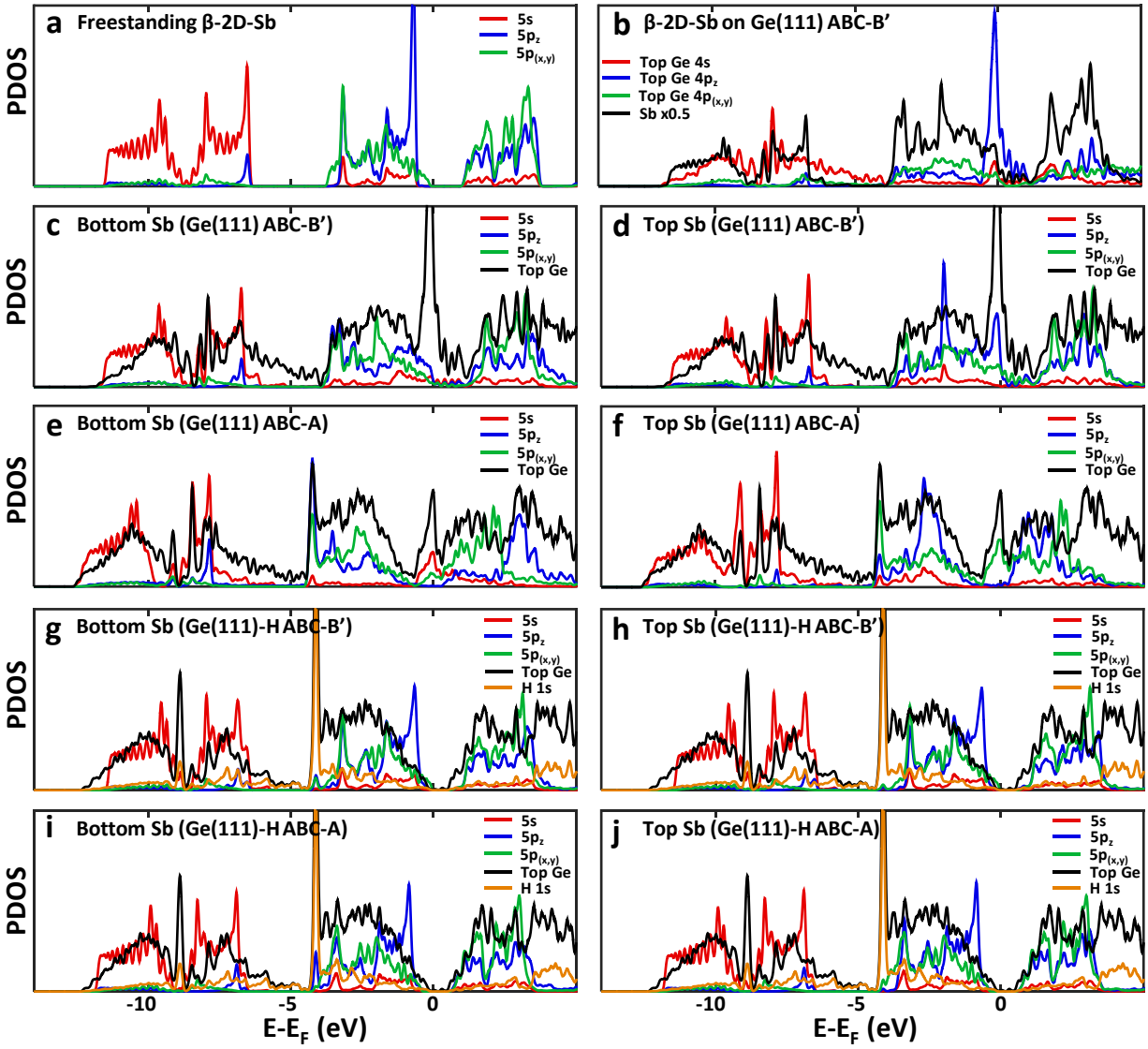

Figure 4.9 PDOS of freestanding and epitaxial β-2D-Sb on Ge(111). (a) Freestanding β-2D-Sb. (b) Epitaxial (ABC-B') β-2D-Sb on Ge(111) showing PDOS of β-2D-Sb and the top Ge atom. (c, d) Top and bottom Sb atoms on Ge(111) misaligned (ABC-B'). (e, f) Top and bottom Sb atoms on Ge(111) aligned (ABC-A). (g, h) Top and bottom Sb atoms on Ge(111)-H misaligned (ABC-B'). (i, j) Top and bottom Sb atoms on Ge(111)-H aligned (ABC-A). Adapted with permission from

Fortin-Deschênes, M; Moutanabbir, O., J. Phys. Chem. C 2018, 122, 9162-9168 [35]. Copyright (2018) American Chemical Society.

The effectiveness of the passivation can also be observed in the band structure (Figure 4.10). The hybridization with the Ge surface dangling bonds responsible for the loss of the semiconducting behavior of epitaxial β-2D-Sb on Ge(111) can be visualized in the Sb 5s and 5p weighted band structure (Figure 4.10 (b, c)). The Ge surface band crossing the Fermi level is indicated by the blue arrows and presents significant hybridization with Sb, especially in aligned stackings. However, passivation of the dangling bond moves the band down by ~5 eV and the surface is no longer metallic (Figure 4.10 (d, e)). Moreover, the lack of Sb-Ge and Sb-H interaction allows the recovery of the freestanding behavior, as expected from the PDOS.

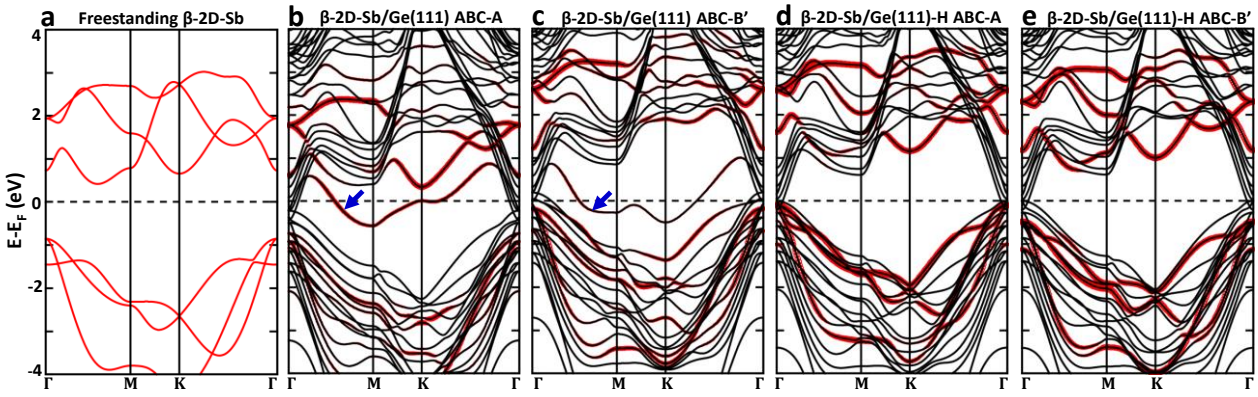

Figure 4.10 (a) Band structure of freestanding β-2D-Sb. (b-e) Weighted band structure of epitaxial β-2D-Sb on (b) Ge(111) ABC-A, (c) Ge(111) ABC-B', (d) Ge(111)-H ABC-A and (e) Ge(111)-H ABC-B'. The width of the red bands is proportional to the sum of the projected contributions ($|c_n|^2$) of Sb 5s and 5p. The blue arrow indicates the Ge surface dangling bond responsible for the metallic nature of epitaxial β-2D-Sb. Adapted with permission from *Fortin-Deschênes, M; Moutanabbir, O., J. Phys. Chem. C 2018, 122, 9162-9168* [35]. Copyright (2018) American Chemical Society.

The results presented above indicate that semiconductor surfaces are relatively weakly interacting with epitaxial group VA 2D materials and may be adequate as growth substrates. Nonetheless, stacking-dependent substrate-layer interaction may lead to a loss of the semiconducting behavior in single layers and should be carefully assessed in experiments. On the other hand, substrate passivation is a promising avenue to obtain quasi-freestanding group VA 2D materials on semiconductor substrates. Next, we examine the efficiency of various passivation methods and

assess their potential to tune the electronic properties of epitaxial 2D pnictogens. The properties of the 2D layers are summarized in Table 4.5 and the PDOS are presented in Figure 4.11. The calculated E_{ads} (Table 4.5) confirm the efficiency of the various passivation methods at reducing the substrate-layer interactions. Like H, most passivation methods reduce E_{ads} by more than 50% and the most efficient passivation is achieved with CH_3 (from 363-368 down to 68-106 meV/atom). Moreover, the structural parameters remain relatively unperturbed in most cases.

Table 4.5 Properties of epitaxial β-2D-Sb, β-2D-AsSb and β-2D-As on bare and passivated Ge(111) and Si(111) calculated using DFT-D2. For E_{ads} and the adsorption height, the values in parentheses are for the ABC-B' stacking and the values without parentheses for the ABC-A. Δq is the average charge transfer to Sb calculated using Löwdin charges differences as compared to isolated layers and substrates (negative values indicate that electrons are transferred to the substrate). Adapted with permission from *Fortin-Deschênes, M; Moutanabbir, O., J. Phys. Chem. C 2018, 122, 9162-9168* [35]. Copyright (2018) American Chemical Society.

	E_{ads} (meV/ atom)	Adsorption height (Å)	Δq (e^- /unit cell)	Type
β-2D-Sb/Ge(111)	363 (368)	2.71 (2.83)	-0.083	Metal
β-2D-Sb/Ge(111)-F	175 (103)	2.21 (3.29)	-0.081	Degenerate SC (p)
β-2D-Sb/Ge(111)-Cl	114 (78)	2.94 (3.66)	-0.041	Degenerate SC (p)
β-2D-Sb/Ge(111)-Br	135 (92)	3.00 (3.68)	-0.035	Degenerate SC (p)
β-2D-Sb/Ge(111)-I	166 (112)	3.12 (3.75)	-0.015	Semimetal
β-2D-Sb/Ge(111)-S	166 (194)	1.98 (1.83)	-0.052	Semimetal
β-2D-Sb/Ge(111)-Se	158 (176)	2.21 (1.99)	-0.035	Semimetal
β-2D-Sb/Ge(111)-Te	152 (155)	2.46 (2.45)	-0.001	Semimetal
β-2D-Sb/Ge(111)-Na	237 (216)	2.42 (2.67)	-0.13	Semimetal/Degenerate SC (p)
β-2D-Sb/Ge(111)-K	238 (254)	2.55 (2.44)	-0.003	Degenerate SC (p)
β-2D-Sb/Ge(111)-H	178 (76)	1.66 (2.97)	-0.007	SC
β-2D-Sb/Ge(111)-CH_3	106 (68)	2.65 (3.35)	-0.002	SC
β-2D-Sb/Ge(111)-Sb	176 (99)	3.03 (3.84)	0	SC/ Degenerate SC (p)
β-2D-AsSb/Si(111)	321 (520)	2.47 (2.77)	-0.056	Metal
β-2D-AsSb/Si(111)-H	95 (54)	1.86 (3.09)	-0.006	SC
β-2D-As/Si(111)	321	2.21	-0.039	Metal
β-2D-As/Si(111)-H	55	2.37	-0.002	SC

With halogen passivation, d_{Sb-Sb} increases up to 2.901 Å (F passivation) and the freestanding structure is gradually restored as the atomic number of the halogen increases. Considering the large distances between Sb and the halogens (3.29-3.92 Å) as well as the quasi-freestanding PDOS (Figure 4.11a), the increase in bond length can be attributed to the increased core repulsion

associated to the charge transfer. In fact, Löwdin charges analysis indicate a transfer of ~0.08 e^- /unit cell from Sb to Ge(111)-F. The charge transfer becomes less important as the electronegativity of the halogen decreases. Due to the charge transfer, the Fermi level moves in the valence band of β-2D-Sb. Considering the position of the Fermi level and the quasi-freestanding nature of the PDOS, epitaxial β-2D-Sb on halogen passivated Ge can be considered as degenerate semiconductors. However, the Ge(111)-I surface interacts more strongly with β-2D-Sb and hybridization with I occurs. This leads to a non-zero PDOS in the band gap and β-2D-Sb on Ge(111)-I can be qualified as a semimetal.

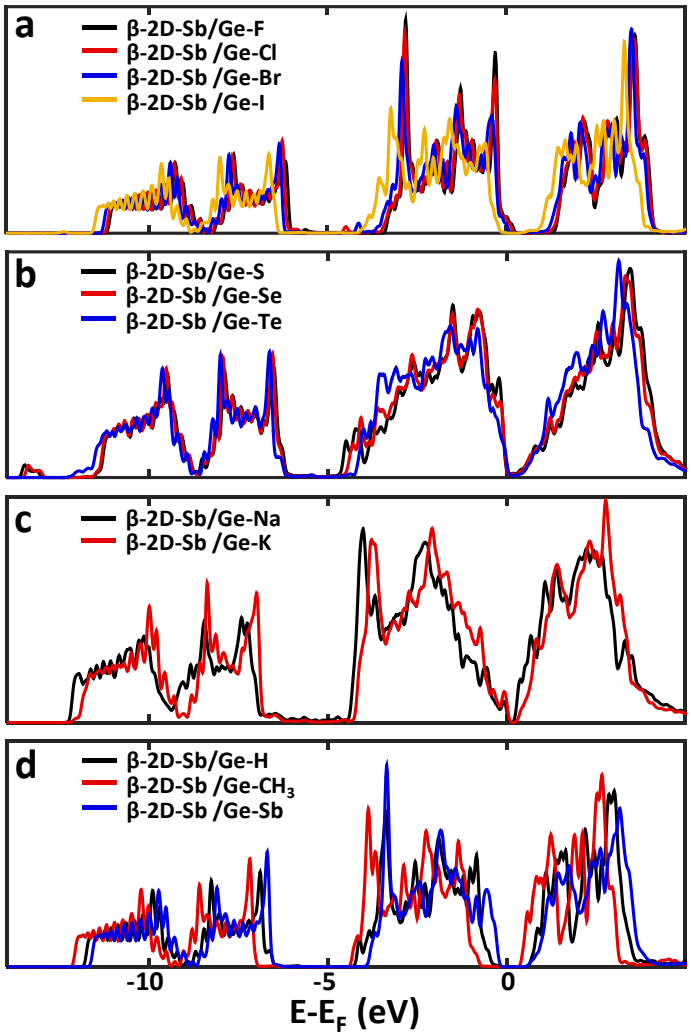

Figure 4.11 PDOS (sum of Sb5s and Sb 5p) of epitaxial (ABC-A) β-2D-Sb on Ge(111) passivated by various methods. Adapted with permission from *Fortin-Deschênes, M; Moutanabbir, O., J. Phys. Chem. C 2018, 122, 9162-9168* [35]. Copyright (2018) American Chemical Society.

Chalcogen passivation is less effective than halogen passivation. In fact, E_{ads} (152-194 meV/atom) is slightly larger than for halogens (78-175 meV/atom). Moreover, the PDOS shows more signs of hybridization between Sb and the chalcogens. For instance, the peaks at ~ -13 eV are due to hybridization with the 3s, 4s and 5s orbitals of S, Se and Te. Nonetheless, the $d_{Sb\text{-}Chalcogen}$ are significantly larger than the sum of the covalent radii. The (2×1) superstructure leads to an uneven epitaxial layer. For instance, the two top Sb atoms have a height difference of 0.185 Å for β-2D-Sb on Ge(111)-S. Moreover, $d_{Sb\text{-}Sb}$ varies by 0.031 Å within the supercell. Still, these distortions of the β-2D-Sb lattice have a smaller impact on the electronic structure than the electronic interactions, as evidenced by the PDOS of the isolated distorted structures (not shown). The interaction with the chalcogen passivated substrates leads to relatively important modifications of the electronic structure, almost independently of the chalcogen (Figure 4.11). The resulting layers are semimetallic. The charge transfer between Sb and the substrate is consistent with the electronegativity of chalcogens (2.58 for S, 2.55 for Se, 2.1 for Te and 2.05 for Sb).

As expected, alkali metals yield the poorest passivation, with E_{ads} between 216-254 meV/atom. The PDOS is also strongly affected by the interaction (Figure 4.11c). However, the band gap remains present, but shrinks to ~0.2 eV. The Fermi level is below the band gap, making β-2D-Sb a degenerate semiconductor. Surprisingly, alkali metal passivation does not lead to electron doping of the layer. This might be caused by additional states forming within the gap due to bonding with the substrate, rather than by hole doping. The interaction with the (3×1) superstructure also leads to structural modifications. For instance, on Ge-K, the height of the top and bottom Sb atoms vary by 0.48 Å and 0.45 Å, respectively.

Like H, CH_3 gives very good substrate passivation. With weak charge transfers to the substrate, β-2D-Sb remains semiconducting on both surfaces and its PDOS is unperturbed by the interaction. Sb also passivates the Ge substrate relatively well. In the aligned ABC-A stacking, E_{ads}=99 meV/atom and β-2D-Sb is semiconducting with a 0.7 eV band gap. In the misaligned ABC-B' stacking, the interaction is stronger (E_{ads}=176 meV/atom) and β-2D-Sb becomes a hole doped degenerate semiconductor with a band gap of ~0.5 eV. Other than this, it appears as the PDOS of β-2D-Sb on Ge-Sb is relatively similar to the freestanding one.

Interestingly, the behavior of β-2D-As and β-2D-AsSb on Si(111) and Si(111)-H are very similar to the behavior of β-2D-Sb on Ge/Ge-H. β-2D-AsSb interacts slightly more with Si(111) (up to

520 meV/atom) than β-2D-Sb with Ge(111). The E_{ads} for β-2D-As on Si(111) is however smaller (321 meV/atom). This may be due to the lattice mismatch. In fact, the rotated supercells do not allow for perfect alignment of the two lattices, which reduces the interaction. With H passivation, E_{ads} drops down to 55-95 meV/atom and β-2D-As/β-2D-AsSb transition from metals to semiconductors.

4.3 Conclusion

This chapter presented an *ab initio* study of the behavior of epitaxial group VA 2D materials on various substrates. The stability, the adsorption energetics and the effect of substrate-layer interactions on the properties of the epitaxial layers have been examined for TM, semiconductor and passivated semiconductor surfaces. It was found that TM substrates interact strongly with group VA 2D materials (~700-817 meV/atom in the most stable configurations). α-2D-P was determined to be structurally unstable on Nb(110) and to decompose into parallel chains strongly bonded to the substrate. On the other hand, the β-2D phase is structurally stable on hcp (0001) TM surfaces, as well as semiconductors and passivated semiconductors. Nonetheless, the substrate-layer interaction with TM substrates has important effects on the electronic structure of the epitaxial layers. TM surfaces can be useful substrates to demonstrate the growth of novel group VA 2D materials, but their interaction with the layers should be studied thoroughly.

Semiconductors were found to interact more weakly than TM substrates with the epitaxial layers (321-520 meV/atom). Nonetheless, the hybridization between the group VA orbitals and the substrate surface dangling bonds was found turn the semiconducting monolayers into metals. This effect is especially important when the bottom group VA atom lays directly on top of the dangling bond. This behavior is common to all the studied group VA 2D materials (β-2D-As and β-2D-AsSb on Si(111) as well as β-2D-Sb on Ge(111)). Semiconductors may be useful substrates to allow the future integration of group VA 2D materials in emerging technologies. However, their interaction with the layers should be taken into account, especially for epitaxial monolayer group VA 2D materials. The substrate-layer interactions might be less important for multilayer group VA 2D materials and should be studied theoretically and experimentally.

Semiconductor substrate passivation was found to be an effective method to recover the freestanding properties of epitaxial group VA 2D materials. H, CH_3 and Sb allow the recovery of

the semiconducting nature of β-2D-Sb on Ge(111). On the other hand, halogens provide an efficient passivation and allow for doping of the epitaxial layers, without compromising their electronic structure. Other methods (alkali metals and chalcogens) provide relatively weak passivation. The results seem to apply to 2D pnictogens. In particular, substrate passivation was found to be effective for β-2D-As and β-2D-AsSb on Si(111).

Overall, the results presented in this chapter are useful to establish general guidelines for the epitaxial growth of group VA 2D materials, as well as to better interpret the experimental data.

CHAPTER 5 GROWTH OF GROUP VA 2D MATERIALS

Based on the DFT analysis presented in the previous chapter, we have identified few relevant substrates for the growth of group VA 2D materials. This chapter mainly discusses the MBE growth of single and multilayer β-2D-Sb. First, the synthesis of β-2D-Sb on Ge substrates is demonstrated. Given the novelty of this emerging material, exhaustive characterization has been carried out to properly identify the phase and basic properties of the grown layers. Then, nucleation and growth dynamics are studied in detail using *in situ* LEEM and STM. These results have been published in the following paper:

Fortin-Deschênes, M. et *al*. "Synthesis of Antimonene on Germanium." *Nano Letters* 2017, 17 (8): 4970-4975.

Next, the growth on weakly interacting (vdW) substrates is studied in detail. The growth is demonstrated on two of the substrates studied in Chapter 4 (Ge(111)-Cl and Ge(111) (2×1)-Sb), as well as on epitaxial graphene on Ge. Extensive real-time LEEM analysis of the growth of multilayer β-2D-Sb on graphene/Ge allows to determine the underlying nucleation and vdW growth mechanisms. These results were published in the following paper:

Fortin-Deschênes, M. et *al*. "Dynamics of antimonene-graphene van der Waals growth." *Advanced Materials* 2019, 31 (21): 1900569.

Building on these results, the incorporation of As in β-2D-Sb by co-deposition of As_4 and Sb_4 using MBE is demonstrated. These results pave the way for the eventual fine-tuning of the electronic and optical properties of vdW grown group VA 2D materials based on composition engineering. These results were published in:

Fortin-Deschênes, M. et *al*. "2D Antimony-Arsenic Alloys." *Small* 2020, 16 (3): 1906540.

Finally, α-2D-P growth experiments are briefly discussed. Two growth methods were attempted. First, MBE deposition of P_4 species on Nb(110) surfaces is studied. Then, the sublimation of III-V semiconductor surfaces (InP) covered by graphene is examined. The sublimated phosphorus gas is trapped using at the InP/graphene interface in an attempt to reach high pressures in a confined 2D space.

5.1 Growth of β-2D-Sb

5.1.1 β-2D-Sb on Ge

5.1.1.1 Substrate preparation

The growth substrate were prepared by cleaving ~7×7 mm^2 square pieces from 0.5 mm thick Ge(111) wafers. The substrates were then cleaned by ultrasonication in acetone (5 min), rinsed with isopropanol and dried with a N_2 flow. The substrates were then immediately introduced in the LEEM system under UHV. At this point, the surface is covered by a native Ge oxide as indicated by the absence of Ge LEED pattern (Figure 5.1). In fact, only a faint (0, 0) spot is visible. Annealing above 600 °C leads to the desorption of the oxide layer. However, some contamination remains on Ge and the surface is not atomically smooth. Annealing at higher T (>800 °C) leads to some surface reordering. In fact, annealed substrates have a faint c(2×8) LEED pattern (Figure 5.1b). A bright-field LEEM micrograph of the annealed Ge(111) surface is shown in Figure 5.2a. Atomic steps are not visible and some substrate roughness and step bunches are observed. The surface is not ordered on a large scale due to the remaining surface carbon contamination. The contamination was then removed by Ar^+ sputtering. During sputtering, the surface roughens (not shown). The substrates were then annealed for at least one hour at ~650 °C, leading to the re-emergence of the blurred c(2×8) pattern. To achieve larger scale ordering, the substrates were flash annealed at ~850 °C (5-20 seconds) and stabilized at 600 °C for several minutes. This process was repeated until atomic terraces were seen in LEEM (Figure 5.2b). The thin dark lines in Figure 5.2b are atomic steps and the thicker lines are step bunches. After the flash annealing cycles, the c(2×8) LEED pattern becomes slightly sharper (Figure 5.1c). The sample T was then brought down below 300 °C, and the c(2×8) LEED becomes sharp (Figure 5.1d). Typically, two cycles of sputtering/annealing are required to obtain a sharp c(2×8) LEED pattern and atomic terraces. However, this process often leads to the apparition of surface defects such as the small Ge mounts indicated by white arrows in Figure 5.2b. Deposition of Sb_4 was therefore carried out on sputtered-annealed samples such as the one in Figure 5.2b as well as on simply annealed samples such as the one in Figure 5.2a.

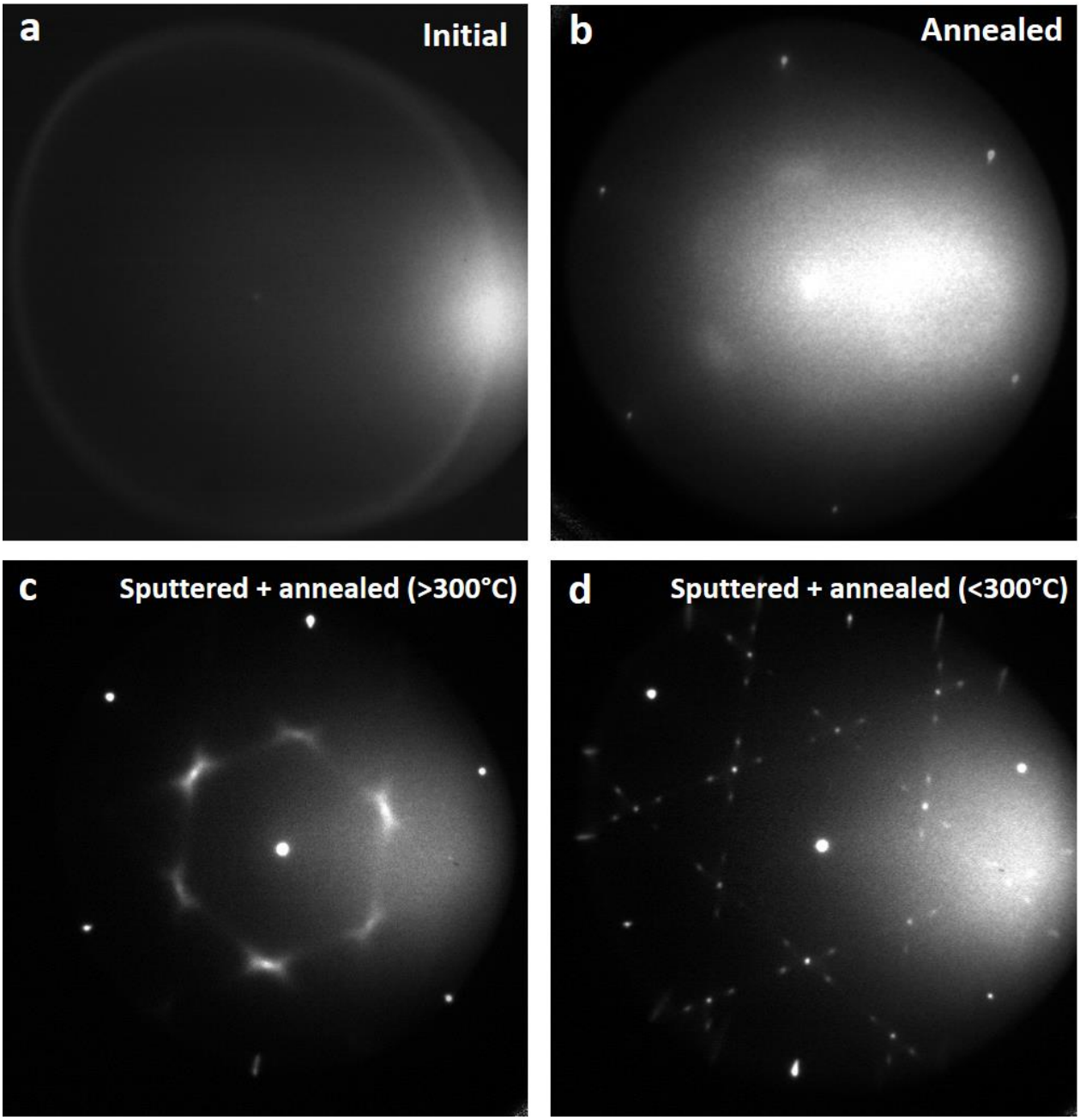

Figure 5.1 LEED patterns at different stages of the Ge(111) surface conditioning process. a) Initial surface before annealing (32 eV). b) Annealed for ~1 hour at 650 °C followed by flash annealing at ~850 °C (16 eV). c) Sputtered-annealed (two cycles). Recorded above 300 °C (16 eV). d) Sputtered-annealed (two cycles). Recorded below 300 °C (16 eV).

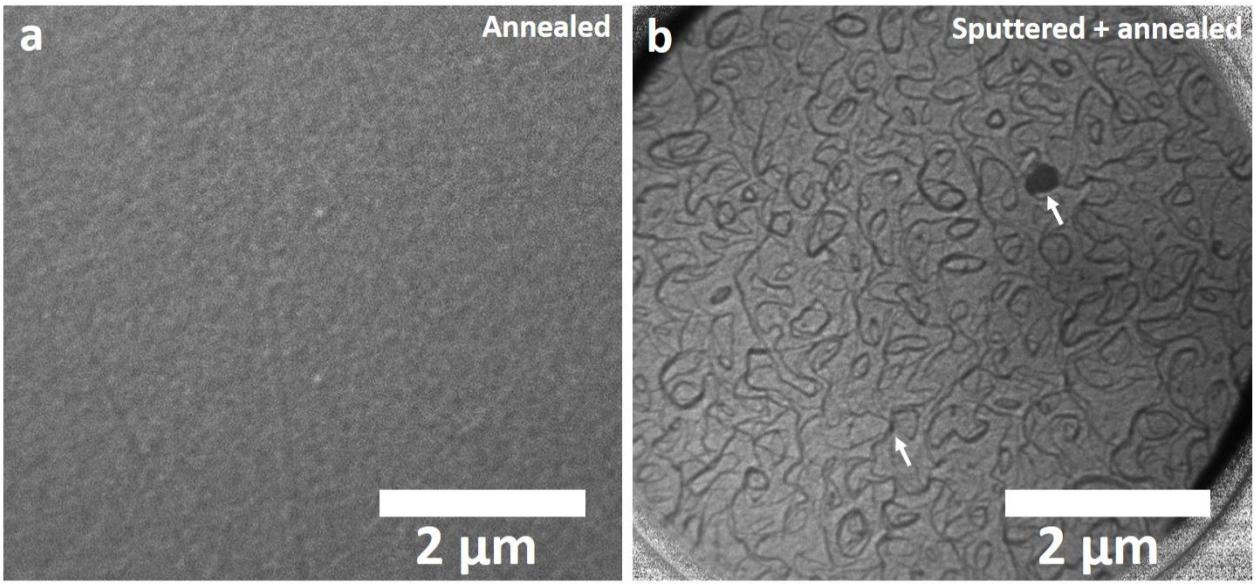

Figure 5.2 Bright-field LEEM images of Ge(111). (a) The substrate was annealed at 600 °C for one hour and repeatedly flash annealed at ~850 °C. (b) The substrate was annealed at 600 °C, then went through two cycles of sputtering and annealing. The final annealing was done overnight and followed by repeated flash annealing at 850 °C.

5.1.1.2 Sb deposition on Ge(111)

Sb_4 species were deposited on annealed Ge(111) under various experimental conditions (sample T and deposition rate (*F*)) using a Knudsen cell loaded with 99.9999% pure Sb crystals. The deposition rate was first calibrated on Ge(111) at RT using a Knudsen cell temperature of 420 °C. The thickness of the grown film was measured with AFM and divided by the growth time to give F_0. The T dependence is accounted for using $F(T) = C_0 P_{Sb}(T) T^{-\frac{1}{2}}$, where $C_0 = \sqrt{693} F_0 / P_{Sb}(693)$ is a constant and $P_{Sb} = \exp(-2.431 \times 10^4 T^{-1} + 30.48)$ is the vapor pressure of Sb. This estimated *F* provides an order of magnitude and is not should not be used for quantitative analysis. The substrate T was monitored using a pyrometer.

in situ post-growth LEEM and LEED of Sb deposited on Ge(111) under various conditions are shown in Figure 5.3. The growth T increases when going down in the figure and F increases when going from left to right. We note that the growth rate also increases when going down in the figure since the sticking coefficient decreases with increasing T (due to enhanced thermal desorption of

deposited species). The decrease becomes significant above 200 °C and growth above 325 °C was not possible in the LEEM system.

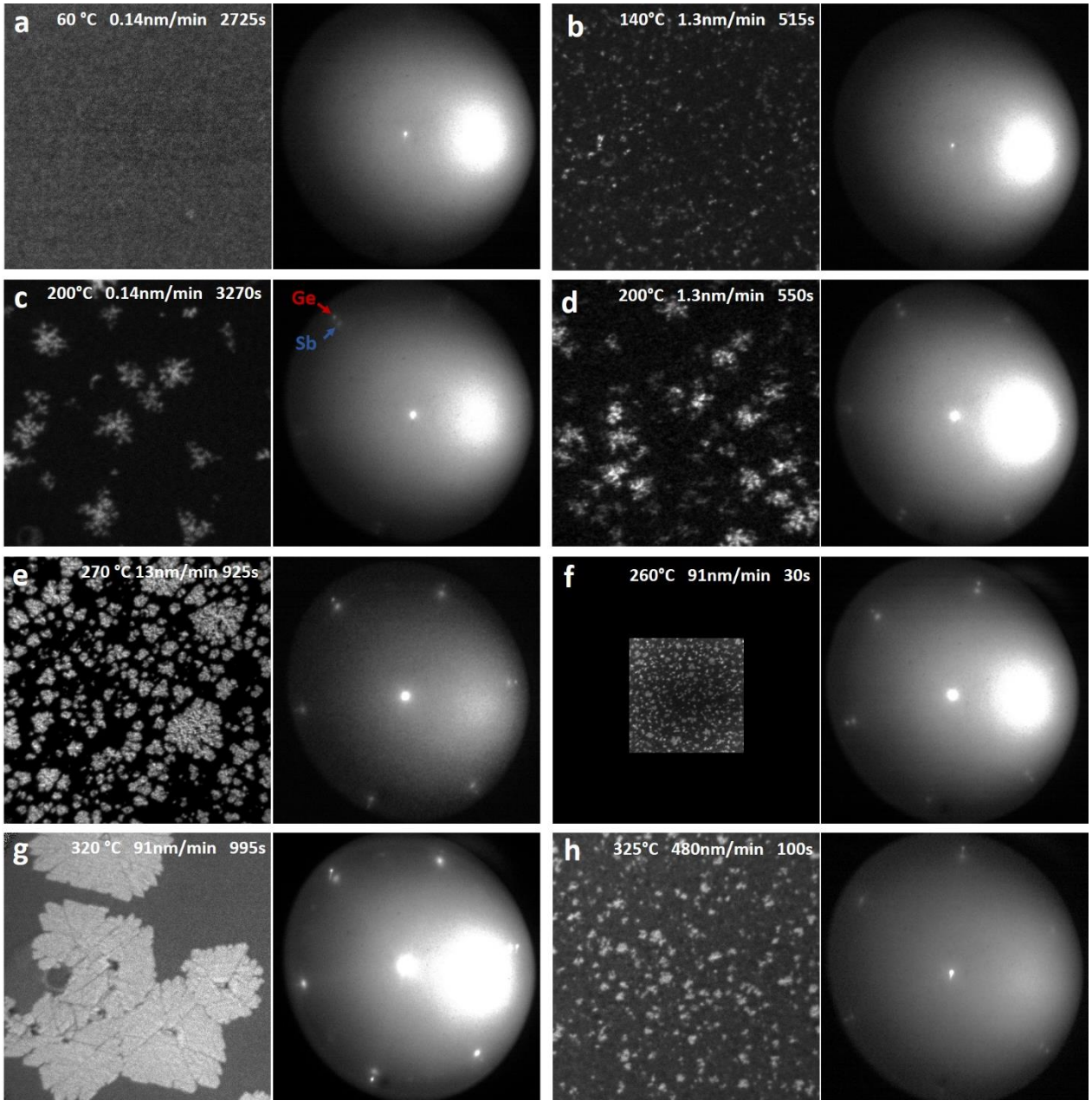

Figure 5.3 Bright-field LEEM and LEED of Sb deposited on Ge(111). The scale of all LEEM images is the same and the images are 7×7 μm^2, with the exception of (d), which is 3×3 μm^2. The deposition rates are calibrated at RT. The effective growth rate is lower than the deposition rate, especially at higher temperatures. Adapted with permission from *Fortin-Deschênes et al., Nano Letters 2017, 17, 4970-4975.* [36] Copyright (2017) American Chemical Society.

At low growth T, Sb_4 deposition leads to a homogeneous decrease of the LEEM intensity and to a disappearance of the Ge LEED spots (Figure 5.3). This suggests that an amorphous film covers the substrate. The homogeneity of the film is due to the limited mobility of deposited Sb_4 species (hit and stick). While the amorphous nature of the film cannot be directly confirmed, it is likely that the thermal energy is insufficient for the dissociation of the Sb_4 molecules. Nonetheless, we cannot exclude the possibility that the film is unoriented and polycrystalline with nanoscale grains. At T = 140 °C, crystalline features begin to form. In fact, bright spots are visible in bright field LEEM, which means that the observed features are crystalline, with surfaces parallel to the substrate. The lateral size of the grains is however very limited (in the order of 100-200 nm). Moreover, no Sb LEED pattern is observed and the Ge(111) LEED disappears during growth. This indicates that even though the thermal energy is sufficient for Sb_4 dissociation, the surface diffusion is still too slow to allow for the formation of well-defined flakes. There is still formation of an amorphous-like film on the substrate at this T, as evidenced by the disappearance of the Ge LEED spots.

At T= 200 °C, the growth of well-defined dendritic flakes is observed in LEEM (Figure 5.3 (c, d)). A Sb LEED pattern is also observed. Two rotationally aligned sets of spots with 6-fold symmetry are observed (Figure 5.3 (c, d)). The outside spots (red arrow in Figure 5.3c) are the Ge(111) LEED and the inside spots (blue arrow) come from Sb. Since the Sb and Ge spots are very close, the Sb lattice parameter a_{Sb} can be precisely measured using the ratio of the reciprocal lattice vectors of Ge and Sb: $a_{Sb} = a_{Ge} \times (a^*_{Ge}/a^*_{Sb})$, where a_{Ge}=4.00 is the surface lattice constant of Ge(111) and a^*_{Ge} and a^*_{Sb} are the LEED measured Ge and Sb reciprocal lattice parameters. We find $a_{Sb} = 4.28 \pm 0.02$ Å. Considering the LEED symmetry and the lattice parameter, the grown flakes are multilayer β-2D-Sb. In fact, bulk Sb has a lattice constant is 4.31 Å and the predicted lattice constant of monolayer β-2D-Sb is 4.04-4.12 Å[172]. A detailed investigation of the grown phase (β-2D-Sb) and its epitaxial relationship with Ge(111) is presented in sections 5.1.1.3 and 5.1.1.4. The dendritic nature of the flakes comes from the limited mobility of diffusing species on the flakes' edges at this low T. Interestingly, increasing the deposition rate by a factor of 10 has very little impact on the growth behavior (Figure 5.3d). Nonetheless, a slight increase in the number of flakes per unit area is observed, in agreement with homogeneous nucleation theory. Moreover, there are two distinct populations of flakes displaying different LEEM intensities. This will be discussed in more details in the following sections.

At T = 260-270 °C, the compacity of the grown β-2D-Sb flakes significantly increases, but some dendritic behavior is still observed. The lateral size of the flakes is in the order of 0.5-1.5 μm at F=13 nm/min but decreases to ~0.1-0.2 μm at F=91 nm/min, suggesting homogeneous nucleation. The LEED pattern is more intense than at lower T and the Ge LEED is still clearly visible. This is due to the larger coverage of β-2D-Sb and to the absence of amorphous layer. We also note that the sticking coefficient is considerably smaller than at 200 °C.

At T=320 °C and F=91 nm/min, the flakes' lateral sizes are ~2-4 μm (Figure 5.3). The shape of the flakes is more compact and almost hexagonal. LEED indicates that the edges are oriented with the zigzag directions of β-2D-Sb. Nonetheless, each sides of the hexagon alternate between two types of edges. One side is almost straight and the other is composed of several tips. The edges of the tip align with the straight edges, indicating that it is the lowest energy edge direction. There is also a dark region in the center of each flake. These regions are 3D nuclei and will be discussed below. In addition to the 6-fold symmetric LEED aligned to Ge, some randomly rotated grains can be observed.

5.1.1.3 Identification of the grown phase

The LEEM and LEED data provides good indications that the grown Sb on Ge(111) is multilayer β-2D-Sb. Nonetheless, thorough characterization is necessary to come to that conclusion, especially since β-2D-Sb had never been observed at the time of these experiments. STM, as well as various spectroscopic measurements of the grown flakes are shown in Figure 5.4. STM of a 2.3 nm thick Sb flake on Ge can be seen in Figure 5.4a. This corresponds to a ~6 layers thick β-2D-Sb flake, considering the 1.127 nm out-of-plane lattice constant of A7 Sb. Atomic-resolution STM of the flake's surface is shown in Figure 5.4b. The surface is atomically smooth and a lattice parameter of 4.26 ± 0.05 Å is measured (Figure 5.4b). This is in good agreement with the LEED data and DFT calculations of multilayer β-2D-Sb. The buckled honeycomb lattice of β-2D-Sb is clearly visualized in Figure 5.4c. In the STM topography, the top atoms are higher (brighter) than the bottom atoms, which are barely visible. However, the buckling height cannot be measured directly with STM. Monolayer β-2D-Sb flakes are also observed on Ge(111) (Figure 5.4 (d-f)). Note that the STM images in Figure 5.4 (d-f) were obtained after post-growth annealing of the samples at T≈300 °C.

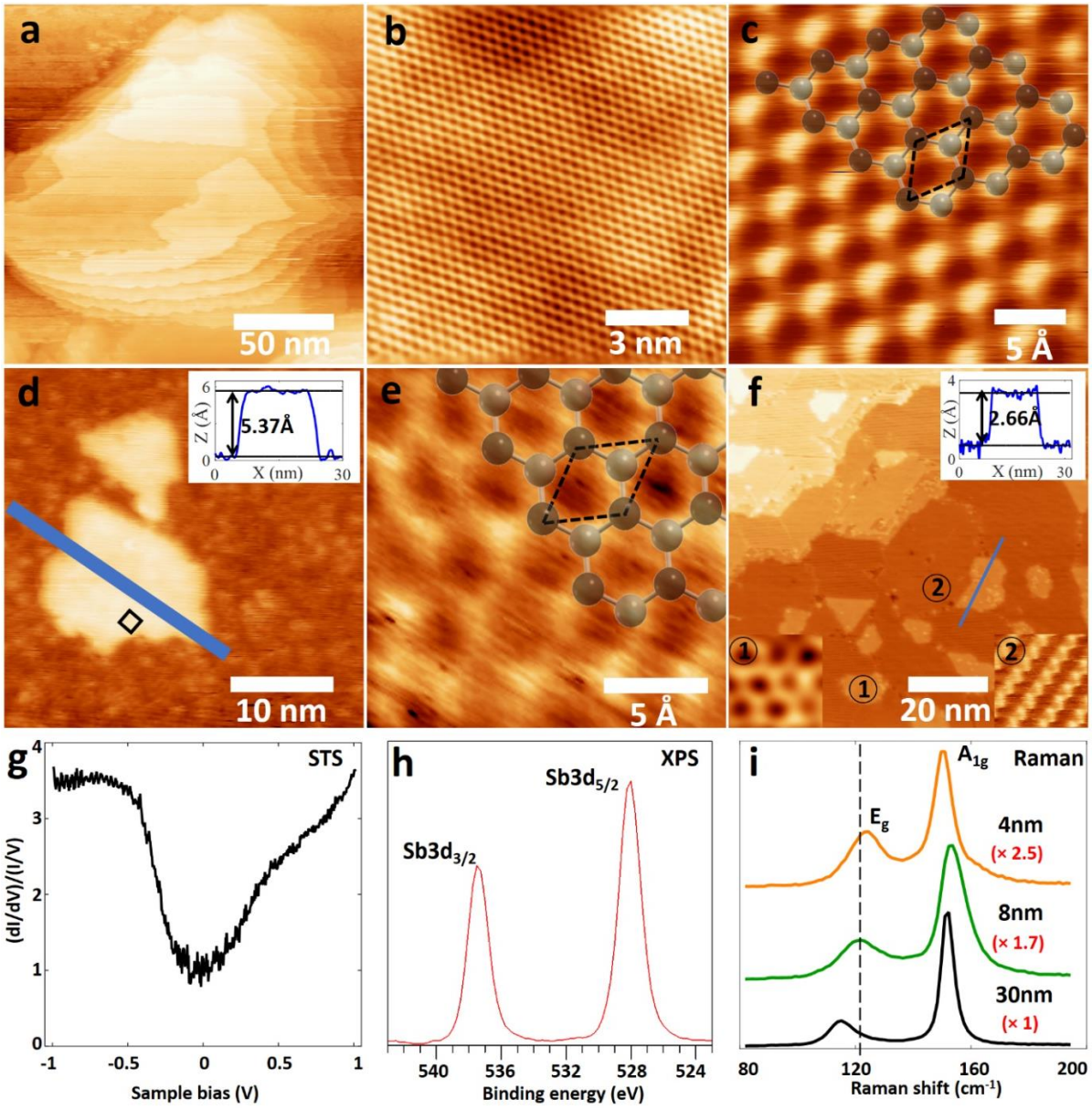

Figure 5.4 (a-f) Constant current STM of multilayer and single layer β-2D-Sb. (a) Multilayer β-2D-Sb imaged with a tunneling voltage V_t=1.3 V and tunnelling current I_t=1.5 nA. (b) Large magnification of the surface of the flake in (a) (V_t=1.3 V, I_t=2.2 nA). (c) STM of multilayer β-2D-Sb showing the buckled honeycomb lattice (V_t=2 V, I_t=0.14 nA). (d) Single layer β-2D-Sb (V_t=2 V, I_t=0.14 nA). (e) Atomic resolution of (d) (V_t=2 V, I_t=0.14 nA). (f) Single layer β-2D-Sb (V_t=2 V, I_t=0.79 nA). (g) STS of few-layer β-2D-Sb. (h) XPS of few-layer β-2D-Sb. (i) Raman spectra of β-2D-Sb as a function of thickness. Adapted with permission from *Fortin-Deschênes et al., Nano Letters 2017, 17, 4970-4975.* [36] Copyright (2017) American Chemical Society.

Post-growth annealing leads to the formation of well-defined single-layer β-2D-Sb flakes (Figure 5.4f), as will be discussed in section 5.1.1.4. Single layer β-2D-Sb were also observed without post-growth annealing, but no high-quality STM images were recorded. The single-layer thickness is confirmed by the step height with respect to the Ge substrate. The step height in Figure 5.4d is 5.37 Å and the step height in Figure 5.4f is 2.66 Å. These step heights are in relatively good agreement with the DFT calculated values of 3.89-4.55 Å. The discrepancy between the 2.66 Å and 5.37 Å values might be due to the Seiwatz chains on the Ge(111) substrate with the 2.66 Å step height. In fact, it is possible that the β-2D-Sb lays directly on Ge(111) and that the Seiwatz chains formed after the single layer β-2D-Sb, at higher T during the annealing process. Moreover, we note that a lattice parameter of 4.07 ± 0.05 Å is measured for single layer β-2D-Sb (Figure 5.4e).

Spectroscopic measurements of β-2D-Sb on Ge(111) are shown in Figure 5.4 (g-i). STS of ~5 layers β-2D-Sb is shown in Figure 5.4g. In first approximation, the $\frac{dI}{dV} / \frac{I}{V}$ spectrum should be proportional to the DOS. A considerable decrease of $\frac{dI}{dV} / \frac{I}{V}$ occurs close to zero bias, indicating a small DOS at the Fermi level. Note that the $\frac{dI}{dV}$ signal is not measured directly with a lock-in amplifier, but rather by differentiating the I(V) curve numerically. This method gives a poor signal to noise ratio due to noise amplification during numerical differentiation. To circumvent this issue, 1024 I(V) curves are recorded (32×32). The I(V) are averaged and smoothed using a moving average over 150 mV. The numerical derivative is then calculated for the smoothed data. Moreover, the STS was measured at ~100 °C. For these reasons, the data should be analysed with caution and poor energy resolution is expected. Still, it indicates that multilayer β-2D-Sb is semimetallic. Unfortunately, it was not possible to acquire good quality STS on single-layer β-2D-Sb. In fact, due to the large applied electric field and the small lateral dimensions of the flakes, single layer β-2D-Sb was either destroyed or exfoliated from the substrate during the measurements. The XPS spectra of multilayer β-2D-Sb grown on Ge(111) are show in Figure 5.4h. The Sb $3d_{5/2}$ and Sb $3d_{3/2}$ peaks are located at 537.4 eV and 528.1 eV, respectively. Moreover, the peaks can be well fitted with a single component. This indicates the absence of Sb compounds and suggests that mainly crystalline Sb is present on the sample (a binding energy shift could be present in amorphous Sb but may be too small to resolve). Nonetheless, it was reported that there is no shift associated to Sb-Ge bonding in Sb Seiwatz chains on Ge, due to the similar electronegativities of both elements.

XPS therefore do not allow to conclude anything about Sb-Ge interactions. The Raman spectra of multilayer β-2D-Sb of various thicknesses (determined by AFM) are presented in Figure 5.4i. The data agrees with other early reports on β-2D-Sb synthesis[98, 153, 154]. E_g and A_{1g} modes are observed. The E_g mode shifts from 115.6 cm^{-1} to 124.0 cm^{-1} as the thickness goes from 30 nm to 4 nm. On the other hand, the A_{1g} mode is relatively stable at 150 cm^{-1}. These spectra will be useful in the next sections to understand the growth of group VA alloys and other allotropes.

5.1.1.4 Nucleation and growth

in situ LEEM observations of the growth dynamics as well as *in situ* STM and *ex situ* AFM characterization were carried out to better understand the nucleation and growth of β-2D-Sb. Understanding the flakes' morphology can provide insight into the nucleation and growth mechanisms. We therefore start by looking at scanning probe micrographs of the deposited Sb.

Deposition of Sb on Ge(111) leads to the growth of many types of flakes and islands. The AFM images in Figure 5.5a are from the sample presented in Figure 5.3c (growth T=200 °C). The Ge surface is covered by small dome-shaped islands with diameters of ~50 nm and heights of ~5 nm. The small islands might correspond to the amorphous-like film observed in LEEM which was responsible for the disappearance of the Ge LEED pattern. Nonetheless, the AFM measurement do not provide any information about their crystalline nature. Dendritic flakes are also observed and have lateral dimensions of up to 1 μm and thicknesses of ~3nm or ~8 layers.

At higher growth T (T>270 °C, Figure 5.5b), the surface is covered by β-2D-Sb as well as 3D islands and there are almost no amorphous domes. The 2D flakes are not perfectly flat. In fact, their edges are ~4 nm thick and their center is ~7 nm. Descending single-layer steps are seen when going from the center to the edges, suggesting that multilayer nucleation occurs in the center and is followed by outward growth. Moreover, the height of the flakes increases with the lateral dimensions. On the other hand, the 3D islands are ~30 nm thick and ~150 nm wide. Their rectangular shapes suggest that they are A7 Sb(110), as will be discussed in Chapter 6. Looking closely, we notice that the islands are in fact nanowires with multiple 90° kinks.

Several types of β-2D-Sb flakes are observed (Figure 5.5 (c-f)). These include flat hexagonal flakes as well as clover-shaped flakes with thicker centers. STM of an atomically flat ~5 layers β-2D-Sb flake is shown in Figure 5.5c. The flake has an irregular hexagonal shape with multiples kinks on

the top edge. Ge atomic steps can be seen, but the surface is covered by small Sb aggregates too small to be resolved with AFM. Clover-shaped flakes are frequently observed (Figure 5.5 (d, e)). These flakes have a central elevated region and three elongated branches. Single atomic steps are visible on the surface of the branches and a multilayer step is seen on the edges of the flake (usually 1-4 nm thick). The step edges on the surface are straight, whereas the edges of the flake are wavy. Interestingly, some flakes have a similar shape, but with a much thicker 3D central region (Figure 5.5e).

In addition to the β-2D-Sb flakes, some rectangular flakes and islands are observed (Figure 5.5 (f-i)). A β-2D-Sb flake and a 3D island can be seen in Figure 5.5f. The 3D island is in its early growth stage and has a height of ~ 4 nm. At this stage, the top surface is flat and the side edges are facetted. Thinner rectangular flakes are shown in Figure 5.5 (g-i). Note that multiple copies of the same flake are imaged in Figure 5.5 (g, h). This is due to multiple secondary STM tips. These images should therefore be interpreted with caution. The flake in Figure 5.5g has a length of 100 nm and width of 40 nm. The thickest region of the flake is ~7 Å and the center region is ~4.5 Å. The flake in Figure 5.5h has an L-shape with a ~90° angle but its thickness cannot be determined due to the multiple superposed image. However, the largest measured height is ~7 nm and a step of ~2.7 Å can be seen on the top of the flake. A rectangular nanoribbon with a width of ~13 nm and height of ~7 Å can be seen in Figure 5.5i. The edges of the ribbon are parallel. This chapter focuses on the growth of β-2D-Sb, but the rectangular islands will be discussed in detail in Chapter 6. Nonetheless, the STM data allows to speculate about their nature. The rectangular shape suggests that the crystal structure of the surface also has rectangular symmetry. In fact, a clear 90° can be seen in Figure 5.5h. This means that the low-energy edges are at 90° from each other. Moreover, the large aspect ratio (length/width) of the flakes indicates that the short and long axis edges are non-equivalent crystallographic directions. The 2D growth mode and flatness of the flake implies the low surface energy of the top surface. The STM data therefore suggests that the flakes are single-layer and multilayer α-2D-Sb. Unfortunately, atomic resolution was not achieved on those flakes and the crystal structure cannot be confirmed. Moreover, the 2.7 Å step height on the L-shaped flake is not consistent with this interpretation. In fact, multilayer α-2D-Sb should have bilayer step heights of ~6 Å. The 2.7 Å could be associated to a monolayer step in A7 Sb(110).

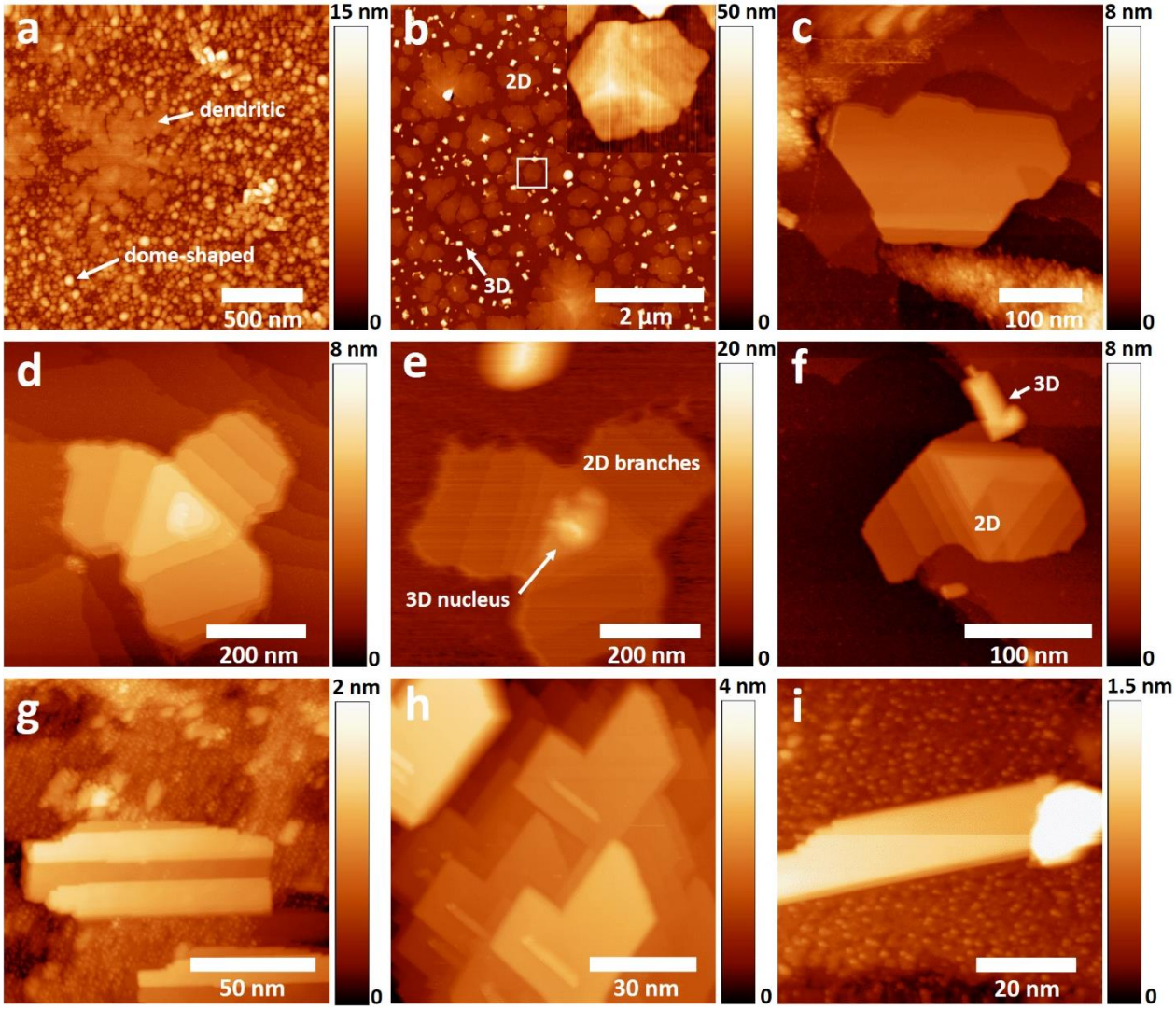

Figure 5.5 AFM and STM images of 2D-Sb flakes and 3D Sb islands grown on Ge(111). (a) AFM image of dendritic growth accompanied by dome-shape islands (growth T = 200 °C). (b) AFM of 2D and 3D growth (growth T = 270 °C). (c) STM of flat β-2D-Sb flake (growth T = 270 °C). (d) STM of stepped clover-shaped β-2D-Sb flake with flat top (growth T=270 °C). (e) STM of stepped clover-shaped β-2D-Sb flake shaped with central 3D nucleus (growth T=270 °C). (f) STM of β-2D-Sb flake and L-shaped 3D island (growth T=270 °C). Panel (e) is adapted with permission from *Fortin-Deschênes et al., Nano Letters 2017, 17, 4970-4975.* [36] Copyright (2017) American Chemical Society.

To better understand the nucleation and growth of the various types of 2D flakes, we look at real-time LEEM observations of the growth dynamics. Snapshots of a LEEM growth video are

presented in Figure 5.6 (a-f). The nucleation sites of various types of islands are indicated by white arrows and labelled “A”, “B”, “C”, “D” and “E”. Here, “A” and “C” are Ge mounts formed during the annealing process. “B”, “D” and “E” are step bunches. As soon as the Sb deposition begins, a (2×1) LEED pattern appears (not shown). This is due to the Seiwatz chains, which form on the clean Ge(111) c(2×8). Then, heterogeneous nucleation occurs relatively quickly on the Ge mounts. A clover-shaped 2D flake nucleates on mount “A” after ~80 seconds. This type of flake is likely the same type as the one shown in Figure 5.5e. In fact, a dark spot is seen in the center of the flake throughout the growth. This either indicate that the surface is not flat or not in the same phase as the rest of the flake. By comparing the LEEM and ATM/AFM images, we conclude that the clover-shaped flakes with 3D centers nucleate a defects on the Ge(111) surface. The Ge mounts are also nucleation centers for 3D islands. For instance, the diameter of the dark region of the “C” mount immediately grows during deposition due to Sb accumulation.

The nucleation and growth of clover-shaped flakes with flat centers can also be observed. Often, these clover-shaped flakes nucleate at step bunches such as those labelled by “D” and “E”. The flat triangular centers are clearly seen in the high resolution bright-field LEEM image (Figure 5.6g) and the homogeneous contrast confirms their flatness. The nucleation of flat hexagonal-like flakes is also seen at step bunches (Figure 5.5c). For instance, the flake labelled “B” nucleates on a step bunch in Figure 5.6d and then grows laterally. The flake grows in all directions, but its growth rate across the step bunch is significantly lower. This indicates that the energy barrier for diffusing Sb species to cross step bunches is relatively high. It is plausible that the growth across step edges is fed by Sb species deposited on the flake, rather than on the Ge surface. There are also several rectangular Sb(110) flakes. The Sb(110) appear as dark patches in the growth video, but are brighter in the high-resolution bright-field LEEM. Interestingly, the Sb(110) flakes do not nucleate at visible defects.

While LEEM provides detailed information about the nucleation and growth dynamics, its ~10 nm lateral resolution is insufficient to characterize the early stages of 2D-Sb nucleation. On the other hand, atomic resolution images of the nucleation process can be obtained by STM. To study the nucleation process with STM, Sb was deposited on Ge(111) c(2×8) until nucleation was observed with LEEM (T=250 °C and F=36 nm/min for 30 seconds). The sample was then transferred to

STM under UHV for imaging. After imaging, the substrate was annealed at T≈300 °C for 10 min and imaged again.

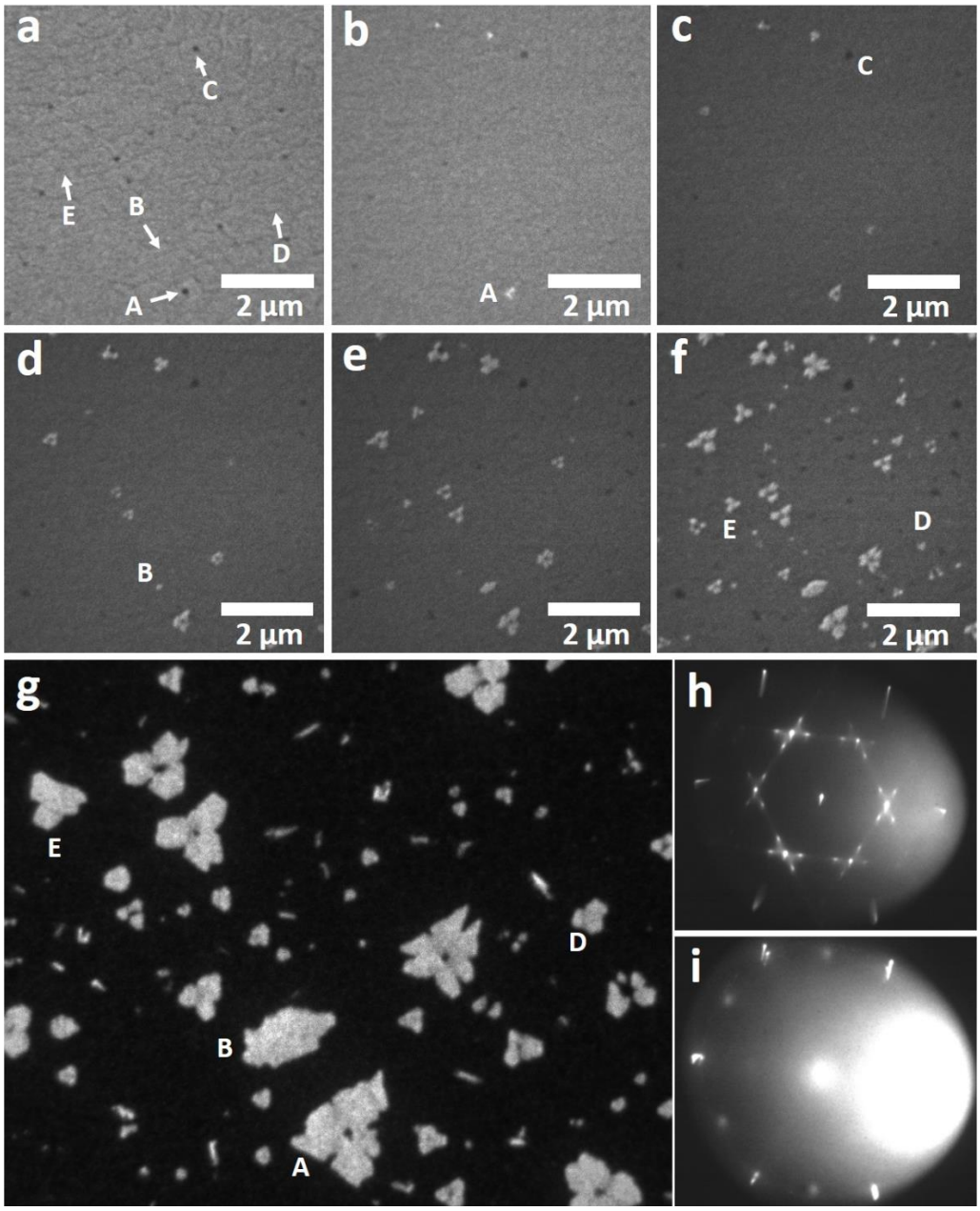

Figure 5.6 a-f) Bright-field LEEM snapshots (1.2 eV) of β-2D-Sb growth dynamics on Ge(111) c-(2×8). T=270 °C, F=9 nm/min. The images are taken 30 seconds apart. The letters A, B, C, D, E identify the nucleation centers of various flakes discussed in the main text. g) Post-growth high-resolution bright-field LEEM image (1.2 eV). h) LEED pattern before growth (17 eV). i) LEED pattern after growth (17 eV).

STM images of as-deposited Sb/Ge(111) c(2×8) are shown in Figure 5.7 (a-c). Ge atomic steps are visible and the surface is mainly covered by small Sb flakes (~35% coverage) which appear to be single-layer β-2D-Sb nuclei with thicknesses of 6.7 Å and lateral dimensions between a few nm and ~40 nm. The nuclei neither have dendritic nor compact shapes. There are Sb nuclei on atomic terraces and Ge atomic steps, but the coverage is slightly higher at atomic steps. Larger nuclei often have bilayer regions. The measured bilayer step height is 6.8 Å, which is surprising considering that the interlayer distance in bulk A7 Sb is 3.76 Å. However, as mentioned earlier, constant current STM does allow accurate thickness measurements when the electronic structure is not constant. Nonetheless, we cannot completely exclude the possibility that the steps are two bilayers thick. Interestingly, the Ge surface beneath the β-2D-Sb nuclei is covered by Sb species (Figure 5.7), which can difficultly be identified at this resolution.

STM images of the sample after annealing at ~300 °C for 10, 20 and 30 minutes are shown in Figure 5.7 (d, e), Figure 5.7f and Figure 5.7 (g-i), respectively. Unfortunately, no accurate measurements of the sample T are available. The β-2D-Sb nuclei coverage decreases to ~9% after 10 min annealing and down to ~6% after 30 min. Multilayer nuclei disappear after the 1st annealing cycle and the lateral size of the nuclei decreases and becomes less dispersed, with most nuclei between 5-10 nm. This suggest that both ripening and desorption occurred during annealing. The shape of the nuclei becomes more compact and 120° and 60° angles are observed (Figure 5.7i). Atomic resolution STM of the surface of the nuclei confirm that they are monolayer β-2D-Sb (Figure 5.7f). Even after annealing, the surface is still covered by chemisorbed Sb species (Figure 5.7 (e, g-i)). The Sb species have low mobility on the Ge surface at the imaging T (~100 °C). In fact, they remain immobile during the acquisition of multiple images (compare Figure 5.7 (h, i) for instance). This indicates that the surface diffusion activation energy E_a is at least 1 eV (with a jump frequency of $f = f_0 e^{-E_a/k_B T}$ and $f_0 \approx 10^{12}$). In fact, using optical second harmonic microscopy, Schultz and Seebauer[246] found E_a=2.06 eV and a pre-exponential diffusion coefficient of D_0=8.7×10^3 to 1.6×10^2, as the coverage increases from 0 to 0.6. The authors also determined a desorption activation energy of E_D=2.82 eV. This suggests that the Sb species are chemisorbed on the surface. This is surprising considering the observed LEEM growth dynamics. In fact, considerable surface diffusion occurs during growth, as evidenced by the competition for diffusing

Sb species as flakes get close to each other (more details in the following sections). We can therefore conclude that there is a chemisorbed Sb layer on top of which Sb species can diffuse.

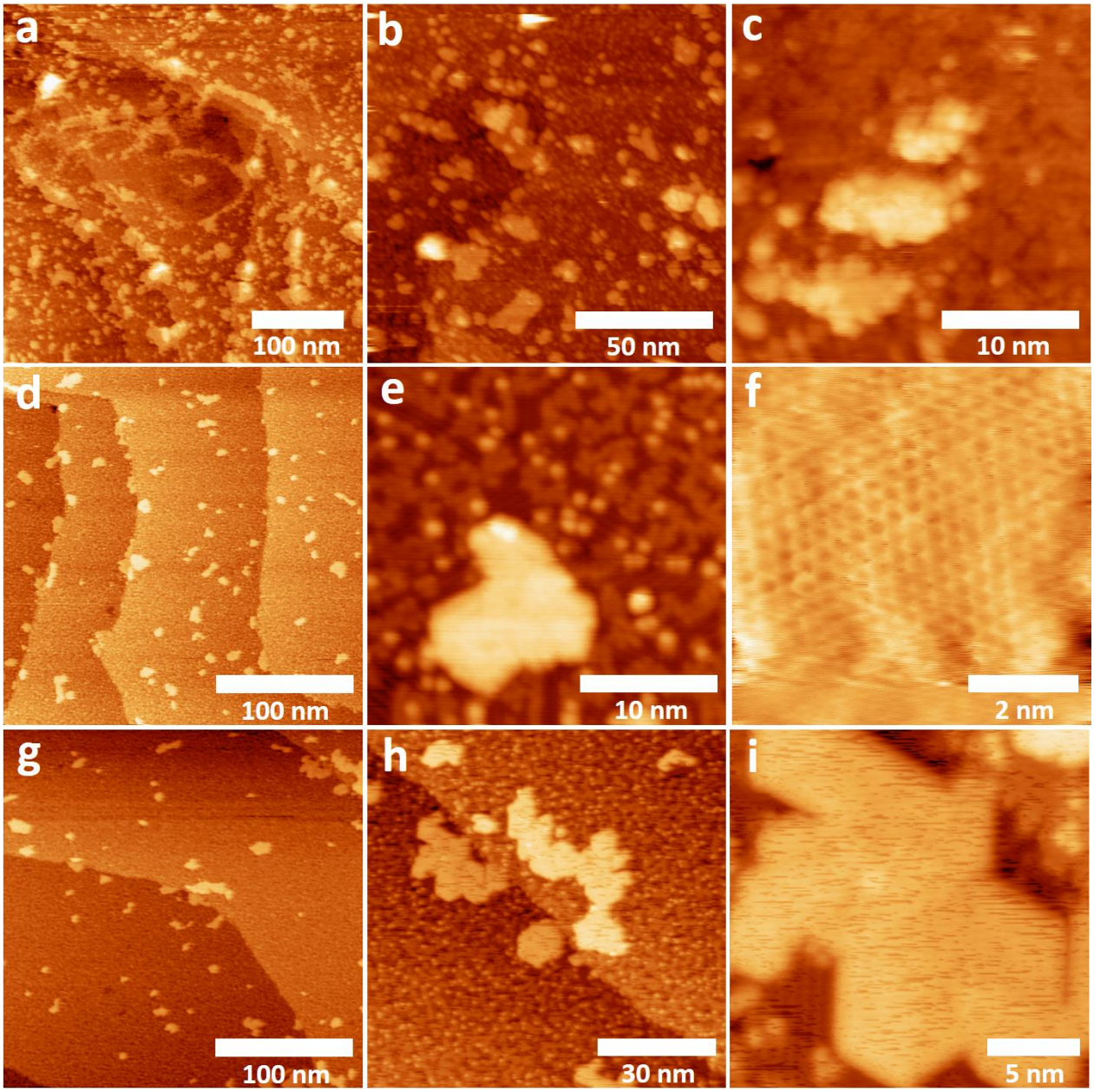

Figure 5.7 Constant current STM images of a-c) As-deposited Sb on Ge(111) (T=250 °C, F=36 nm/min for 30 seconds). d-e) STM images of the same sample after post growth annealing (300 °C, 10 minutes). f) STM images of the same sample after post growth annealing (300 °C, 20minutes). h-i) STM images of the same sample after post growth annealing (300 °C, 30 minutes)

5.1.1.5 β-2D-Sb/Ge(111) interface

The LEED data presented above indicates that the β-2D-Sb and Ge lattices are rotationally aligned but not coherent. This raises questions regarding the nature of the Sb/Ge interface. In fact, in the heteroepitaxial growth of thin films, the film usually grows lattice matched to the substrate up to a critical thickness at which its strain energy is greater than the energy required to release the strain.

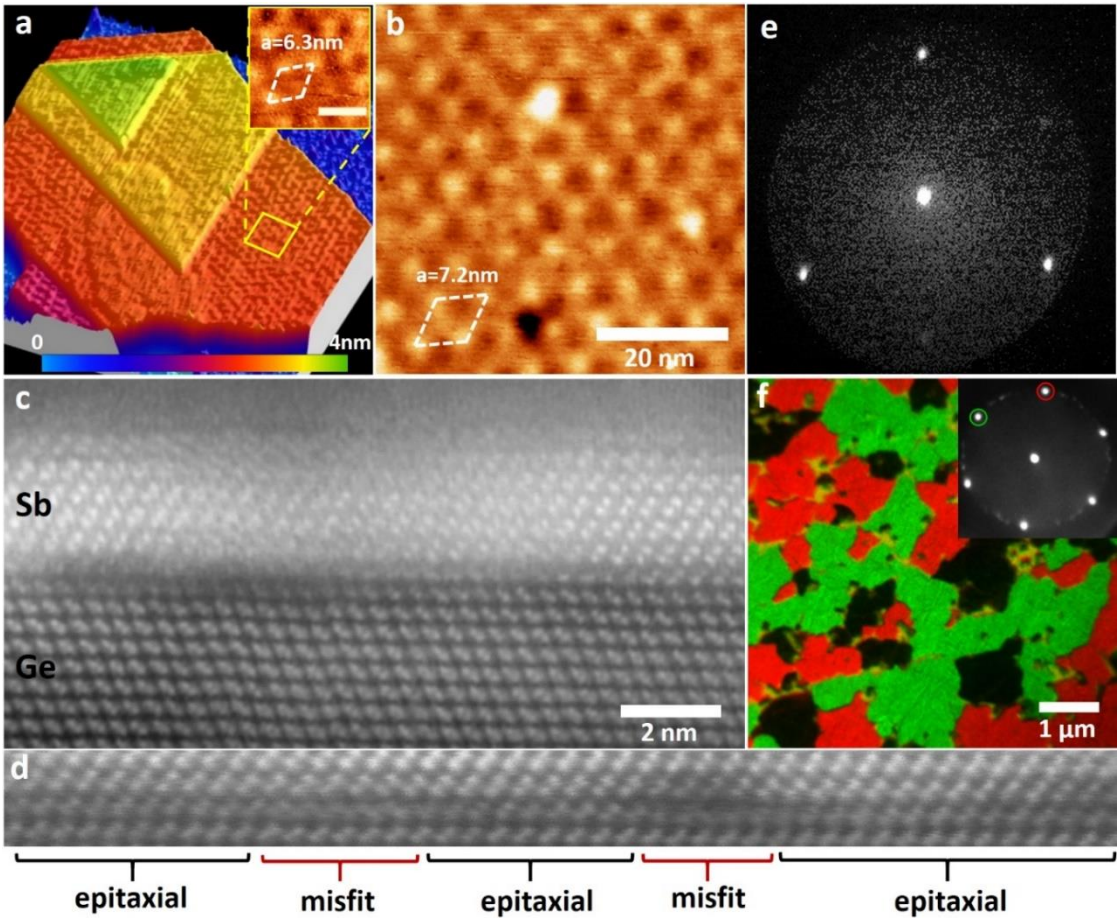

Figure 5.8 (a) STM (V_t=1.5 V, I_t=0.2 nA) of multilayer β-2D-Sb flake on Ge(111). The pink, orange, yellow and green terraces are 4, 5,6 and 7 layers thick, respectively. Inset: moiré pattern on the orange terrace. Scale bar is 10 nm (b) STM (V_t=1.5 V, I_t=0.2 nA) of a moiré on 5 layers thick β-2D-Sb flake. (c) STEM of β-2D-Sb on Ge(111). (d) STEM of a β-2D-$As_{0.08}Sb_{0.92}$/Ge(111) interface. (e) µ-LEED (15.8 eV) of a single β-2D-Sb flake. (f) Composite image of the two main β-2D-Sb orientations on Ge(111). Inset: corresponding LEED (30 eV) with the main orientations circled (green and red). Adapted with permission from *Fortin-Deschênes et al., Nano Letters 2017, 17, 4970-4975.* [36] Copyright (2017) American Chemical Society.

The strain is usually released by the formation of misfit dislocations at the interface with the substrate. Considering the relatively weak substrate-layer interactions in quasi-vdW materials, it is interesting to examine how this process takes place.

An STM image of β-2D-Sb on Ge(111) is shown in Figure 5.8a. The first terrace (pink) is 4 layers thick and the subsequent steps are single BL steps. Constant current STM indicates a periodic hexagonal height modulation of ~60 pm on the pink terrace, ~40 pm on the orange terrace (5 layers), ~20 pm on the yellow terrace (6 layers), and barely visible on the top terrace (7 layers). The lattice parameter of the modulation is ~6.3 nm. A similar pattern with a 7.2 nm periodicity can be seen on a flat 5 layers thick flake (Figure 5.8b). The pattern can be associated to a moiré pattern, similar to those observed for epitaxial graphene on TM surfaces[247]. Moiré patterns are formed when two lattices with different lattice constants and/or rotated lattices overlap. The reciprocal lattice vector of the moiré is given by $\vec{k}_{moiré} = \vec{k}_1 - \vec{k}_2$, where $\vec{k}_1$ and $\vec{k}_2$ are the reciprocal lattice vectors of the overlapping lattices. Considering the alignment of the Sb and Ge lattices, as well as the 4.00 Å surface lattice constant of Ge, the 6.3 nm and 7.3 nm moirés imply lattice constants of 4.27 Å and 4.24 Å for β-2D-Sb, in good agreement with the LEED results.

The fact that moirés are observed on 4-6 layers thick β-2D-Sb is interesting for two reasons. First, it shows that the substrate-layer interactions have a strong impact on the electronic structure of β-2D-Sb. In fact, the measured height corrugation of ~0.6 Å is most likely due to a modulation of the local DOS, rather than a real height modulation. This is surprising since the moiré is visible even at a thickness of 6 bilayers (2.2 nm). The strong substrate-layer coupling is therefore expected to have deep implications on the electronic structure and transport properties of β-2D-Sb. Proper low-T STS would shed light on the moiré formation mechanisms and its effect on the electronic structure. Moreover, the moiré indicates that the relaxation of the heteroepitaxially grown β-2D-Sb lattice takes place at a thickness of four layers or less. We can safely assume that β-2D-Sb is lattice matched to Ge during the nucleation stage. In fact, the rotational alignment of the two lattices is most likely due to epitaxial alignment of the nuclei with the Ge lattice. This alignment is more energetically favorable if the nuclei is lattice matched to the substrate. Considering the calculated 163 meV/atom difference between the different epitaxial stackings, the energetic gain of rotationally aligning the two lattices, but having different lattice constants is most likely not enough

to explain the prevalence of rotationally aligned grains. The lattice mismatch induced strain is therefore relaxed between the nucleation and the growth of 4 layers.

STEM of the Sb/Ge interface allows to better understand the strain relaxation mechanism (Figure 5.8 (c, d). The image in Figure 5.8c is β-2D-Sb on Ge(111) and the image in Figure 5.8d is β-2D-$As_{0.08}Sb_{0.92}$. The growth of β-2D-As_xSb_{1-x} alloys is presented in section 5.2, but the STEM is included here since its high quality allows to better understand the strain relaxation process. Moreover, the relatively low As content should not have a significant effect on the strain relaxation behavior since As and Sb form substitutional alloys with perfect miscibility. The flakes in Figure 5.8c and Figure 5.8d have different stacking configurations. In fact, the β-2D-Sb flake has a ABC-X' type staking and the β-2D-$As_{0.08}Sb_{0.92}$ flake has a ABC-X configuration. This can be readily seen by looking at the orientation of the Ge and Sb dumbbell (same orientation for ABC-X and different orientation for ABC-X'). The stacking difference is not related to the As content. In fact, the μ-LEED pattern of single β-2D-Sb flakes (Figure 5.8e) has 3-fold symmetry due to the trigonal crystal symmetry. The observed 6-fold symmetry in large area LEED (Figure 5.3 for instance) is due to the superposition of the two main orientations of β-2D-Sb, which are rotationally aligned to Ge(111), but rotated by 180° from each other. The two orientations are associated to ABC-X and ABX-X' stackings. The orientations of β-2D-Sb on Ge(111) can be visualized in the composite dark-field image (Figure 5.8f). The red and green grains are the dark-field LEEM images of the two main orientations. The dark patches correspond to the randomly oriented grains visible in the large area LEED pattern (Figure 5.8f inset).

The STEM measured lattice parameters of β-2D-Sb and β-2D-$As_{0.08}Sb_{0.92}$ on Ge(111) are 4.27 ± 0.05 Å and 4.25 ± 0.05 Å, respectively (Figure 5.8 (c, d)). This agrees with the LEED results and confirms that the Sb and Ge lattices are not coherent. However, local coherence between the β-2D-Sb and Ge(111) lattices is observed on the right side of the STEM image. This is much clearer in the β-2D-$As_{0.08}Sb_{0.92}$ image (due to FIB sample preparation). Locally, the stackings appear to be ABC-C' and ABC-B, in agreement with the DFT calculations presented in Chapter 4. In fact, the ABC-B is the most energetically favorable stacking by at least 100 meV/atom and ABC-X' stackings are roughly all energetically equivalent. There are ~2 nm wide incoherent regions between the coherent regions. These are misfit dislocations. The dislocations are confined at the interface and no other type of dislocations are observed (such as threading dislocations). Moreover,

we can notice that the top layer of the Ge lattice is distorted in the dislocation region (Figure 5.8d). This might be associated to a surface reconstruction to accommodate the un-passivated Ge dangling bond. This distortion is not as clear in the ABC-X' stacked β-2D-Sb/Ge(111) interface (Figure 5.8c). In fact, the top Ge dumbbells are relatively well resolved on most of the interface. On the other hand, the Sb bottom layer appears to have some distortions. Whether this is due to beam damage, sample preparation or actual stacking dependant distortions of the β-2D-Sb lattice is hard to tell.

It is plausible that the strain field induced by the misfit dislocations is at the origin of the moiré pattern observed in STM. In fact, the coherent β-2D-Sb regions are compressively strained and the misfit regions are tensile strained. The maximal strain is in the order of 6.5%, which should have considerable effects on the electronic band structure. It would be interesting to investigate the effect of this periodic strain field on the electronic and topological properties of few-layer β-2D-Sb.

5.1.2 β-2D-Sb on passivated Ge

As detailed in Chapter 4, substrate-layer interactions can strongly alter the properties of epitaxial group VA 2D materials. In particular, the surface dangling bonds of the Ge(111) substrates can hybridize with the group VA elements, which modifies their electronic properties. Various substrates passivation methods have been proposed in Chapter 4, including H, CH_3, alkali metals, chalcogens, halogens and Sb. Another way to passivate semiconductor substrates is with another 2D material. For instance, epitaxial graphene can be grown on Ge to passivate the surface. This subsection investigated the growth on various passivated substrates including Ge(111)-Cl, Ge(111) (2×1)-Sb and graphene passivated Ge(111), Ge(110) and Ge(100). The growth on Ge(111)-Cl and Ge(111) (2×1)-Sb is briefly discussed and the section mostly details the growth on graphene/Ge.

5.1.2.1 β-2D-Sb growth on Ge(111)-Cl

Ge(111)-Cl were prepared by cleaning Ge(111) pieces using sonication in acetone followed by rising in isopropanol and drying with a N_2 flow. The substrates were then dipped in HCl (37%) for 10 minutes and rinsed in deionized water for 5-10 seconds (dipping consecutively in three clean deionized water beakers), followed by N_2 drying. The substrates were immediately inserted in UHV. Successful substrate passivation is confirmed by the presence of a sharp (1×1) LEED pattern

(Figure 5.9a). In fact, since Ge native oxide immediately forms on bare Ge(111), the LEED pattern indicates that the Ge dangling bonds were passivated by Cl at least until the samples were inserted in UHV. The sample was then annealed at 300 °C for ~10 minutes and Sb_4 was deposited at T=285 °C and F=13 nm/min for 700 seconds. During this time, no Sb growth was observed. The growth T was then slowly decreased until nucleation was observed at 235 °C. The T was then immediately increased to 255 °C for growth.

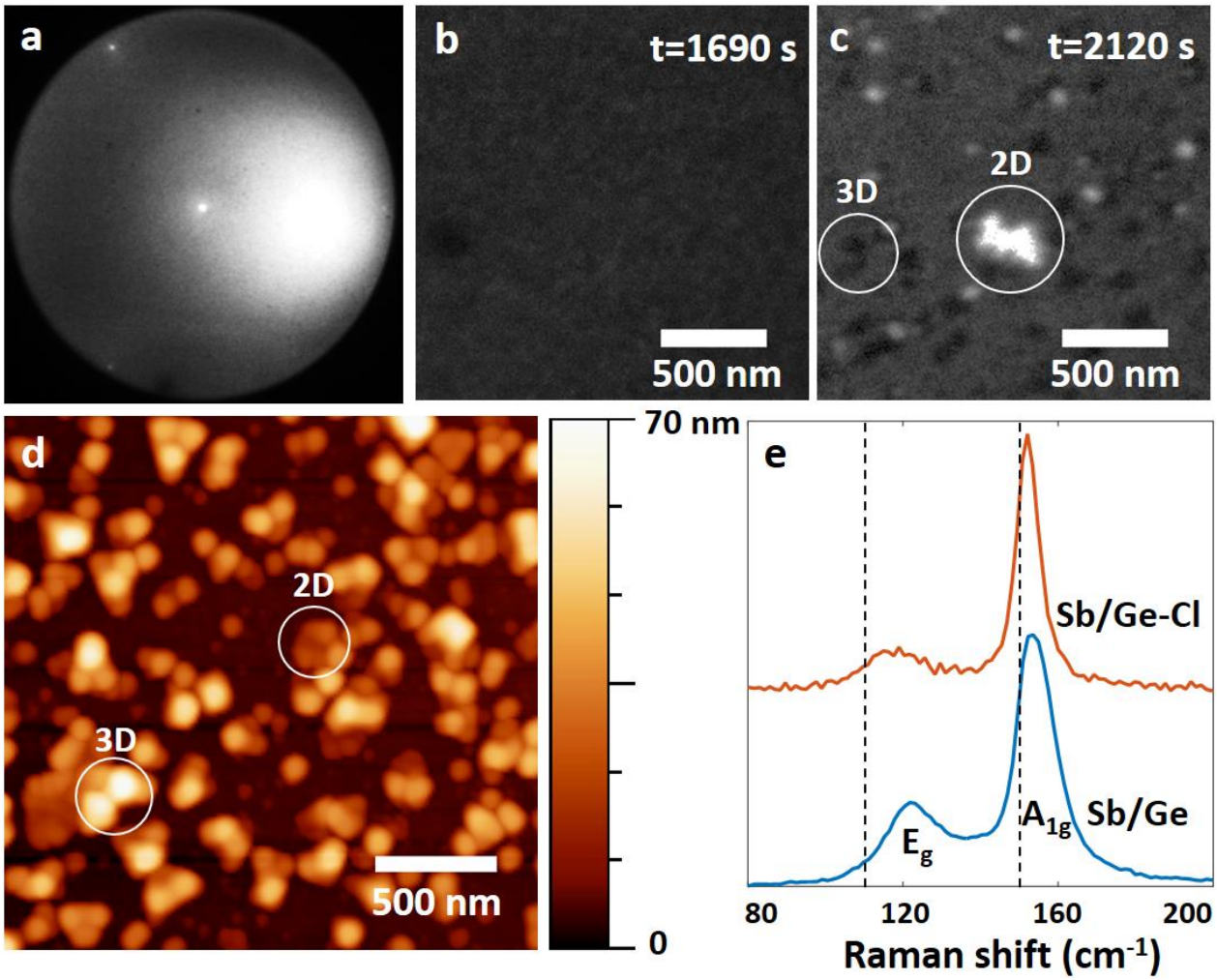

Figure 5.9 (a) LEED pattern (16 eV) of Ge(111)-Cl. (b) LEEM image of Ge(111)-Cl. (d) LEEM image of Sb grown on Ge(111)-Cl. (d) AFM of Sb on Ge(111)-Cl. (e) Raman spectra of 2D-Sb grown on bare Ge(111) and Ge(111)-Cl. The dashed lines indicate the bulk Sb peak positions. Adapted with permission from *Fortin-Deschênes, M; Moutanabbir, O., J. Phys. Chem. C 2018, 122, 9162-9168* [35]. Copyright (2018) American Chemical Society.

LEEM and AFM show that both 2D and 3D structures grow (Figure 5.9 (c, d)). The β-2D-Sb nature of the flakes is confirmed by Raman spectroscopy (Figure 5.9e). In fact, E_g and A_{1g} vibration modes are measured at 119 cm^{-1} and 152 cm^{-1}, respectively. By comparison, the E_g and A_{1g} modes of bulk A7 Sb are at 110 cm^{-1} and 149 cm^{-1}. However, the surface is mainly covered by 3D islands. Most 3D islands are triangular indicating that they are A7 Sb(111). Moreover, we can notice 3D mounts on the vertices of the triangle (up to three per triangular island). As will be discussed in the next subsection, these 3D mounts form when the lateral growth rate is small enough for the flakes' edges to align with the low-energy *Z2* edges of β-2D-Sb. This suggests weak mobility of diffusing Sb species on the Ge(111)-Cl surface or a large desorption rate, leading to a small lateral growth rate. The mobility of Sb species might be limited by surface impurities or by a high concentration of atomic steps. In fact, the typical annealing or sputtering/annealing procedure which removes surface impurities and improve surface ordering cannot be done since it would result in Cl desorption. Moreover, it is possible that the residues from the surface cleaning procedure act as nucleation centers for 3D islands. To properly study 2D-Sb growth on Cl passivated Ge, *in situ* passivation on conditioned surfaces would be required.

5.1.2.2 β-2D-Sb growth on Ge(111) (2×1)-Sb

In contrast to Ge(111)-Cl, the Ge(111) (2×1)-Sb surface can be prepared *in situ* in any MBE system equipped for 2D-Sb growth. LEED patterns of the Ge(111) surface at the different stages of Ge(111) (2×1)-Sb surface preparation are shown in Figure 5.10 (a-c). First, a Ge(111) c-(2×8) surface was prepared by the standard sputtering-annealing procedure (Figure 5.10a). ~2 ML of Sb were then deposited on Ge(111) c-(2×8) at low T (60 °C). The intensity of the Ge(111) LEED decreases after Sb deposition, indicating the presence of an overlayer on Ge(111) (Figure 5.10b). Moreover, the c-(2×8) surface reconstruction disappears. A faint, but sharp (2×1)-Sb LEED pattern is visible at this stage (Figure 5.10b (inset)). This indicates that an ordered (2×1)-Sb is already present at low T. However, the weak LEED intensity suggests either an incomplete coverage of the (2×1)-Sb phase or that the (2×1)-Sb is covered by an amorphous overlayer. The sharp peak indicates a domain size of ~16 nm, based on the full width half maximum (FWHM). This is much larger than the ~4 nm measured when depositing Sb_4 at high T on Ge(111) c-(2×8) (Figure 5.6i). The sample was then annealed up to 550 °C. The intensity of the (2×1)-Sb LEED spots begins to increase at ~400 °C. At 550 °C, a clear (2×1)-Sb LEED pattern is observed (Figure 5.10c). This

LEED pattern is associated to the formation of Seiwatz chains on the surface. The three equivalent orientations of Sb chains give rise to the LEED pattern with 6-fold symmetry. The successful surface passivation and formation of Seiwatz chains was confirmed by STM (Figure 5.10d). The passivating Sb chains are seen on top of the substrate and the bottom tetravalent Ge atoms are also imaged.

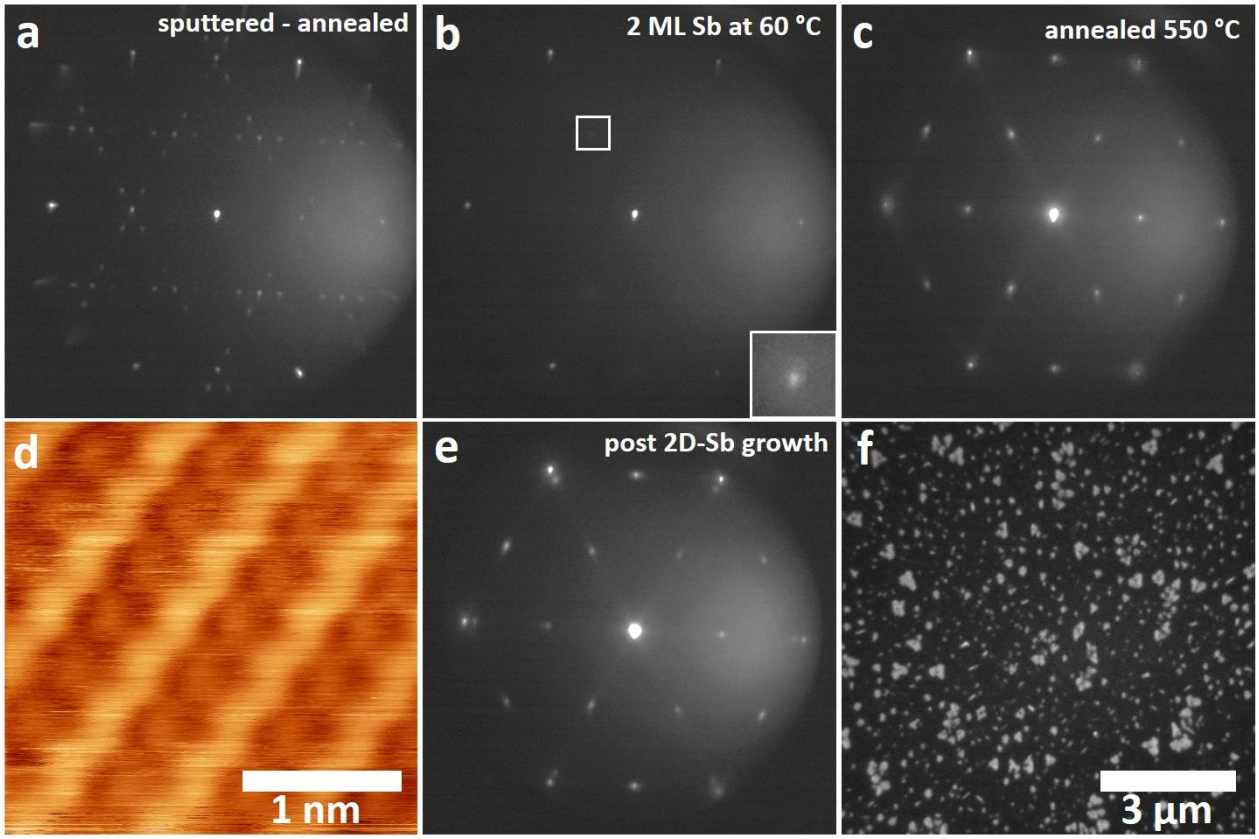

Figure 5.10 (a) LEED pattern of Ge(111) c-(2×8) prepared by sputtering/annealing (21 eV). (b) LEED pattern after deposition of ~2 ML Sb on Ge(111) c-(2×8) (21 eV). Inset: close up of (2×1) LEED spot (increased brightness and contrast). (c) LEED pattern of Ge(111) (2×1)-Sb at 550 °C. (d) STM image of the Ge(111) (2×1)-Sb surface (V_t=1268 mV, I_t=0.595nA). (e) LEED pattern of 2D-Sb grown on Ge(111) (2×1)-Sb at T=260 °C and F=17 nm/min for 90 seconds (17 eV). (f) Bright-field LEEM (2 eV) of 2D-Sb grown on Ge(111) (2×1)-Sb.

Sb_4 deposition was then carried out on the Ge(111) (2×1)-Sb at T=260 °C and F=17 nm/min for 90 seconds. Similar to the growth on bare Ge(111), β-2D-Sb grows aligned to the Ge(111) lattice, but with a relaxed lattice parameter of 4.27 ± 0.02 Å. Interestingly, the growth is faster than on bare

Ge(111), suggesting that the diffusion length of Sb_4 species is larger on Ge(111) (2×1)-Sb. Nonetheless, the growth morphology is similar to what was observed on Ge(111) (Figure 5.10f). Sb(110) flakes and hexagonal-like β-2D-Sb flakes are observed. However, the dominant nucleation mechanism is heterogeneous nucleation of clover-shaped flakes with 3D nuclei, due to the formation of Ge mounts during surface conditioning.

5.1.2.3 β-2D-Sb growth on graphene/Ge

The results obtained for the growth of β-2D-Sb on Cl and Sb passivated Ge(111) are a proof of concept that the growth of β-2D-Sb is possible on passivated semiconductor surfaces. On the other hand, this subsection studies in detail the growth dynamics on graphene passivated Ge, as a model system for vdW growth. The growth on graphene on Ge(111), Ge(110) and Ge(100) is demonstrated and the growth dynamics β-2D-Sb on graphene/Ge(110) is analysed in more detail.

5.1.2.3.1 Graphene substrates

Graphene was grown on Ge(111), Ge(110) and Ge(100) by CVD by the *Advanced Materials for Energy and Electronics Group* (Robert Jacobberger and Michael S. Arnold) at UW-Madison. The growth procedures are detailed in the following publications[227, 248]. After growth, the graphene/Ge samples were vacuum packed under inert atmosphere and shipped to Polytechnique Montréal. The vacuum-packed graphene samples were stored in ambient conditions and then loaded in the UHV system. Prior to Sb_4 deposition, the graphene samples were annealed at ~600 °C for 10-30 minutes to desorb contaminants.

LEEM images and LEED patterns of graphene on Ge are shown in Figure 5.11. On Ge(110) and Ge(111), there are two main orientations of graphene, rotated by 30° from each other. One of the two main orientations is split into multiple orientations. On Ge(111), the lone epitaxial orientation is rotated by 30° from the Ge(111) lattice. Several randomly oriented grains can also be observed. It is important to note that the degree of orientation of the graphene with respect to Ge varies from sample to sample. In fact, some samples were almost completely randomly oriented, and some samples had two well-defined epitaxial orientations at 30° from each other. Moreover, the graphene coverage varies from sample to sample between ~0.1 and ~1. Nonetheless, large graphene patches (at least 15 μm) are identified prior to growth and LEEM imaging is carried out on these patches.

The Ge(100) surface is nano-facetted underneath the graphene. In fact, a hills and valley structure made of {107} facets forms during graphene growth. The {107} LEED spots can be seen in Figure 5.11c. Four graphene diffraction rings are seen with LEED. The rings are centered on the Ge{107} spots, meaning that graphene is conformal to the hills and valley structure of the Ge substrate. Moreover, the diffraction rings indicate that the graphene is polycrystalline.

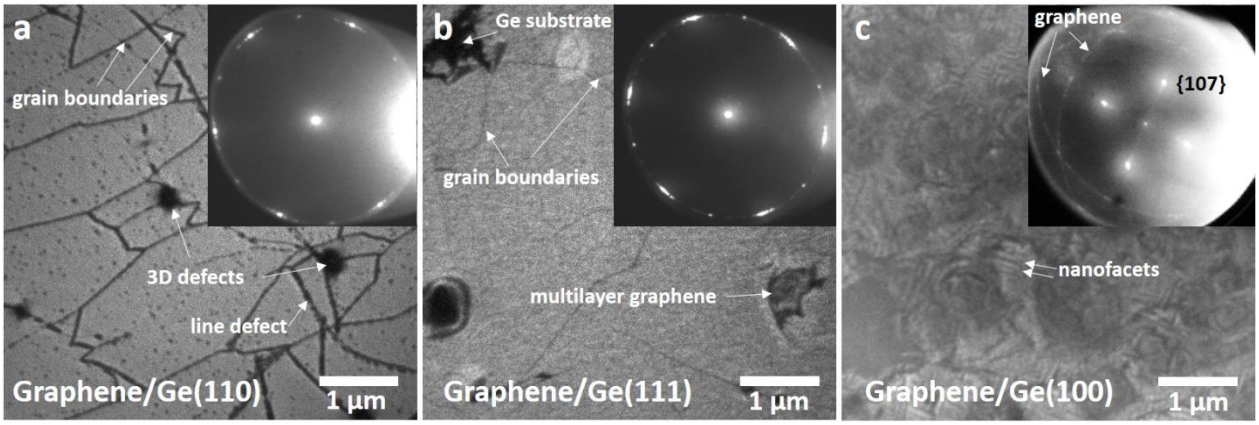

Figure 5.11 Bright-field LEEM images and LEED patterns of: a) graphene/Ge(110), b) graphene/Ge(111) and c) graphene/Ge(100). The LEEM/LEED energies are: a) 2 eV/45 eV, b) 4 eV/ 65 eV and c) 2 eV/50 eV. No contrast aperture is used for the LEEM in (c). Adapted from *Fortin-Deschênes, M. et al., Advanced Materials 2019, 31 (21), 1900569* [37]

The LEEM images reveal various defects of the graphene surfaces. On Ge(110), dark lines forming polygonal shapes correspond to graphene grain boundaries. The graphene grains are elongated with widths of ~1-3 µm and lengths of 3-10 µm. Other line defects can be seen Figure 5.11a. Since these defects cross multiple grains, they are not grain boundaries. They might be wrinkles cause by the thermal expansion mismatch between graphene and Ge, or defects related to the underlying Ge substrate. Blurred dark spots can also be seen on the graphene surface. These blurred spots are 3D defects, which distort the electric field at the surface of the sample due to their large aspect ratio. Other defects can be seen on the graphene/Ge(111) surface (Figure 5.11b). For instance, holes in the graphene surface, which expose the Ge substrate appear as dark patches due to the lower reflectivity of Ge as compared to graphene at this energy. While most of the graphene is one layer thick, some multilayer regions can be seen. We also note that all these defects are present on both the graphene/Ge(110) and graphene/Ge(111) surfaces. On the other hand, imaging the graphene/Ge(100) surface is more challenging due to the nanofacets. In fact, the hills and valleys

form long parallel grooves spaced by ~100 nm and aligned along the [010] and [001] directions. The facets reflect the e-beam at an angle making bright-field imaging of the graphene surface impossible. Dark-field imaging can be done, but only 1/4 of the surface can be imaged at a time due to the equivalent {107} facets.

5.1.2.3.2 2D-Sb growth on graphene/Ge

The LEED patterns of 2D-Sb grown on graphene on the three orientations of Ge are shown in Figure 5.12. Once again, the results on Ge(110) and Ge(111) are similar. A diffraction ring corresponding to multilayer β-2D-Sb is measured on both substrates (Figure 5.12 (a, b)). In fact, accurate measurement of the lattice parameter is possible on graphene/Ge(111) since the Ge(01) LEED spots are visible (Figure 5.12b). Assuming hexagonal/trigonal symmetry, a lattice constant of 4.28 ± 0.02 Å is measured, confirming the grown phase. On graphene/Ge(100), there are four diffraction rings centered on the Ge{107} facets' spots, meaning that the grown β-2D-Sb is rippled and conformal to the hills and valleys nanostructures of graphene and Ge.

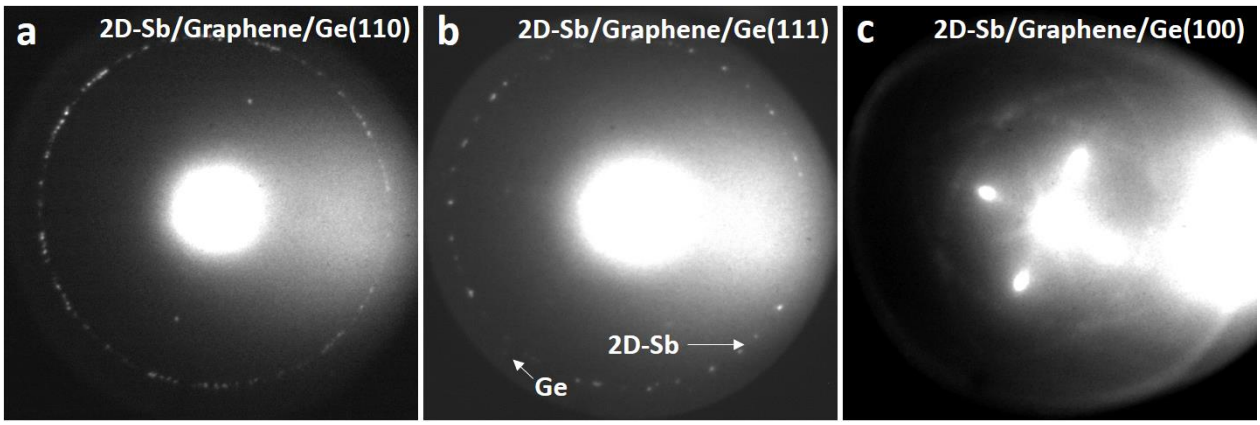

Figure 5.12 LEED pattern of: a) 2D-Sb/graphene/Ge(110) (16 eV), b) 2D-Sb/graphene/Ge(111) (17 eV) and c) 2D-Sb/graphene/Ge(100) (25 eV).

Interestingly, there is no preferential epitaxial orientations with either the underlying Ge substrate or the graphene surface. In fact, the β-2D-Sb grains have their c-axis aligned with the substrate but are randomly rotated in the x-y plane. This support the hypothesis of a weak substrate-layer interaction. In fact, the interaction between the self-passivated graphene and β-2D-Sb surfaces is not strong enough to favor epitaxial orientation of the β-2D-Sb nuclei. In other words, the thermal energy at the ~200 °C growth T is significant, as compared to the fluctuations of the E(θ)

(interaction energy as a function of nuclei epitaxial orientation) relation in the early nucleation stage, when the nuclei are free to rotate on the substrate. The lattice mismatch also contributes to the lack of epitaxial relationship between graphene (a=2.46 Å) and β-2D-Sb (a=4.28 Å). In fact, the large lattice mismatch most likely yields a relatively flat E(θ) distribution. The weak interaction agrees with DFT calculations, which yield a ~150 meV/atom interaction energy along with a freestanding-like electronic structure (APPENDIX A). This is also in good agreement with the fact that 2D-Sb grown on graphene can easily be transferred to other substrates using the scotch tape method (APPENDIX A)

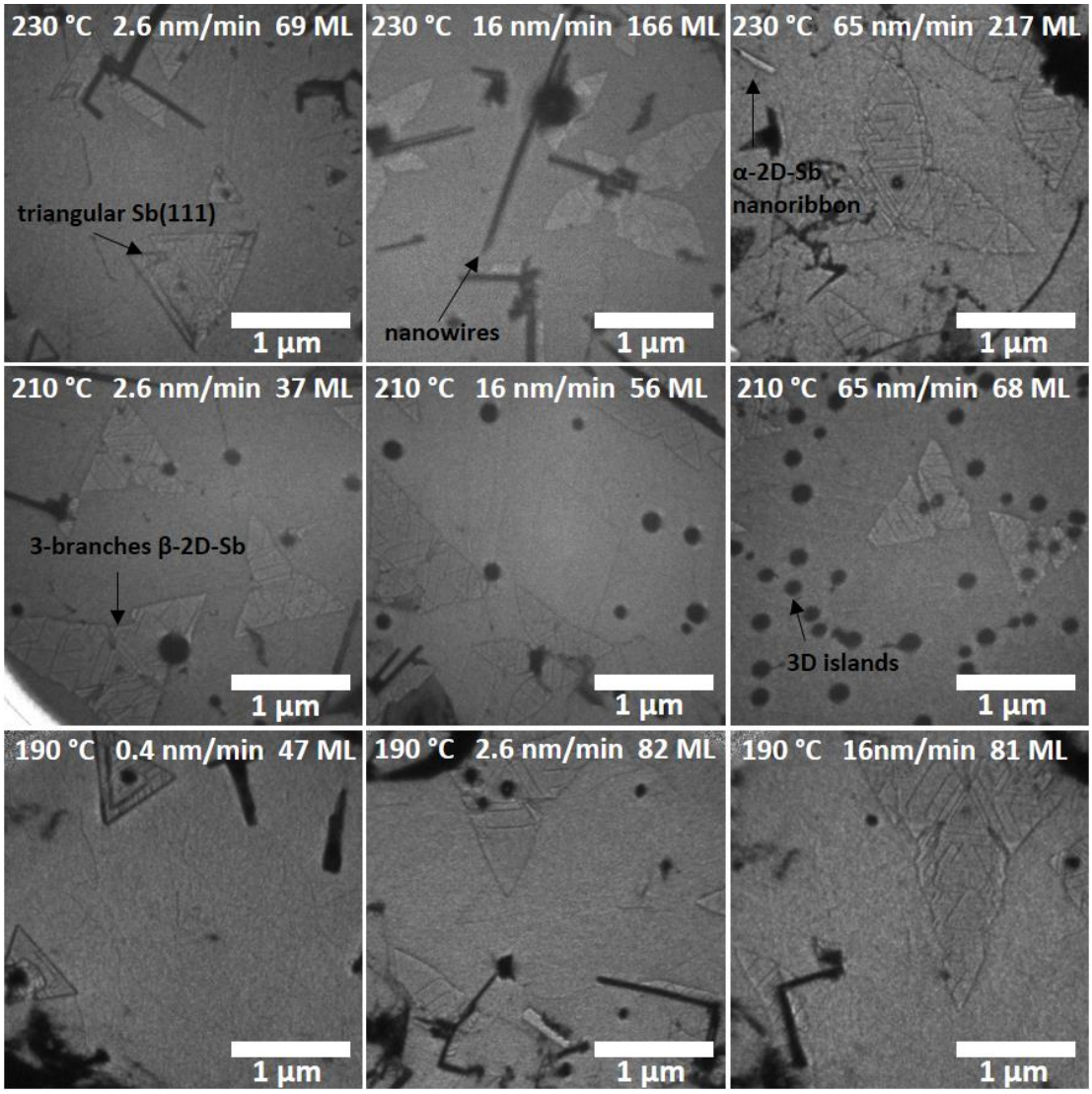

Figure 5.13 Bright-field LEEM images of 2D-Sb grown on graphene/Ge(110) under various experimental conditions. Adapted from *Fortin-Deschênes, M. et al., Advanced Materials 2019, 31 (21), 1900569* [37].

The growth of 2D-Sb on graphene/Ge(110) is studied at substrate T between 170 °C and 245 °C. Similar to Ge(111), low T growth results mostly in dome-shaped 3D islands and the Sb_4 sticking coefficient decreases at high T (not shown). LEEM images of 2D-Sb on graphene/Ge(110) at T between 190-230 °C and F between 0.4-65 nm/min are shown in Figure 5.13. The presented images are at similar growth stages/similar coverages. Five different structures are observed: 3D islands, nanowires, triangular Sb(111) islands, β-2D-Sb flakes with three elongated branches and rectangular α-2D-Sb flakes/nanoribbons. This subsection will focus on β-2D-Sb and Sb(111)

nucleation and growth. α-2D-Sb growth will be addressed in Chapter 6. Every type of structure can be observed in almost every studied growth condition, except for low T growth (<170 °C) and very low deposition rate (0.4 nm/min). However, it is important to note that the graphene surface and defect density varies from sample to sample, which can lead to different proportions of the different structures. For instance, the large proportion of 3D islands in the growth at 210 °C and 65 nm/min is associated to the large defect density. The results presented in this subsection allow to study the growth behavior and dynamics, but not the prevalence of the different structures. Moreover, the defect density affects the nucleation rate and nucleation occurs earlier on highly defective substrates. Therefore, it is not possible to compare the growth times.

Nevertheless, there are clear trends in the growth behavior as a function of growth conditions. At T=190 °C, the low rate growth (0.4 nm/min) results in triangular Sb(111) islands, with lateral dimensions of ~1 μm. Here, the nucleation was achieved at 2.6 nm/min and the deposition rate was then immediately reduced to 0.4 nm/min. In fact, the nucleation rate at 0.4 nm/min is unpractically low for LEEM observations. AFM of typical triangular Sb(111) islands is shown in Figure 5.14a. Interestingly these islands have an atoll-like shape, with well-defined thick bands on the edges and a thinner center part. Increasing the deposition rate to 2.6 nm/min leads to a different growth mode. In fact, β-2D-Sb flakes with three elongated branches can be observed. The flakes are similar to the clover-shaped flakes observed on Ge(111). However, the tips of the flakes' branches are sharp, rather than rounded. Moreover, the flakes are significantly larger and flatter than on Ge(111) (generally in the order of 2-3 μm, with thicknesses of ~5-8 nm (13-21 layers) (Figure 5.14b)). A 3D nuclei can also be seen at the center of the flakes, indicating heterogeneous nucleation, as was observed on Ge(111) at relatively small deposition rates. In fact, under all studied growth conditions, the β-2D-Sb on graphene/Ge have central 3D nuclei. This can be associated with the fast desorption due to the weak interaction of graphene with deposited Sb_4 species. This results in low Sb_4 surface concentration and therefore low homogeneous nucleation rates. In fact, the adsorption energy calculated with DFT (PBE+D2 on bare graphene) is 635 meV/Sb_4. The Sb_4 surface concentration ϕ_{Sb_4} can be estimated by solving:

$$\frac{d\phi_{Sb_4}}{dt} = F - \phi_{Sb_4} f_0 \exp\left(-\frac{E_{ads}}{kT}\right) \tag{5.1}$$

Which has the solution (with $\phi_{Sb_4}(0) = 0$): $\phi_{Sb_4}(t) = \frac{F}{f}(1 - \exp(-ft))$, with $f = f_0 \exp\left(-\frac{E_{ads}}{kT}\right)$. This means that the saturation concentration is $C_{sat} = F/f$ and the time to saturation is in the order of $t_{sat} = 1/f$ (valid when $\phi_{sat} < 1\,BL$). With $f_0 = 10^{11} - 10^{13}\,Hz$, T=190 °C and F=2.6 nm/min, we find $\phi_{sat} = 9.4 \times 10^{-8}$ to 9.4×10^{-6} BL and $t_{sat} = 0.8$ to 80 µsec. This leads to very low homogeneous nucleation rate. As a comparison, the 2.82 eV adsorption energy on bare Ge(111) leads to accumulations well above $\phi_{sat} = 1$ ML for all growth conditions. This is consistent with the fact that no LEEM contrast change is observed during Sb_4 deposition on graphene, as compared to Ge(111).

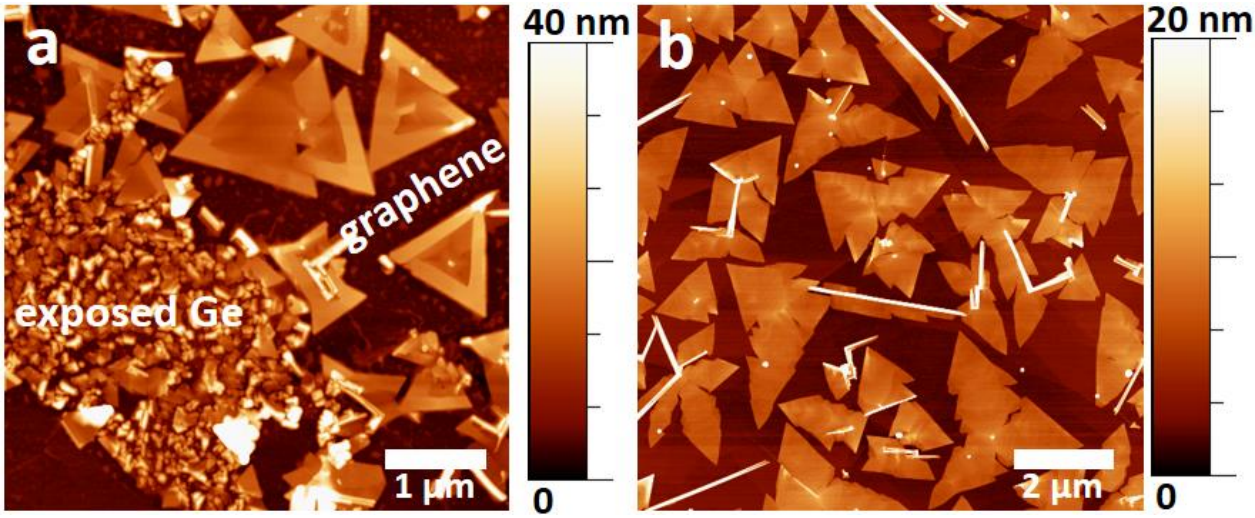

Figure 5.14 AFM images of Sb grown on graphene/Ge(110). a) Triangular atoll-like Sb(111) grown at F=91 nm/min and T=250 °C. b) β-2D-Sb grown at F=91 nm/min and T=210 °C. Adapted from *Fortin-Deschênes, M. et al., Advanced Materials 2019, 31 (21), 1900569* [37].

The growth behavior at higher deposition rate (F=16 nm/min and T=190 °C) is similar. Nonetheless, the shape of the flakes is slightly different. In fact, the angle of the tip of the branches is slightly smaller and the branches are more elongated. This has important implications for the growth mode, as will be discussed in detail below. The effect of the growth T is less pronounced than the deposition rate. In fact, there are no noticeable differences between growth at 190 °C and 210 °C. However, higher deposition rates were studied at 210 °C. We can see that the growth at 65 nm/min yields flakes with different edges orientations. The orientation of the branches is the same, but the tips are chamfered rather than sharp, especially in the early growth stage. This indicates

that the growth becomes more and more out-of-equilibrium as the deposition rate is increased to this range. The growth behavior is still similar at 230 °C, but the triangular Sb(111) islands are present at higher deposition rates (2.6 nm/min). This is due to faster edge diffusion of precursor Sb species due to the larger thermal energy. However, out-of-equilibrium 2D growth is still achievable at higher deposition rates (>16 nm/min).

The results presented in Figure 5.13 and Figure 5.14 show very little variations of the nucleation behavior, but important differences in the growth modes. Low deposition rates and high growth temperatures yield equilibrium Sb(111) islands with atoll-like shapes. Out-of-equilibrium growth conditions (high deposition rates and low temperatures) yield lateral 2D growth of β-2D-Sb. It is therefore useful to study more closely the growth dynamics using real-time LEEM. First, we will look at the lateral growth mechanisms and then we will examine the vertical growth mechanisms.

LEEM snapshots of β-2D-Sb growth dynamics on graphene/Ge(111) (T=242 °C, F=91 nm/min) are shown in Figure 5.15. The growth T is just below the limit of the β-2D-Sb to atoll growth mode transition. For the first 30 sec (deposition of 45 nm or 120 ML), all deposited Sb_4 desorbs and no growth is observed. At 35 sec, nucleation occurs at defects such as holes in the graphene and linear defects. Then, anisotropic growth of flakes with sharp tips (~40° tip angle) and flakes with three branches and central nuclei (such as the one nucleating a 95s) is observed. The growth behavior of these two types of flakes is nonetheless very similar. The flakes initially grow rapidly laterally (~30 nm/sec), but the lateral growth rate decreases as the flakes get closer to each other (~1 μm). As the growth rate decreases, the angle of the tips increases. Due to the decrease in lateral growth rate, there is very little coalescence of the flakes. Moreover, we can expect that there is a transition from a lateral 2D growth mode to a more 3D vertical growth as the flakes get closer to each other. This hypothesis can be confirmed using a Voronoi analysis.

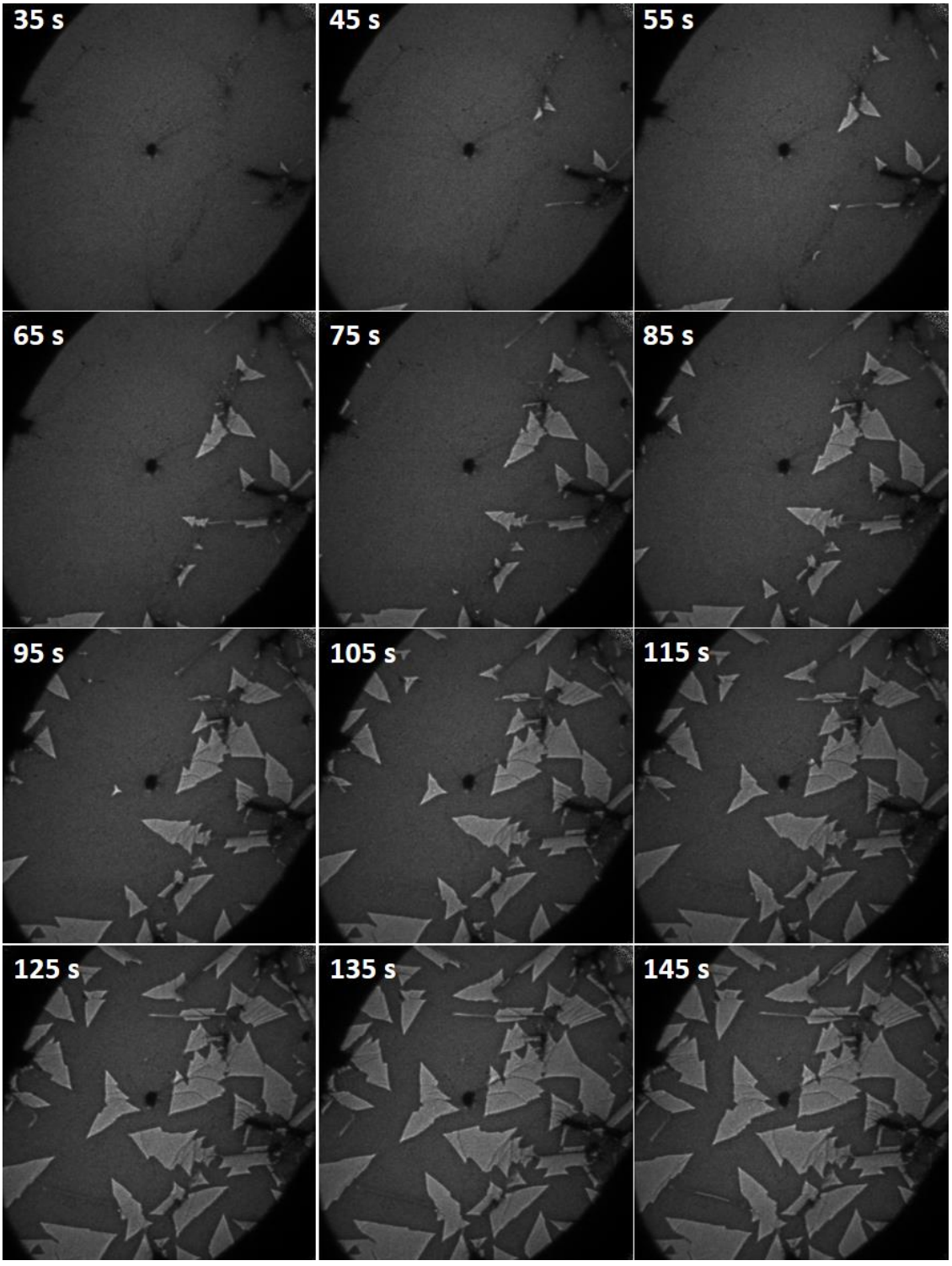

Figure 5.15 Bright-field LEEM (4.3 eV) snapshots of β-2D-Sb growth on graphene/Ge(111) (T=242 °C, F=91nm/min). Images are 7.5×7.5 μm^2. Adapted from *Fortin-Deschênes, M. et al., Advanced Materials 2019, 31 (21), 1900569* [37].

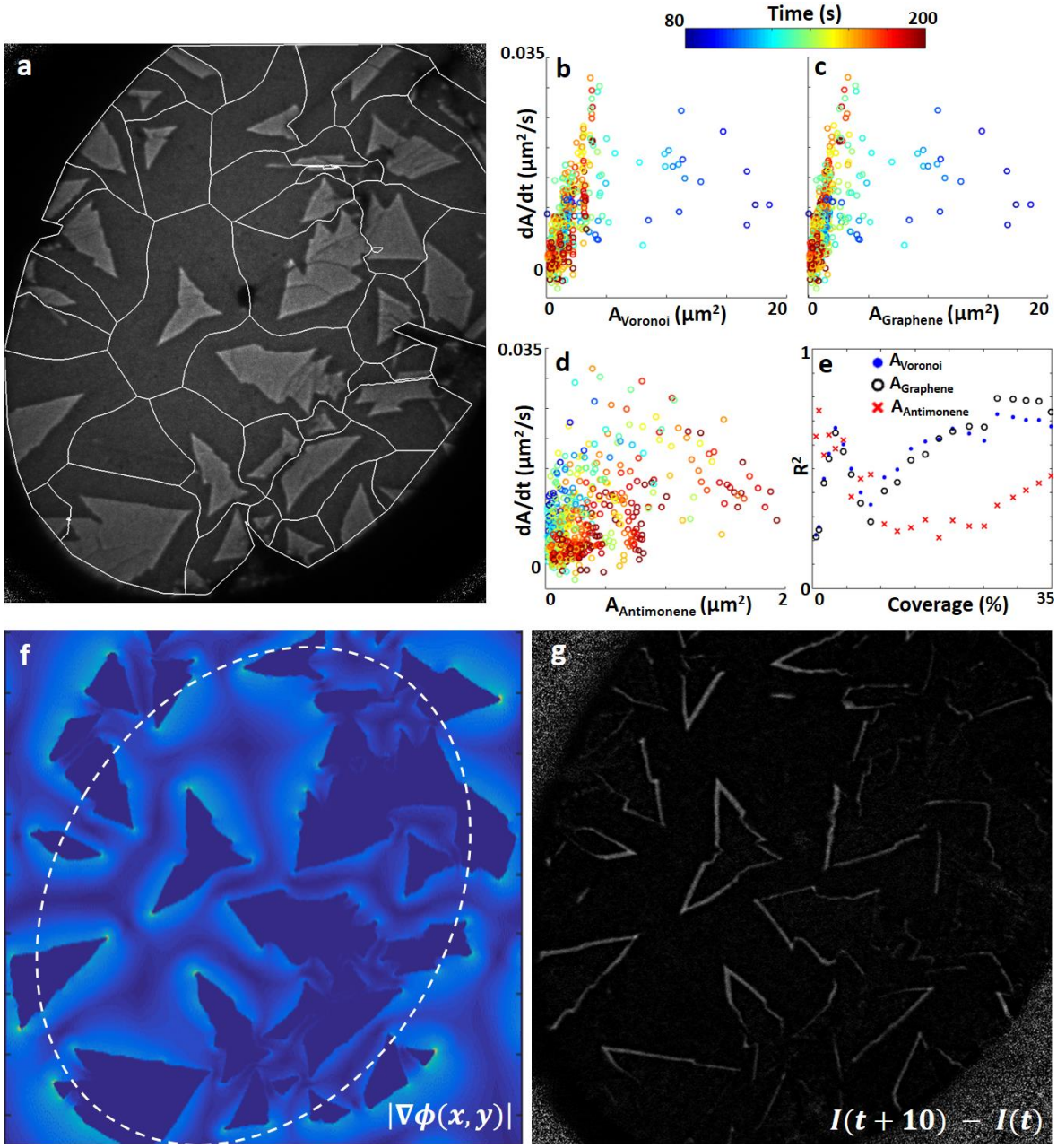

Figure 5.16 a) Voronoi tessellation for the growing Sb flakes and NWs calculated from the LEEM data. (b-d) Lateral growth rate as a function of b) $A_{Voronoi}$, c) $A_{graphene}$, d) $A_{2D\text{-}Sb}$ plotted for all 2D-Sb flakes in the field of view and all frames of the growth video. The color scale indicates the time elapsed since the beginning of Sb_4 deposition. e) Coeff. of determination R^2 as a function of coverage for linear fits of the growth rate (15 s intervals) as a function of $A_{Voronoi}$, $A_{graphene}$ and $A_{2D\text{-}Sb}$. f) Simulated Sb_4 diffusion flux ($\sim|\nabla\phi|$). g) Difference between LEEM frames at 10 sec intervals. *Fortin-Deschênes, M. et al., Advanced Materials 2019, 31 (21), 1900569* [37].

The Voronoi cell associated with a flake is defined as the area containing all points which are closer to this flake than to any other flake. Mulheran and Blackman determined that the growth rate of an island is proportional to its Voronoi cell[249]. In fact, if the deposited Sb_4 stays on the surface, a flake with a larger Voronoi cell has a larger capture zone for diffusing Sb_4 species. The LEEM dynamics allows to accurately measure the lateral growth rate dA/dt [$\mu m^2/s$]. In the case of 2D growth, a linear relationship between dA/dt and the capture zone is expected, whereas a sub-linear relationship should be observed in 3D growth.

An example of calculated Voronoi cells is presented in Figure 5.16a. The Voronoi cells are calculated for the 2D-Sb flakes and NWs at every frame of the growth video. The lateral growth rates are then measured by taking the difference between the flakes' areas in consecutive frames. The growth rates are then plotted as a function of the Voronoi cell area ($A_{Voronoi}$), with the colorscale indicating the elapsed time since the beginning of Sb_4 deposition (Figure 5.16b). Moreover, in order to better understand the origin of the precursor species contributing to lateral growth, the growth rate is also plotted as a function of the uncovered graphene area in the Voronoi cell $A_{graphene}$ (Figure 5.16c), as well as a function of the 2D-Sb flake area $A_{2D\text{-}Sb}$ (Figure 5.16d). In fact, if lateral growth is mainly fed by Sb_4 deposited on the flakes surface, the growth rate will be proportional to $A_{2D\text{-}Sb}$. On the other hand, the relationship between dA/dt and $A_{graphene}$ gives an indication on the contribution of Sb_4 species deposited on the graphene surface. These different relationships are then fitted at different stages of the growth over 15 seconds periods and the determination coefficients R^2 are plotted as a function of coverage Figure 5.16e.

In the early growth stage (blue points in Figure 5.16 (b-d)), there is almost no correlation between growth rate and $A_{Voronoi}$ or $A_{graphene}$. This means that the distance between the 2D-Sb flakes is larger than the Sb_4 diffusion length on graphene. The growth rate saturates at ~0.02 $\mu m^2/s$ for $A_{Voronoi}$>~4 μm^2 indicating a diffusion length of $L_d \approx 1$ µm (radius of Voronoi cell at saturation). This is in good agreement with a 2D-Sb growth fed by Sb_4 diffusing on graphene. In fact, the diffusion length (range of diffusing species before desorption) yields the following relation: $E_{ads} = k_B T ln(L_d^2/a^2) + E_{diff}$, where $a = 1.42$ Å is the diffusion jump length and $E_{diff} = 60\ meV$ is the diffusion activation energy (estimated from the Sb_4 diffusion on graphite[156]). This yields $E_{ads} = 0.847\ eV$, slightly larger than the 0.635 eV calculated by DFT. Note that an additional energy barrier might be present and is not considered in the DFT calculation. In this early growth stage, there is however

a relatively good correlation between dA/dt and $A_{2D\text{-}Sb}$. In fact, the A(t) relationship for individual flakes is superlinear in this early stage (APPENDIX B). This can be explained by either a reaction limited incorporation of by the fact that larger flakes are able to capture more diffusing Sb_4, as will be briefly discussed in Chapter 6. As more flakes nucleate and the Voronoi cell areas decrease, the relationship between dA/dt and $A_{Voronoi}$ and $A_{graphene}$ becomes more and more linear. This indicates that the growth mode is two-dimensional and that the flakes are competing for the diffusing Sb_4 species. At the same time, the correlation between dA/dt and $A_{2D\text{-}Sb}$ becomes weaker and weaker (R^2 down to 0.21), even though $A_{2D\text{-}Sb}/A_{Voronoi}$ increases considerably. The decreasing contribution of Sb_4 species deposited directly on 2D-Sb to lateral growth indicates a shorter diffusion length on 2D-Sb than on graphene. Moreover, it suggests that the Sb_4 deposited on 2D-Sb either desorbs or contributes to vertical growth of the flakes. In the later stages of the growth (coverage >20%), the best correlation is between dA/dt and $A_{graphene}$, even though $A_{graphene}<A_{Voronoi}$. This confirms that the main contribution to lateral growth is Sb_4 deposited directly on the graphene surface. Moreover, the linear relationship suggests that Sb_4 deposited on graphene contributes mostly to lateral growth, rather than vertical growth. Otherwise, a sub-linear relationship should be observed.

The Voronoi analysis presented above suggests that there are two distinct contributions to 2D-Sb growth. First, the Sb_4 deposited on graphene drives the lateral 2D growth. On the other hand, the Sb_4 deposited on 2D-Sb flakes may initially contribute slightly to lateral growth but ends up contributing mostly to vertical growth as the size of the flakes increase. To better understand the validity of this assumption, surface diffusion simulations are carried out. As mentioned above, the small t_{sat} along with fast diffusion of Sb_4 on graphene allows to make a steady-state assumption of the surface diffusion. In fact, the lateral growth rate is several orders of magnitude smaller than the diffusion speed. We therefore test the proposed model by solving the steady-state surface diffusion equation with deposition and desorption:

$$D\nabla^2\phi(x,y) + F - \phi(x,y)f = 0 \tag{5.2}$$

Where D is the diffusion coefficient, ϕ is the surface concentration, F is the deposition rate and f is the desorption rate. $D = D_0 \exp(-E_{diff}/k_BT)$, with $D_0 = f_0 a^2/4$ can be estimated from the Sb_4 diffusion parameters determined by STM on HOPG. Stegemann et *al.*[156] found $E_{diff} = 60\ meV$ and $f_0 = 6 \times 10^{12}$ Hz. The desorption rate can be estimated by $f = 10^{13} \exp(-0.85eV/k_BT)$.

The diffusion equation (5.2) is solved with the finite differences method over the domain defined by the LEEM field of view. Periodic boundary conditions are used and the flakes edges are considered as perfect sinks of diffusing Sb_4 ($\phi_{edges} = 0$). In accordance with the proposed model, the diffusion equation is only solved on the graphene surface ($\phi_{2D-Sb} = 0$ and $F_{2D-Sb} = 0$). The discretized equations are:

$$D\left(\frac{\phi(x_{i-1}, y_j) - 2\phi(x_i, y_j) + \phi(x_{i+1}, y_j)}{dx^2} + \frac{\phi(x_i, y_{j-1}) - 2\phi(x_i, y_j) + \phi(x_i, y_{j+1})}{dy^2}\right) + F(x_i, y_j) - \phi(x_i, y_j)f = 0 \qquad (5.3)$$

with proper forward and backward differences at edges. The equations are solved by matrix inversion using Matlab. The growth rate at the flakes edges can then be computed (not shown here) by calculation the diffusion flux at the edges $J = -D\nabla\phi$. The $|\nabla\phi|$ is proportional to the growth rate and shown in Figure 5.16f. Due to the limited FOV and periodic boundary conditions, only the results far from the edges of the e-beam are meaningful (inside white dashed ellipse). Moreover, simulation of the flakes' growth using the calculated $|\nabla\phi|$ done here. In fact, the discretization of the flakes edges extracted from the LEEM data is not precise enough and leads to unphysical behavior at artificial kinks due to the pixelization. Nonetheless, the $|\nabla\phi|$ allows for a qualitative interpretation of the growth.

While very simple, this model captures most of the important growth features. Moreover, discrepancies between the simulated and observed behavior provides insight into the growth mechanisms not captured by the model. The calculated $|\nabla\phi|$ can be compared to the growth rate measured by subtracting consecutive frames (Figure 5.16g). The diffusion simulation confirms the conclusions of the Voronoi analysis. In fact, lateral 2D-Sb growth appears to be dominated by surface diffusion on graphene. The enhancement of the growth rate at the tips of the flakes, which leads to the elongated branches and rapid lateral growth is well captured by the simulation. This enhancement is also responsible for the growth of the side branches (Christmas tree like features). There is a significant decrease of the growth rate in the regions where the flakes are close to each other (Figure 5.16g). This is associated to the smaller capture zone and is well reproduced by the simulation. The agreement between the LEEM data and the diffusion simulation confirms the validity of the various assumptions (to a certain extent). For instance, the flakes edges behave as good Sb_4 sinks. Otherwise, the shielding of the diffusion flux by flakes' edges would not be that

significant. Moreover, edge diffusion is limited in these growth conditions. In fact, edges which are shielded by other flakes or edges have limited growth rates.

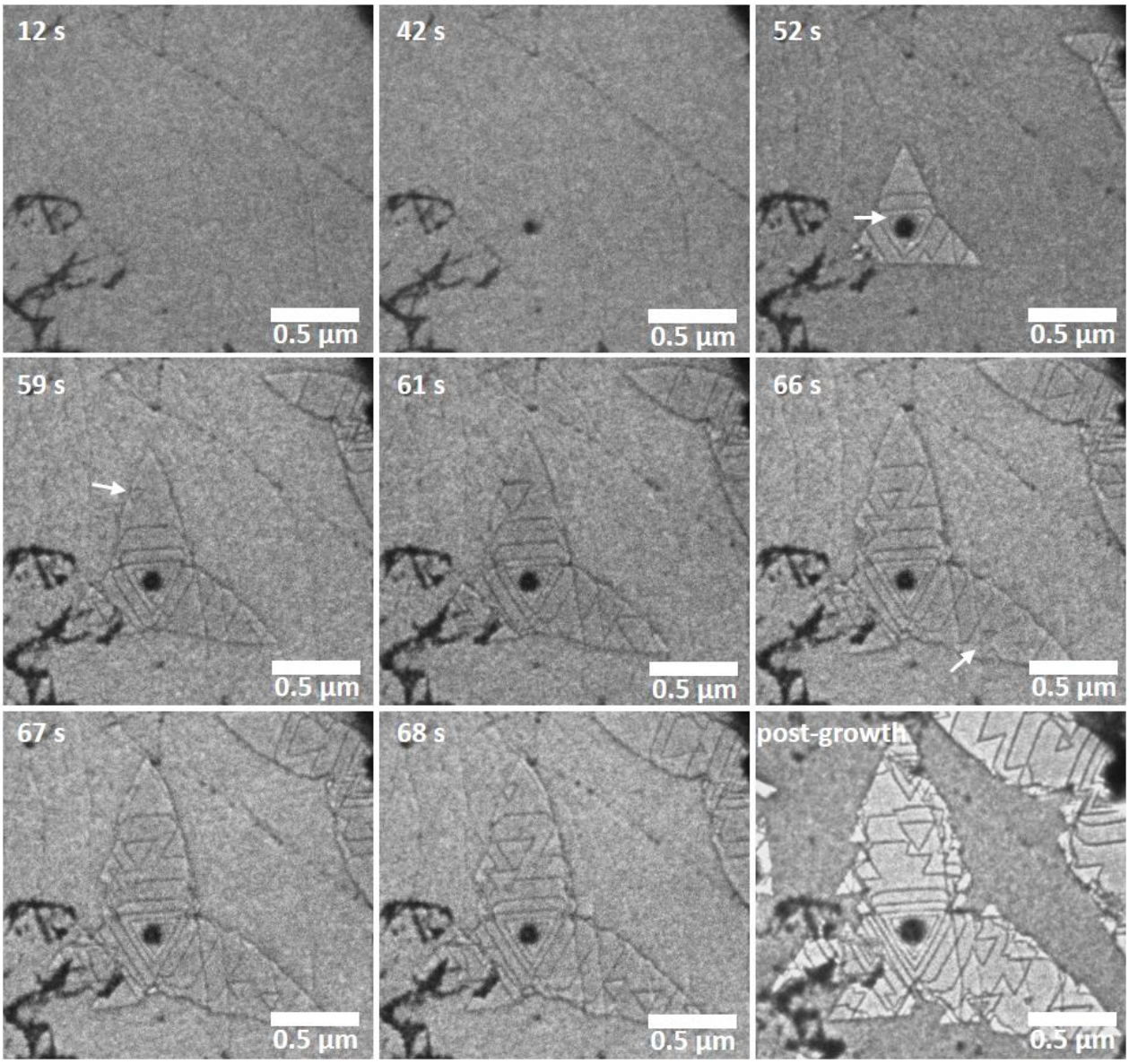

Figure 5.17 Bright-field LEEM (1.8 eV) of β-2D-Sb growth dynamics. F=65 nm/min and T=230 °C. The different types of multilayer nucleation are identified by white arrows. Adapted from *Fortin-Deschênes, M. et al., Advanced Materials 2019, 31 (21), 1900569* [37].

Now that we have a better understanding of the lateral growth mechanisms, it is instructive to look at the vertical growth mechanisms. This can be achieved by real-time LEEM observations of the growth using imaging conditions that provide good contrast at atomic steps. Slightly de-focused

bright-field LEEM at ~2 eV is found to be optimal to image the atomic steps. The two main types of vertical growth are analysed: 1) multilayer growth on β-2D-Sb flakes with elongated branches, typical of high deposition rate and low T; 2) multilayer growth leading to the formation of atoll-like Sb(111) islands at low deposition rate and high T (see Figure 5.14).

The high deposition rate multilayer growth mechanisms are identified from the LEEM data oFigure 5.17. Nucleation of the 3D seed occurs after 34 s of Sb_4 deposition. No 2D growth is seen for the first 8 s (see image at 42s). Then, lateral 2D growth of the three branches begins. As the branches grow outward, three main types of multilayer nucleation occur (indicated by white arrows in Figure 5.17). The dark lines seen in LEEM are single atomic steps. In fact, coalescence of steps growing in opposite directions always leads to an atomically flat surface (see 61s and 66s images for instance). Moreover, the monolayer step height is corroborated by AFM measurements. The first multilayer nucleation mechanism is steps originating from the central 3D nuclei (indicated by white arrow at 52 s). At first, it appears as several multilayers nucleate on the central 3D nucleus and then grow outwards forming concentric triangular terraces. Closer inspection of their growth dynamics however reveals another mechanism (Figure 5.17 and Figure 5.18). In fact, the growth of the triangular terraces initially accelerates as the steps get further away from the center, leading to larger and larger distances between steps. This process occurs in a regular fashion for successive steps. This suggests that rather than nucleating on the 3D nucleus, the multilayer terraces are already present at the start of the 2D lateral growth. This means that the nucleus is in fact a Sb(111) pyramidal island. The growth rate of the multilayer steps is initially low due to the limited Sb_4 reservoir (considering the small proportion of Sb_4 species diffusing from the graphene up to the 2D-Sb surface). However, when the 2D-Sb flake expands laterally and the Sb_4 reservoir becomes larger, the multilayer lateral growth rate increases. The bottom terraces are the first to grow since they have a larger Sb_4 reservoir. As the distance between the steps increases, more Sb_4 becomes available for the growth of the upper terraces.

This hypothesis is confirmed by a simple model of the growth dynamics (Figure 5.18). Two different models are tested. For simplicity and generality, the exact geometry of the flake is not taken into account and circular terraces are modelled. In the first model, the growth rate the terrace n is proportional to the area of the bottom terrace ($\frac{dA_n}{dt} = \alpha A_{n-1}$). To account for Sb_4 desorption

from 2D-Sb, an upper limit of $\alpha A_{max} = \alpha\pi((r_n + L_d)^2 - r_n^2)$ is imposed on the growth rate. This corresponds to the surface of a ring with an inner radius r_n (radius of terrace n) and outer radius $r_n + L_d$, where L_d is the diffusion length of Sb_4 on 2D-Sb. For the simulation, the initial conditions are a pyramidal structure with steps spaced by 2 nm and a height of >20 layers (the exact height has no influence the growth rate of the lower layers in this model). The equations are numerically solved and the experimental r_n are measured and fitted using α and L_d as parameters. The data (dots) and fit (solid lines) for $\alpha = 0.091\ s^{-1}$ and $L_d = 193\ nm$ are shown in Figure 5.18b. The second model assumes attachment of Sb_4 from upper and lower terraces to atomic steps. The rate is given by $\frac{dA_n}{dt} = \frac{\beta\pi}{4}((r_{n-1} + r_n)^2 - (r_n + r_{n+1})^2)$, with upper limits corresponding to surfaces of rings extending to $r_n \pm L_d$. The data (dots) and fit (solid lines) for $\beta = 0.134\ s^{-1}$ and $L_d = 104\ nm$ are shown in Figure 5.18c.

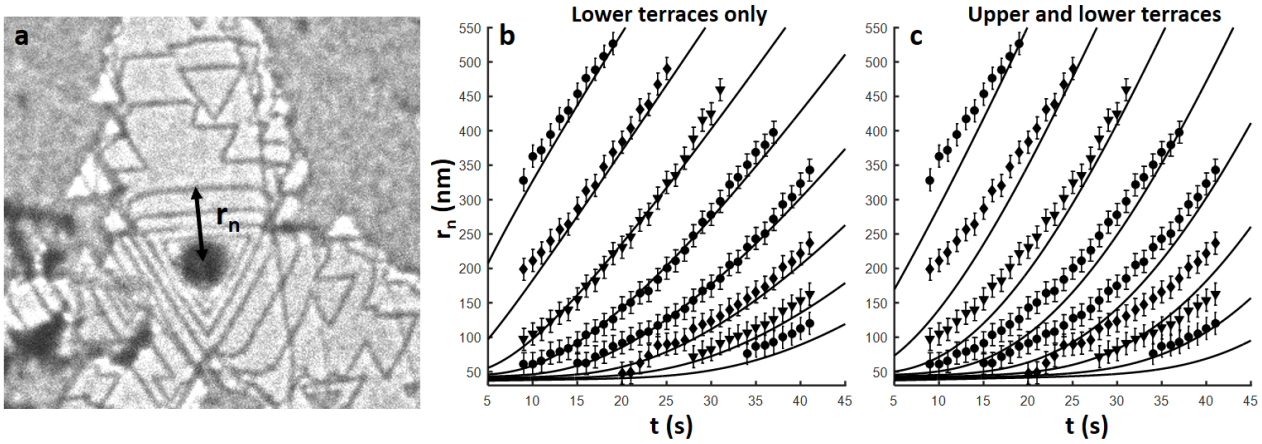

Figure 5.18 a) Bright-field LEEM (1.9 eV) of a clover-shaped β-2D-Sb flake with central 3D nucleus grown on graphene/Ge(110) (T=230 °C, F=66 nm/min). r_n indicates the position of the n^{th} observed multilayer step, with respect to the center of the nucleus. b-c) Experimental (black dots) and fitted (solid lines) $r_n(t)$ for the multilayer terraces of the flake in (a) considering attachment from lower terraces (b) and upper and lower terraces (c). Details of models in the text.

The striking agreement between the fit and experimental data confirms the multilayer growth mechanism. In fact, only two parameters (L_d and α (or β)) are used to fit the dynamics of 8 growing terraces. Note here that L_d and α were fitted by minimization of the weighted root mean square error (RMSE) (weighted inversely to the number of data point per layer). Moreover, the RMSE weight of the first layer is set to zero since the area of its lower terrace is much smaller than what

is considered in the model, due to the limited size of the flake in the early growth stage. The first model (attachment from lower terraces) better fits the data. The growth dynamics of the first 6 steps very well reproduced. However, the 7^{th} and 8^{th} steps growths occur a few seconds earlier than for the fit. Still, their growth is relatively well reproduced. There is an initial accelerated growth of the multilayer steps followed by a saturation and linear growth. The layers accelerate successively, giving the illusion that they nucleate on the central 3D pyramid. The second model reproduces the general growth behavior but not as well as the first model. This suggest that there is a non negligible energy barrier for Sb_4 to go down atomic steps. The data supports the hypothesis that atomic steps capture most of the diffusing Sb_4 molecules and that attachment occurs mostly from lower terraces. Nonetheless, some diffusion must occur at atomic steps. In fact, there is usually a multilayer step at the edges of the flake, which indicates that the Sb_4 flux coming from the graphene is distributed on these few atomic steps. We note however that the crystallographic orientation of the steps at the edges of the flake and on the surface of the flake are different and therefore are expected to interact differently with the diffusing Sb_4 molecules.

The assumption that the 3D nuclei is a Sb(111) pyramidal island is supported by LEEM and AFM data. In fact, a triangular flat surface aligned with the 2D-Sb lattice can be seen in the post-growth image (Figure 5.17 and clearer in Appendix C). The crystalline orientation of the three branches is inherited from the 3D nuclei, as evidenced by the alignment of the growing steps with the triangular structure. Nonetheless, the presence of the Sb(111) nucleus brings another question: if the nucleus is Sb(111), then why doesn't lateral 2D growth occur immediately after nucleation? In fact, there is a delay between the 3D nucleation and the 2D growth (8 seconds for the flake in Figure 5.17). The logical explanation is that the nucleus is initially not Sb(111) and later goes through a phase transition or a crystallographic orientation transition. Immediately after the transition, lateral 2D growth can begin from the multilayer edges. Appendix C provides strong evidence for this mechanism. In fact, the LEEM data shows several 3D nuclei and some 2D-Sb flakes. As soon as the 2D flakes coalesce with the 3D structures, 2D flakes nucleate from the 3D islands and flat triangular surfaces form on the nuclei. The crystallographic orientation of the new 2D flakes is inherited from the first 2D flakes. The 3D islands are therefore metastable and transition to the equilibrium phase. The 3D islands are potentially amorphous Sb_4 aggregates. In fact, the main stable orientations of A7 Sb are Sb(111) and Sb(110). Sb(111) forms either β-2D-Sb flakes or

Sb(111) triangular islands, whereas Sb(110) forms NWs. As will be discussed in Chapter 6, A17 Sb (α-2D-Sb) grows in rectangular flakes, which transition to the A7 Sb phase at a critical thickness. We also note that the phase transition from 3D to 2D occurs much more rapidly at higher T. For instance, growth at 170 °C and 2.6 nm/min leads to amorphous 3D nuclei which do not transition even after >450 seconds. Increasing the substrate T to 215 °C triggers the phase transition and 2D growth mode.

The two other types of multilayer growth occur directly on the branches of the flake by homogeneous nucleation (see 59s and 66s in Figure 5.17). Triangular multilayer terraces nucleate either on the branches (66s) or on the edges of the flake (59s). The triangles all have the same orientation and their edges are along one of the two non-equivalent zigzag directions of β-2D-Sb, as will be discussed below. The rate of homogeneous nucleation is expectedly larger on wider terraces with low step density, where the Sb_4 concentration is higher. We note that the homogeneous nucleation rate on the 2D-Sb surface is orders of magnitude larger than on the graphene surface. In fact, homogeneous nucleation on graphene was never observed. Interestingly, the multilayer nucleation on the terraces seem to be a first order reaction. In fact, increasing the deposition rate by 25 (from 2.6 nm/min to 64 nm/min) at T=210 °C led to an increase in the multilayer nucleation rate per unit area by a factor 22 (measured on similar islands). Since ϕ_{sat} is proportional to F and that the islands were similar, we can assume that the surface concentration also increased by ~25.

Reducing the deposition rate also leads to a growth mode transition to atoll-like growth (Figure 5.19). AFM of a typical triangular atoll-like Sb(111) island is shown in Figure 5.19a. The term *atoll* comes from coral atolls, which are ring-shaped coral reefs with empty center regions. The atoll-like Sb(111) islands have thin central regions (~5-20 nm thick) and well-defined thicker bands (~10-100 nm) on the edges. The atoll-like structures grow at low depositions rates and high T, as well as at lower T and higher rates during the late stages of the growth, as the β-2D-Sb get close to each other and their lateral growth rate decreases.

To better understand how these atoll-like triangular islands form, we need to look at the crystallography of the growing β-2D-Sb. As mentioned earlier, the edges of the multilayer terraces are always oriented along the same crystallographic direction (unless the diffusing flux is highly

inhomogeneous along the step). By comparing the LEEM image with its corresponding LEED pattern, it is possible to determine the crystallographic orientations (Figure 5.19b). The β-2D-Sb flake associated with the LEED pattern circled in blue (Figure 5.19b) is identified using dark-field LEEM. The LEEM and LEED modes are rotationally aligned within 3° and therefore the real-space lattice vectors can be directly determined from the reciprocal lattice. The results show that the growing β-2D-Sb multilayer steps are oriented along the zigzag directions. Nonetheless, since the β-2D-Sb has 3-fold symmetry, there are two types of zigzag edges: Z1 and Z2. For the Z1 edges, the atoms at the front of the growing edge are on the bottom of the buckled β-2D-Sb bilayer. For the Z2 edges, they are on the top. Without modelling the I-V LEED, it is not possible to distinguish between the two possible orientations. On the other hand, atomic resolution STM (Figure 5.19c) confirms that the edges are in fact oriented along the Z1 direction.

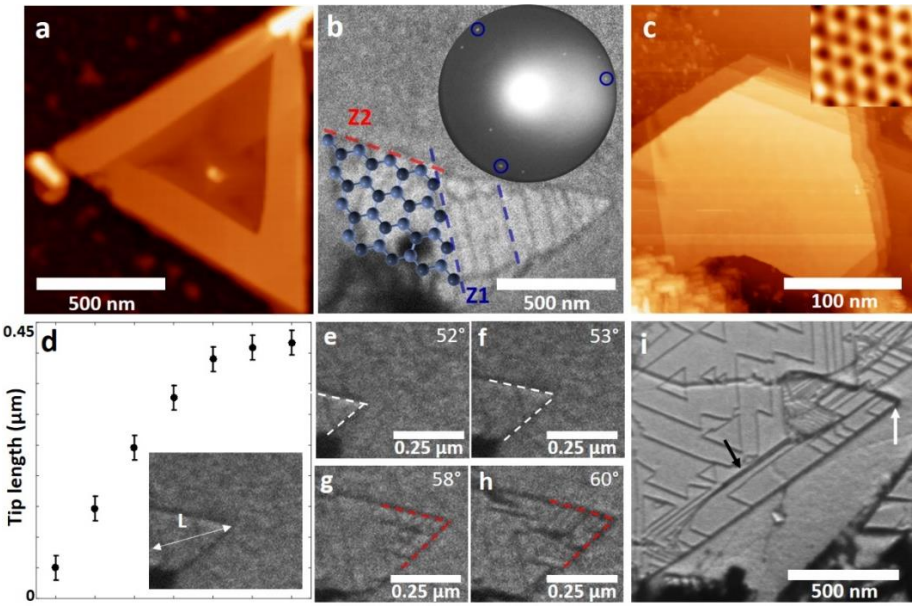

Figure 5.19 a) AFM image of atoll-like Sb island grown on graphene. C) LEEM image (2 eV) and corresponding LEED pattern (16 eV) of β-2D-Sb on graphene. The LEED spots of the 2D-Sb flake are circled in blue and the crystal structure is overlaid on the flake. Darker atoms are on the bottom of the β-2D-Sb bilayer and lighter atoms on top. c) STM of β-2D-Sb on Ge. Inset: atomic resolution STM showing that the steps are along the Z1 orientation. d) Time evolution of the length of a β-2D-Sb branch grown at T=190 °C and F=2.6 nm/min. (e-h) Corresponding LEEM images and tip angle evolution during growth. i) Post-growth LEEM during the atoll island formation. Adapted from *Fortin-Deschênes, M. et al., Advanced Materials 2019, 31 (21), 1900569*[37].

The formation of the atoll islands can be seen in Figure 5.19 (d-h). The time evolution of the length of a branch of a β-2D-Sb flake is plotted in Figure 5.19d. During the 2D growth phase, the length increases almost linearly. At this stage, the flakes' edges are oriented in between the armchair and Z2 directions and form a tip angle of <60°. During lateral growth, the tip angle slowly increases due to edge diffusion of precursor species. As detailed in the previous section, the initial 2D growth stage and the rapid growth of branches with narrow tips is mostly determined by surface diffusion of Sb_4 on graphene. However, the ratio of edge diffusion to lateral growth should be roughly inversely proportional to F and proportional to e^{-E_{edge}/k_BT}, where E_{edge} is the edge diffusion activation energy. Increasing T and decreasing F therefore allow the edges to reach equilibrium shapes more rapidly. When the tip angle reaches 60° and its edges become oriented with the Z2 directions, the lateral growth rate decreases by a factor of ~5-10. At this point, there is a dramatic increase of the multilayer nucleation rate at the tip of the flake and on the Z2 edges to a smaller extent (Figure 5.19 (g, h)). The increased multilayer nucleation rate is at the origin of the thick bands which form on the edges. In fact, as the steps grow inward, step bunches begin to form. High-resolution LEEM allows to better visualize the step bunch formation (Figure 5.19i). The white arrow indicates the tip of the flake where the multilayer nucleation rate is the highest and the black arrow indicate a forming step bunch. Many factors can contribute to the step bunch formation. Contrarily to the initial growth of clover-shaped flakes where the steps accelerate and get further away from each other, here steps slow down as they grow inward. This may be caused by the competition with the growing terraces inside the flake, along with the decrease of the bottom terrace size as steps grow inwards. Nonetheless, the step bunching process cannot be fully explained without some Sb_4 diffusion across step edges. We can also speculate as for why multilayer nucleation occurs at an higher rate on the Z2 edges. The obvious answer is that Z2 edges are more efficient than Z1 edges at capturing more Sb_4 molecules and catalysing their decomposition, due to the proximity of the top Sb atom with a dangling bond. For the Z1 edge, the dangling bond is on the bottom of the bilayer, which means that nucleation will occur on the lower terrace without formation of additional layers. It is also possible that the energy barrier for Sb_4 molecules to go down atomic steps is larger for the Z2 edges. This would lead to an increased Sb_4 concentration on the top surface, and therefore to and increased nucleation rate.

5.2 Growth of β-2D-As_xSb_{1-x}

There are several possible methods to finely tune the physical properties of group VA 2D materials. For instance, the DFT calculations in Chapter 4 show that substrate passivation may allow to tune the doping and band gap of epitaxial single layer group VA 2D materials on semiconductors. Since group VA elements are generally miscible in each other, controlling the composition of group VA binary alloys is potentially a powerful paradigm to fine tune their electronic, topological and optical properties. For instance, the Sb content was found be an important factor controlling the topological surface states in Bi_xSb_{1-x} ultrathin films[250, 251]. On the other hand, if the challenges preventing the large-scale growth of 2D group VA β phase monolayers can be overcome, the composition will allow to tune the semiconducting properties such as the band gap and carrier mobility. For the direct band gap 2D group VA α phase multilayers, alloying can provide a pathway to tune their optical properties to design photonic devices operating in the visible to mid-infrared.

With the growth of β-2D-Sb on Ge(111) and graphene being well understood, the addition of As is relatively straightforward. This section explores the possibility to grow 2D-As_xSb_{1-x} by MBE on semiconductor (Ge and Si) and graphene substrates. The Si(111) substrate is considered for β-2D-As_xSb_{1-x} growth since it has the same surface symmetry as Ge(111), but a smaller lattice constant which should be lattice matched to β-2D-$As_{0.5}Sb_{0.5}$ monolayers. The results presented in this section are published in:

Fortin-Deschênes, M.; Waller, O.; An, Q.; Lagos, M. J.; Botton, G. A.; Guo, H.; Moutanabbir, O. "2D Antimony-Arsenic Alloys." *Small*, 16, (3) (2020): 1906540.[38]

5.2.1 Methodology

The methodology used for the MBE growth of β-2D-As_xSb_{1-x} is similar to the one used for β-2D-Sb growth. The growth was done in the LEEM system by co-deposition of As_4 and Sb_4 from 99.999% As powder and 99.9999% Sb crystals using Knudsen cells. To understand the incorporation of As in the β-2D-Sb lattice, the As to Sb deposition rate ratio F_{As}/F_{Sb} was varied between 0 and 6. Growth was carried out in the 140-285 °C range, but the effect of growth T on As incorporation was not studied systematically. Like β-2D-Sb, temperatures above 180 °C were found to be required for the formation of the β-2D phase (on Ge(111)). Ge(111) substrates were

cleaned in acetone, isopropanol and then HCl (10%) for 10 minutes. The Si(111) was cleaned in a Piranha solution (3:1 96% H_2SO_4 to 30% H_2O_2) for 10 minutes followed by a HF dip (1%) for 1 minute and then rinsed in deionized water. The graphene substrates were grown by CVD on 25 μm thick Cu foil at 1000 °C under H_2 (2 sccm) and CH_4 (35 sccm). The graphene was then transferred to a 300 nm SiO_2/Si substrate by a wet transfer method. The graphene was coated with poly(methyl methacrylate) (PMMA) and the Cu is dissolved in ammonium persulfate. The graphene/PMMA was then transferred on SiO_2/Si and the PMMA was dissolved in acetone. Prior to growth, the substrates were annealed in UHV (800°C and 30 minutes for Ge(111), few cycles of flash annealing at >1200 °C for Si(111) and 30 minutes at 600 °C for graphene).

To determine the growth morphology, the samples were characterized by LEEM and AFM. However, *in situ* LEEM during growth is more challenging than for β-2D-Sb due to the high As pressure (~1 E-7 mbar), which interferes with imaging. Post-growth LEED, XPS and Raman measurements were carried out to determine the crystal structure and assess the incorporation of As in the β-2D-Sb lattice.

5.2.2 β-2D-As_xSb_{1-x} characterization

LEED, XPS and AFM of β-2D-As_xSb_{1-x} on the three growth substrates can be seen in Figure 5.20. On Ge, a LEED pattern with 6-fold symmetry aligned with the Ge(111) lattice is observed (Figure 5.20a). The LEED pattern is reminiscent of β-2D-Sb on Ge(111), but has a shorter lattice constant of 4.21 ± 0.01 Å. The symmetry and lattice constant confirm the presence of the β-2D-As_xSb_{1-x}. The shorter lattice constant is indicative of the incorporation of As in the lattice as will be discussed below. The LEED 6-fold symmetry indicates that there are two main crystal orientations aligned with Ge and rotated by 180° from each other. On the other hand, a diffraction ring is observed on Si(111) (Figure 5.20b). Nonetheless, there is an angular intensity modulation with 6-fold symmetry and maxima aligned with the Si(111) spots. We note that some samples also display LEED patterns with well-defined epitaxial orientations. The lattice constant is 4.25 ± 0.01 Å suggesting the presence of β-2D-As_xSb_{1-x}. On graphene/SiO_2, a diffraction ring is also observed. It is however not possible to precisely determine the lattice parameter due to the large lattice mismatch between graphene and β-2D-As_xSb_{1-x}, which prevents accurate reciprocal space calibration. The presence of a diffraction ring is expected on graphene substrates due to the weak substrate-layer interactions.

On the other hand, the weak alignment of the β-2D-As_xSb_{1-x} and Si(111) lattice, as compared to Ge(111) may originate from the larger lattice mismatch. In fact, the larger strain decreases the energetic gain of aligning the two lattices.

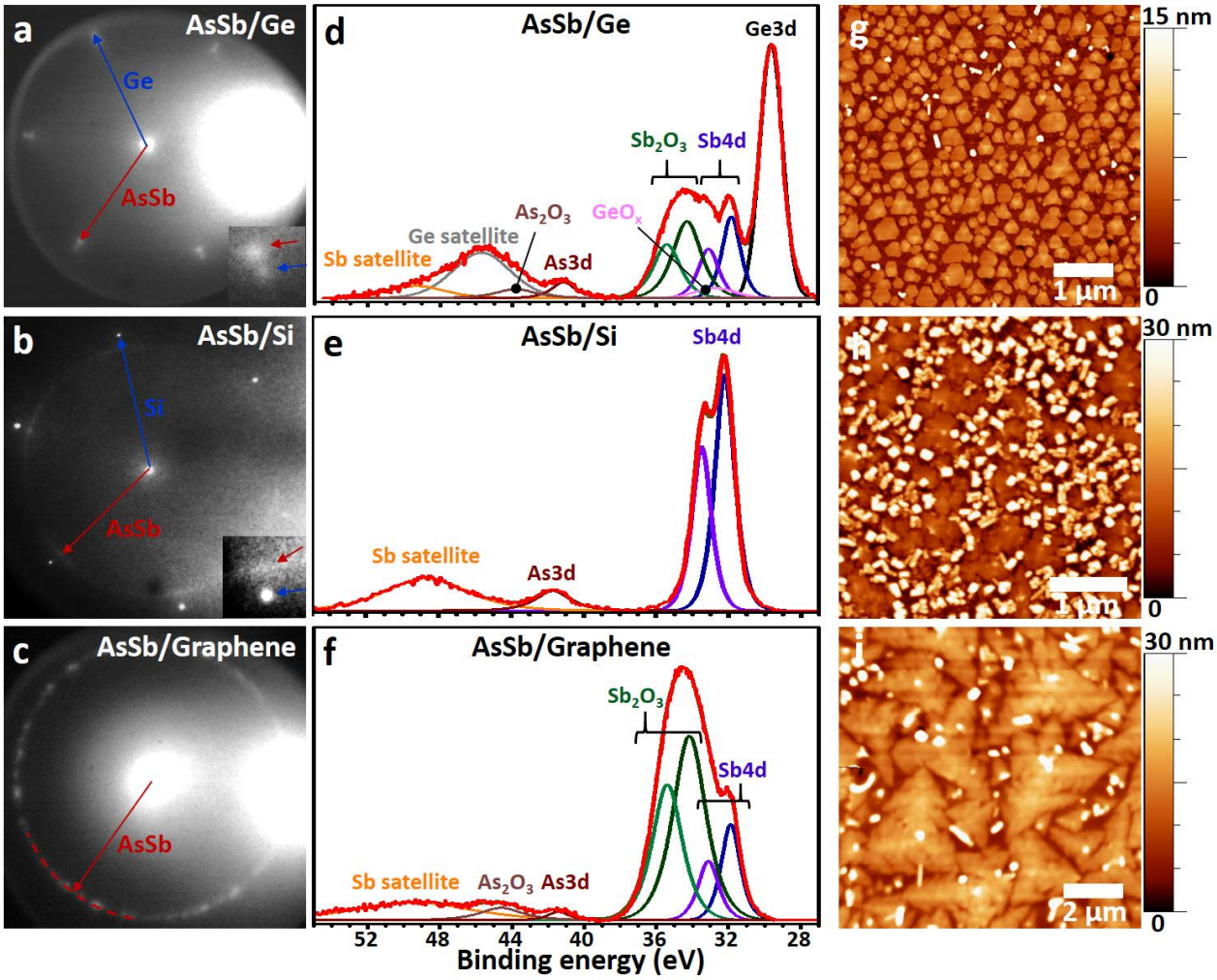

Figure 5.20 (a-c) LEED patterns of β-2D-As_xSb_{1-x} grown on a) Ge(111) (25 eV), b) Si(111) (35 eV) and c) graphene/SiO_2 (20 eV). (d-f) XPS spectra of As_xSb_{1-x} on d) Ge(111), e) Si(111) and f) graphene/SiO_2. AFM images of β-2D-As_xSb_{1-x} on g) Ge(111), h) Si(111) and i) graphene/SiO_2. (a, d) T=180 °C, F_{As}/F_{Sb}=6.6. (b, e) T=220 °C, F_{As}/F_{Sb}=1.5. (c, f) T=220 °C, F_{As}/F_{Sb}=1.5. Adapted from *Fortin-Deschênes et al., Small 2020, 16 (3): 1906540.*[38]

XPS measurements confirm the incorporation of As (Figure 5.20 (d-f)). Note that the XPS spectra of β-2D-As_xSb_{1-x} on Ge(111) and on graphene was measured after exposition to air, but that the spectrum of β-2D-As_xSb_{1-x} on Si(111) was acquired *in situ*. Sb 4d and As 3d peaks are seen on all

substrates and additional Sb_2O_3 and As_2O_3 peaks are seen for the samples exposed to air. The *ex situ* spectra, especially on Ge(111) are difficult to analyse quantitatively due to the presence of several overlapping peaks including Sb and Ge satellite peaks with As 3d, As_2O_3 and potentially As_2O_5. Nonetheless, the results provide a qualitative picture of the chemical composition. A rough estimate of the As composition can be determined for the samples presented in Figure 5.20 (a-f): 14% on Ge(111), 12% on Si(111) and 8% on graphene.

Since XPS is not spatially resolved, the presence of As 3d and Sb 4d peaks do not necessarily imply the presence of a β-2D-As_xSb_{1-x} alloy. There could be chemical segregation and the detected As or Sb could be adsorbed on the substrate or unequally distributed in different phases. For instance, the composition of 2D and 3D islands might differ. The same thing can be said about the Sb_2O_3 and As_2O_3. In fact, the oxidation rate of the 2D and 3D islands is different, as will be discussed in Chapter 6. On the other hand, LEED can directly probe the β-2D phase. As confirmed by LEED, STM and STEM, the β-2D phase is free to relax on the Ge(111) surface. Assuming that the same is true with β-2D-As_xSb_{1-x} on Ge(111) and Si(111), we can determine the composition of the β-2D flakes. The LEED determined lattice constant of pure multilayer β-2D-Sb on Ge(111) is 4.285 Å. The lattice constants of bulk A7 As and Sb are 3.760 Å and 4.307 Å, respectively. Assuming the same 2D to bulk lattice constant ratio for As and Sb and using Vegard's law, the As content is given by: $3.741x + (1 - x)4.285 = a_{\beta-2D-As_xSb_{1-x}}$, where x is the As atomic concentration. This yields As contents of 14% on Ge(111) and 6% on Si(111) for the samples in Figure 5.20. There is indeed a discrepancy between the XPS and LEED determined concentrations. Moreover, the LEED determined lattice constants indicate that a substitutional alloy is formed. In fact, interstitial As in the β-2D-Sb lattice would lead to an increase of the lattice constant, whereas substitutional As leads to a decrease of the lattice constant due to the smaller atomic radius.

The morphology of the grown β-2D-As_xSb_{1-x} is characterized by AFM (Figure 5.20 (g-i)). On Ge(111) β-2D-As_xSb_{1-x} primarily forms 2D flakes (Figure 5.20g). Clover-shaped flakes and hexagonal-like flat flakes are observed. Expectedly, the dimensions of the flakes vary with the growth conditions. Nonetheless, for the sample in Figure 5.20g, the diameter of the flakes is ~200 nm and their thickness is ~5 nm (13 layers). There are also some 3D rectangular islands, which are most likely As_xSb_{1-x} (110). No significant difference is observed between the growth behavior of β-2D-As_xSb_{1-x} and pure β-2D-Sb on Ge(111). After As_4 and Sb_4 co-deposition on Si(111), the

surface is covered by rectangular 3D islands along with 2D flakes (~500 nm diameter and ~8 nm height). The ratio of 3D to 2D islands is much higher on Si(111) than on Ge(111). The growth modes are however relatively similar on the two substrates, according to the shape of the islands. The increased 3D growth is due to the prevalence of the (110) orientation as compared to the (111) 2D growth. This difference most likely comes from the lattice mismatch between β-2D-As_xSb_{1-x} and Si(111). In fact, with the relatively low As content, the β-2D-As_xSb_{1-x} lattice constant is closer to Ge(111) than Si(111), even at the single layer nucleation stage. If the hypothesis that the β-2D-Sb is lattice matched to the substrate during nucleation is true, then the lattice mismatch to Si(111) increases the energy of the β-2D-As_xSb_{1-x} nuclei, which in turn favors a higher Sb(110) to Sb(111) nucleation ratio. On graphene substrates, As_xSb_{1-x} forms mostly 2D flakes with three elongated branches and central 3D nuclei, along with 3D islands and NWs (Figure 5.20i). It appears as the nucleation and growth mechanisms are the same for β-2D-As_xSb_{1-x} and β-2D-Sb on graphene. In fact, the 3D nuclei and flakes with three branches indicate that the flakes nucleate after a phase transition of the central 3D nuclei. Moreover, the shape of the flakes (thicker in the center region) agrees with the multilayer nucleation processes observed for β-2D-Sb. Moreover, the absence of coalescence between flakes indicates that lateral growth is mostly fed by Sb_4 and As_4 deposited directly on the graphene surface. This similarity is expected considering the analogous chemical behavior of both elements.

While LEED and XPS give an idea about the incorporation of As in β-2D-Sb, Raman scattering spectroscopy can give some insight on how the incorporation affects the physical properties. Given the good growth quality of β-2D-As_xSb_{1-x} on Ge(111) and the possibility to precisely determine its lattice constant using LEED, only samples grown on Ge(111) are analysed by Raman. The As content of samples grown at F_{As}/F_{Sb} between 0 and 6.6 is determined using Vegard's law and the Raman spectra are measured (Figure 5.21). As mentioned above, the growth T is not the same for every sample and therefore no quantitative conclusion about the incorporation can be drawn. It is also important to mention that all samples display mostly 2D growth (~5-8 nm flakes) except for the sample at 11% As, which displays thicker 2D islands, with some atoll-like islands as well as some 3D growth. Even though the growth T is not constant from sample to sample, the As concentration appears to increase linearly with F_{As}/F_{Sb}. This implies that the As incorporation is solely limited by the amount of available As_4 species. Again, this is not surprising considering the

chemical similarity and perfect miscibility of As and Sb. Moreover, it suggests that larger As contents can be obtained by increasing F_{As} further, which was not possible in the MBE/LEEM system.

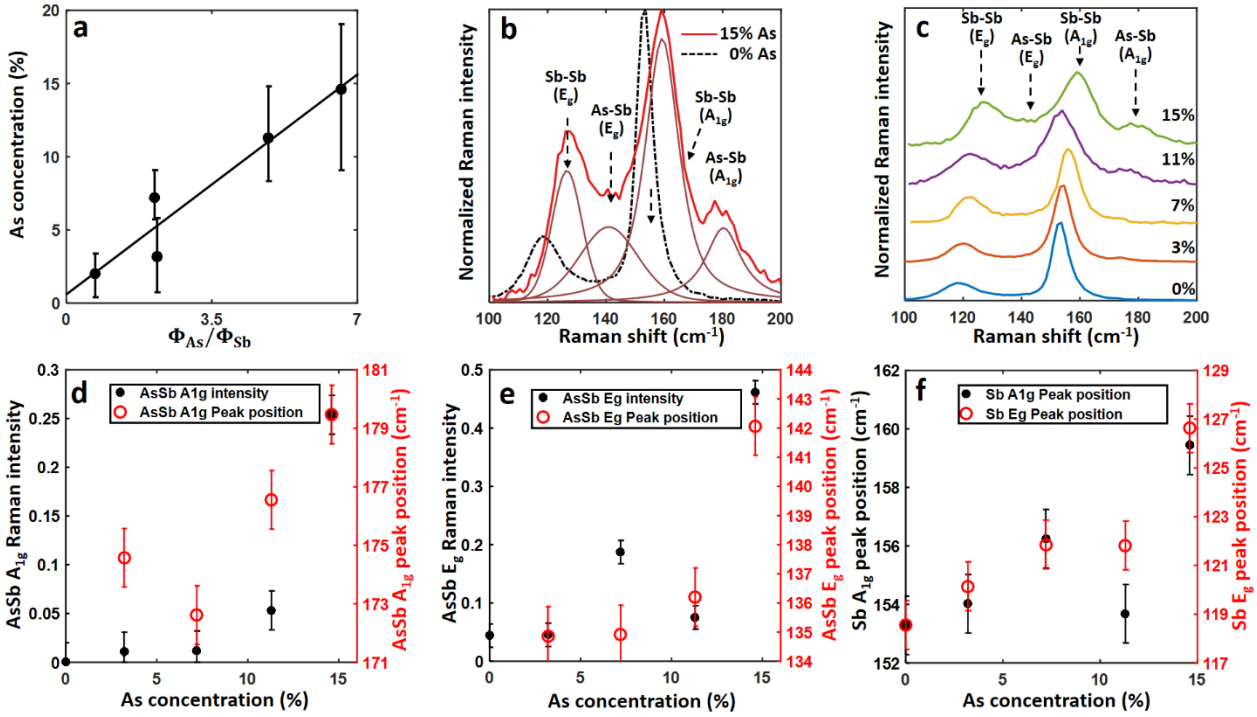

Figure 5.21 a) LEED determined As concentration in β-2D-As_xSb_{1-x} grown on Ge(111) as a function of F_{As}/F_{Sb}. Raman spectra of β-2D-Sb (dashed black) and β-2D-$As_{0.15}Sb_{0.85}$ (red) with fitted Sb-Sb and As-Sb E_g and A_{1g} components. c) Raman spectra of β-2D-$As_{0.15}Sb_{0.85}$ with As content going from 0% to 15%. (c-f) Fitted parameters for the Sb-Sb and As-Sb E_g and A_{1g} vibrational modes. The growth T are 260 240 270 200 and 180 °C and F_{As}/F_{Sb} is 0, 2.2, 2.1, 4.9 and 6.6 for the samples with 0%, 3%, 7%, 11% and 15% As content, respectively. Adapted from *Fortin-Deschênes et al., Small 2020, 16 (3): 1906540*.[38]

As mentioned in the first section of this chapter, A7 Sb has two Raman active modes: E_g at 110 cm^{-1} and A_{1g} at 149 cm^{-1}. The positions of the peaks blue shift as the thickness decreases. On the other hand, 50 nm A7 As(111) has Raman peaks at 194 cm^{-1} and 253 cm^{-1}, which also blue shift with decreasing thickness[168]. The Raman spectra of β-2D-Sb and β-2D-$As_{0.15}Sb_{0.85}$ on Ge(111) are shown in Figure 5.21b. The E_g and A_{1g} peaks of β-2D-Sb are located at 119 cm^{-1} and 153 cm^{-1}. The Sb-Sb E_g and A_{1g} vibration modes are also present in β-2D-$As_{0.15}Sb_{0.85}$, but are shifted to 126.6

cm^{-1} and 159.4 cm^{-1}. The shift can be attributed to the larger force constant of As as compared to Sb. In fact, As has larger cohesive energy and shorter bond lengths than Sb.

Due to the relatively small As content, there are no detectable As-As Raman modes. Nonetheless, additional As-Sb vibration modes are detected (Figure 5.21b). The peak at 179 cm^{-1} of β-2D-$As_{0.15}Sb_{0.85}$ is attributed to the As-Sb vibration mode. In fact, assuming that the force constant is unchanged by the As incorporation, the harmonic approximation predicts that the As-Sb mode should be located at 175 cm^{-1}. It also predicts that the As-Sb E_g peak should be located at 136 cm^{-1}. The As-Sb E_g peak is not clearly visible, most likely due to the overlap with the more intense Sb-Sb E_g and A_{1g} peaks. Nonetheless, the spectrum can be fitted, and the As-Sb E_g peak is found at 142 cm^{-1}.

Expectedly, the intensity of the As-Sb peaks increases with the As content in β-2D-As_xSb_{1-x} (Figure 5.21 (d, e)). We note that the growth mode of the 11% sample was mostly atoll-like (thicker flakes), and therefore is expected to have red-shifted peaks compared to the other samples. There is a general trend of increasing wavenumber with As content for the Sb-Sb and As-Sb A_{1g} and E_g peaks (Figure 5.21 (d-f)). This is due to the increase force constant due to the stronger As bonds. Moreover, there is an increase in the FWHM of the Sb-Sb modes with the As content. For instance, the Sb-Sb A_{1g} FWHM increases from 7 to 13 cm^{-1} as the As concentration increases from 0 to 15%. This can be associated with lattice disorder (shorter phonon lifetime) or due to inhomogeneity of the As content, leading to inhomogeneous peak positions within the probed regions. Moreover, we cannot exclude the possible effect of the introduction of defects in the lattice due to the faster oxidation of AsSb, as compared to pure Sb.

5.3 Growth of α-2D-P

The growth of α-2D-P has been attempted by exploring two methods: (i) solid-source MBE; and (ii) sublimation of graphene capped InP substrates. These studies were not successful in leading to the growth of α-2D-P and are briefly summarized below.

5.3.1 MBE growth on Nb(110)

As described in Chapter 4, Nb(110) was chosen as a growth substrate due to its lattice parameter and surface symmetry. 30 nm Nb(110) films were grown on Al_2O_3 $(11\bar{2}0)$ by the Nanodynamics

group at the Karlsruhe Institute of Technology. The oxidized samples were transferred to the UHV cluster and the surface was prepared by cycles of Ar^+ sputtering and annealing to remove the oxide and obtain a flat surface. P_4 was deposited on Nb(110) at RT from a red P source using a Knudsen cell. The substrate was then annealed up to 280 °C. PEEM and LEED observations of the process are presented in APPENDIX D. During deposition, the PEEM intensity decreases and the LEED pattern of the substrate disappear. During annealing, the PEEM intensity increases and the LEED pattern partially re-appears. No new LEED spots are observed during the process. The results suggest that an amorphous film was formed on the substrate at RT and desorbed with annealing. However, these studies were not pursued further. In fact, optimizing the surface preparation procedure would have required additional Nb(110) samples. Ideally, these would have been grown in the UHV cluster to obtain a better surface quality and remove the need for sputtering. Still, the results show that the deposition of P from red P on Nb(110) is possible and is worth investigating.

5.3.2 Sublimation of graphene capped InP

As explained above, sublimation of InP capped graphene was done in an attempt to obtain a high phosphorus pressure in a confined 2D space for α-2D-P synthesis. An InP(100) substrate was cleaned in HCl to remove the surface oxide and obtain a passivated surface. A graphene layer was then transferred to the InP substrate by coating a graphene/Cu foil with PMMA, dissolving the Cu in an ammonium persulfate solution, fishing the graphene/PMMA with the InP and dissolving the PMMA in acetone. The graphene/InP substrate was then introduced in the UHV cluster and annealed under LEEM observation (Figure 5.22). The annealing process leads to the decomposition of InP in liquid In and gaseous P. At 230 °C (Figure 5.22a), circular low-intensity regions with a diameter of ~1 μm are observed in LEEM. These regions are believed to be phosphorus bubbles trapped in the InP/graphene interface. The white arrow in Figure 5.22a shows a bubble which appears in the LEEM field of view and then seems to spread out for two seconds and disappear after three seconds. On the other hand, the blue arrow shows a bubble which moves in the graphene/InP interface. The LEED pattern (Figure 5.22a) indicates that the InP(100) surface is clean and mostly oxide free. It is unclear whether the bubbles are re-absorbed by the InP or leak out by holes in the graphene layer, but they do not stay long enough to coalesce and form larger bubbles. Still, the graphene seems to trap relatively well the P gas.

As the temperature increases, the decomposition accelerates and In droplets form (Figure 5.22b). The droplets move on the substrate. The motion of the droplets was previously explained by Tersoff et *al*. for the GaAs system[252] and is due to the difference in surface energy at the front and back of the droplet. As the droplets move, they leave a flat surface behind. Here, the droplets are surrounded by P bubbles, which appear as dark regions in LEEM. Several bubbles are labelled in Figure 5.22b. We can confirm that the dark regions are P bubbles and not In droplets since the substrate is visible through the bubble (see bubble A for instance). The bubbles form during the nucleation and growth of In droplets due to the dissociation of In and P (see bubbles B and C). As the droplets begin to move, the edges of the bubbles become pinned to the interface between the flat and rough surfaces, most likely due to the higher interface energy between graphene and the flat surface. The motion of the droplets/bubbles lead to their coalescence, as the larger bubbles absorb the smaller ones (see bubble C and D, E and C as well as E and A).

The deposition of solid phosphorus was observed at no point in the annealing process (neither by LEEM nor LEED). This is potentially due to the insufficient phosphorus pressure. In fact, we can ask ourselves what the phosphorus pressure in the bubbles is. In first approximation, we could assume that the pressure is the equilibrium phosphorus vapor pressure of the phosphorus/InP system. According to experimental data[253], the vapor pressure at 500 °C is ~2 $\times 10^{-7}$ mbar. This is clearly too small to explain the presence of sub-μm bubbles, which must have high internal pressure. In fact, the internal pressure of the graphene bubble can be estimated by: $P = 3.09Yt[h^3/r^4]$, where Y is the Young's modulus, t is the thickness of the elastic membrane (graphene), h is the height of the bubble and r is its radius[254, 255]. Yt can be approximated to 347 N/m. This means that the height of a 1 μm wide bubble at 2 $\times 10^{-7}$ mbar would be 0.1 Å, much smaller than the size of a phosphorus atom. The height of the bubbles cannot be directly measured by LEEM or PEEM, but by comparing to experimental data of bubbles trapped between graphene and a substrate, we can estimate that it is in the tens to hundreds of nm[256, 257], which puts the pressure in the MPa range. Even though the synthesis of α-2D-P was not achieved, these results show that complex phenomena worth investigating can occurs using this sublimation approach.

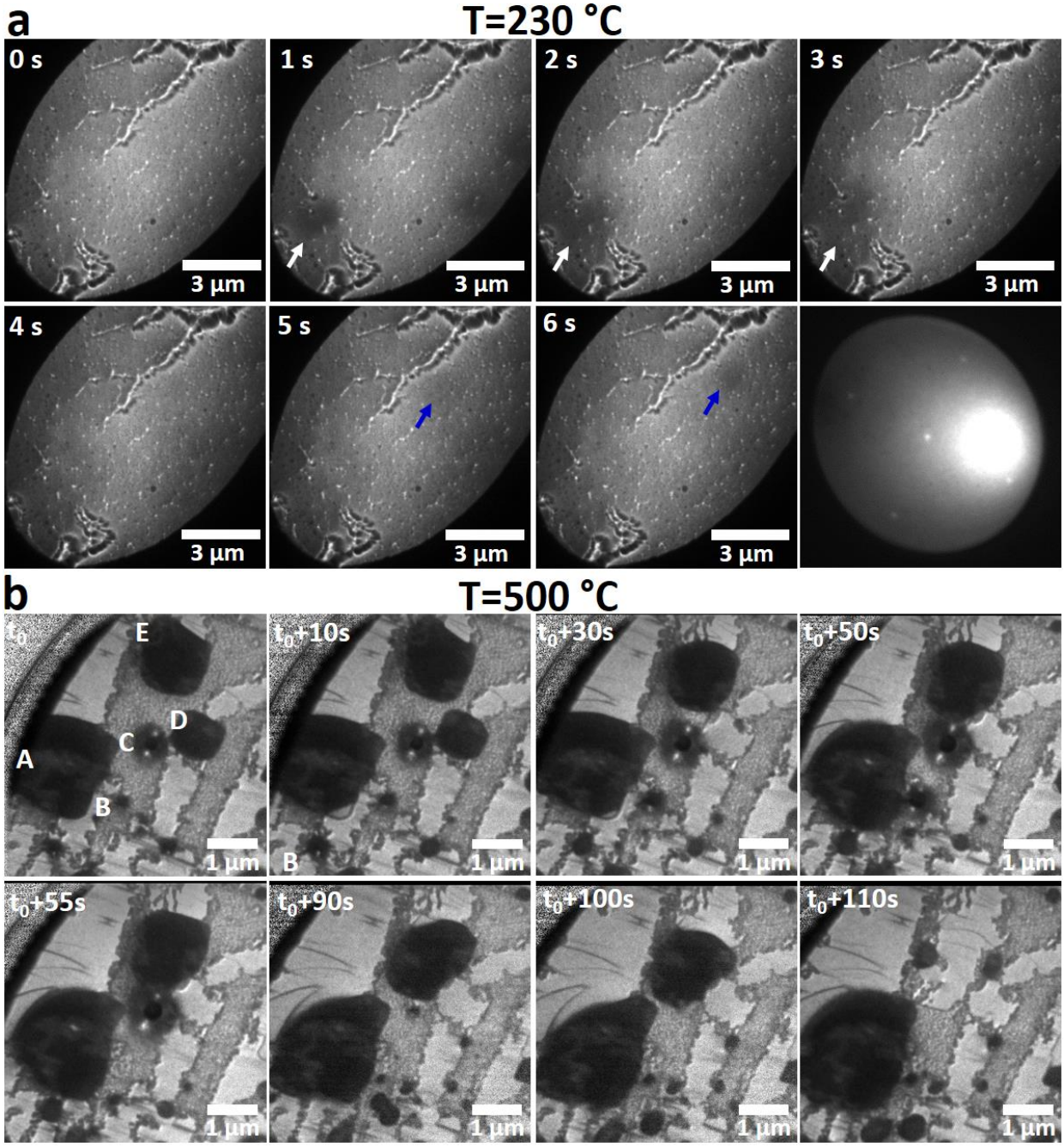

Figure 5.22 LEEM snapshots of the thermal decomposition of graphene capped InP. Brightness and contrast are enhanced for visibility a) LEEM images at 1 frame/s and LEED pattern (22 eV) at T=230 °C. The white arrow indicates a phosphorus bubble between the graphene and InP surface. The size of the bubble increases and then it disappears. The blue arrow indicates a bubble which moves underneath the graphene. b) LEEM images at T=500 °C. The labels A-F identify bubbles which are discussed in the main text.

5.4 Conclusion

In this chapter the MBE growth of β-2D-Sb on Ge(111), passivated Ge and graphene was demonstrated. The atomic structure of the β-2D-Sb phase was identified by STM, LEED and STEM measurements. STM revealed the presence of monolayer and multilayer β-2D-Sb. The effect of the growth conditions was examined by LEEM/LEED. Substrate temperatures above 140 °C were found to be necessary for the growth of β-2D-Sb. However, the decrease of the sticking coefficient of Sb_4 prevented the growth over 330 °C. The substrate-layer interactions had an important role on the growth behavior. On the more interacting Ge(111) substrate, β-2D-Sb was epitaxially oriented with the substrate. On the other hand, multiple randomly oriented grains were observed on graphene. Nevertheless, the β-2D-Sb was found to be relaxed even on Ge(111), at thicknesses as small as four layers. Still, the effect of the substrate-layer interactions were identified by the presence of moiré patterns in STM and misfit dislocations at the Sb/Ge interface. In depth analysis of the growth dynamics of β-2D-Sb on graphene/Ge revealed the nucleation and growth mechanisms. Due to the rapid Sb_4 desorption, only heterogeneous nucleation occurred. Amorphous dome-shaped islands were found to form at graphene defects and then to transition to A7 Sb(111), which led to the nucleation of the β-2D-Sb phase. Voronoi analysis and surface diffusion simulations based on the LEEM data showed that the lateral growth is determined by Sb_4 deposited directly on graphene. On the other hand, Sb_4 deposited on the islands contribute to vertical growth. A growth mode transition to atoll-like growth was found to occur at high temperature and low deposition rate and the homogeneous multilayer nucleation was determined to be a first order reaction.

The growth of lighter group VA 2D material was also studied. Co-deposition of As and Sb led to the formation of β-2D-As_xSb_{1-x}, as confirmed by XPS, LEED and Raman measurements. The LEED and Raman data show that the alloy is substitutional and As concentrations up to 15 at. % were obtained. However, no significant difference in the growth modes of β-2D-As_xSb_{1-x} and β-2D-Sb were observed and larger As_4 flux should allow to reach higher As concentrations. The growth of α-2D-P was attempted by MBE on Nb(110) substrates, but no conclusive data was obtained. Sublimation of InP capped by a graphene layer was also tried. The thermal decomposition led to the formation of In droplets and P gas bubbles. The graphene layer allowed to effectively

trap the P gas, but conversion to α-2D-P was not observed, most likely due to the low phosphorus pressure.

Overall, these results are a considerable step towards the development of novel group VA 2D materials and pave the way for the investigation of β-2D-Sb and β-2D-As_xSb_{1-x}. The results also highlight the importance of *in situ* microscopy in the development of growth methods for emerging 2D materials.

CHAPTER 6 STABILITY OF GROUP VA 2D MATERIALS

Even though important progress has been made on the synthesis of 2D pnictogens, many scientific questions and technical challenges need to be tackled before we can consider their integration in emerging technologies. One of the most important question is their stability. For instance, in addition to the lack of reliable and scalable synthesis methods, α-2D-P oxidizes rapidly in atmospheric conditions which hinders its use in conventional device processing for electronics and photonics. Moreover, the phase stability shift from α to β as the atomic number increases raises additional fundamental questions about the thermodynamic behavior of this emerging class of vdW layered materials.

In this vein, this chapter explores the thermal, atmospheric and phase stability of group VA 2D materials and elucidates its key atomic-level mechanisms. First, the thermal stability and thermal decomposition mechanisms of α-2D-P and β-2D-Sb are studied by real-time LEEM. Then, the oxidation behavior of β-2D-Sb is briefly discussed based on LEEM and synchrotron-based XPEEM measurements. Finally, the phase stability of few-layer α-2D-Sb is investigated and its phase transformation to A7 Sb is evidenced for the first time using a combination of real-time LEEM, STEM, and XPEEM measurements. This is the first direct observation of the thickness dependent stability and allotropic layered-to-layered phase transformation in a 2D system. These results lay the groundwork for the understanding phase stability in vdW and 2D materials.

6.1 Thermal stability

6.1.1 Black phosphorus sublimation

While the ambient stability and thickness dependent oxidation mechanisms of α-2D-P were exhaustively investigated[134], its thermal stability and decomposition mechanisms were elusive by the time this project was initiated. The thermodynamic stability of bulk A17 P was studied in the early 20th century[16, 258, 259]. A17 P was found to be the most stable form of P up to 560 °C, but significant vapor pressures were measured below this temperature[16]. Smits observed that the vapor pressure of A17 P was increasing with time and proposed that A17 P is in fact a metastable phase of P. These results suggest that the thermal dcomposition of α-2D-P will take place at a significant rate at much lower T. In fact, in 2015, Liu et *al*. used *in situ* TEM to study the thermal behavior of

exfoliated α-2D-P layers and observed that the thermal decomposition takes place above 400 °C by the formation and expansion of eye shaped cracks aligned along the [001] direction (Figure 6.1). They proposed a model based on the desorption of single P atoms to explain the formation of the anisotropic cracks. According to their model, the sublimation begins at pre-existing point defects (holes) in the layer. The sublimation takes place by desorbing in priority P atoms with only one P-P bond to the layer, then desorbing atoms with two in-plane bonds to the layer and finally by desorbing P atoms with two out-of-plane bonds to the layer (details in APPENDIX E).

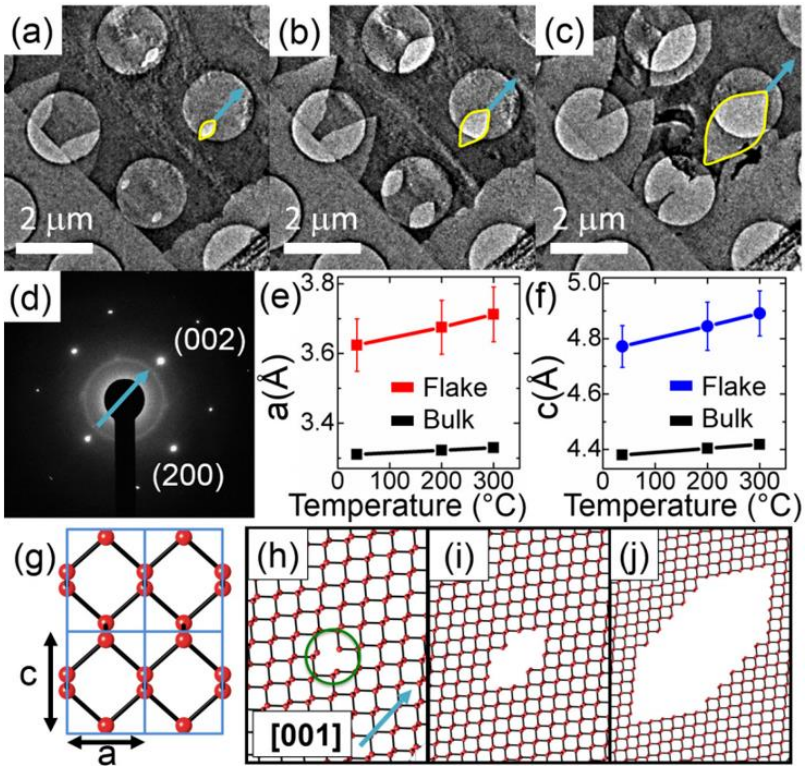

Figure 6.1 Formation of eye-shaped cracks in BP during sublimation. (a–c) Zoomed-in image of the flake in Figure 2, heated for 5, 8, and 12 min at 400 °C, respectively. Eye-shaped cracks (yellow) form and grow. The blue arrow indicates the propagation direction. (d) selected area diffraction pattern of the flake at 300 °C, showing the [001] crack propagation direction. (e, f) Temperature-induced increase in bP lattice parameters a and c. Bulk values from Madelung. (g) In-plane lattice schematic for bP. (h–j) Snapshots from a BP sublimation model, describing the formation of eye shaped cracks along the [001] direction (blue arrow). Reprinted with permission from *Liu, X. et al, The Journal of Physical Chemistry Letters* ***2015,*** *6, (5), 773-778.* [260] Copyright (2015) American Chemical Society.

Moreover, the authors suggest that the thermal decomposition takes place at 400 °C for the 2D phase rather than at 550 °C for the bulk phase due to the higher surface to volume ratio. Considering the self-passivated nature and low surface energies of 2D materials, it is however unlikely that the increased contribution of the surface energy decreases the thermal stability limit by 150 °C. In fact, the discrepancy is likely caused by the fact that early studies were carried out under equilibrium in closed systems, whereas the sublimation is an out-of-equilibrium process occurring in an open system (pumped). The P atom sublimation mechanism is also questionable considering the instability of single P atoms.

To develop a deeper understanding of the thermal decomposition of α-2D-P, this section studies the decomposition of exfoliated α-2D-P layers using real-time LEEM. The experimental results are compared with KMC simulations as well as DFT calculations. The results are published in:

Fortin-Deschênes, M.; Levesque, P. L.; Martel, R.; Moutanabbir, O. "Dynamics and Mechanisms of Exfoliated Black Phosphorus Sublimation" *The Journal of Physical Chemistry Letters*, 7, (9) (2016): 1667-1674. [39]

6.1.1.1 Methodology

α-2D-P flakes were obtained by exfoliation from commercially available bulk A17 P. Prior to exfoliation, Si(100) host substrates were cleaned in piranha solution for 10 minutes followed by a 1 minute HF dip (1%). The substrates were then introduced in a glovebox under N_2 atmosphere within a few minutes. Exfoliation was done by cleaving a A17 P flake from the bulk crystal to expose a pristine surface. The cleaved flake was then placed pristine face up on a polydimethylsiloxane (PDMS) piece. A second half-cylinder PDMS stamp was then pressed on the A17 P/PDMS to exfoliate thin layers. The layers were transferred on the Si(100) substrate by slowly rolling the half cylinder.

The exfoliated α-2D-P/Si(100) were placed in a paraffin sealed container in the glovebox and transferred to the LEEM loadlock while minimizing air exposure to prevent oxidation. The samples were then slowly annealed to investigate their thermal stability. In a first stage, low T annealing (~250 °C) was carried out for a few hours or overnight to obtain a clean surface and desorb hydrocarbons. PEEM, LEEM and LEED of the exfoliated α-2D-P annealed at low T are shown in Figure 6.2. Flakes of various shapes and sizes can be observed. Their exact thickness cannot be

determined with LEEM/LEED/PEEM, but they are certainly multilayer thick. The bright-field LEEM indicates that the surface is smooth and without obvious signs of oxidation (Figure 6.2b). Various linear and point defects can however be seen on the surface. The presence of a sharp LEED pattern indicates that a clean surface is obtained (Figure 6.2c). In fact, the LEED pattern can only be seen after the initial low T annealing, meaning that adsorbates were successfully eliminated. The LEED pattern is rectangular and has surface lattice parameters of 3.2 ± 0.1 Å and 4.5 ± 0.1 Å, confirming that the (010) plane of A17 P is observed. In fact, the a and c lattice parameters of bulk A17 P are 3.31 Å and 4.38 Å. The discrepancy is most likely attributed to the astigmatism and aberrations. In fact, precise lattice parameter measurements were possible for β-2D-Sb and β-2D-As_xSb_{1-x} only due to the proximity of the Ge(111) and Si(111) diffraction spots.

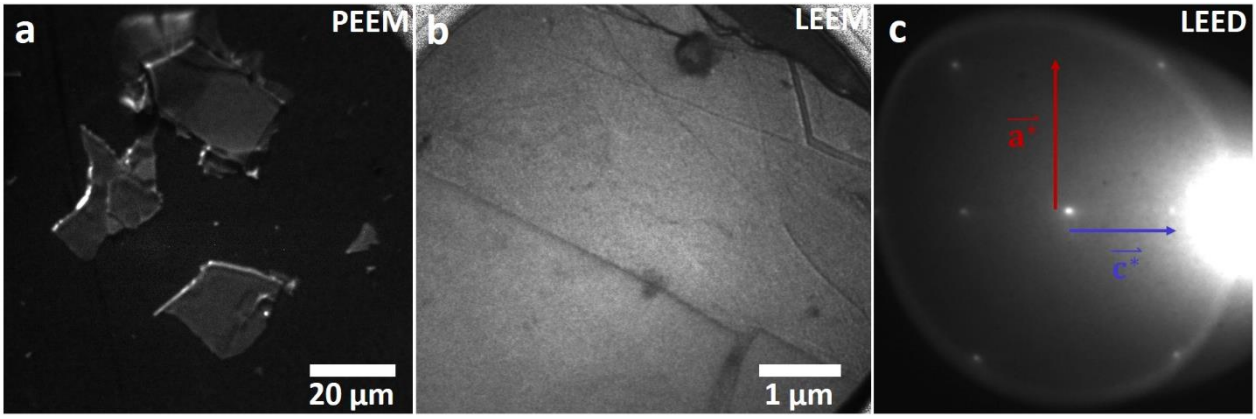

Figure 6.2 a) PEEM image of exfoliated α-2D-P flakes on Si(100) using a short-arc mercury lamp source with a 4.9 eV irradiation cut-off. b) Bright-field LEEM image (35 eV) of the surface of a α-2D-P flake. c) LEED pattern of an α-2D-P flake. (c) is adapted with permission from *Fortin-Deschênes et al., The Journal of Physical Chemistry Letters 2016, 7 (9): 1667-1674.* [39] Copyright (2016) American Chemical Society.

6.1.1.2 Thermal decomposition

After low T annealing, the T was ramped up by steps of ~50 °C under bright-field LEEM imaging until signs of decomposition were observed. LEEM of α-2D-P before prior to thermal decomposition is shown in Figure 6.3a. After five minutes at T = 375 °C, thermal decomposition is observed at edges and on the surface (Figure 6.3b). Expectedly, the layer decomposes by edge sublimation. Sublimation is faster at the edges since the presence of dangling bond reduces the

sublimation activation energy. Nonetheless, it also occurs on the surface by the formation of holes. Most holes appear to be monolayer deep. In fact, coalescence of holes usually exposes a pristine surface (APPENDIX F). While this is not a direct measurement of the number of layers, it indicates that the holes have the same depth since the initial surface is atomically smooth over μm sized regions. Since the layers of a vdW material interact weakly with each other, it is highly unlikely that this monodisperse distribution is centered at a multiple of one layer. Nonetheless, the presence of multilayer holes is also observed, as will be discussed below.

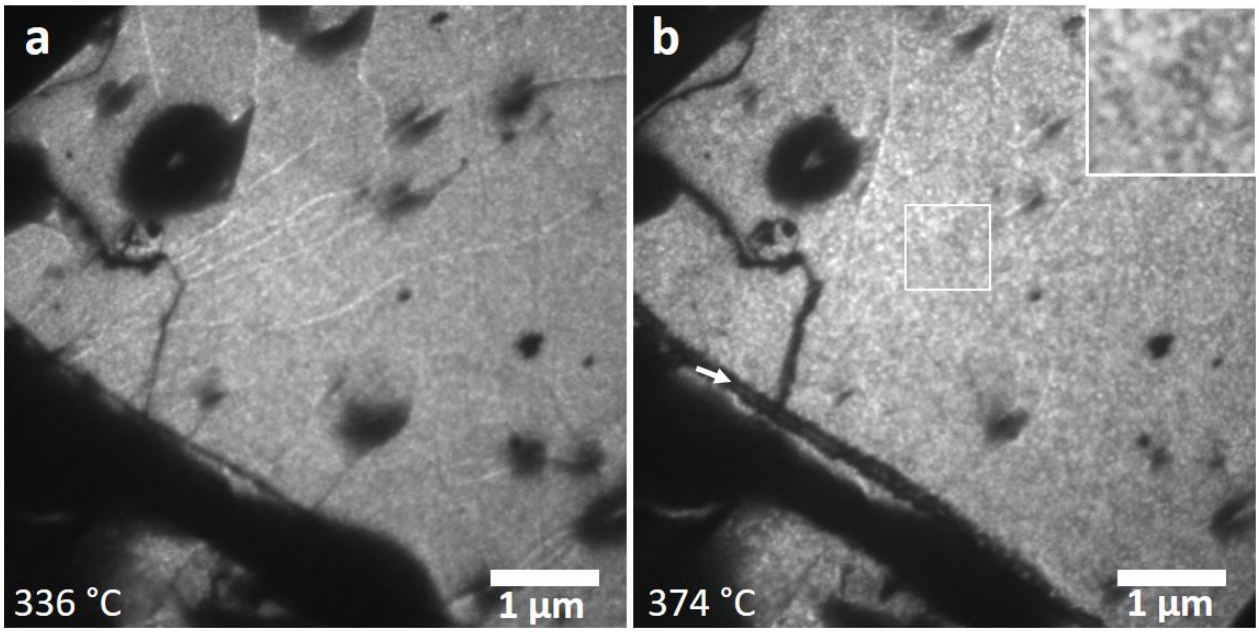

Figure 6.3 Bright-field LEEM images exfoliated α-2D-P during annealing. The sample was kept at T between 260-290 °C for 5 hours prior to the LEEM measurements. a) T=336 °C, before obvious thermal decomposition signs. b) T=374 °C after 5 minutes of annealing at 370-375 °C. Edge decomposition indicated by white arrow and monolayer hole formation on the surface showed in the inset. The brightness, contrast and sharpness was adjusted in the inset to highlight the holes. Adapted with permission from *Fortin-Deschênes et al., The Journal of Physical Chemistry Letters 2016, 7 (9): 1667-1674.* [39] Copyright (2016) American Chemical Society.

To better understand the mechanism governing the sublimation of α-2D-P, we look at the hole expansion dynamics using real-time LEEM. Successive hole nucleation and expansion at ~490 °C is showed in Figure 6.4 (a-h). The crystallographic directions are determined by LEED (Figure 6.4i). The monolayer deep holes are illustrated in Figure 6.4j. Their shape is elongated with a long

to short axis ratio between 1.5-2.3. Moreover, the tips (along the long axis) of the larger holes are often facetted. Smaller holes are usually more elliptic. Interestingly, the holes long axes are oriented in the [100] direction, in contradiction with the reports by Liu et *al.*[260] Careful calibration of the rotation angle between imaging and diffraction modes must be done since both studies were carried out in electron microscopes using magnetic lenses which rotate the image. The LEEM and LEED modes are found to be rotationally aligned within 5°, as can be readily seen by comparing the LEED and dark-field LEEM of Ge{107} nanofacets (APPENDIX G).

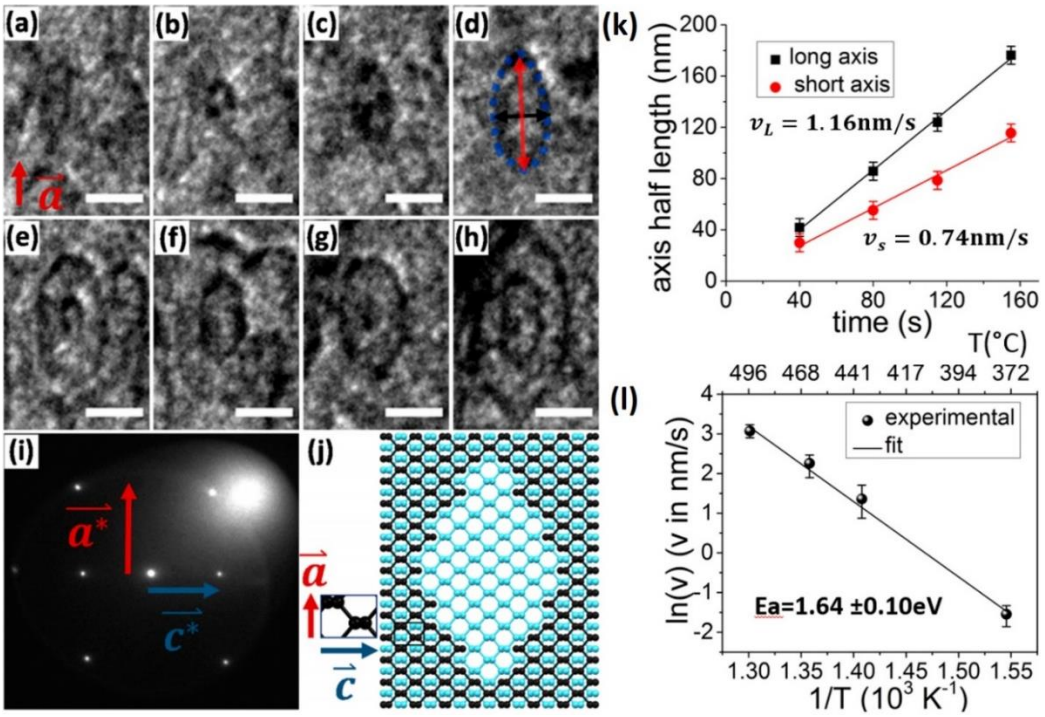

Figure 6.4 Bright-field LEEM snapshots (35 eV) of hole expansion during exfoliated α-2D-P sublimation. Each frame (a-h) are measured two seconds apart during the heating process. The T from (a-h) is 486 °C, 488 °C, 490 °C, 491 °C, 493 °C, 495 °C, 497 °C and 499 °C and the scale bars are 200 nm. The hole is highlighted by a dashed blue line in (d) and its short and long axis are indicated by the black and red double arrows. (i) LEED pattern before sublimation. (j) Illustration of a α-2D-P hole and of the unit cell. The hole is in the top layer (black) and the bottom layer (blue) is still intact. (k) Time evolution of the short and long axis of a α-2D-P hole at 412 °C. (b) Arrhenius plot of the short axis expansion velocity. Adapted with permission from *Fortin-Deschênes et al., The Journal of Physical Chemistry Letters 2016, 7 (9): 1667-1674.* [39] Copyright (2016) American Chemical Society.

Moreover, Kumar et *al*. later also observed the [100] orientation of the holes long axis using STM[261]. Expectedly, the hole expansion is linear in time with a larger long axis expansion velocity v_L and smaller short axis velocity v_S (Figure 6.4k), in the order of 1 nm/s at 410 °C. The linearity implies that the reaction is limited by a process occurring at the edges (sublimation in our case). We can therefore get more information about the mechanisms by analysing the temperature dependence of the sublimation. An Arrhenius plot of the hole expansion velocity is shown in Figure 6.4l. For a thermally activated process (rate $R \sim f_0 e^{-Ea/kT}$), the slope of *ln(R)* as a function of $-1/k_BT$ is proportional to the activation energy E_a of the limiting process. Here E_a=1.64 ± 0.1 eV and $f_0 \approx 10^{13}$ Hz.

The relatively small E_a casts doubt over the single P atom sublimation model proposed by Liu et *al*.[260] An atomistic model based on P_2 sublimation is examined to better understand the thermal decomposition mechanisms. The single P atom (from Liu et *al*. [260]) and the P_2 sublimation models are compared in Figure 6.5 (a, b). Edge sublimation of P_2 molecules with different atomic environments are considered: from [100], [001] and [101] edges and with zero, one or two P_2 nearest neighbors on the edge. KMC simulations of the sublimation dynamics are then carried out for the P and P_2 sublimation models. Hole expansion is studied using a single-layer α-2D-P lattice with an initial nucleus (P or P_2 vacancy). Each sublimation process is attributed a rate of $f_n = f_0 e^{-E_{a_n}/kT}$. The attempt frequency f_0 is set to the average Debye frequency of 2.44 × 10^{13} Hz extracted from [24]. The activation energies are adjusted to reproduce the sublimation behavior (long to short axis ratio, expansion velocity and sharp tip). As a comparison, the activation energies are estimated from DFT calculations. The edges are modelled by single-layer α-2D-P nanoribbons with [100], [001] and [101] edge orientations. A lower bound on the activation energy is calculated using:

$$\Delta E = \frac{\left(E_{N-2x} + 2E_{P_x}\right) - E_N}{2} \leq E_a \qquad (6.1)$$

where E_N is the total energy of the initial nanoribbon (N atoms), E_{N-2x} is the energy of the same nanoribbons from which two P_x were removed (one from each edge). The simulated holes from P and P_2 sublimation are shown in Figure 6.5 (c, d) and the structurally relaxed nanoribbons before and after sublimation are shown in Figure 6.5f.

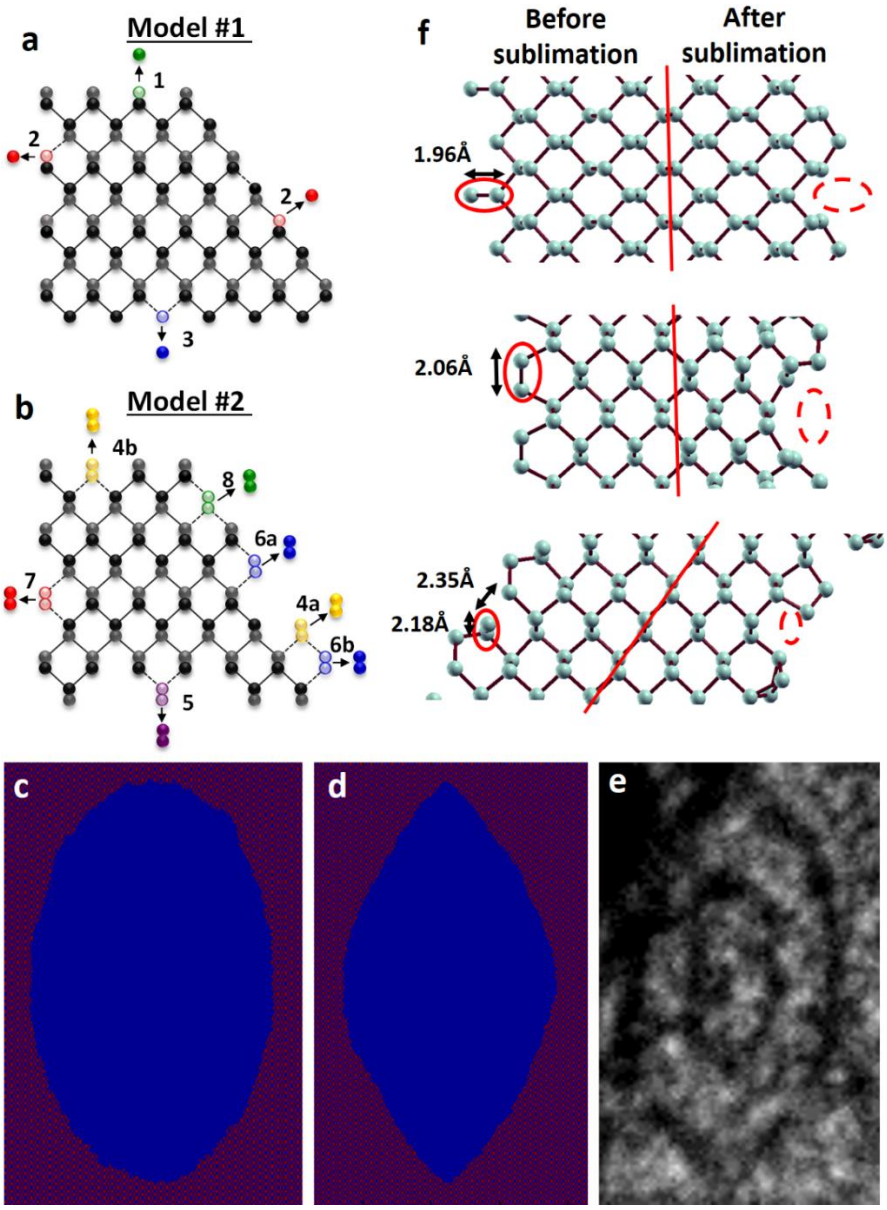

Figure 6.5 a) Illustration of the single P atom sublimation model proposed by Liu et *al.*[260] b) P_2 sublimation model proposed by Fortin-Deschênes et *al.* [39]. c-d) KMC simulated holes according to the models in (a) and (b), respectively. e) Bright-field LEEM of the α-2D-P holes formed during sublimation. f) DFT calculated atomic structure of α-2D-P nanoribbons with [100], [001] and [101] edges orientation. The left side is before sublimation and the right side is after sublimation. Adapted with permission from *Fortin-Deschênes et al., The Journal of Physical Chemistry Letters 2016, 7 (9): 1667-1674.* [39] Copyright (2016) American Chemical Society.

The KMC fitted and DFT estimated sublimation activation energies are shown in Table 6.1. It is important to note that the difference between E_a and ΔE is not necessarily large. In fact, the difference between the two values is the barrier of the inverse process (P_2 attachment at the edges), which likely does not involve bond dissociation in most cases. Sublimation therefore involves mostly slight interatomic distances rearrangements and the transition and final states should differ by few hundreds of meV at the most. Still, full activation energy calculations would be required for quantitative analysis (using the nudged-elastic band method for example).

Table 6.1 DFT calculated lower bounds and KMC fitted sublimation energies for P and P_2 based sublimation models. The KMC values allow to reproduce the long-to-short axis ratio of 1.8 and 21.5 nm/s velocity at 495 °C. For shape optimization, 245 000 atoms are sublimated, and 10 simulations are averaged. For velocity calculations, 40 000 atoms are sublimated, and 1000 simulations are averaged. Adapted with permission from *Fortin-Deschênes et al., The Journal of Physical Chemistry Letters 2016, 7 (9): 1667-1674.* [39] Copyright (2016) American Chemical Society.

	Model #1		Model #2	
	ΔE (DFT)	E_a (KMC fit)	ΔE (DFT)	E_a (KMC fit)
Process #1	2.32 eV	<< 1.62 eV		
Process #2	3.43 eV	1.57 eV		
Process #3	4.02 eV	1.62 eV		
Process #4a			1.69 eV	1.61 eV
Process #5			1.04 eV	1.04 eV
Process #6a			1.69 eV	1.41 eV
Process #7			2.30 eV	1.59 eV
Process #8			N/A	1.66 eV

Both models can reproduce the hole expansion dynamics. However, model #1 (P sublimation) cannot reproduce the hole shape. In fact, only elliptic holes without facetted tips form in the KMC simulations (Figure 6.5 (c, e)). However, model #1 can accurately reproduce the hole geometry rotated by 90° (long axis and sharp tip oriented in the [001] direction). On the other hand, model #2 reproduces accurately the hole expansion dynamics and shape (Figure 6.5 (d, e)). More importantly, the fitted activation energies for model #1 are much smaller than the DFT estimated lower bounds. In fact, KMC yields E_a in the 1.6 eV range, similar to the 1.64 eV found with the Arrhenius plot. The DFT values are in the 2.32-4.02 eV range, meaning that P sublimation is extremely slow in the investigated T range. On the other hand, model #2 yields moderately

consistent DFT and KMC activation energies (Table 6.1), with the exception of process #7 (P_2 sublimation from armchair edges). This indicates that P_2 edge sublimation likely plays an important role in the thermal decomposition of α-2D-P. Moreover, structural relaxation indicates bond reorganization favorable to P_2 sublimation. The P-P bond length is 2.26 Å in α-2D-P and 1.90 Å in P_2. Significant bond contraction occurs for the P-P dimers on the edges of the ribbons (down to 1.96 Å for the [100] ribbon) (Figure 6.5f). This bond contraction suggests that the edge P-P dimers can be removed more easily and without additional significant energy barriers than other P_N species.

Nonetheless, other sublimations processes cannot be excluded. For instance, P_4 sublimation most likely plays an important role in α-2D-P thermal decomposition. In fact, below 1200 °C, P_4 is the main component of P vapor. However, structural relaxation of α-2D-P nanoribbons indicates that the direct detachment of P_4 molecules involves bond reorganization and additional energy barriers in many cases. On the other hand, edge reconstruction and tetramer formation observed in [101] nanoribbons (Figure 6.5f). P_4 sublimation is expected in this case. Moreover, the edge reconstruction indicate that an additional significant energy barrier is present for P_2 detachment from this configuration. Both P_2 and P_4 sublimation are therefore expected to occur.

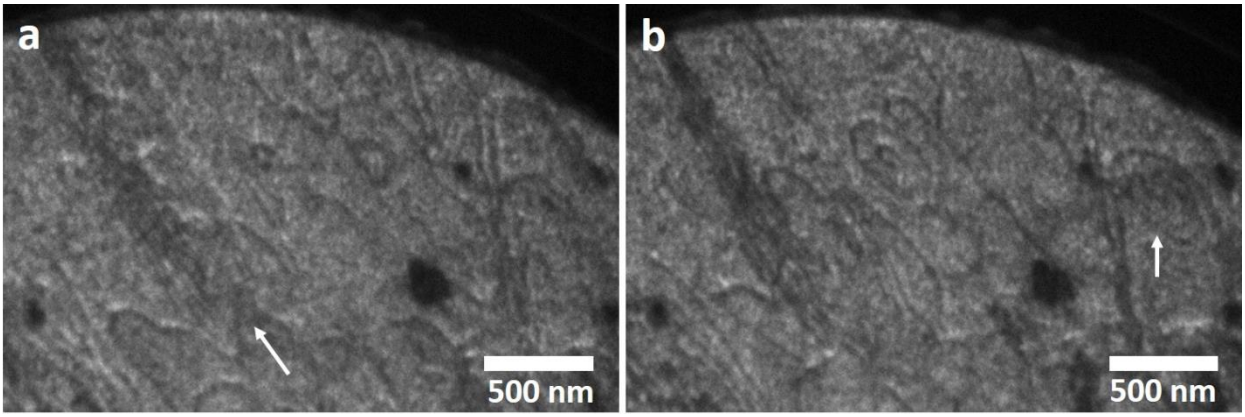

Figure 6.6 Bright-field LEEM images of hole nucleation a defects during α-2D-P sublimation. Linear defect indicated by a white arrow in a). Point defect indicated by a white arrow in b). Adapted with permission from *Fortin-Deschênes et al., The Journal of Physical Chemistry Letters 2016, 7 (9): 1667-1674.* [39] Copyright (2016) American Chemical Society.

Next, we look at the macroscopic sublimation modes of single and multilayer α-2D-P. The sublimation mode depends on the hole nucleation behavior. In the samples analysed in this study, hole nucleation at defects is one of the dominating mechanisms (Figure 6.6). Multiple holes nucleating at a linear defect are shown in Figure 6.6a and holes nucleating at a point defect are seen in Figure 6.6b. Nonetheless, the density and type of defects depends on the synthesis and processing. For instance, point defects such as vacancies located on individual layers should be present at an equilibrium concentration of $\rho_v = \exp(-\Delta G_v/kT)$. On the other hand, oxidation creates point defects extending on multiple layers.

Below is the description of a mathematical model of the sublimation dynamics. First, lets assume a perfect crystal with an equilibrium concentration of vacancy point defects for which holes nucleate at defects as soon as they are exposed to vacuum. For simplicity, we assume circular holes expanding at v_{hole}. The sublimation of a single layer can be understood as a spatial Poisson process. In fact, for randomly distributed point defects with a density ρ_d, the probability of finding *n* defects in an area *A* is described by a Poisson process:

$$P(n, A) = \frac{[\rho_d A]^n}{n!} e^{-\rho_d A} \tag{6.2}$$

The probability of having no defect in a disk of area $A = \pi r^2$ is therefore $e^{-\rho_d \pi r^2}$. Assuming that the T is instantly increased at $t = 0$ and then kept constant, the holes have radii $r = vt$ and the probability that a point is at a distance of more than r from any point defect is given by $e^{-\rho_d \pi v^2 t^2}$. This probability represents the proportion of the α-2D-P layer which is not yet sublimated (or coverage Θ). The sublimation flux is therefore given by:

$$F_1 = \rho_s \frac{d\Theta}{dt} = 2\pi\rho_s\rho_d v^2 t e^{-\rho_d \pi v^2 t^2} \qquad [atoms\ cm^{-2}\ s^{-1}] \tag{6.3}$$

With ρ_s the atomic density of α-2D-P. This means that for an infinite single layer with point defects, the sublimation behavior is not constant with time and is highly temperature sensitive, especially in the early sublimation stage, where the flux is given by $2\pi\rho_s\rho_d v^2 t$. In fact, this yields an initial sublimation rate, which depends on $e^{-2E_a/kT}$. This contrasts with other sublimation modes. For instance, the sublimation of a 3D covalent material often occurs at step edges and therefore doesn't contain a v^2 term and should be proportional to $e^{-E_a/kT}$.

On the other hand, sublimation from the flake's edges plays a more important role at low defect densities or in small α-2D-P flakes. The lateral dimensions at which edge sublimation become dominant can be estimated to be the size of a flake for which the sublimation half-time considering only edge sublimation or only defect sublimation are equal. We find $r_c \approx 1.60\rho_d^{-0.5}$. In our case, the nucleation rate measured in LEEM indicates that $\rho_d = 20\ \mu m^{-2}$ and therefore $r_c \approx 360\ nm$.

It is also instructive to look at the multilayer sublimation modes to better understand the effects of thermal processing on multilayer α-2D-P based devices. For instance, it has been suggested by Luo et *al*. that multilayer α-2D-P can be thinned down by controlled sublimation[262]. As for single layers, the sublimation modes of multilayer α-2D-P are highly dependent on the type of defects. For instance, if multilayer point defects are present (for an oxidized layer), then the sublimation mode will be then same as what was derived for a single layer with point defects. For randomly distributed point defect located on individual layer, we can derive expressions of the sublimation rate of all the layers. We can view equation (6.3) as:

$$F_1 = l_1 v \rho_s X_1 \tag{6.4}$$

with l_1 the length of holes' edges per unit surface (neglecting coalescence) and X_1 a correction term for coalescence. $l_1 = 2\pi v t \rho_d$ since holes expand at constant velocity. The correction factor is $X_1 = e^{-\rho_d \pi v^2 t^2}$, which correspond to the probability that there is no defect in a radius of $r = vt$ (or the proportion of edges which have not coalesced). Next, we assume that a hole nucleates at a defect as soon as it is exposed to vacuum by the sublimation of the layer above it. Equation (6.4) can be generalized for all layers by introducing the hole nucleation rate on layer *i*:

$$\frac{dn_i}{dt} = -\rho_d \frac{d\Theta_{i-1}}{dt} \tag{6.5}$$

where Θ_i is the un-sublimated fraction of layer i and n_i is the number of holes on layer i per unit surface. We then correct for the fact that holes nucleate at different times:

$$r = v \times (t - t_0) \times H(t - t_0) \tag{6.6}$$

where $H(t - t_0)$ is the Heaviside function for holes nucleating at t_0. The sublimation flux from layer *i* is given by:

$$F_i = v \rho_s l_i e^{-A_i} \tag{6.7}$$

With the edge length per unit surface on layer *i* neglecting coalescence:

$$l_i = \int_0^t -\rho_d \frac{d\Theta_{i-1}}{dt}\Big|_{t=t_0} 2\pi v \times H(t-t_0) \times (t-t_0) dt_0 \tag{6.8}$$

and the fraction of the surface of layer *i* covered by holes neglecting coalescence:

$$A_i = \int_0^t -\rho_d \frac{d\Theta_{i-1}}{dt}\Big|_{t=t_0} \pi v^2 \times H(t-t_0) \times (t-t_0)^2 dt_0 \tag{6.9}$$

Where

$$\frac{d\Theta_i}{dt} = -l_i v e^{-A_i} \tag{6.10}$$

Analytical expressions are found only for the first two layers. For the second layer:

$$F_2 = v\rho_s \pi \sqrt{\rho_d}(2tv\sqrt{\rho_d} - \text{erf}\,(tv\sqrt{\pi\rho_d}))\exp\,[1 - t\pi v\sqrt{\rho_d}\,\text{erf}\big(tv\sqrt{\pi\rho_d}\big) + \pi\rho_d v^2 t^2 - e^{-t^2\pi\rho_d v^2}]$$

For the other layers, the flux can be found numerically. It is important to note that the results found for multilayer sublimation are based on the assumption that the coalescence correction factor $X_i = e^{-A_i}$ can be generalized from $X_1 = e^{-\rho_d \pi v^2 t^2}$ for an arbitrary distribution of hole diameters. To understand the sublimation behavior of thick multilayer flakes, we look at the sublimation flux calculated for a 300-layer thick flake (Figure 6.7). At t = 0, the sublimation flux increases rapidly due to hole expansion in the first layer. Even when the sublimation flux of first layer decreases, the total flux increases due to the additional sublimation from the bottom layers. There is a significant and increasing overlap of the sublimation flux of different layers and the sublimation of the bottom layers becomes more and more spread over time. This overlap leads to a multilayer sublimation mode, rather than layer-by-layer sublimation. According to this model, the roughness of multilayer α-2D-P flakes will increase over time. Thinning multilayer α-2D-P by sublimation is therefore not possible unless defects can be introduced in a controlled fashion. Moreover, we note that the sublimation flux doesn't stabilize with time, which may explain the observations from Smits[259] indicating that the vapor pressure increases over time during A17 P annealing. Nonetheless, Smits measurements were carried out in a closed system, where deposition from the vapor phase should allow to eventually reach an equilibrium state. Perhaps the vapor pressure of A17 P stabilizes over longer timescales when a steady state is reached. The role of defect can be assessed by calculating

the sublimation flux as a function of defect density (Figure 6.7b). By plotting the flux as a function of defect density at fixed mass loss in log-log scale (Figure 6.7b), we determine a $F \sim \rho_d^{0.5}$ dependency. The defects therefore have a large impact on the sublimation rate. Nonetheless, they play a more important role in the initial sublimation stage, where $F \sim \rho_d$.

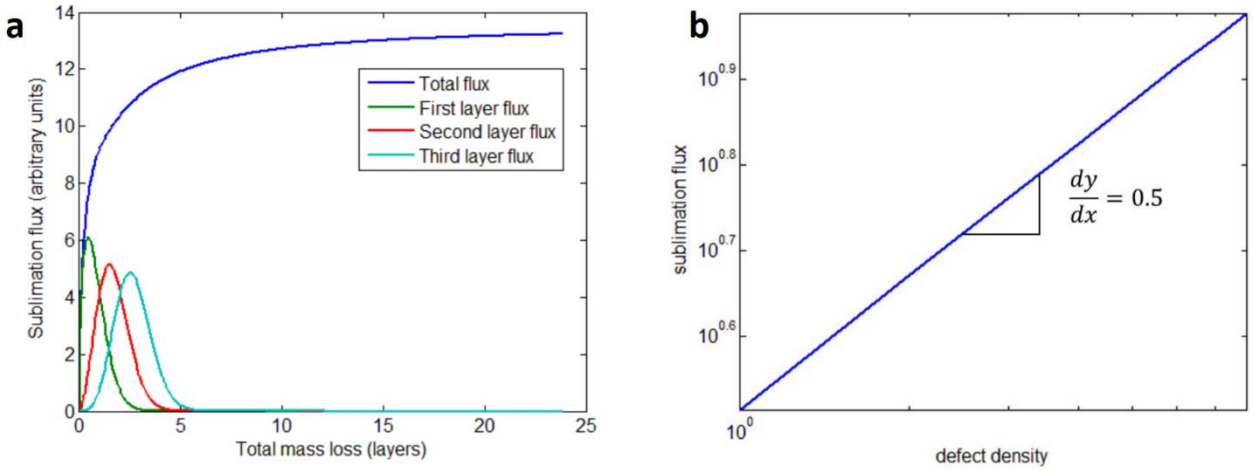

Figure 6.7 a) Calculated sublimation flux of multilayer α-2D-P according to the randomly dispersed defect-nucleation mechanism. Total flux as well as flux of individual layers is shown. b) Calculated sublimation flux as a function of defect density in log-log scale showing the square root dependency. Adapted with permission from *Fortin-Deschênes et al., The Journal of Physical Chemistry Letters 2016, 7 (9): 1667-1674.* [39] Copyright (2016) American Chemical Society.

6.1.2 β-2D-Sb sublimation

We now look briefly at the thermal decomposition of β-2D-Sb using the same method but with epitaxially grown β-2D-Sb flakes rather than flakes exfoliated from a bulk crystal. Below 400 °C, the thermal decomposition is very slow. LEEM of β-2D-Sb at 400 °C is shown in Figure 6.8 (a, b). As expected, the main decomposition pathway is sublimation from edges. In fact, in contrast to 3D covalent materials, we do not expect a significant melting point depression for vdW layered at reduced thicknesses. The cohesive energy of a vdW crystal can be approximated by $E_{2D} = E_{bulk} - \frac{1}{n}E_{interlayer}$, where E_{bulk} and $E_{interlayer}$ are the molar bulk cohesive energy and interlayer interaction energy. Since the melting point is generally proportional to the cohesive energy of the solid[263], a melting point of the 2D film is approximatively $T_{m_{2D}} = T_m\left(1 - \frac{1}{n}\frac{E_{interlayer}}{E_{bulk}}\right)$, where

T_m is the bulk melting point. With $E_{bulk} = 3.1\ eV/atom$ and $E_{interlayer} \approx 140\ meV/atom$, a maximal melting point depression of ~5% is expected at single layer thickness (down to ~590 °C from the bulk melting point of 631 °C). Here, the thinnest observed clover-shaped β-2D-Sb flakes are 3 bilayers thick and should melt at ~617 °C. However, the sublimation rate is significant below these temperatures and melting will only occur if the temperature is ramped up extremely fast.

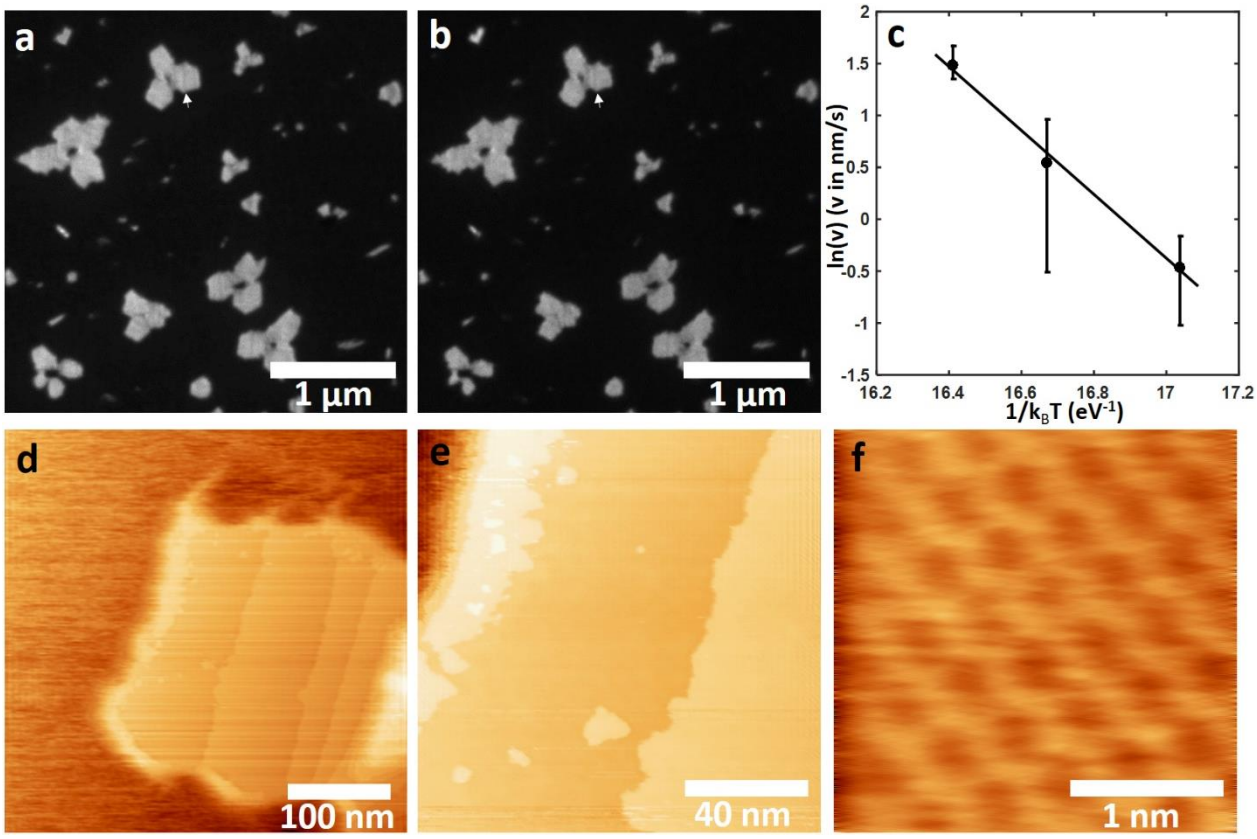

Figure 6.8 a) Bright-field LEEM image of β-2D-Sb flakes on Ge(111) at T=400 °C. b) Bright-field LEEM of the same area after annealing at T=400 °C for 170 seconds. The white arrows indicate the edge sublimation. c) Arrhenius plot of the edge sublimation velocity. d-f) Post-annealing STM images of the sample in (a, b).

In contrast to α-2D-P, hole formation is not observed in β-2D-Sb. LEEM indicates that sublimation occurs at similar rates from the edges of the flakes as well as from step edges on the surface of the flakes (Figure 6.8). This indicates that the layers evolve independently from each other at the edges. At T=400°C, the edge sublimation rate is ~ 1-2 Å/sec depending on the edge orientation. Moreover, the Z1 and Z2 outside edges and step edges remain relatively straight during sublimation. On the

other hand, higher energy edges roughen during sublimation. The β-2D-Sb sublimation study was carried out to understand the general behavior and define the temperature at which these layers start degrading, rather than repeating the set of in-depth analyses done for α-2D-P. To appreciate the overall behavior, a tentative Arrhenius plot is shown in Figure 6.8c. The sublimation is measured in a limited temperature range (408-434 °C). The fitted sublimation activation energy is $E_a = 3.1 \pm 1\ eV$. The energy barrier is certainly overestimated since it requires attempt frequencies in the order of 10^{22}-10^{23} Hz to reproduce the observed edge sublimation rates. Still, an E_a at the bottom of the uncertainty range would be higher than for α-2D-P, even though the cohesive energy of Sb is much smaller.

in situ STM images of β-2D-Sb after the annealing process are shown in Figure 6.8 (d-f). The outside edges of the flake are roughened by the sublimation process (especially the side edges of the branches). The Z1 step edges on the surface of the flake are also roughened but still macroscopically aligned with the Z1 direction. Interestingly, there is an accumulation of Sb on the edges of the flake (~ one monolayer thick and 30 μm wide). We currently do not have any explanation for this phenomenon. We note that the atomic structure of β-2D-Sb is preserved, and that hole formation is not observed even at the atomic scale. This does not necessarily indicate a different sublimation mode and could be due to a small defect density. In fact, defect assisted sublimation might become the dominating sublimation process in larger flakes (tens to hundreds of microns) or in flakes, which have been exposed to air (depending on the oxidation mechanisms).

6.2 Oxidation of β-2D-Sb

Next, we examine the atmospheric stability of 2D-Sb. Several recent studies reported on the ambient stability of β-2D-Sb and its resistance to oxidation[98, 153-155]. However, these studies mostly focused on demonstrating the superior stability of β-2D-Sb as compared to other 2D materials such as α-2D-P and were conducted over limited periods of time. Moreover, they either used local methods such as atomically resolved AFM which do not inform about the global behavior or methods with low spatial resolution such as XPS, which give the average behavior of the sample. In fact, while XPS provides highly accurate chemical information about the surface of the sample, its resolution is typically limited to ~1 mm.

Here, the ambient stability and oxidation of β-2D-Sb is studied using XPEEM. Synchrotron-based XPEEM operates under the same principle as XPS but has a spatial resolution of ~30 nm and a better energy resolution (~300 meV). Moreover, it readily gives a hyperspectral image of the sample over a relatively large region (~10 μm). The increased XPEEM spatial resolution allows to probe locally the early stages of the oxidation process. Moreover, since multiple phases and crystallographic orientations can coexist on the same sample, XPS gives the average behavior and cannot distinguish between the oxidation of the different constituents. β-2D-Sb samples were grown on graphene/Ge in Polytechnique Montreal and were exposed to atmospheric conditions for one week to three months. The samples were then transferred to the Nanospectroscopy beamline in Elettra Sincrotrone Trieste and were characterized by LEEM and XPEEM.

Even though short exposure times to atmospheric conditions have not been studied here, it seems that the first signs of oxidation can be detected after a few days (Figure 6.9 (a-e)). XPEEM images from pristine Sb $4d_{5/2}$ photoelectrons and Sb_2O_3 Sb $4d_{5/2}$ photoelectrons are shown in Figure 6.9 (a, b). The XPS spectra of the flake's surface and edges are shown in Figure 6.9c. There is an oxide layer at the edges of the flake, but the center of the flake is oxide-free. In fact, the XPS spectrum of the flake's center can be fitted with only one component (Sb $4d_{3/2}$ at 33.6 eV and Sb $4d_{5/2}$ at 32.4 eV). On the other hand, the spectrum of the edges has two components (Sb $4d_{3/2}$ at 33.7 eV and Sb $4d_{5/2}$ at 32.4 eV, as well as Sb_2O_3 at 35.7 eV (Sb $4d_{3/2}$) and 34.6 eV (Sb $4d_{5/2}$)). No significant Sb_2O_5 or Sb_2O_4 components are measured. It is important to note that the ratio of pristine to oxidized Sb at the edges cannot be determined from the XPS spectrum. In fact, the XPEEM spatial resolution is insufficient to fully isolate the narrow oxide region at the edges. For the same reason, the measured Ge 3d intensity is much higher at the edges than at the center. Nonetheless, we can expect the ratio of Sb_2O_3 to pristine Sb at the edges to be higher than what is observed in the XPS spectrum. In fact, the pristine Sb 4d intensity is lower at the edges than at the center. Moreover, nanowires and 3D islands are also oxidized. 3D islands oxidize faster than β-2D-Sb. In fact, XPEEM measured after one week of air exposure (not shown) indicates that 3D islands are significantly oxidized.

LEEM has a better spatial resolution than XPEEM and can have a much stronger signal. The correlation between the XPEEM and LEEM image indicates that Sb_2O_3 appears dark in bright-field LEEM at 3.2 eV (Figure 6.9 (d, e)). After 19 days, the width of the oxide layer on the edges varies

between 30 ± 10 nm and 110 ± 10 nm (Figure 6.9d). The width of the oxide layer increases close to the tip of the branches of the flake. Moreover, smaller flakes typically have wider oxide layers. This suggests that thinner β-2D-Sb may oxidize more rapidly. In fact, smaller flakes are thinner than larger flakes and their thicknesses decrease as we go further from the center.

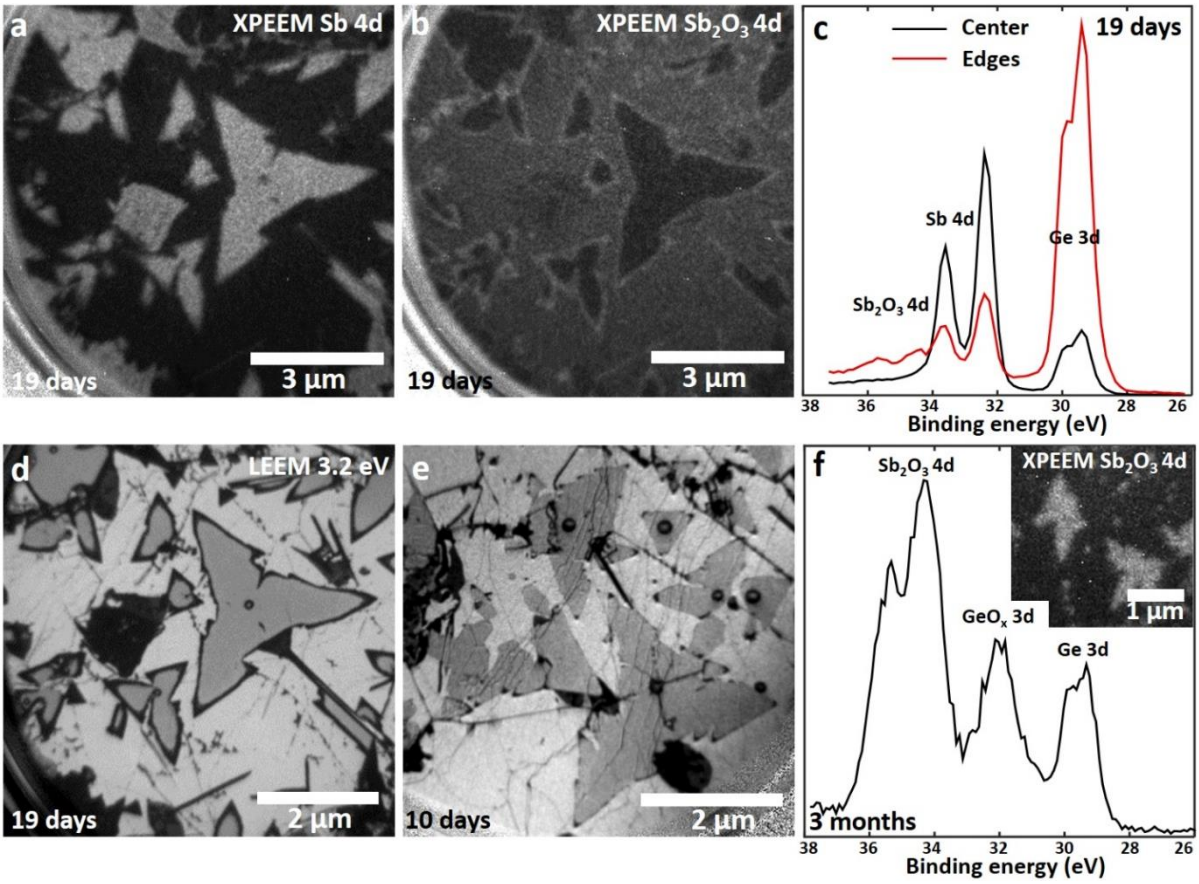

Figure 6.9 a) XPEEM image of β-2D-Sb exposed to atmospheric conditions for 19 days at a binding energy of 32.4 eV (Sb $4d_{5/2}$). Measured using a 250 eV photon energy. b) XPEEM of the same region at a binding energy of 34.6eV (Sb_2O_3 $4d_{5/2}$). c) Corresponding XPS spectra of the flakes' edges and center. d) Corresponding bright-field LEEM image (3.2 eV). e) Bright-field LEEM image (3.2 eV) of β-2D-Sb exposed to atmospheric conditions for 10 days. f) XPS spectrum and XPEEM image of β-2D-Sb on graphene/Ge(111) exposed to atmospheric conditions for three months at a binding energy of 34.3 eV (Sb $4d_{5/2}$). Measured using a 400 eV photon energy.

LEEM of β-2D-Sb exposed to air for 10 days reveals the early stages of β-2D-Sb oxidation (Figure 6.9e). The oxide nucleates primarily at the tips of the flakes. There are also oxide patches beginning

to form on some of the edges of the flakes. The width of the oxide regions is larger at the tips (~80 nm vs. ~20 nm) and all tips are oxidized. This suggests that Sb_2O_3 nucleates at regions with kinks and dangling bonds, which are concentrated at the tips and edges with high index crystallographic directions. While XPEEM is not sensitive enough to detect monolayer oxide regions at step edges on the surface of the flake, LEEM should be able to resolve them. Still, no oxide is detected at step edges. In fact, the steps on the surface are usually oriented along the Z1 directions and are atomically smooth, as observed with LEEM and STM. These edges are believed to be less reactive due to the lack of kinks. One could also hypothesize that oxidation nucleates at the edges of the flakes due to a potential catalytic effect of the graphene surface. Bulk Sb is stable in dry air and oxidizes slowly in moist air [17]. Two potential mechanisms therefore come to mind. First, graphene could have a direct catalytic effect on the oxidation reaction. However, since graphene is a self-passivated inert material with a small DOS at the Fermi level, it is unlikely that it would catalyse the oxidation reaction. In fact, both the adsorption energy and charge transfer between O_2/H_2O and graphene is small[264, 265]. The second potential mechanism would be to increase the availability of O_2 and/or H_2O species at the edges of β-2D-Sb flakes due to an increased adsorption on graphene. While graphite is known to be hydrophobic under ambient conditions[266], there is some debate about the hydrophobicity of graphene[267-270]. In fact, the hydrophilicity increases for monolayer graphene[268] and substrate doped p-type graphene[269]. Nonetheless, graphene remains only moderately hydrophilic under all conditions and unlikely has any catalytic effect on β-2D-Sb oxidation at the edges.

After three months of ambient exposure, β-2D-Sb flakes are oxidized over their whole surface (Figure 6.9f). The XPS spectrum reveals only Sb_2O_3 (Sb $4d_{3/2}$ at 35.4 eV and Sb $4d_{5/2}$ at 34.2 eV) and GeO_x 3d (32.0 eV) is present underneath the flakes. Even though no pristine Sb 4d peaks are detected, the oxide does not go through the whole thickness of the flake. In fact, Raman modes are typically detected on β-2D-Sb samples exposed to ambient conditions for more than a year and long exposition times to the high-intensity X-ray beam leads to the reduction of the oxide and the recovery of the initial crystallographic orientation of the flakes[36] (not shown).

6.3 Growth of metastable ultrathin A17 antimony

As mentioned in Chapter 2, the A17 phase is the most stable phase for P and becomes more and more unstable as the atomic number increases in the group VA. Metastable bulk A17 As exists, but A7 As is the stable phase. On the other hand, only A7 is observed in bulk Sb and Bi. Nonetheless, single and few-layer α-2D-Sb (ultrathin A17 Sb) were recently synthesized by molecular beam epitaxy on WTe_2 [163]. Moreover, the authors claim that the A17 phase is stable up to at least 20 layers, based on a (flawed) Raman analysis.

This section sheds light on the metastability of A17 Sb and describes its phase transition to A7, which occurs at a thickness of ~8 α-2D-Sb bilayers.

6.3.1 Growth of α-2D-Sb

In addition to the β-2D-Sb flakes, A7 Sb(111) atoll islands and A7 nanowires, the deposition of Sb_4 on graphene leads to the nucleation of rectangular α-2D-Sb flakes (Figure 6.10a). There are two main types of rectangular islands seen in LEEM: bright homogeneous flakes as well as textured dark islands. As will be discussed below, the bright rectangular flakes are the α-2D phase, and the dark flakes are the A7 phase in the (110) orientation. The μ-LEED pattern of a single rectangular island is shown in Figure 6.10a (inset). The rectangular LEED pattern has a (10) spot extinction is reminiscent of the LEED of α-2D-P. Here the lattice constants are 4.25 ± 0.05 Å and 4.57 ± 0.05 Å. Considering the symmetry and lattice parameters, the LEED pattern could originate from three possible phases: AB stacked α-2D-Sb (A17), AA stacked α-2D-Sb and A7 Sb(110). To identify the possible phases, structural relaxation of single and few-layer AB α-2D-Sb, AA α-2D-Sb and A7 Sb(110) films is carried out using DFT. The calculated in-plane lattice constants for α-2D-Sb are are a_{AA}=4.28 Å, a_{AB}=4.27 Å, c_{AA}=4.55 Å and c_{AB}=4.81 Å. The surface lattice parameters of bulk A7 Sb(110) are 4.31 Å and 4.51. Moreover, the calculations indicate few bilayers thick A7 Sb(110) rearranges into AA α-2D-Sb (APPENDIX H). While these results tend to indicate that the LEED patterns belong to AA α-2D-Sb, larger area LEED (~100 μm^2 beam) paints a clearer picture of the grown phases (Figure 6.10b). In order to see all LEED spots, two LEED patterns (29 eV and 44 eV) are shown. A total of six diffraction rings associated to randomly oriented Sb islands on the weakly interacting graphene substrates are observed. The LEED pattern of β-2D-Sb (fourth ring)

is used for reciprocal space calibration and the other rings are indexed as follows (from smallest to largest). The first two rings with lattice parameters of 4.71 ± 0.1 Å and 4.52 ± 0.1 Å are the (01) spots of AB and AA α-2D-Sb, respectively. The third ring has a lattice parameter of 4.29 ± 0.1 Å and is the (10) spot of AB α-2D-Sb. The fourth ring is β-2D-Sb (4.28 Å). The last two rings are the (11) spots of AB and AA α-2D-Sb. We note here that AA α-2D-Sb refers to both AA α-2D-Sb and A7 Sb(110) since they are undistinguishable at low thickness.

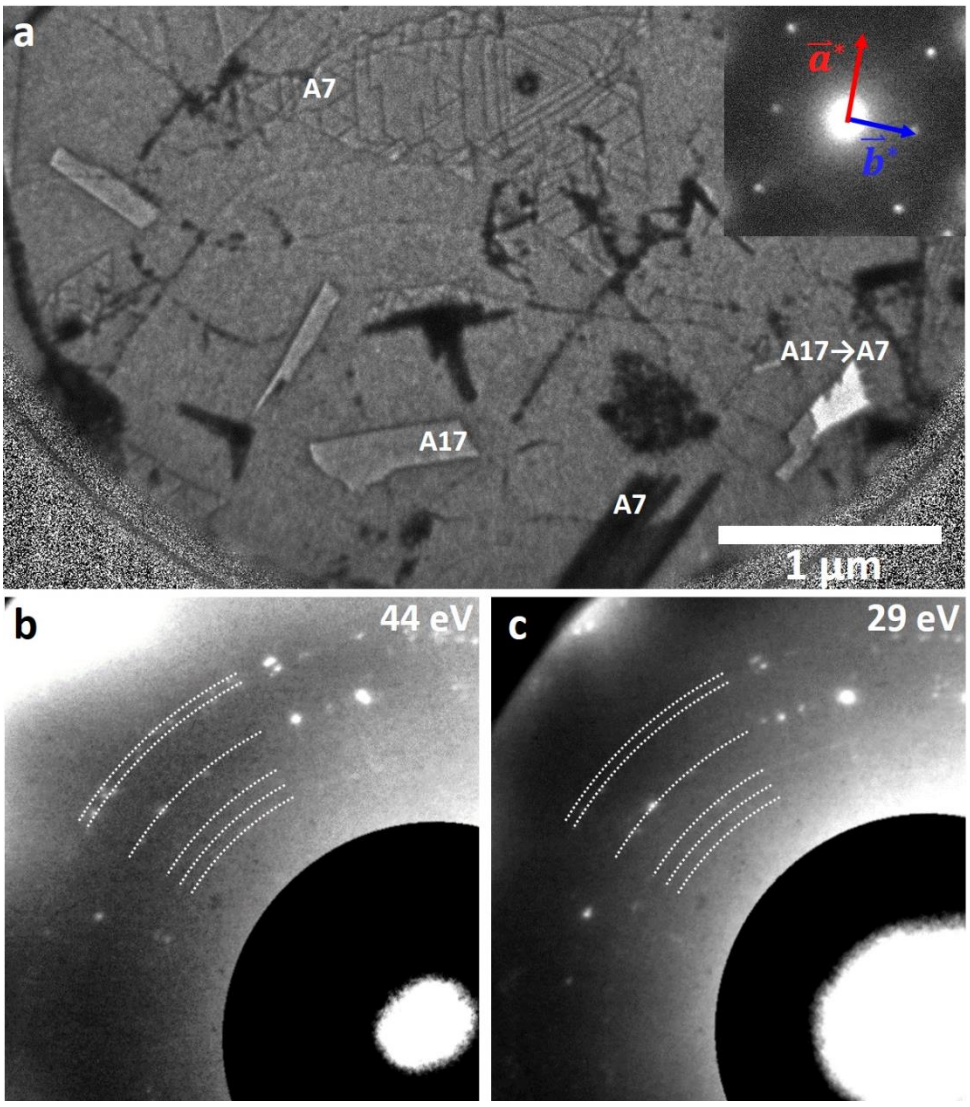

Figure 6.10 a) Bright-field LEEM (1.9 eV) of the various Sb phase grown on graphene/Ge(110) at T=230 °C and F=66 nm/min. Inset: *ex situ* LEED pattern of Sb(110). b-c) *in situ* LEED pattern of the various Sb phases grown on Sb/Ge(110) at T=250 °C and F=130 nm/min. ~1/4 of the Ewald sphere is shown and brightness/contrast corrections are applied. Adapted from [40].

While these results tend to indicate that the LEED patterns belong to AA α-2D-Sb, larger area LEED (~100 μm^2 beam) paint a clearer picture of the grown phases (Figure 6.10b). In order to see all LEED spots, two LEED patterns (29 eV and 44 eV) are shown. A total of six diffraction rings associated to randomly oriented Sb islands on the weakly interacting graphene substrates are observed. The LEED pattern of β-2D-Sb (fourth ring) is used for reciprocal space calibration and the other rings are indexed as follows (from smallest to largest). The first two rings with lattice parameters of 4.71 ± 0.1 Å and 4.52 ± 0.1 Å are the (01) spots of AB and AA α-2D-Sb, respectively. The third ring has a lattice parameter of 4.29 ± 0.1 Å and is the (10) spot of AB α-2D-Sb. The fourth ring is β-2D-Sb (4.28 Å). The last two rings are the (11) spots of AB and AA α-2D-Sb. We note here that AA α-2D-Sb refers to both AA α-2D-Sb and A7 Sb(110) since they are undistinguishable.

Cross-sectional STEM of rectangular Sb flakes grown on graphene provides atomic-scale information and allow to confirm the grown phases (Figure 6.11). STEM lamella are prepared using FIB by cutting either at 45° (Figure 6.11a) or perpendicular (Figure 6.11b) to the long-axis of the flakes. There is a sharp vdW interface between the Sb flake and the graphene substrate. In fact, the dark band corresponds to the graphene layer, which has a lower HAADF STEM intensity due to the small atomic number of C, as compared to Sb and Ge. There is a ~0.9 nm gap between the Ge substrate meaning that the Sb-C and C-Ge interfaces are weakly interacting and without covalent bonds. The faint bright band in the center of the interface located 3.7 ± 0.1 Å below the bottom Sb atoms is the graphene layer. On the other hand, the C-Ge distance is more difficult to measure since the top Ge atoms are not well resolved.

The two views confirm that the flakes are AB α-2D-Sb. For the flake in Figure 6.11a (45° cut), four bilayers are observed. The bilayer thickness is 2.7 ± 0.1 Å and the inter-bilayer distance is 3.3 ± 0.1 Å. By comparison, the DFT calculated values for four-bilayer freestanding AB α-2D-Sb are 2.83 Å and 3.23 Å. The measured and calculated projections are in good agreement (Figure 6.11a). The AB stacking of A17 Sb is observed, and the lateral periodicity is 3.2 ± 0.1 Å (as compared to the calculated 3.19 Å ($\bar{1}01$) d-spacing of few-layer A17 Sb). This indicates that the flake is viewed along the [101] direction and that the long-axis is oriented with either the [100] or [001] direction of A17 Sb, which are at 48.6° and 41.4° from the [101] direction, respectively. Indeed, STEM shows that the long-axis corresponds to the [100] direction of A17 Sb (Figure 6.11b). The lateral

periodicity is 4.7 ± 0.1 Å, which corresponds to the c-axis of few-layer A17 Sb (4.81 Å DFT calculated value and 4.7 ± 0.1 Å LEED value). There are nonetheless some differences between the calculated and measured structures. In contrast to α-2D-P, DFT calculations indicate that α-2D-Sb is buckled (each monolayer within the bilayer is split into two atomic planes with a buckling height of ~0.3 Å, depending on the number of bilayers). This buckling is not observed in the STEM image. Interestingly, the layer structure of the flake in Figure 6.11b is closer to AA α-2D-Sb than AB α-2D-Sb. In fact, for four bilayer α-2D-Sb, the calculated buckling height varies between 0.03-0.05 Å (larger buckling for the top and bottom bilayers). The calculated bilayer thicknesses are 2.92 Å (top and bottom) and 3.03 Å (center bilayers) and the inter-bilayer distances are 3.15 Å (outside bilayers) and 3.09 Å (center bilayers). This suggests that the flakes in Figure 6.11 (a, b) are possibly two different stacking of α-2D-Sb. Nonetheless, the STEM data confirms the presence of the A17 Sb phase, which was previously thought to be an unstable bulk phase.

Raman scattering spectroscopy points in the same direction as the STEM and LEED data (Figure 6.11c). Since the A17 and A7 phases grow simultaneously on graphene, most regions of the samples yield a mixed Raman signal. Nonetheless, some regions display almost exclusively the Raman signal of single phases. The regions with two peaks (~124 cm^{-1} and ~150 cm^{-1}) are β-2D-Sb. Other regions have three active Raman modes (133.7 cm^{-1}, 146.7 cm^{-1} and 160.6 cm^{-1}) and are associated to α-2D-Sb. In fact, the Raman spectrum of the A17 phase has been extensively studied in α-2D-P and bulk A17 P samples[19]. With in-plane polarization, α-2D-P has three active Raman modes: A_g^1, B_{2g} and A_g^2. Considering that A17 Sb and P share the same symmetry, we label the peaks as follows: A_g^1 (133.7 cm^{-1}), B_{2g} (146.7 cm^{-1}) and A_g^2 (160.6 cm^{-1}). On the other hand, Shi et *al*. [163] identified two Raman peaks (A_g^1 at 131 cm^{-1} and A_g^3 at 147 cm^{-1}). According to the authors, the A_g^1 and A_g^3 peaks shift to 118 cm^{-1} and 150 cm^{-1} as the flake thickness increases from 3 to 20 bilayers. This labelling was based on DFT calculations for monolayer α-2D-Sb. However, DFT and experimental Raman peak positions do not agree for 2D-Sb, at least for the β phase[153]. Moreover, it seems that a third peak (A_g^2 at 160.6 cm^{-1}) could not be resolved due to its overlap with the WTe_2 substrate peak. The shift reported by the authors most likely comes from the fact that the thicker flakes were in the A7 phase (potentially due to a phase transition).

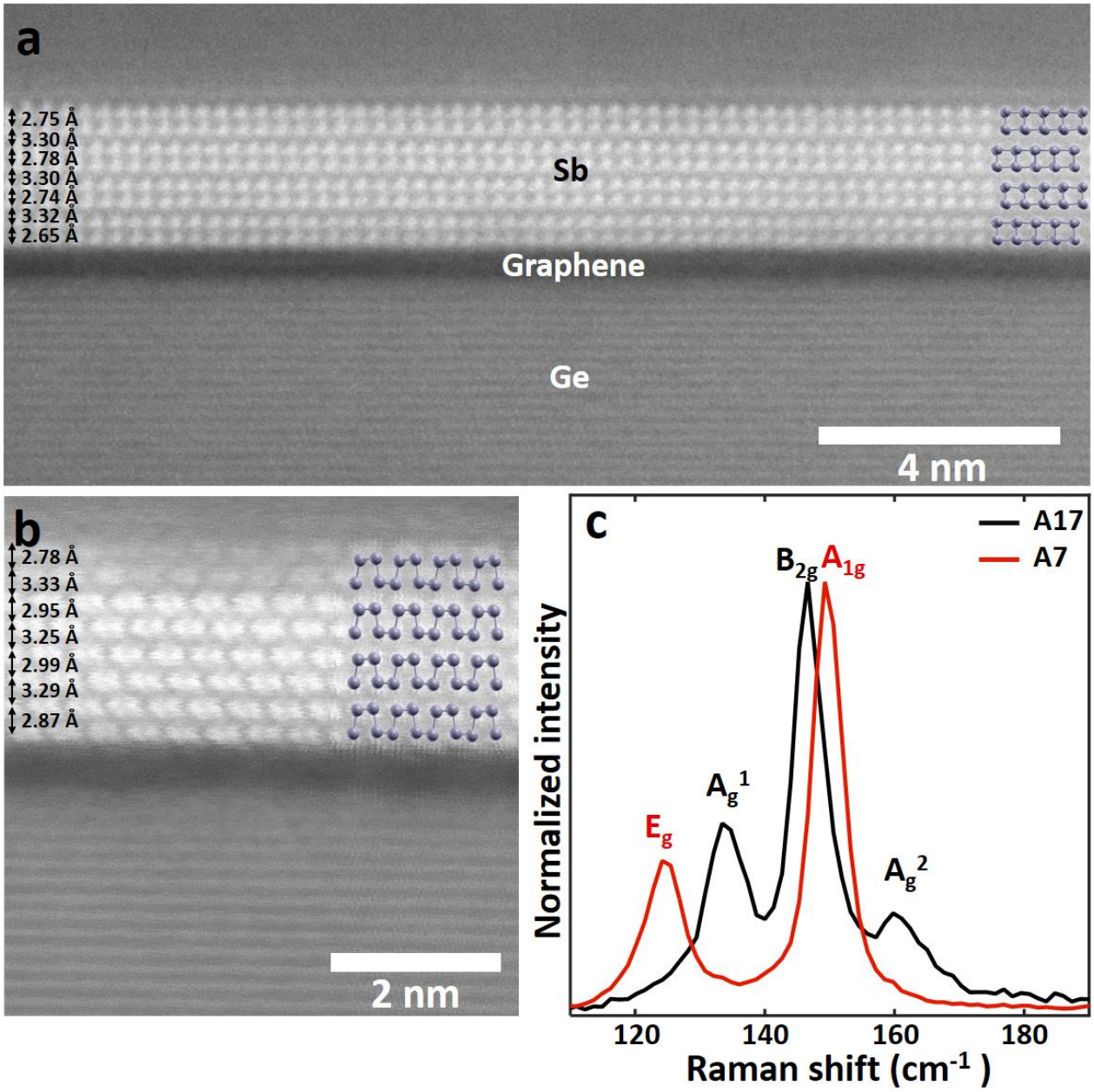

Figure 6.11 a) HAADF STEM (200 kV) of α-2D-Sb on graphene/Ge(110) viewed along the [101] direction. b) HAADF STEM (200 kV) of α-2D-Sb on graphene/Ge(110) viewed along the [100] direction. c) Raman spectra (633 nm irradiation) of β-2D-Sb (A7) and α-2D-Sb grown on graphene/Ge(110). Adapted from [40].

Next, using real-time LEEM, we look at the growth dynamics of α-2D-Sb and its transition to A7 Sb. Unfortunately, it is not possible to pinpoint the experimental conditions leading to their nucleation and growth. The α-2D-Sb flakes were observed across most of the studied growth

conditions range (170-250 °C and 2.6-130 nm/min). Nonetheless, the highest ratio of A17/A7 nucleation was observed at high deposition rate and T. On the other hand, the nature of the surface seems to play a role in their nucleation. In fact, important sample to sample variations of the A17/A7 nucleation ratio were observed, independently of the growth conditions. Moreover, A17 flakes are often concentrated in particular areas of the samples, hinting to substrate effects.

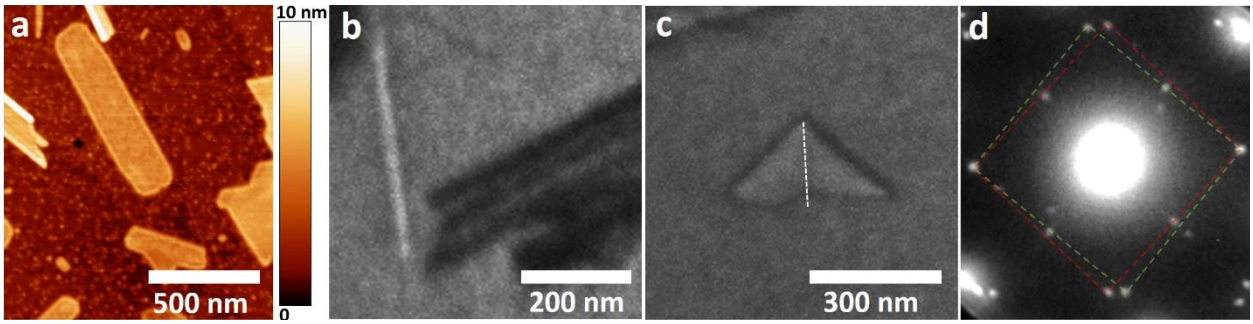

Figure 6.12 a) AFM image of α-2D-Sb flake on graphene/Ge(110). b) Bright-field LEEM image of α-2D-Sb nanoribbon on graphene/Ge(110). c) Bright-field LEEM image of L-shaped α-2D-Sb flake on graphene/Ge(110). d) Energy-averaged μ-LEED pattern of L-shaped α-2D-Sb flake on graphene/Ge(110). Note that the *ex situ* LEED might come from a flake which has undergone the A17→A7 Sb(110) phase transition. Adapted from [40].

There are various types of α-2D-Sb flakes which grow on graphene. The most prevalent type is rectangular flakes such as those shown in Figure 6.10. AFM indicates that these flakes are generally thinner than β-2D-Sb. In fact, they are generally between 2.5-4.5 nm (4-8 bilayers). In most cases, their long-to-short axis aspect ratio varies between 2-5 and the STEM data indicates that the long axis is oriented in the [100] (armchair) direction. Typically, the long edges of the flakes are straight, whereas the short edges are wavier. Some flakes are however much more elongated and have aspect ratios up to 20 and can be as narrow as 20 nm (Figure 6.12b). These flakes can be qualified as nanoribbons. This is particularly interesting since quantum confinement and edge-dominated electronic transport is likely to be observed in the nanoribbons. L-shaped flakes are also observed (Figure 6.12 (c, d)). These flakes are formed by two NWs, which make a ~90° angle. α-2D-Sb grows in the inside angle formed by the NWs. Dark-field LEEM (not shown) indicates that the flakes are composed of two grains which join at the bisector of the ~90° angle. The μ-LEED pattern sheds light on the crystallography of the L-shaped flakes (Figure 6.12d). At first sight, only 10

first-order LEED spots are visible. However, dark-field LEEM indicates that the (11) and $(\bar{1}\bar{1})$ LEED spots of one grain overlap with the $(1\bar{1})$ and $(\bar{1}1)$ LEED spots of the other grain. This means that the grain boundary is along the $[101]$ and $[\bar{1}01]$ directions of the two grains.

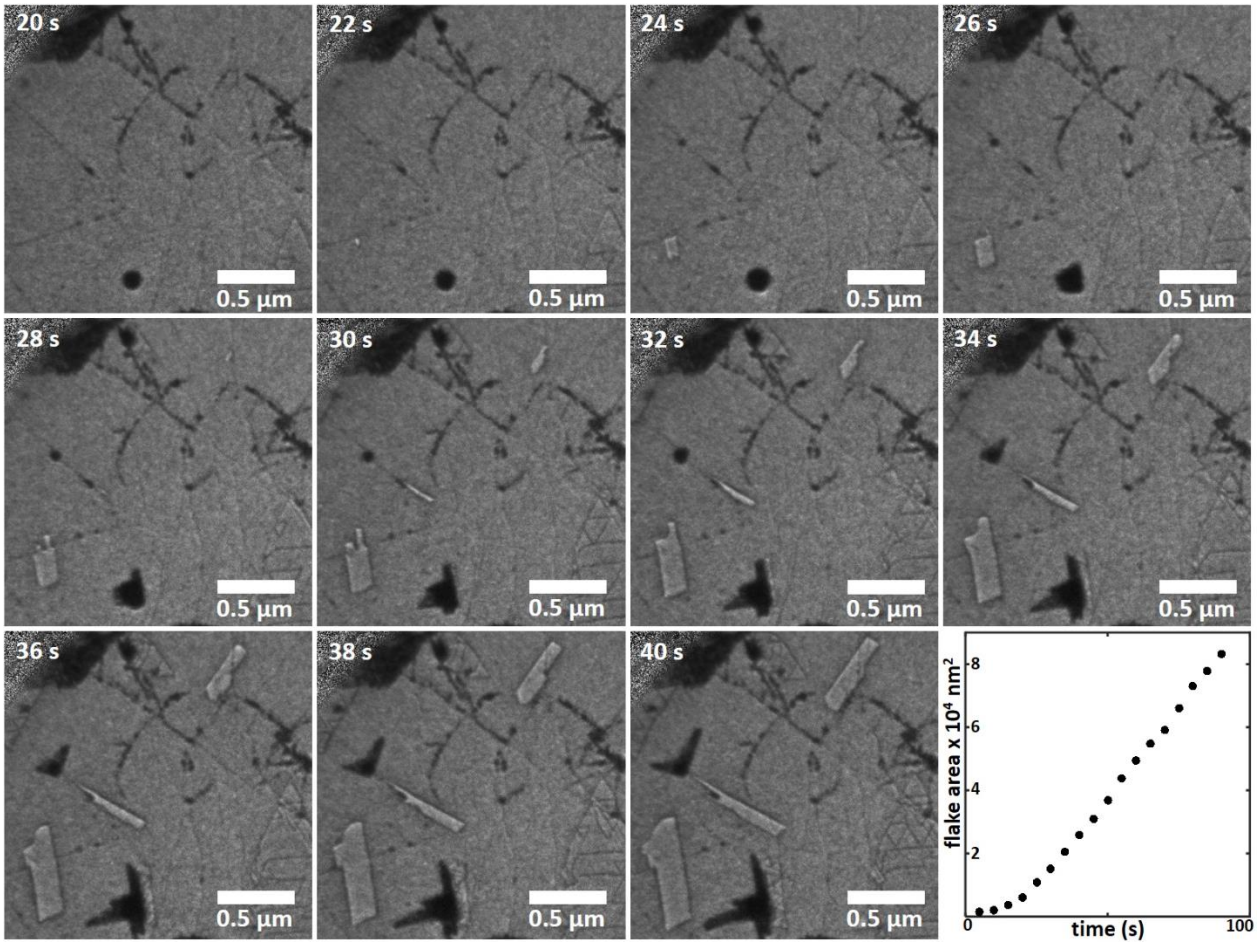

Figure 6.13 Bright-field LEEM snapshots (1.8 eV) of α-2D-Sb growth dynamics on graphene/Ge(110) at F=65 nm/min and T=230 °C. Bottom right: α-2D-Sb flake area evolution. F=2.6 nm/min and T=190 °C. Adapted from [40].

Below, we look at the growth dynamics of the rectangular α-2D-Sb flakes. Bright-field LEEM snapshots of the nucleation and growth of three α-2D-Sb flakes on graphene/Ge(110) are presented in Figure 6.13. Like the A7 phase, the rectangular α-2D-Sb flakes nucleate at defects on the graphene surface (see Figure 6.13 (22 s and 28 s)). The flakes in Figure 6.13 all nucleate a linear graphene defects. However, nucleation at point defects and holes in the graphene surface were also observed on other samples. The α-2D-Sb flakes are flat and do not form 3D nuclei as was observed

for the clover-shaped β-2D-Sb flakes on graphene. This suggests that the flakes nucleate directly in the A17 phase and possibly at single layer thickness. This nucleation mode indicates that the growth of thin α-2D-Sb on weakly interacting substrates can be controlled more easily than β-2D-Sb.

The LEEM measured growth dynamics of isolated flakes (Figure 6.13) suggests a 2D growth mode with the graphene surface being the main source of Sb_4 precursor species. In fact, there is an initial acceleration of the growth rate (dA/dt) followed by a linear region. The linear region is a sign that the growth is limited by the diffusion length of Sb_4 on graphene, similar to β-2D-Sb. On the other hand, the origin of the initial accelerated growth is slightly more difficult to explain. The early growth stage (first 30 seconds) is well fitted by an either an exponential ($A \sim e^{\alpha t}$) or by $A \sim t^2$. An exponential rate means that the growth rate is proportional to the flake area and a quadratic behavior indicate that the growth rate is proportional to the flake's radius or edge length. Here it makes more sense that the growth rate is limited by the flake's radius since we know that the growth is mainly fed by Sb_4 diffusing on graphene (in opposition to growth from Sb_4 deposited on the flake, which would lead to $dA/dt \sim A$). This behavior implies a reaction limited process. It is therefore likely that the initial growth stage is limited by the dissociation of Sb_4 species at the edges of the flakes. Moreover, for the growth rate to be quadratic, the flakes' edges need to be saturated by Sb_4 molecules. Studying the dynamics of the early growth stage under different conditions (T and F) would provide important information regarding the nature of the processes occurring at the edges. However, high-resolution and high-quality data of the early growth stages of α-2D-Sb flakes is not available.

6.3.2 A17 to A7 phase transition

Since A7 is the most stable Sb bulk phase, thermodynamics tells us that A17 2D flakes eventually become unstable or metastable and are expected to transition to A7. However, it does not tell us anything about the phase transition mechanisms. On the other hand, STEM and *in situ* LEEM can provide unprecedented insight into the phase transition mechanisms. Two different phase transition mechanisms have been observed (Figure 6.14). The first is the coalescence with A7 grains and the second is a spontaneous diffusionless shuffle transition.

The transition from A17 to A7 by grain coalescence occurs when an α-2D-Sb flake coalesce with either an A7 Sb(111) flake or Sb(110) island. The coalescence with a Sb(111) flake is shown in Figure 6.14a. Here, it is not clear what the intermediate state is. As the A17 (L-shaped) flake coalesce with the A7 flake, a transition front moves across the flake in ~20 seconds. It is also possible that the front is an overlayer. However, the front is not oriented with any particular crystallographic direction as an atomic step would be. Moreover, it does not leave an atomically smooth surface behind. It is therefore most likely that the front is the interface between the A7 and A17 phase, which expands due to the higher stability of the A7 phase.

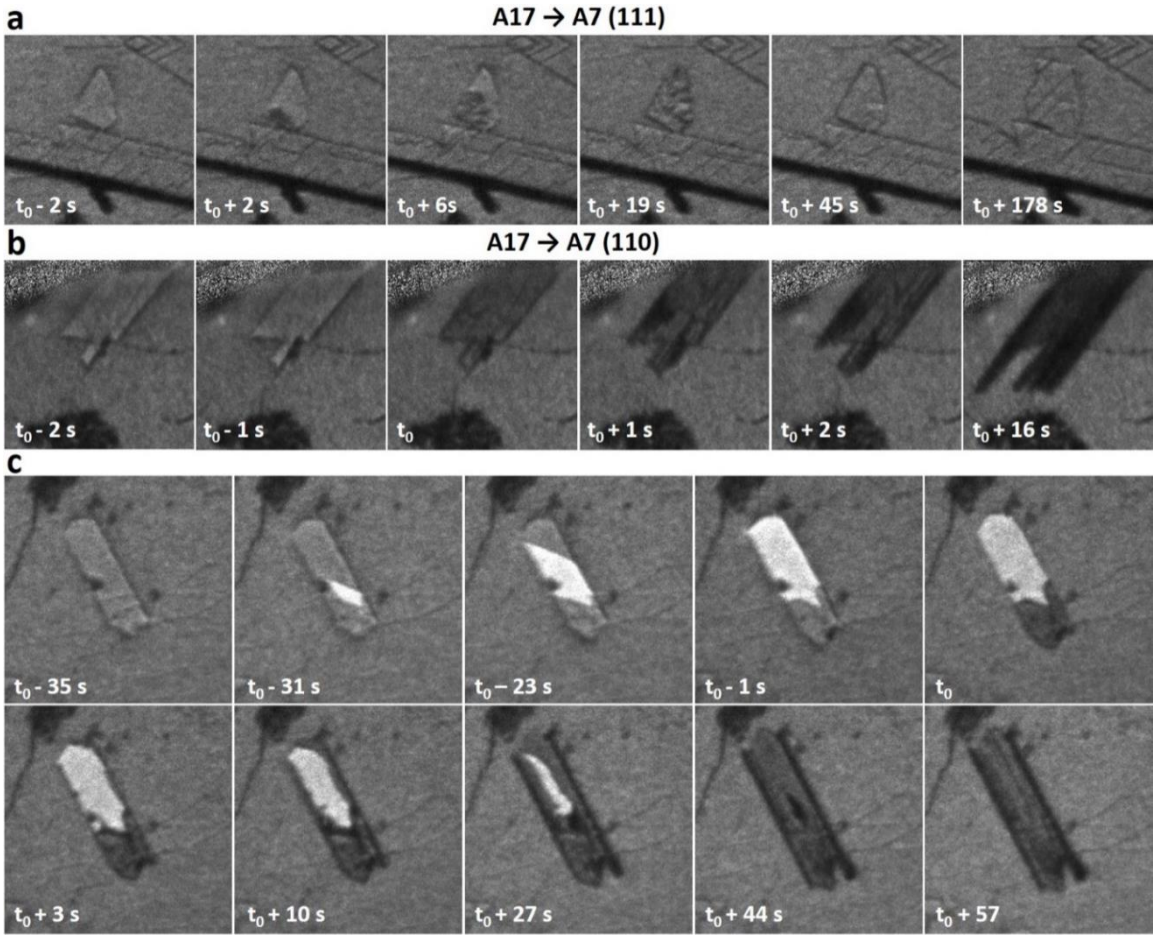

Figure 6.14 *in situ* bright-field LEEM snapshots of the A17 → A7 phase transition. Images are 1×1 μm^2. a) A17 → A7 (111) by grain coalescence (F=2.6 nm/min, T=190 °C). b) A17 → A7 (110) by spontaneous diffusionless transition (F=66 nm/min, T=230 °C). c) A17 → A7 (110) by spontaneous diffusionless transition with the growth of an overlayer (F=2.6 nm/min, T=190 °C). Adapted from [40].

After the phase transition, the surface of the flake becomes atomically smooth due to deposition and new A7 Sb(111) terraces grow. The orientation of the atomic steps indicates that the crystallographic orientation of the two flakes is the same. Moreover, a sharp tip similar to those observed in the clover-shaped β-2D-Sb begin to form, confirming that the phase is homogeneous throughout the thickness of the flake, rather than being an A17/A7 heterostructure. Coalescence of A17 flakes with A7 Sb(110) islands display a similar behavior, but will not be discussed here.

While the A17 → A7 phase transition by grain coalescence is interesting, we will focus mostly on the spontaneous phase transition mechanism, which is the most frequently observed. At first sight, it seems that the spontaneous transition occurs in two different ways (Figure 6.14 (b, c)). However, the underlying mechanisms is the same. In the first case (Figure 6.14b), the α-2D-Sb flake grows laterally as was described in the previous sub-section. Then, a sudden and homogeneous decrease of the LEEM intensity is observed over the whole surface of the flake. This contrast change cannot be caused by a growth-related process and is attributed to the A17 → A7 phase transition. In fact, it occurs in a timescale shorter than the LEEM data acquisition time (1 s), no matter the deposition rate. Since no motion blur is observed, we can ascertain that the transition happens in a much smaller timescale. Immediately after the transition, elongated nanostructures begin to form along the long axis of the flake. At the same time, nanowires form on the edges of the flake. At this point, lateral growth of the flake along the short axis stops and the flake only grows along its long axis. Moreover, the nanostructures evolve and eventually lead to the formation of additional nanowires which grow from the central region of the flake.

In the second case of spontaneous transition, an overlayer first forms on the α-2D-Sb flake (bright layer in Figure 6.14c). We can ascertain that the bright layer comes from a growth-related process since stopping the Sb_4 deposition freezes the spread of the layer. The bright contrast (in bright-field LEEM) indicates that the overlayer is crystalline and flat. It is however not possible to determine its exact nature. Potential candidates include an α-2D-Sb stacking fault and a β-2D-Sb overlayer. We note that the overlayer only grows in one direction from its nucleation point and never fully cover the whole surface of the flake. Then, a contrast change occurs on the whole surface of the flake. The contrast change is more pronounced on the uncovered regions but can be seen underneath the overlayer. This indicates that the phase transition occurs everywhere in the flake (but does not necessarily affect the overlayer). After the phase transition, the overlayer begins to

shrink and a darker layer takes its place. The dark layer also shrinks until both layers disappear. The final state is the same as for the first spontaneous transition mechanism and it appears that the formation of the overlayer has nothing to do with the phase transition.

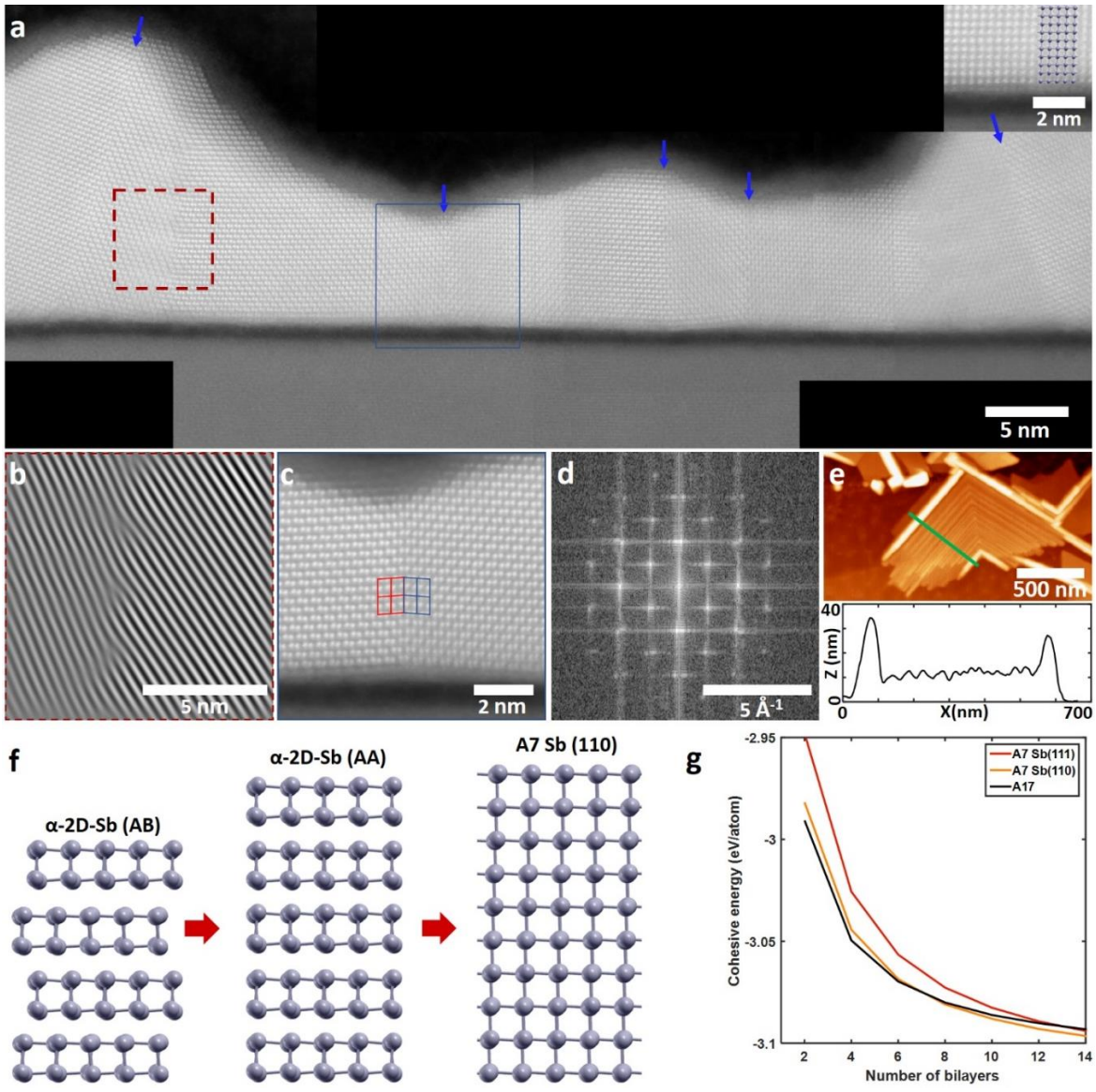

Figure 6.15 a) Cross-sectional STEM of a four bilayers thick α-2D-Sb flake on graphene/Ge(110) viewed along the [101] direction. FFT filtered STEM image ((111) planes) of the rotated grain boundary in (a). c) High-resolution STEM of a twin boundary. d) FFT of the STEM in (c). e) AFM of an L-shaped facetted Sb(110) flake. The profile shows the edge NWs and periodic nanoridges. f) Schematics of the proposed phase transition mechanism. g) DFT calculated (PBE+D2) cohesive energy as a function of thickness of A7 Sb(111), A7 Sb(110) and A17 Sb (010). Adapted from [40].

To better understand the spontaneous phase transition mechanism, we look a STEM images of the flakes after the transition (Figure 6.15). The flakes are selected by SEM in a dual beam SEM/FIB based on their shape and presence of nanostructures along their long axes. Lamella are prepared with FIB by cutting perpendicular to the flakes' long axes. Atomic resolution STEM (Figure 6.15a) viewed along the $[1\bar{1}0]$ and $[\bar{1}1\bar{1}]$ directions indeed confirm that the A17 flakes transition to A7 Sb(110). However, the flakes are polycrystalline with multiple parallel nanoscale domains oriented along the long axis of the flake. The average surface orientation is (110) but each nanodomain is slightly tilted. The nanostructures seen in LEEM are nanoridges aligned along the flake's long axis and nanowires can be seen at the edges of the flake. There are rotated grain boundaries at the interface between the nanowires and the center of the flake. Rotations of ~9.7° and ~13.7° around the $[1\bar{1}0]$ direction are observed at the right and left interfaces, respectively. The rotation leads to the formation of dislocations at the interface with the NW, clearly seen in the FFT filtered image ((111) planes) (Figure 6.15b). These rotated boundaries suggest that the nanowires potentially nucleate on the flakes' edges after the transition. However, we note that most flakes observed in STEM do not have rotated grain boundaries at the interfaces with the edge NWs (Appendix I). In fact, most edge nanowires have the same atomic structure as the nanostructures inside the flake.

There are twin boundaries at every hill and every valley of the nanostructure and edge NWs (Figure 6.15 (a, c, d)). High-resolution STEM and its FFT indicate that the twinned planes are (112) planes. The formation of the twin domains has the obvious effect of allowing every facet of the nanostructures and nanowires to orient with the low energy (111) planes of A7 Sb. However, before reaching equilibrium, the top facets are oriented with the (110) planes, which also have low surface energies due to surface reconstruction and self passivation of the dangling bonds. Interestingly, the parallel nanoridges array have a relatively constant periodicity of 35 nm, as can be seen with AFM (Figure 6.15e).

The LEEM and STEM data allow to propose a phase transition mechanism for the spontaneous phase transition (Figure 6.15f), similar to the shuffle and shear mechanism hypothesized for bulk P[61] but with an additional intermediate step. First, we note that the A17 (010) and A7 (110) phases are closely related. A17 Sb(010) is made of AB stacked α-2D-Sb bilayers. A7 Sb(110) can be thought of as AA stacked α-2D-Sb bilayers with additional interlayer bonds and broken plane bonds. The similarity between the two phases is even more obvious at nanoscale thicknesses. In

fact, DFT calculations indicate that A7 Sb(110) and AA stacked α-2D-Sb both have the same structure up to ~12 bilayers (~7 nm) (APPENDIX H). The bilayer structure of A7 Sb(110) is oriented with the (110) planes, rather than the (111) planes of bulk A7 Sb. Moreover, few-layer Sb(110) has the same orthorhombic unit cell as AA α-2D-Sb (Figure 6.16). In fact, the rhomboheral unit cell of A7 Sb can also be described by a monoclinic unit cell with β=87°. However, below 12 bilayers β increases to ~90°, making it orthorhombic and identical to AA α-2D-Sb.

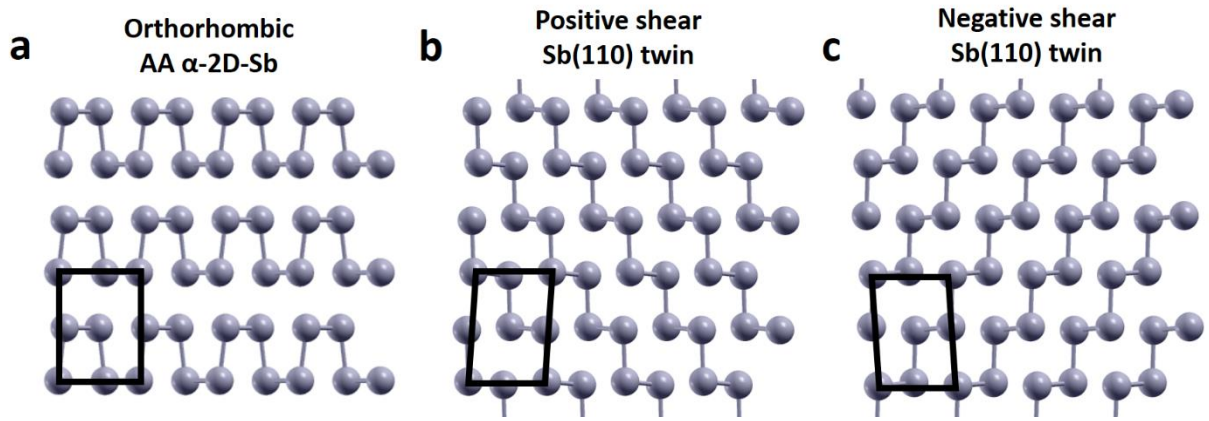

Figure 6.16 a) Stick and balls model for AA α-2D-Sb showing the orthorhombic unit cell. b-c) Stick and balls model of A7 Sb(110) with monoclinic unit cell which can be obtained by positive or negative shear of the orthorhombic AA α-2D-Sb unit cell. Adapted from [40].

We therefore propose that the phase transformation is a simple shuffle from AB to AA α-2D-Sb, followed by a gradual shear deformation of the orthorhombic unit cell, as the nanoridges form (Figure 6.15f). The transition is believed to occur at a critical thickness of ~8 bilayers (4.5 nm), when AA α-2D-Sb becomes more stable than AB α-2D-Sb. This hypothesis is supported by DFT calculation and AFM measurements. DFT calculations show that the most stable phase is AB α-2D-Sb up to a thickness of 7 bilayers. Below this thickness, the phase transition is not thermodynamically possible. Above it, the stability crossover makes the transition possible, even though an additional energy barrier is likely present. AFM measurements (APPENDIX J) indicate that the large majority of flat rectangular flakes are thinner than 4.5 nm, whereas the nanostructured rectangular flakes are all above this thickness. After the transition, AA α-2D-Sb gradually transforms to A7 Sb(110) by a shear deformation and by the formation of twin domains. This hypothesis is supported by the LEEM and STEM data. In fact, the presence of multiple twin

domains with their (110) planes only slightly off from the substrate surface plane suggests a common previous state allowing for their formation. Since A7 Sb(110) reorganizes into AA α-2D-Sb at the transition thickness, we propose that this common previous state is AA α-2D-Sb. In fact, the two twin domains can be directly obtained by either a positive or negative shear of the AA α-2D-Sb orthorhombic unit cell (Figure 6.16).

LEEM supports the hypothesis of an intermediate AA α-2D-Sb state. In fact, immediately after the transition, the LEEM contrast is homogeneous over the surface of the flake, indicating that the twin domains have likely not formed at this point. The nanoridges begin to form after the phase transformation. The nanoridges usually nucleate on the short edges of the flakes and expand inward during deposition (APPENDIX K). The formation of twin domains is driven by the minimization of surface energy. Since twin boundaries form during deposition, their energetic cost is compensated for by the energetic gain of the (111) surface planes formation. This process is at the origin of the growth of the periodic array of parallel nanoridges.

To better understand the twin domains formation, we look at the atomic and electronic structure of thin A7 Sb(110) and AA α-2D-Sb (Figure 6.17 and Figure 6.18). The DFT calculated (PBE+D2) charge density minus superposition of atomic charge densities for four bilayers AA α-2D-Sb, bulk A7 Sb and 8 nm A7 Sb(110) are shown in Figure 6.17 (a-c) respectively. Thin AA α-2D-Sb films have a bilayer structure similar to AB α-2D-Sb. The strongest Sb-Sb bonds are within the α-2D-Sb bilayers, as seen in the isosurface at 0.0067 e^-/a_0^3. However, there is significant interlayer bonding, especially in the center of the flake (0.0055 e^-/a_0^3 isosurface). The 0.0035 e^-/a_0^3 isosurface indicates that the covalent bonding is still significant even for the top and bottom bilayers. This contrasts with true layered phases, such as AB α-2D-Sb, A17 Sb and A7 Sb, which can be considered as quasi-vdW layered materials. AA α-2D-Sb has a true layered behavior below four bilayers, but interlayer bonding increases with thickness, especially in the center of the flake.

Nevertheless, DFT shows that there is a gradual transition of the bilayer structure from the (110) planes to the (111) planes as the film thickness increases (Figure 6.17 (b-e)). At first sight, both A7 Sb and Sb(110) thin films (~8 nm) have a (111) oriented bilayer structure. In bulk A7 Sb (Figure 6.17b), each Sb atoms forms three covalent bonds in the (111) planes and three weaker interlayer bonds. For A7 Sb(110) thin films, (111) bonding is dominating in the center of the flake. However, there is a fourth strong interlayer bond, typical of (110) bilayer bonding. This fourth bond plays a

key role in the twin domain formation after the AB→AA phase transformation. In fact, the third and fourth bonds are almost equivalent in thin Sb(110) films, for which β=90°. This bonding configuration makes the relaxation to either twin domain equivalent, and without significant energy barrier.

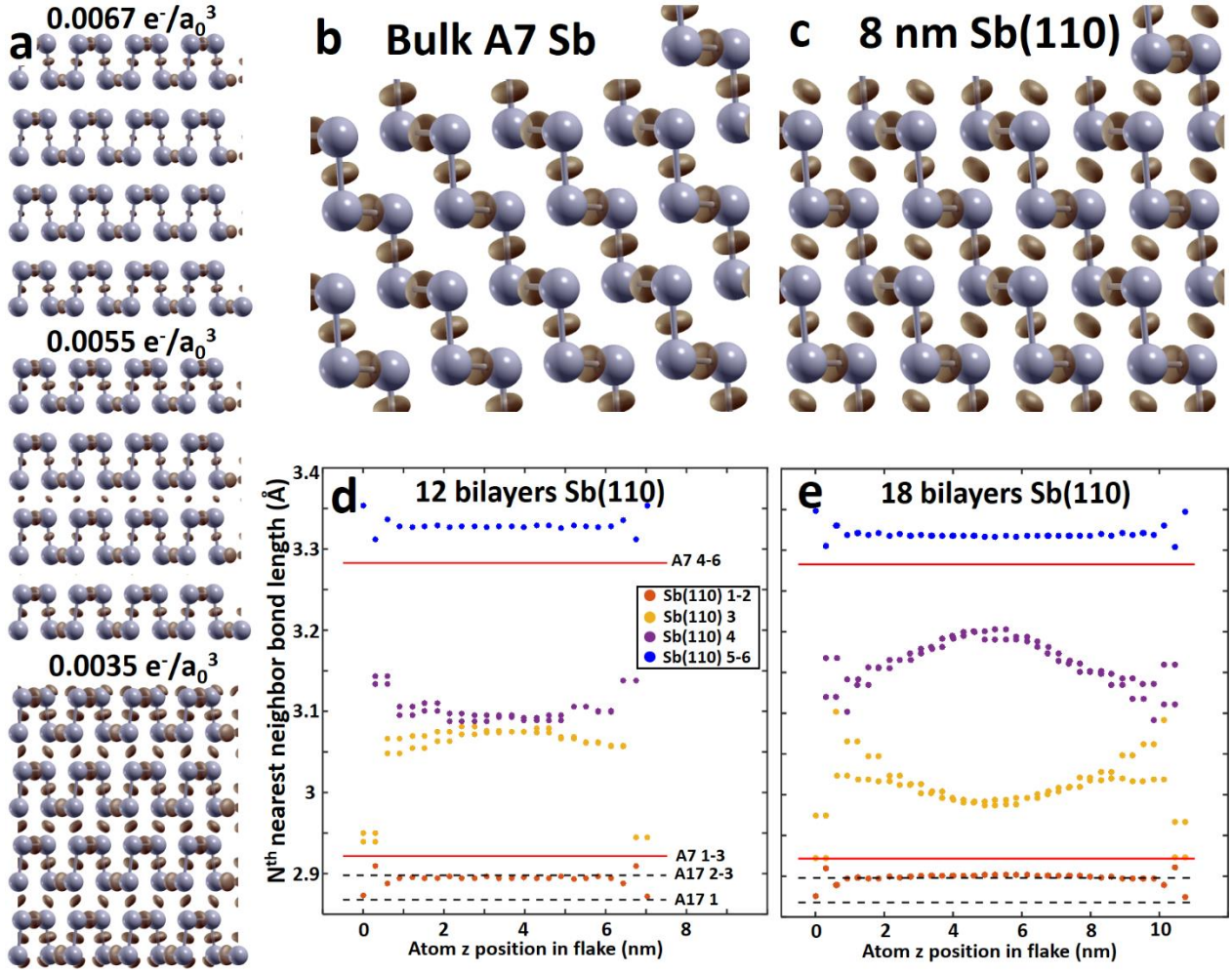

Figure 6.17 a) Charge density minus superposition of atomic charge densities isosurfaces of four bilayers thick AA α-2D-Sb. Calculated with DFT (PBE+D2). b-c) Charge density minus superposition of atomic charge densities of bulk A7 Sb (b) and 8 nm A7 Sb(110) (middle layers). Isosurfaces plotted at 0.0035 e^-/a_0^3. d-e) First to sixth nearest-neighbors distances for A7 Sb(110) thin films as a function of z-position (DFT calculated). Dashed black lines are the NN distances of bulk A17 Sb and red lines are the NN distances of bulk A7 Sb. Adapted from [40].

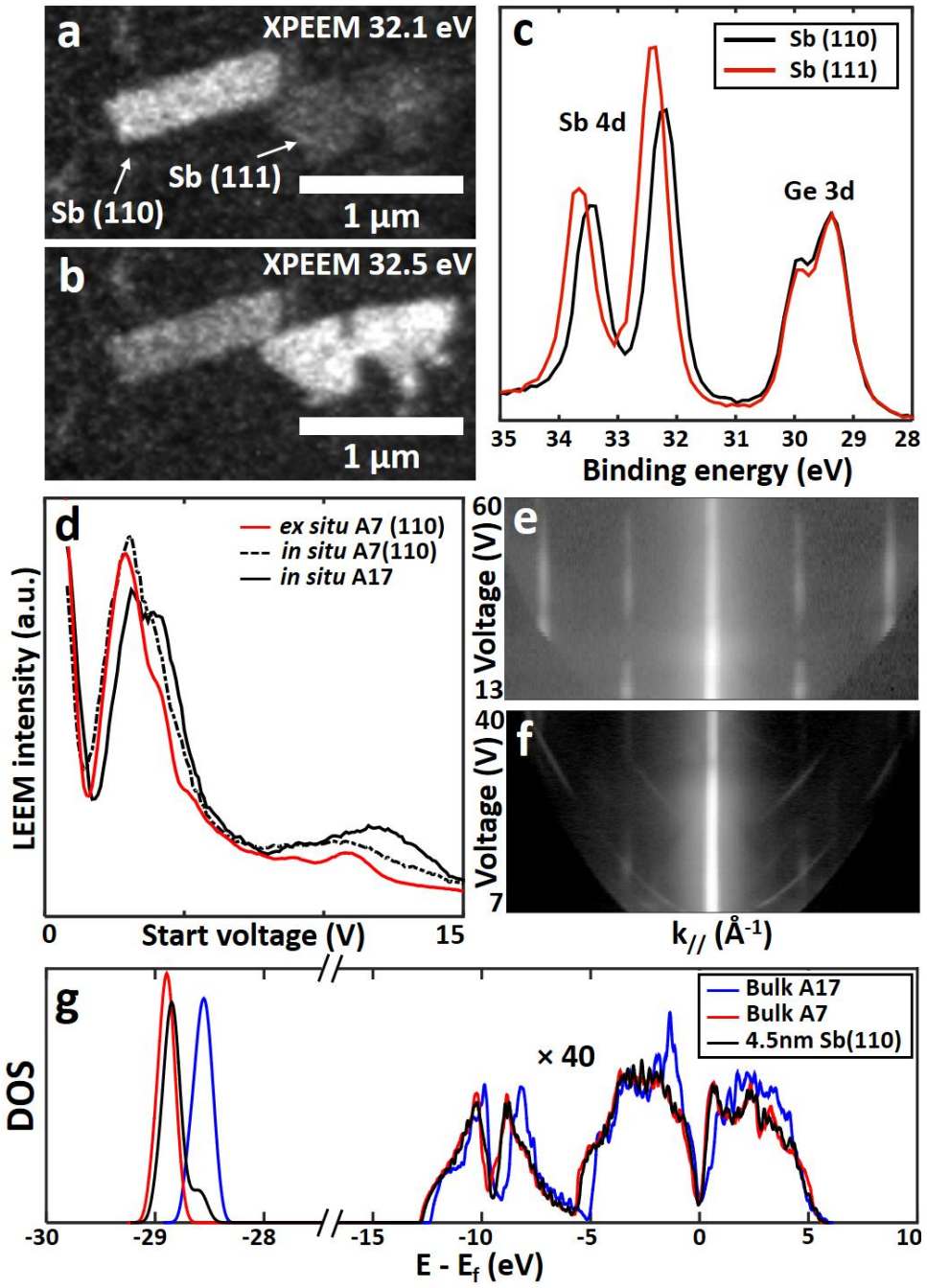

Figure 6.18 a-b) XPEEM images of an unfaceted Sb(110) rectangular flake and Sb(111) flakes taken at 32.1 eV and 32.5 eV binding energy. The data is obtained using at 250 eV photon energy. c) Corresponding XPS spectra of the two types of flakes. d) LEEM I-V curves of A7 Sb(110) and A17 Sb used to identify the phase of the flakes. e-f) LEED I-V profiles along the [001] direction for the rectangular Sb(110) flake (e) and a faceted Sb(110) flake (f). g) DFT calculated DOS of bulk A7 and A17 Sb as well as 8 bilayers thick A17 Sb (AB α-2D-Sb). Adapted from [40].

The nearest neighbors (NN) distances paint a clear picture of the bonding behavior of thin Sb(110) films (Figure 6.17 (d, e)). For thin flakes (<12 layers), the outside layers (closest to the surface) have two NNs and a third close neighbor. This bond structure is similar to A17 Sb. However, as we go inside the flake, the third neighbor distance increases by almost 0.15 Å and the fourth and third neighbor distances become almost equal. The surface structure of thicker films (Figure 6.17e) is similar. This surface reconstruction is driven by the dangling bond passivation. However, as we go inside the flake, the structure approaches the A7 structure (red lines). The third neighbor distance decreases and the fourth neighbor distance increases. We note that even at 18 bilayers, the bonding structure in the center of the flake is still not bulk-like. This peculiar behavior comes from the unique electronic structure of group VA elements (sp^3 hybridization with five valence electrons). The competing quasi-vdW bilayer structures of the bulk (111) and surface (110) create a large transition region and leads to the formation of the nanofacets and twin domains. In fact this structure allows for a (110) bottom surface and (111) top facetted surfaces, at relatively small thicknesses.

XPEEM of thin A7 Sb(110) and Sb(111) supports the hypothesis of an hybrid bonding structure allowing for the twin domain formation after the phase transformation. For XPEEM measurements, samples were grown in Polytechnique Montreal and shipped to the Elettra Sincrotrone Trieste (Italy). The samples were exposed to ambient conditions for a maximum of two weeks post growth. XPEEM of a rectangular Sb(110) flake and triangular Sb(111) island at 32.1 eV and 32.5 eV binding energy are shown in Figure 6.18 (a, b). The corresponding XPS spectra are plotted in Figure 6.18c. The phase of the rectangular flake is identified by comparing the *in situ* and *ex situ* LEEM I-V curves (Figure 6.18d). *in situ*, the flakes are identified by analysing the growth behavior. LEEM I-V is measured on flakes before (A17) and after (A7) the transition (Figure 6.18d). The position of the first minimum (1.5 eV) and the shape of the first maximum indicate that the rectangular flake is A7 Sb(110). However, the flake is at an early stage of the transition. In fact, no nanofaceting is observed by LEED (Figure 6.18 (e, f)). The LEED intensity as a function of the in-plane electron wave vector $\boldsymbol{k}^{||}$ and energy are shown for the rectangular flake (Figure 6.18e) and for a facetted flake (Figure 6.18f). The position $\boldsymbol{k}^{||}$ of the LEED spots of the rectangular flake is independent of the electron kinetic energy since the incident electrons are perpendicular to the surface lattice. This indicates that the flake is not facetted. In fact, the position of the LEED spots

is given by the Laue condition $\boldsymbol{k}^{||} - \boldsymbol{k}_{\boldsymbol{0}}^{||} = \boldsymbol{G}_{\boldsymbol{hk}}$. However, for a facetted surface, the lattice is not perpendicular to the incident electron beam and $\boldsymbol{k}_{\boldsymbol{0}}^{||}$ changes when in incident kinetic energy is changed. This means that the LEED spots of facets have an energy dependent position $\boldsymbol{k}^{||}$. In theory, it would be possible to identify the facets using LEED I-V. However, the I-V curve indicates that there are multiple facets on the same flake and that they are not necessarily oriented with low-index crystal planes. Moreover, the LEED is asymmetric, meaning that both sides of the nanoridges are different. This is due to the fact that the nanofacets are still forming. We also note that the LEED pattern of different facetted flakes are all different from one another since equilibrium has not yet been reached.

The Sb $4d_{5/2}$ and Sb $4d_{3/2}$ binding energies of thin Sb(110) are 32.19 eV and 33.42 eV, respectively. This represents a 210 meV red shift, as compared to Sb(111) (32.45 eV and 33.58 eV). Moreover, the Sb 4d peaks can be fitted with a single narrow component (FWHM=0.6 eV). This indicates that the shift is associated with electronic structure differences of the pristine material, rather than to bonding with other elements. We also note that no Sb oxide component is measured for either orientation. The binding energy shift of the Sb 4d electrons is in qualitative agreement with DFT calculations (Figure 6.18g). In fact, a 47 meV red shift is calculated for 8 bilayers Sb(110)/AA α-2D-Sb, with respect to bulk A7 Sb and a 336 meV shift is calculated for bulk A17 Sb. Moreover, the surface layers of Sb(110) have a larger shift (310 meV), due to their similarity to the A17 phase. On the other hand, the Sb 5s and Sb 5p PDOS of Sb(110) has more in common to A7 than A17 Sb. Overall, the DOS and core-level spectra confirm the hypothesis of an hybrid bonding state in thin Sb(110).

The data presented above allows to better understand the phase transition mechanisms. However, it does not give any information about the nucleation of AA α-2D-Sb. The LEEM data indicates that the nucleation of the new phase occurs shortly after the transition thickness is reached (< 10 s) and at a relatively low T (< 230 °C). The concerted shuffling of the layers would have a very large energy barrier and therefore local nucleation of AA α-2D-Sb must happen. According to classical nucleation theory, homogeneous nucleation of the new phase occurs when a critical nucleus of sufficient size forms ($\frac{d\Delta G}{dr} \leq 0$), where r is the size of the nucleus and ΔG is the Gibbs free energy cost of the nucleus. For a 2D layer (expansion of a cylindrical nucleus), we have $\Delta G =$

$-\pi r^2 h\Delta G_V + \gamma 2\pi r h$, where ΔG_V is the Gibbs free energy difference per unit volume, h is the flake thickness and γ is the nucleus surface energy. At the critical nuclei size ($\frac{d\Delta G}{dr} \leq 0$), we find $\Delta G^* = \pi h\gamma^2/\Delta G_V$ and $r^* = \gamma/\Delta G_V$. The nucleation rate is given by $f = f_0 e^{-\Delta G_V/kT}$, where f_0 can be estimated as $10^{11}N$, where N is the number of possible nucleation sites (flake area divided by nucleus area). With $\Delta G_V = 0.036\ meV/\text{Å}^3$ (from DFT) at $h = 45$ Å, we find $r^* = 18$ Å and $\gamma = 0.64\ meV/\text{Å}^2$ in order to explain the observed nucleation rate of ~0.1 Hz. This scenario is highly unlikely since it implies that the critical nucleus size is about one unit cell wide with only ~35 meV surface energy per cell wall. This strongly suggests that heterogeneous nucleation occurs, perhaps at the edges or corners of the flake. We also note that nucleation on all layers at once is the favored transition mechanism. In fact, DFT shows that stacking faults (such as ABBA) are not energetically favorable, as compared to both AB and AA α-2D-Sb. Similarly, Boulfelfel et *al*. studied the A17 → A7 phase transformation of P at high pressure[61] using molecular dynamics. They found that interlayer bonding chains form during shuffling, followed by the growth of interlayer bonding regions. We can therefore assume that a similar phase transition mechanism occurs in Sb, but with the thickness dependent cohesive energy, rather than the pressure playing the role of the thermodynamic force.

6.4 Conclusion

This chapter studied the thermal, environmental and phase stability of group VA 2D materials. The thermal decomposition of exfoliated α-2D-P was observed in real time using LEEM. The decomposition occurs by edge sublimation and by the nucleation and anisotropic expansion of monolayer deep holes aligned with the [100] direction. Significant sublimation begins at ~375 °C and its dynamics indicates an activation energy of 1.64 eV. The height of the barrier suggests that the previous published model based on single P atom sublimation cannot explain the kinetics of the decomposition at these relatively low temperatures. Another model based on P_2 sublimation was developed and tested using KMC simulations supported by DFT calculations. The model reproduces most features of the sublimation, with reasonable activation energies. Nevertheless, P_4 detachment should be included in the model and barriers should be estimated using the NEB method. A mathematical model based on the nucleation of holes at defects was also proposed to explain the sublimation of single layers and multilayers. The model highlights the important role

of defects on the thermal stability of α-2D-P and potentially other 2D materials. Moreover, it explains the slow stabilization of the vapor pressure of bulk A17 P. The sublimation of epitaxial β-2D-Sb was then examined using LEEM and STM. The results show that β-2D-Sb also undergoes edge sublimation at ~400 °C, but no holes were observed. However, more extensive characterization of its sublimation needs to be carried out.

The atmospheric stability of β-2D-Sb on graphene was studied by XPEEM and LEEM. The first signs of degradation were observed after 10 days in ambient conditions. Sb_2O_3 forms at the tips and edges of the β-2D-Sb islands, but no oxide was observed at step edges on the surface. Longer exposure (three months) led to the growth of the Sb_2O_3 over the whole area of the flakes. Nonetheless, Raman scattering spectroscopy has shown that the pristine β-2D-Sb E_g and A_{1g} modes can be detected after more than a year.

The phase stability of 2D-Sb was also studied. LEEM, LEED, STEM and Raman spectroscopy have shown that the unstable A17 Sb bulk phase can grow on graphene at small thicknesses in the form of α-2D-Sb. STEM measurements confirmed the AB stacking of the α-2D-Sb layers, which allowed to distinguish between the A17 Sb(010) and the A7 Sb(110) phases for the first time. Real-time LEEM observations showed that AB α-2D-Sb undergoes a transition to AA α-2D-Sb at a critical thickness of ~4.5 nm followed by a relaxation to A7 Sb(110) by the formation of a periodic array of twin domains, driven by the minimization of surface energy. DFT calculations showed that the transition is made possible by a stability shift between the AB and AA α-2D-Sb phases at ~7 layers. Moreover, the results provide an indirect experimental confirmation of the hypothesized shuffle and shear diffusionless transition mechanisms of bulk P. XPEEM measurements support the hypothesis of an intermediate α-2D-Sb phase, which has both A17- and A7-like bonding features. Atoms in the AA α-2D-Sb phase form four covalent bonds, which allows the relaxation to either of the two A7 Sb(110) twin domains.

Overall, these results provide a better understanding of the stability of group VA 2D materials, which can facilitate their integration in emerging technologies. Moreover, the new understanding of the phase stability of pnictogens allotropes at reduced dimensions developed in this chapter may allow to expand this new family of 2D materials.

CHAPTER 7 DISCUSSION AND CONCLUSION

The previous chapters presented studies of the growth, stability and electronic properties of novel group VA 2D materials. These atomic-level investigations expand the breadth of this emerging class of materials and provide insight into the key mechanisms governing their growth, decomposition and phase transformations. Several questions on the behavior and potential of these materials were also raised and addressed. This chapter summarizes the main findings of the thesis, puts them in a broader context and discusses their implications. First, the growth mechanisms determined by real-time LEEM are summarized and potential avenues to optimize and control the growth are outlined. Next, the main theoretical and experimental results on the effect of substrate-layer interactions on the properties of epitaxial group VA 2D materials are presented. Then, salient observations of the thermal, atmospheric and phase stability of 2D pnictogens elucidated by LEEM, STEM and DFT and are discussed along with the thermodynamic stability of pnictogens and polymorphic materials on vdW substrates. Finally, a general conclusion to the thesis is presented.

7.1 Growth of group VA 2D allotropes

Most of the growth efforts have been centered on the synthesis of β-2D-Sb. The growth was first demonstrated on Ge(111), onto which multilayer islands with lateral dimensions of ~1 μm as well as ~30 nm single layer islands have been obtained. Later, the growth was also achieved on Cl and Sb passivated Ge(111) substates as well as graphene grown on Ge. Perhaps the most important question left unanswered by these experiments is how to reach the large-scale control of the synthesis of single-layer and multilayer group VA 2D homogeneous films. In fact, the island growth mode seems unavoidable. Nevertheless, the real-time LEEM data provided key insight on the nucleation and growth mechanisms. This information is highly valuable to elaborate potential solutions to better control the kinetics of the growth and optimize this island growth mode, as described below.

Both homogenous and heterogeneous nucleation of β-2D-Sb were observed on Ge(111), whereas only heterogenous nucleation was observed on graphene. This difference can be attributed to two factors. First, the Ge(111) surface has dangling bonds and is almost lattice matched to β-2D-Sb, which can promote the formation of 2D nuclei directly on terraces. This idea is supported by the

STM observations of oriented monolayer β-2D-Sb at ~35% coverage on Ge(111). The second factor is the extremely fast desorption of Sb_4 on graphene, which considerably reduces the homogeneous nucleation rate. The LEEM results have also shown that heterogeneous nucleation mostly leads to islands with central 3D nuclei. These nuclei form by the accumulation of Sb_4 species at surface defects and are most likely amorphous dome-shaped islands. The nuclei eventually transform into more stable A7 Sb(111) pyramidal 3D islands. 2D multilayer clover-shaped islands then forms by the successive lateral growth of the bottom terraces of the pyramids, limited by the available Sb_4 precursor species on lower terraces. On the other hand, homogeneous nucleation and nucleation at atomic step bunches was found to produce flat 2D islands.

After nucleation, the growth morphology of β-2D-Sb islands is determined by the interplay between vertical growth, lateral growth and edges orientation. The LEEM analysis of the dynamics suggests that the lateral growth rate initially accelerates and then stabilizes, as it is first limited by the incorporation of Sb_4 species at the edges and then by the availability of these species. The Voronoi analysis of the growth dynamics has highlighted the competition for diffusing Sb_4 species between growing islands and showed that the lateral growth is mostly fed by precursors deposited directly on the substrate. Surface diffusion simulations support this hypothesis and indicate that the fast growth of the tips of the islands is due to surface diffusion on the substrate. On the other hand, vertical growth is driven by Sb_4 deposition on the surface of the islands. In that sense, vertical growth is mostly an intrinsic property of β-2D-Sb, but lateral growth also depends on the nature of the substrate. The lateral growth rate is roughly proportional to the diffusion length on the substrate $L_d = ae^{(E_D - E_{diff})/2k_BT}$. In fact, the size of the islands is much larger on graphene than on Ge(111). On the other hand, many factors were found to influence the vertical growth. As mentioned above, heterogeneous nucleation leads to 3D nuclei which are a source of multilayer growth. Moreover, multilayers nucleate homogeneously on the surface of the islands and heterogeneously on the edges of the islands. Surprisingly, varying the deposition rate has shown that this type of nucleation decreases approximately linearly with the Sb_4 surface concentration, pointing towards a first-order reaction. This interpretation needs to be confirmed by more targeted experimental investigations. Nonetheless, it suggests that the ratio of lateral growth rate to multilayer nucleation rate can difficultly be increased. In fact, the lateral growth rate is roughly proportional to FL_d and the nucleation rate for a first-order reaction is proportional to $Fe^{E_D^{Sb}/k_BT}$, where E_D^{Sb} is the adsorption

energy of Sb_4 on the Sb surface. This yields a ratio proportional to $\exp[(E_D - E_{diff} - 2E_D^{Sb})/2k_BT]$, which does not depend on the deposition rate F, but increases with T for most substrates. While increasing T might favor the lateral growth, the LEEM data has shown that this can also lead to a growth mode transition. In fact, the increased diffusion of precursors on the edge (also present at low F) allows the edges to align with the low energy Z2 crystallographic direction. At this point, triangular atoll-like vertical structure with well-defined thick bands on the edges form. Nonetheless, it is not clear if this growth mode transition can occur in very thin islands since Z2 edges are extremely rarely observed at the surface of the islands, which suggests that they are unstable and grow very fast. The stabilization of the Z2 edges at thicker steps is most likely due to the formation of facets, which can only occur if the island is thick enough. This interpretation is supported by the STM observation of flat thin hexagonal islands.

General guidelines to optimize the island growth mode of β-2D-Sb to obtain large flakes with controllable thicknesses can be established based on these mechanisms. The first and most important step is to avoid heterogeneous nucleation and favor homogeneous nucleation to produce flat 2D nuclei. In principle, this can be achieved by using high-quality substrates with low defect densities such as epitaxial graphene on SiC to avoid Sb_4 aggregation. It is also worthwhile to explore different precursors such as Sb_2 and Sb or low-temperature CVD precursors, which may not aggregate into the amorphous phase. Moreover, the homogeneous nucleation should be increased by using relatively low substrate T and high deposition rates. Pre-patterned substrates, such as graphene/Ge(111) with nanoscale holes in the graphene may allow to locally increase the homogeneous nucleation of single layer epitaxially oriented β-2D-Sb. After nucleation, the growth conditions should be modified to promote lateral growth, while reducing multilayer nucleation. Two questions need to be answered to determine how this can be done. The first is whether the atoll-like growth occurs at low thicknesses and the second is whether the homogeneous multilayer nucleation rate is really a first-order reaction. If the answer to both questions is yes, then there is not a big margin for optimization. Nonetheless, using substrates with large L_d and increasing the T as much as possible would provide the optimal ratio of lateral to vertical growth. Increasing T too much would trigger the growth mode transition, but this can be mitigated by increasing the deposition rate. If the atoll-like growth can be avoided at low thicknesses, then the T can be increased higher (as long as the sublimation of the islands is slower than the growth). On the other

hand, if the multilayer nucleation rate is not a first-order reaction, then changing the deposition rate could be used to tune the thickness of the islands since the multilayer nucleation rate to lateral growth rate ratio would be proportional to F^{n-1}, where n is the order of the reaction. Here also, the use of different precursors should be considered. For instance, it would be very surprising that the multilayer nucleation would be a first order reaction when using atomic Sb precursors. Still, these questions deserve to be analyzed in depth before conclusions can be drawn.

7.2 Role of substrate-layer interactions

Throughout the thesis, the important role of substrate-layer interactions in shaping the electronic properties, growth behavior and thermodynamic stability of epitaxial group VA 2D materials has been ubiquitous. The DFT analysis in Chapter 4 highlighted the effect of substrate-layer interactions on the atomic and electronic structure of epitaxial group VA 2D materials. A competition between the stabilizing behavior of the substrate and the conservation of the intrinsic properties of the layer was observed. In fact, DFT investigations found that strongly interacting substrates like TMs can bond relatively strongly with group VA 2D materials. For α-2D-P, the interaction was found to be important enough to compromise the structural integrity of the layer. On the other hand, the structure of the β-2D phase on hexagonal TM surfaces is relatively well conserved. Nonetheless, the strong interaction and substrate-layer bonds transform the electronic band structure of the epitaxial layers. The upside of these substrates is that the interaction has the potential to stabilize the more elusive light group VA 2D materials such as β-2D-N and β-2D-P. The effect of the strongly interacting substrates was only studied for single-layer group VA 2D materials. However, it is expected to be less critical for multilayers, since only the first layer bonds with the substrate. While the electronic transport properties of these epitaxial multilayers might be dominated by the metallic substrates, other properties such as light emission and absorption should be mostly preserved.

The DFT investigation revealed that group IVA semiconductors (Si, Ge) also interact relatively strongly with epitaxial group VA 2D materials due to their surface dangling bonds. The orbital hybridization with these dangling bonds makes single layer group VA 2D materials transition from semiconductors to metals. Nonetheless, the analysis demonstrated that the dangling bonds can be easily passivated by several atomic and molecular species. The passivation not only allows the

recovery of the intrinsic freestanding-like behavior of the layers, but also provides an opportunity to engineer their properties. For instance, the passivation of the substrate by electronegative elements like halogens leads to a charge transfer and doping of the layer. This method could eventually be used for the fabrication of a variety of devices if the substrate passivation can be controlled. For example, lithography might allow to use different passivation methods on different regions of the substrate in order to design p-n junctions, FETs, etc. Moreover, the growth of β-2D-Sb on passivated Ge(111) should allow to verify the band-gap opening at single-layer thickness using STS. In fact, this prediction is one of the main reasons behind the interest in heavy group VA 2D materials, but still has not been confirmed experimentally.

The effects of substrate-layer interactions and substrate passivation on epitaxial group VA 2D materials was observed experimentally in Chapter 5 and Chapter 6. In fact, 2D-Sb and 2D-As_xSb_{1-x} were grown on relatively strongly interacting substrates (Si(111) and Ge(111)) as well as on passivated substrates (Sb and graphene passivated Ge and graphene on SiO_2). The influence of the interaction was evidenced by the epitaxial relationship between the strongly interacting substrates and the layers and by the growth of randomly oriented (textured) grains on graphene. The effects of the strong substrate-layer interactions on the electronic structure was directly observed by STM. In fact, moiré patterns were observed on multilayer β-2D-Sb on Ge(111) at thicknesses up to 7 layers. Whether the moiré is due to a strain field or to coupling with the band structure of the substrate, its presence over a thickness of several layers indicates an important modification of the electronic structure. This phenomenon should be investigated further by low-T STS to determine its origin and impact on the electronic properties of β-2D-Sb.

These results also show that the vdW epitaxy of 2D materials has fundamental limitations. The competition between the stabilizing effect of the substrate and the conservation of the intrinsic properties of the layer hinders the direct growth of quasi-freestanding homogeneous films. In fact, large substrate-layer interactions are necessary to thermodynamically favor homogeneous monolayer 2D growth, but they alter the electronic structure of the layer. On the other hand, weak substrate-layer interactions allow to conserve the freestanding nature but favor multilayer island growth and random epitaxial orientations. This however does not mean that the growth of 2D materials on weakly interacting substrates is set up to fail, as the island growth mode can be potentially optimized, as described in the previous section. Moreover, growth on strongly

interacting substrates followed by transfer of the layers can be used to produce homogeneous 2D films and large scale vdW heterostructures.

7.3 Stability of group VA 2D materials

The thermal stability of exfoliated α-2D-P in vacuum was studied by real-time LEEM. α-2D-P was found to decompose by edge sublimation and by the formation and expansion of elongated monolayer deep holes aligned with the [100] crystallographic direction. Analysis of the dynamics along with KMC simulations and DFT calculations revealed that the sublimation takes place by the detachment of P_2 and P_4 molecules. An analytical model of the sublimation was proposed based on the nucleation of holes at pre-existing point defects. The model is thought to be valid under vacuum for monolayer and multilayer vdW layered materials with low step densities and relatively high defect densities. It would be interesting to extend the model to other conditions, but this is not straightforward. For instance, to describe the sublimation in closed systems, we need to consider the inverse reaction (attachment of P_2/P_4 at edges). This can be done by adding a pressure dependence to the hole expansion velocity: $v(P) = v_0 - k_1 P$. However, this results in an integrodifferential equation for the pressure, which has no obvious analytical solution. Similar equations are obtained if we consider the thermally activated nucleation of holes (these equations can however be easily solved numerically). Nevertheless, the simple model still has some value. It shows the critical impact of defects on the thermal stability of α-2D-P and 2D materials. In fact, the sublimation rate increases with the square root of the defect density due to the creation of new edges, which is equivalent to the roughening of the surface of 3D materials. The model also shows that defective α-2D-P decomposes by multilayer sublimation, rather than by layer-by-layer sublimation. Adapting the model to account for different types of defects or external conditions may allow to understand how to engineer thermal processing methods such as the controlled thinning of multilayer vdW layered materials.

It is often said that 2D-Sb has a considerable advantage over α-2D-P due to its high stability in atmospheric conditions. However, this claim has not been supported by thorough investigations of the oxidation behavior of 2D-Sb. Here, the oxidation of β-2D-Sb exposed to ambient conditions for one week to three months was studied by LEEM and XPEEM. β-2D-Sb was found to resist relatively well to oxidation. In fact, the surface of the islands does not oxidize during the first few

weeks. However, Sb_2O_3 nucleates at the tips and edges of the islands within 10 days due to the presence of dangling bonds. The oxide then grows inward and can cover the islands within three months. In contrast to α-2D-P, the Sb_2O_3 was found to be stable and to not affect the morphology of the islands. Moreover, the Sb_2O_3 can be converted back to β-2D-Sb by exposure to high-intensity X-rays. These results confirm the stability of β-2D-Sb, but also establish its limits, which highlights the need to use capping methods to protect future β-2D-Sb based devices. This study also raised several questions, such as the role of the substrate in catalyzing the oxidation as well as the dependence on the thickness of the islands and orientation of the edges.

The deposition of Sb on weakly interacting substrates revealed the particular thermodynamics of pnictogens by unambiguously identifying the A17 phase in heavy pnictogens for the first time. The combination of LEEM, LEED and STEM characterization allowed observing both the surface structure and the stacking of the layers to distinguish between the A7 (110) and A17 (010) phases. DFT calculations showed that the stabilization of the A17 Sb phase at few-layer thicknesses is explained by the reduced role of interlayer interactions. In fact, the gradual stability shift from the layered A17 phase to the layered A7 phase as we go down in the periodic table is due to the more important interlayer bonding in the A7 phase. Since heavier elements have stronger interlayer interactions, the higher interlayer coordination of the A7 phase stabilizes it as compared to the A17 phase. On the other hand, the single layer A17 (α-2D) phase is slightly more stable than the A7 (β-2D) phase for all pnictogens. In that sense, the appearance of the A17 phase at small thicknesses is expected since the effect of interlayer interactions is reduced. These results also suggest that alloying could be an interesting avenue to extend the stability range of the A7 and A17 phases to lighter or heavier pnictogens. The A7 phase could be explored in lighter elements by growing AsP or AsN alloys for instance. On the other hand, ultrathin A17 Bi or SbBi could be grown on weakly interacting substrates and the synthesis of bulk A17 PBi, PSb, etc. could be attempted. Extending the range of the A17 phase to heavy elements is an interesting way to study the effect of large spin-orbit coupling (Bi, Sb) in new crystal structures.

It is also important to note that the growth of the A17 phase was facilitated by the weakly interacting substrate. This concept might allow for the discovery of new 2D materials or vdW layered phases, as explained below. While novel allotropes and polymorphs are often discovered at high pressure (or temperature), vdW materials might not emerge in these conditions. In fact, the

Gibbs free energy varies differently for vdW layered materials and typical 3D materials. High-pressure favors 3D coordinated materials over vdW materials since the latter have low densities due to the long-range vdW interactions. High temperature may promote the formation of some vdW phases since they often have lower symmetry and more complex crystal structures, which can lead to higher vibrational entropy. Decreasing the thicknesses can however favor the formation of vdW layered polymorphs. In fact, the self-passivated nature and low surface energies of vdW layered materials makes them almost insensitive to decreased thicknesses. On the other hand, surface dangling bonds in thin films of 3D coordinated materials have a strong destabilizing effect. By removing the stabilizing substrate-layer bonds, deposition of potentially polymorphic materials on weakly interacting substrates is therefore analogous, in a sense, to exploring the negative pressure phase diagram, as far as vdW materials are concerned.

7.4 General conclusion

The main objective of this thesis was to lay the groundwork for the exploration of emerging 2D pnictogens. In particular, the thesis aimed at demonstrating the existence of novel group VA 2D allotropes, establishing epitaxial growth methods for their synthesis, elucidating the mechanisms governing their growth and understanding their stability. Overall, significant progress was made in all these directions. The MBE growth of single and multilayer β-2D-Sb, multilayer α-2D-Sb as well as multilayer β-2D-As_xSb_{1-x} has been demonstrated. At the time, these materials had never been observed experimentally, even though some of these results have been independently published more rapidly by other groups. The use of real-time LEEM proved to be highly valuable to the study of emerging 2D materials. In fact, it allowed to rapidly develop the synthesis while supplying detailed information on the dynamics of the growth, thermal decomposition and phase transformations of group VA 2D materials. While previous research on 2D pnictogens was mostly theoretical, the *in situ* microscopic observations revealed the complexity of this materials system. This highlighted the challenges related to the development of these materials, but also provided several potential avenues to engineer their properties. Moreover, the analysis of the growth dynamics allowed to establish the basic mechanisms controlling the synthesis of these 2D materials. The combination of *ab initio* electronic structure calculations with vdW epitaxy and microscopic observations (STM, STEM, LEEM) played a key role in understanding the substrate-

layer interactions and the stability of epitaxial group VA 2D materials. In fact, it allowed to guide the choice of growth substrates and to appreciate the importance of interlayer interactions in shaping the stability of the A7 and A17 phases.

The knowledge on the behavior of 2D pnictogens developed in this thesis opens several potential research directions. In fact, multiple avenues to engineer the properties of group VA 2D materials were identified. Interface engineering could be used to directly modify the electronic structure of epitaxial layers, but also to add another degree of freedom by inducing tunable moiré patterns. The emergence of moirés was demonstrated by the growth on a substrate with a slight lattice mismatch but could also be obtained by the growth of 2D pnictogens vdW heterostructures for instance. Alloying between group VA elements also provides significant opportunities to engineer their physical properties and expand the stability range of the A7 and A17 phases. In fact, the direct growth of 2D-As_xSb_{1-x} suggests that other 2D alloys can be obtained by vdW growth. On the other hand, various nanostructures such as α-2D-Sb nanoribbons and triangular atoll-like β-2D-Sb islands were found to readily emerge during the vdW growth. No attempts were made at controlling the growth of these nanostructures, but the real-time LEEM data indicates that their dimensions and aspect ratio could be tuned by modifying the growth conditions. The richness of these nanostructures was evidenced in the Sb system and it is expected to be present in other vdW grown pnictogen elements and alloys. It is not difficult to imagine the freedom that this can provide. For example, changing the ratio of precursors during the co-deposition could allow the synthesis of nanoribbons containing lateral heterostructures, superstructures, etc. While the large-scale growth of these nanostructures may be difficult to control, this provides the opportunity to explore interesting emerging physical phenomena.

Overall, this thesis took a fresh look at a long-known class of material. Even though pnictogens have been studied for hundreds of years and are one of the main groups of the periodic table, it reminds us that their behavior, especially at reduced dimensions, is still obscure. Hopefully, the results presented in the thesis may motivate researchers to begin untangling the properties of this rich and unique system.

REFERENCES

1. Novoselov, K. S.; Geim, A. K.; Morozov, S. V.; Jiang, D.; Katsnelson, M. I.; Grigorieva, I. V.; Dubonos, S. V.; Firsov, A. A. *Nature* **2005,** 438, (7065), 197-200.

2. Zhang, Y.; Tan, Y.-W.; Stormer, H. L.; Kim, P. *Nature* **2005,** 438, (7065), 201-204.

3. Novoselov, K. S.; Jiang, D.; Schedin, F.; Booth, T. J.; Khotkevich, V. V.; Morozov, S. V.; Geim, A. K. *Proceedings of the National Academy of Sciences of the United States of America* **2005,** 102, (30), 10451.

4. Butler, S. Z.; Hollen, S. M.; Cao, L.; Cui, Y.; Gupta, J. A.; Gutiérrez, H. R.; Heinz, T. F.; Hong, S. S.; Huang, J.; Ismach, A. F.; Johnston-Halperin, E.; Kuno, M.; Plashnitsa, V. V.; Robinson, R. D.; Ruoff, R. S.; Salahuddin, S.; Shan, J.; Shi, L.; Spencer, M. G.; Terrones, M.; Windl, W.; Goldberger, J. E. *ACS Nano* **2013,** 7, (4), 2898-2926.

5. Zhang, S.; Guo, S.; Chen, Z.; Wang, Y.; Gao, H.; Gómez-Herrero, J.; Ares, P.; Zamora, F.; Zhu, Z.; Zeng, H. *Chemical Society Reviews* **2018,** 47, (3), 982-1021.

6. Mounet, N.; Gibertini, M.; Schwaller, P.; Campi, D.; Merkys, A.; Marrazzo, A.; Sohier, T.; Castelli, I. E.; Cepellotti, A.; Pizzi, G.; Marzari, N. *Nature Nanotechnology* **2018,** 13, (3), 246-252.

7. Wang, H.; Li, C.; Fang, P.; Zhang, Z.; Zhang, J. Z. *Chemical Society Reviews* **2018,** 47, (16), 6101-6127.

8. Schaibley, J. R.; Yu, H.; Clark, G.; Rivera, P.; Ross, J. S.; Seyler, K. L.; Yao, W.; Xu, X. *Nature Reviews Materials* **2016,** 1, (11), 16055.

9. Chhowalla, M.; Jena, D.; Zhang, H. *Nature Reviews Materials* **2016,** 1, (11), 16052.

10. Dean, C. R.; Young, A. F.; Meric, I.; Lee, C.; Wang, L.; Sorgenfrei, S.; Watanabe, K.; Taniguchi, T.; Kim, P.; Shepard, K. L.; Hone, J. *Nature Nanotechnology* **2010,** 5, (10), 722-726.

11. Dan, Y.; Lu, Y.; Kybert, N. J.; Luo, Z.; Johnson, A. T. C. *Nano Letters* **2009,** 9, (4), 1472-1475.

12. Schedin, F.; Geim, A. K.; Morozov, S. V.; Hill, E. W.; Blake, P.; Katsnelson, M. I.; Novoselov, K. S. *Nature Materials* **2007,** 6, (9), 652-655.

13. Geim, A. K.; Grigorieva, I. V. *Nature* **2013,** 499, (7459), 419.

14. Novoselov, K.; Mishchenko, A.; Carvalho, A.; Neto, A. C. *Science* **2016,** 353, (6298), aac9439.

15. Chung, D. *Journal of Materials Science* **2002,** 37, (8), 1475-1489.

16. Bridgman, P. *Journal of the American Chemical Society* **1914,** 36, (7), 1344-1363.

17. Greenwood, N. N.; Earnshaw, A., Arsenic, Antimony and Bismuth. In *Chemistry of the Elements (Second Edition)*, Greenwood, N. N.; Earnshaw, A., Eds. Butterworth-Heinemann: Oxford, 1997; pp 547-599.

18. Chen, Y.; Chen, C.; Kealhofer, R.; Liu, H.; Yuan, Z.; Jiang, L.; Suh, J.; Park, J.; Ko, C.; Choe, H. S.; Avila, J.; Zhong, M.; Wei, Z.; Li, J.; Li, S.; Gao, H.; Liu, Y.; Analytis, J.; Xia, Q.; Asensio, M. C.; Wu, J. *Advanced Materials* **2018,** 30, (30), 1800754.

19. Castellanos-Gomez, A.; Vicarelli, L.; Prada, E.; Island, J. O.; Narasimha-Acharya, K. L.; Blanter, S. I.; Groenendijk, D. J.; Buscema, M.; Steele, G. A.; Alvarez, J. V.; Zandbergen, H. W.; Palacios, J. J.; Van der Zant, H. S. J. *2D Materials* **2014,** 1, (2), 025001.

20. Li, L.; Yu, Y.; Ye, G. J.; Ge, Q.; Ou, X.; Wu, H.; Feng, D.; Chen, X. H.; Zhang, Y. *Nature Nanotechnology* **2014,** 9, (5), 372.

21. Qiao, J.; Kong, X.; Hu, Z.-X.; Yang, F.; Ji, W. *Nature Communications* **2014,** 5, (1), 4475.

22. Özçelik, V. O.; Aktürk, O. Ü.; Durgun, E.; Ciraci, S. *Physical Review B* **2015,** 92, (12), 125420.

23. Zhang, Y.; Lee, J.; Wang, W.-L.; Yao, D.-X. *Computational Materials Science* **2015,** 110, 109-114.

24. Zhu, Z.; Tománek, D. *Physical Review Letters* **2014,** 112, (17), 176802.

25. Kamal, C.; Ezawa, M. *Physical Review B* **2015,** 91, (8), 085423.

26. Aktürk, O. Ü.; Özçelik, V. O.; Ciraci, S. *Physical Review B* **2015,** 91, (23), 235446.

27. Wang, G.; Pandey, R.; Karna, S. P. *ACS Applied Materials & Interfaces* **2015,** 7, (21), 11490-11496.

28. Zhang, S.; Yan, Z.; Li, Y.; Chen, Z.; Zeng, H. *Angewandte Chemie International Edition* **2015,** 54, (10), 3112-3115.

29. Aktürk, E.; Aktürk, O. Ü.; Ciraci, S. *Physical Review B* **2016,** 94, (1), 014115.

30. Ersan, F.; Kecik, D.; Özçelik, V. O.; Kadioglu, Y.; Aktürk, O. Ü.; Durgun, E.; Aktürk, E.; Ciraci, S. *Applied Physics Reviews* **2019,** 6, (2), 021308.

31. Murakami, S. *Physical Review Letters* **2006,** 97, (23), 236805.

32. Koroteev, Y. M.; Bihlmayer, G.; Chulkov, E. V.; Blügel, S. *Physical Review B* **2008,** 77, (4), 045428.

33. Liu, Z.; Liu, C.-X.; Wu, Y.-S.; Duan, W.-H.; Liu, F.; Wu, J. *Physical Review Letters* **2011,** 107, (13), 136805.

34. Zhang, P.; Liu, Z.; Duan, W.; Liu, F.; Wu, J. *Physical Review B* **2012,** 85, (20), 201410.

35. Fortin-Deschênes, M.; Moutanabbir, O. *The Journal of Physical Chemistry C* **2018,** 122, (16), 9162-9168.

36. Fortin-Deschênes, M.; Waller, O.; Mentes, T. O.; Locatelli, A.; Mukherjee, S.; Genuzio, F.; Levesque, P. L.; Hebert, A.; Martel, R.; Moutanabbir, O. *Nano Letters* **2017,** 17, (8), 4970-4975.

37. Fortin‐Deschênes, M.; Jacobberger, R. M.; Deslauriers, C. A.; Waller, O.; Bouthillier, É.; Arnold, M. S.; Moutanabbir, O. *Advanced Materials* **2019,** 31, (21), 1900569.

38. Fortin-Deschênes, M.; Waller, O.; An, Q.; Lagos, M. J.; Botton, G. A.; Guo, H.; Moutanabbir, O. *Small* **2020,** 16, (3), 1906540.

39. Fortin-Deschênes, M.; Levesque, P. L.; Martel, R.; Moutanabbir, O. *The Journal of Physical Chemistry Letters* **2016,** 7, (9), 1667-1674.

40. Fortin-Deschênes, M.; Zschiesche, H.; Mentes, T. O.; Locatelli, A.; Jacobberger, R. M.; Genuzio, F.; Lagos, M. J.; Biswas, D.; Jozwiak, C.; Miwa, J. A.; Ulstrup, S.; Bostwick, A.; Rotenberg, E.; Arnold, M. S.; Botton, G. A.; Moutanabbir, O. *arXiv* **2020,** arXiv:2005.14041.

41. Streib, W. E.; Jordan, T. H.; Lipscomb, W. N. *The Journal of Chemical Physics* **1962,** 37, (12), 2962-2965.

42. Schuch, A.; Mills, R. *The Journal of Chemical Physics* **1970,** 52, (12), 6000-6008.

43. Mailhiot, C.; Yang, L. H.; McMahan, A. K. *Physical Review B* **1992,** 46, (22), 14419-14435.

44. Radousky, H.; Nellis, W.; Ross, M.; Hamilton, D.; Mitchell, A. *Physical Review Letters* **1986,** 57, (19), 2419.

45. Goncharov, A. F.; Gregoryanz, E.; Mao, H.-k.; Liu, Z.; Hemley, R. J. *Physical Review Letters* **2000,** 85, (6), 1262.

46. Eremets, M. I.; Hemley, R. J.; Mao, H.-k.; Gregoryanz, E. *Nature* **2001,** 411, (6834), 170.

47. Popov, M. *Physics Letters A* **2005,** 334, (4), 317-325.

48. Eremets, M. I.; Gavriliuk, A. G.; Trojan, I. A.; Dzivenko, D. A.; Boehler, R. *Nature Materials* **2004,** 3, (8), 558.

49. Benchafia, E. M.; Yao, Z.; Yuan, G.; Chou, T.; Piao, H.; Wang, X.; Iqbal, Z. *Nature Communications* **2017,** 8, (1), 1-6.

50. Tassini, L.; Gorelli, F.; Ulivi, L. *The Journal of Chemical Physics* **2005,** 122, (7), 074701.

51. Tomasino, D.; Kim, M.; Smith, J.; Yoo, C.-S. *Physical Review Letters* **2014,** 113, (20), 205502.

52. Martin, R. M.; Needs, R. J. *Physical Review B* **1986,** 34, (8), 5082.

53. Stevenson, D.; Yost, D. M. *The Journal of Chemical Physics* **1941,** 9, (5), 403-408.

54. Kane, J. S.; Reynolds, J. H. *The Journal of Chemical Physics* **1956,** 25, (2), 342-349.

55. Simon, A.; Borrmann, H.; Craubner, H. *Phosphorus, Sulfur, and Silicon and the Related Elements* **1987,** 30, (1-2), 507-510.

56. Liu, C.; Wang, Y.; Sun, J.; Chen, A. *Transactions of Tianjin University* **2020,** 26, (2), 104-126.

57. Scelta, D.; Baldassarre, A.; Serrano‐Ruiz, M.; Dziubek, K.; Cairns, A. B.; Peruzzini, M.; Bini, R.; Ceppatelli, M. *Angewandte Chemie* **2017,** 129, (45), 14323-14328.

58. Bridgman, P. W. *Physical Review* **1934,** 45, (11), 844-845.

59. Köpf, M.; Eckstein, N.; Pfister, D.; Grotz, C.; Krüger, I.; Greiwe, M.; Hansen, T.; Kohlmann, H.; Nilges, T. *Journal of Crystal Growth* **2014,** 405, 6-10.

60. Gaspard, J.-P. *Comptes Rendus Physique* **2016,** 17, (3), 389-405.

61. Boulfelfel, S. E.; Seifert, G.; Grin, Y.; Leoni, S. *Physical Review B* **2012,** 85, (1), 014110.

62. Seo, D.-K.; Hoffmann, R. *Journal of Solid State Chemistry* **1999,** 147, (1), 26-37.

63. Häussermann, U.; Söderberg, K.; Norrestam, R. *Journal of the American Chemical Society* **2002,** 124, (51), 15359-15367.

64. Seidl, M.; Balázs, G.; Scheer, M. *Chemical Reviews* **2019,** 119, (14), 8406-8434.

65. Greaves, G.; Elliott, S.; Davis, E. *Advances in Physics* **1979,** 28, (1), 49-141.

66. Hintze, C., *Ueber Arsenolamprit, Zeitschrift für Krystallographie und Mineralogie*. Wilhelm Engelmann: Leipzig, 1886; Vol. 11.

67. Pušelj, M.; Ban, Z.; Grdenić, D. *Journal of Inorganic and General Chemistry* **1977,** 437, (1), 289-292.

68. Yoshiasa, A.; Tokuda, M.; Misawa, M.; Shimojo, F.; Momma, K.; Miyawaki, R.; Matsubara, S.; Nakatsuka, A.; Sugiyama, K. *Scientific Reports* **2019,** 9, (1), 6275.

69. Matsubara, S.; Miyawaki, R.; Shimizu, M.; Yamanaka, T. *Mineralogical Magazine* **2001,** 65, (6).

70. Beister, H.; Strössner, K.; Syassen, K. *Physical Review B* **1990,** 41, (9), 5535.

71. Rouillard, Y.; Lambert, B.; Toudic, Y.; Baudet, M.; Gauneau, M. *Journal of Crystal Growth* **1995,** 156, (1-2), 30-38.

72. Krebs, H.; Steffen, R. *Zeitschrift für Anorganische und Allgemeine Chemie* **1964,** 327, (3‐4), 224-237.

73. Kolobyanina, T.; Kabalkina, S.; Vereshchagin, L.; Fedina, L. *Soviet Physics - JETP* **1969,** 28, (1), 88-90.

74. Schiferl, D.; Cromer, D.; Jamieson, J. *Acta Crystallographica* **1981,** 37, (4), 807-810.

75. Degtyareva, O.; McMahon, M. I.; Nelmes, R. J. *Physical Review B* **2004,** 70, (18), 184119.

76. McMahon, M.; Degtyareva, O.; Nelmes, R. *Physical Review Letters* **2000,** 85, (23), 4896.

77. Schwarz, U.; Akselrud, L.; Rosner, H.; Ormeci, A.; Grin, Y.; Hanfland, M. *Physical Review B* **2003,** 67, (21), 214101.

78. Aoki, K.; Fujiwara, S.; Kusakabe, M. *Solid State Communications* **1983,** 45, (2), 161-163.

79. Ormeci, A.; Rosner, H. *Zeitschrift für Kristallographie-Crystalline Materials* **2004,** 219, (6), 370-375.

80. Coleman, A.; Stevenson, M.; McMahon, M.; Macleod, S. *Physical Review B* **2018,** 97, (14), 144107.

81. Akhtar, D.; Vankar, V.; Goel, T.; Chopra, K. *Thin Solid Films* **1979,** 58, (2), 327-332.

82. Akhtar, D.; Vankar, V. D.; Goel, T. C.; Chopra, K. L. *Journal of Materials Science* **1979,** 14, (4), 988-994.

83. Farrow, R. F. C. *Journal of Vacuum Science & Technology B* **1983,** 1, (2), 222-228.

84. Hunderi, O. *Journal of Physics F: Metal Physics* **1975,** 5, (11), 2214.

85. Komik, Y. F.; Belevtsev, B.; Yatsuk, L. *Soviet Journal - JETP* **1973,** 36, 1177.

86. Brugger, R.; Bennion, R.; Worlton, T. *Physics Letters A* **1967,** 24, (13), 714-717.

87. Iwasaki, H.; Kikegawa, T. *Acta Crystallographica Section B: Structural Science* **1997,** 53, (3), 353-357.

88. Schaufelberger, P.; Merx, H.; Contre, M. *High Temperatures - High Pressures* **1973,** 5, 221-230.

89. Klement Jr, W.; Jayaraman, A.; Kennedy, G. *Physical Review* **1963,** 131, (2), 632.

90. Takagi, M. *Journal of the Physical Society of Japan* **1954,** 9, (3), 359-363.

91. Nanda, K. *Pramana* **2009,** 72, (4), 617-628.

92. McMahon, M. I.; Nelmes, R. J. *Physical Review Letters* **2005,** 95, (21), 215505.

93. Mishra, A.; Titova, L.; Hoang, T.; Jackson, H.; Smith, L.; Yarrison-Rice, J.; Kim, Y.; Joyce, H.; Gao, Q.; Tan, H. *Applied Physics Letters* **2007,** 91, (26), 263104.

94. Glas, F.; Harmand, J.-C.; Patriarche, G. *Physical Review Letters* **2007,** 99, (14), 146101.

95. Tan, C.; Cao, X.; Wu, X.-J.; He, Q.; Yang, J.; Zhang, X.; Chen, J.; Zhao, W.; Han, S.; Nam, G.-H.; Sindoro, M.; Zhang, H. *Chemical Reviews* **2017,** 117, (9), 6225-6331.

96. Novoselov, K. S.; Geim, A. K.; Morozov, S. V.; Jiang, D.; Zhang, Y.; Dubonos, S. V.; Grigorieva, I. V.; Firsov, A. A. *Science* **2004,** 306, (5696), 666-669.

97. Li, H.; Wu, J.; Yin, Z.; Zhang, H. *Accounts of Chemical Research* **2014,** 47, (4), 1067-1075.

98. Ares, P.; Aguilar-Galindo, F.; Rodriguez-San-Miguel, D.; Aldave, D. A.; Diaz-Tendero, S.; Alcami, M.; Martin, F.; Gomez-Herrero, J.; Zamora, F. *Advanced Materials* **2016,** 28, (30), 6332-6336.

99. Murugan, C.; Sharma, V.; Murugan, R. K.; Malaimegu, G.; Sundaramurthy, A. *Journal of Controlled Release* **2019,** 299, 1-20.

100. Nicolosi, V.; Chhowalla, M.; Kanatzidis, M. G.; Strano, M. S.; Coleman, J. N. *Science* **2013,** 340, (6139), 1226419.

101. Bonaccorso, F.; Bartolotta, A.; Coleman, J. N.; Backes, C. *Advanced Materials* **2016,** 28, (29), 6136-6166.

102. Lalmi, B.; Oughaddou, H.; Enriquez, H.; Kara, A.; Vizzini, S.; Ealet, B.; Aufray, B. *Applied Physics Letters* **2010,** 97, (22), 223109.

103. Vogt, P.; De Padova, P.; Quaresima, C.; Avila, J.; Frantzeskakis, E.; Asensio, M. C.; Resta, A.; Ealet, B.; Le Lay, G. *Physical Review Letters* **2012,** 108, (15), 155501.

104. Dávila, M.; Xian, L.; Cahangirov, S.; Rubio, A.; Le Lay, G. *New Journal of Physics* **2014,** 16, (9), 095002.

105. Ogrin, Y. F.; Lutskii, V.; Elinson, M. *ZhETF Pisma Redaktsiiu* **1966,** 3, 114.

106. Nagao, T.; Doi, T.; Sekiguchi, T.; Hasegawa, S. *Japanese Journal of Applied Physics* **2000,** 39, (Part 1, No. 7B), 4567-4570.

107. Cho, S.; Um, Y.-H.; Kim, Y.; Wong, G. K. L.; Ketterson, J. B.; Hong, J.-I. *Journal of Vacuum Science & Technology A* **2002,** 20, (4), 1191-1194.

108. Sadowski, J.; Nagaoq, T.; Saito, M.; Oreshkin11, A.; Yaginuma, S.; Hasegawac, S.; Ohno, T.; Sakurai, T. *Acta Physica Polonica A* **2003**.

109. Nagao, T.; Sadowski, J. T.; Saito, M.; Yaginuma, S.; Fujikawa, Y.; Kogure, T.; Ohno, T.; Hasegawa, Y.; Hasegawa, S.; Sakurai, T. *Physical Review Letters* **2004,** 93, (10), 105501.

110. Nagao, T.; Yaginuma, S.; Saito, M.; Kogure, T.; Sadowski, J. T.; Ohno, T.; Hasegawa, S.; Sakurai, T. *Surface Science* **2005,** 590, (1), 247-252.

111. Scott, S. A.; Kral, M. V.; Brown, S. A. *Surface Science* **2005,** 587, (3), 175-184.

112. Yaginuma, S.; Nagao, T.; Sadowski, J. T.; Saito, M.; Nagaoka, K.; Fujikawa, Y.; Sakurai, T.; Nakayama, T. *Surface Science* **2007,** 601, (17), 3593-3600.

113. Hatta, S.; Ohtsubo, Y.; Miyamoto, S.; Okuyama, H.; Aruga, T. *Applied Surface Science* **2009,** 256, (4), 1252-1256.

114. Chen, M.; Peng, J.-P.; Zhang, H.-M.; Wang, L.-L.; He, K.; Ma, X.-C.; Xue, Q.-K. *Applied Physics Letters* **2012,** 101, (8), 081603.

115. Hirahara, T.; Bihlmayer, G.; Sakamoto, Y.; Yamada, M.; Miyazaki, H.; Kimura, S.-i.; Blügel, S.; Hasegawa, S. *Physical Review Letters* **2011,** 107, (16), 166801.

116. Gusmão, R.; Sofer, Z.; Bouša, D.; Pumera, M. *Angewandte Chemie* **2017,** 129, (46), 14609-14614.

117. Lu, L.; Liang, Z.; Wu, L.; Chen, Y.; Song, Y.; Dhanabalan, S. C.; Ponraj, J. S.; Dong, B.; Xiang, Y.; Xing, F.; Fan, D.; Zhang, H. *Laser & Photonics Reviews* **2018,** 12, (1), 1700221.

118. Hussain, N.; Liang, T.; Zhang, Q.; Anwar, T.; Huang, Y.; Lang, J.; Huang, K.; Wu, H. *Small* **2017,** 13, (36), 1701349.

119. Takao, Y.; Asahina, H.; Morita, A. *Journal of the Physical Society of Japan* **1981,** 50, (10), 3362-3369.

120. Xia, F.; Wang, H.; Jia, Y. *Nature Communications* **2014,** 5, 4458.

121. Liu, H.; Neal, A. T.; Zhu, Z.; Luo, Z.; Xu, X.; Tománek, D.; Ye, P. D. *ACS Nano* **2014,** 8, (4), 4033-4041.

122. Ling, X.; Wang, H.; Huang, S.; Xia, F.; Dresselhaus, M. S. *Proceedings of the National Academy of Sciences* **2015,** 112, (15), 4523-4530.

123. Tran, V.; Soklaski, R.; Liang, Y.; Yang, L. *Physical Review B* **2014,** 89, (23), 235319.

124. Liang, L.; Wang, J.; Lin, W.; Sumpter, B. G.; Meunier, V.; Pan, M. *Nano Letters* **2014,** 14, (11), 6400-6406.

125. Zhang, S.; Yang, J.; Xu, R.; Wang, F.; Li, W.; Ghufran, M.; Zhang, Y.-W.; Yu, Z.; Zhang, G.; Qin, Q.; Lu, Y. *ACS Nano* **2014,** 8, (9), 9590-9596.

126. Phaneuf-L'Heureux, A.-L.; Favron, A.; Germain, J.-F.; Lavoie, P.; Desjardins, P.; Leonelli, R.; Martel, R.; Francoeur, S. *Nano Letters* **2016,** 16, (12), 7761-7767.

127. Liu, H.; Du, Y.; Deng, Y.; Peide, D. Y. *Chemical Society Reviews* **2015,** 44, (9), 2732-2743.

128. Carvalho, A.; Wang, M.; Zhu, X.; Rodin, A. S.; Su, H.; Neto, A. H. C. *Nature Reviews Materials* **2016,** 1, (11), 1-16.

129. Buscema, M.; Groenendijk, D. J.; Blanter, S. I.; Steele, G. A.; Van Der Zant, H. S.; Castellanos-Gomez, A. *Nano Letters* **2014,** 14, (6), 3347-3352.

130. Deng, Y.; Luo, Z.; Conrad, N. J.; Liu, H.; Gong, Y.; Najmaei, S.; Ajayan, P. M.; Lou, J.; Xu, X.; Ye, P. D. *ACS Nano* **2014,** 8, (8), 8292-8299.

131. Engel, M.; Steiner, M.; Avouris, P. *Nano Letters* **2014,** 14, (11), 6414-6417.

132. Guo, Q.; Pospischil, A.; Bhuiyan, M.; Jiang, H.; Tian, H.; Farmer, D.; Deng, B.; Li, C.; Han, S.-J.; Wang, H.; Xia, Q.; Ma, T.-P.; Mueller, T.; Xia, F. *Nano Letters* **2016,** 16, (7), 4648-4655.

133. Yuan, H.; Liu, X.; Afshinmanesh, F.; Li, W.; Xu, G.; Sun, J.; Lian, B.; Curto, A. G.; Ye, G.; Hikita, Y.; Shen, Z.; Zhang, S.-C.; Chen, X.; Brongersma, M.; Hwang, H. Y.; Cui, Y. *Nature Nanotechnology* **2015,** 10, (8), 707-713.

134. Favron, A.; Gaufrès, E.; Fossard, F.; Phaneuf-L'Heureux, A.-L.; Tang, N. Y.; Lévesque, P. L.; Loiseau, A.; Leonelli, R.; Francoeur, S.; Martel, R. *Nature Materials* **2015,** 14, (8), 826-832.

135. Wood, J. D.; Wells, S. A.; Jariwala, D.; Chen, K.-S.; Cho, E.; Sangwan, V. K.; Liu, X.; Lauhon, L. J.; Marks, T. J.; Hersam, M. C. *Nano Letters* **2014,** 14, (12), 6964-6970.

136. Ryder, C. R.; Wood, J. D.; Wells, S. A.; Yang, Y.; Jariwala, D.; Marks, T. J.; Schatz, G. C.; Hersam, M. C. *Nature Chemistry* **2016,** 8, (6), 597-602.

137. Smith, J. B.; Hagaman, D.; Ji, H.-F. *Nanotechnology* **2016,** 27, (21), 215602.

138. Li, C.; Wu, Y.; Deng, B.; Xie, Y.; Guo, Q.; Yuan, S.; Chen, X.; Bhuiyan, M.; Wu, Z.; Watanabe, K.; Taniguchi, T.; Wang, H.; Cha, J. J.; Snure, M.; Fei, Y.; Xia, F. *Advanced Materials* **2018,** 30, (6), 1703748.

139. Xu, H.; Han, X.; Li, Z.; Liu, W.; Li, X.; Wu, J.; Guo, Z.; Liu, H. *Advanced Materials Interfaces* **2018,** 5, (21), 1801048.

140. Gu, C.; Zhao, S.; Zhang, J. L.; Sun, S.; Yuan, K.; Hu, Z.; Han, C.; Ma, Z.; Wang, L.; Huo, F.; Huang, W.; Li, Z.; Chen, W. *ACS Nano* **2017,** 11, (5), 4943-4949.

141. Zhang, J. L.; Zhao, S.; Han, C.; Wang, Z.; Zhong, S.; Sun, S.; Guo, R.; Zhou, X.; Gu, C. D.; Yuan, K. D.; Li, Z.; Chen, W. *Nano Letters* **2016,** 16, (8), 4903-4908.

142. Höchst, H.; Ast, C. R. *Journal of Electron Spectroscopy and Related Phenomena* **2004,** 137, 441-444.

143. Yi, X.; Wang, H.; Chen, S.; Lai, J.; He, M.; Wang, S.; Wong, G. K. *Infrared Physics & Technology* **2005,** 46, (3), 263-266.

144. Bian, G.; Wang, X.; Liu, Y.; Miller, T.; Chiang, T. C. *Physical Review Letters* **2012,** 108, (17), 176401.

145. Wang, D.; Chen, L.; Liu, H.; Wang, X. *EPL* **2014,** 104, (5), 57011.

146. Yan, Z.; Kushvaha, S.; Xiao, W.; Wang, X.-S. *Applied Physics A* **2007,** 88, (2), 299-307.

147. Wang, X.-S.; Kushvaha, S.; Yan, Z.; Xiao, W. *Applied Physics Letters* **2006,** 88, (23), 233105.

148. Pizzi, G.; Gibertini, M.; Dib, E.; Marzari, N.; Iannaccone, G.; Fiori, G. *Nature Communications* **2016,** 7.

149. Wang, Y.; Ding, Y. *Nanoscale Research Letters* **2015,** 10, (1), 254.

150. Üzengi Aktürk, O.; Aktürk, E.; Ciraci, S. *Physical Review B* **2016,** 93, (3), 035450.

151. Zhang, S.; Xie, M.; Cai, B.; Zhang, H.; Ma, Y.; Chen, Z.; Zhu, Z.; Hu, Z.; Zeng, H. *Physical Review B* **2016,** 93, (24), 245303.

152. Zhang, S.; Zhou, W.; Ma, Y.; Ji, J.; Cai, B.; Yang, S. A.; Zhu, Z.; Chen, Z.; Zeng, H. *Nano Letters* **2017,** 17, (6), 3434-3440.

153. Gibaja, C.; Rodriguez‐San‐Miguel, D.; Ares, P.; Gómez‐Herrero, J.; Varela, M.; Gillen, R.; Maultzsch, J.; Hauke, F.; Hirsch, A.; Abellán, G.; Zamora, F. *Angewandte Chemie International Edition* **2016,** 55, (46), 14345-14349.

154. Ji, J.; Song, X.; Liu, J.; Yan, Z.; Huo, C.; Zhang, S.; Su, M.; Liao, L.; Wang, W.; Ni, Z.; Hao, Y.; Zeng, H. *Nature Communications* **2016,** 7, 13352.

155. Wu, X.; Shao, Y.; Liu, H.; Feng, Z.; Wang, Y. L.; Sun, J. T.; Liu, C.; Wang, J. O.; Liu, Z. L.; Zhu, S. Y.; Wang, Y.-Q.; Du, S.-X.; Shi, Y.-G.; Ibrahim, K.; Gao, H.-J. *Advanced Materials* **2016,** 29, (11), 1605407.

156. Stegemann, B.; Opitz, J.; Kaiser, B.; Rademann, K., Investigation of the Mobility of Small Antimony Clusters on HOPG with Scanning Tunneling Microscopy. In *Cluster And Nanostructure Interfaces*, World Scientific: 2000; pp 601-606.

157. Niu, T.; Zhou, W.; Zhou, D.; Hu, X.; Zhang, S.; Zhang, K.; Zhou, M.; Fuchs, H.; Zeng, H. *Advanced Materials* **2019,** 31, (29), 1902606.

158. Niu, T.; Meng, Q.; Zhou, D.; Si, N.; Zhai, S.; Hao, X.; Zhou, M.; Fuchs, H. *Advanced Materials* **2019,** 32, 1906873.

159. Sun, X.; Lu, Z.; Xiang, Y.; Wang, Y.; Shi, J.; Wang, G.-C.; Washington, M. A.; Lu, T.-M. *ACS Nano* **2018,** 12, (6), 6100-6108.

160. Mao, Y.-H.; Zhang, L.-F.; Wang, H.-L.; Shan, H.; Zhai, X.-F.; Hu, Z.-P.; Zhao, A.-D.; Wang, B. *Frontiers of Physics* **2018,** 13, (3), 138106.

161. Shao, Y.; Liu, Z.-L.; Cheng, C.; Wu, X.; Liu, H.; Liu, C.; Wang, J.-O.; Zhu, S.-Y.; Wang, Y.-Q.; Shi, D.-X.; Ibrahim, K.; Sun, J.-T.; Wang, Y.-L.; Gao, H.-J. *Nano Letters* **2018,** 18, (3), 2133-2139.

162. Märkl, T.; Kowalczyk, P. J.; Le Ster, M.; Mahajan, I. V.; Pirie, H.; Ahmed, Z.; Bian, G.; Wang, X.; Chiang, T. C.; Brown, S. A. *2D Materials* **2017,** 5, (1), 011002.

163. Shi, Z.-Q.; Li, H.; Yuan, Q.-Q.; Song, Y.-H.; Lv, Y.-Y.; Shi, W.; Jia, Z.-Y.; Gao, L.; Chen, Y.-B.; Zhu, W.; Li, S.-C. *Advanced Materials* **2019,** 31, (5), 1806130.

164. Zhang, H.; Ma, Y.; Chen, Z. *Nanoscale* **2015,** 7, (45), 19152-19159.

165. Wang, Y.-p.; Zhang, C.-w.; Ji, W.-x.; Zhang, R.-w.; Li, P.; Wang, P.-j.; Ren, M.-j.; Chen, X.-l.; Yuan, M. *Journal of Physics D: Applied Physics* **2016,** 49, (5), 055305.

166. Tsai, H.-S.; Wang, S.-W.; Hsiao, C.-H.; Chen, C.-W.; Ouyang, H.; Chueh, Y.-L.; Kuo, H.-C.; Liang, J.-H. *Chemistry of Materials* **2016,** 28, (2), 425-429.

167. Tsai, H.-S.; Chen, C.-W.; Hsiao, C.-H.; Ouyang, H.; Liang, J.-H. *Chemical Communications* **2016,** 52, (54), 8409-8412.

168. Hu, Y.; Qi, Z.-H.; Lu, J.; Chen, R.; Zou, M.; Chen, T.; Zhang, W.; Wang, Y.; Xue, X.; Ma, J.; Jin, Z. *Chemistry of Materials* **2019,** 31, (12), 4524-4535.

169. Shah, J.; Wang, W.; Sohail, H. M.; Uhrberg, R. I. *2D Materials* **2019**.

170. Zhong, M.; Xia, Q.; Pan, L.; Liu, Y.; Chen, Y.; Deng, H.-X.; Li, J.; Wei, Z. *Advanced Functional Materials* **2018,** 28, (43), 1802581.

171. Laniel, D.; Geneste, G.; Weck, G.; Mezouar, M.; Loubeyre, P. *Physical Review Letters* **2019,** 122, (6), 066001.

172. Ersan, F.; Aktürk, E.; Ciraci, S. *Physical Review B* **2016,** 94, (24), 245417.

173. Li, J.-S.; Wang, W.-L.; Yao, D.-X. *Scientific Reports* **2016,** 6, (1), 34177.

174. Kadioglu, Y.; Üzengi Aktürk, O.; Aktürk, E.; Ciraci, S. *The Journal of Physical Chemistry C* **2017,** 121, (11), 6329-6338.

175. Lin, W.; Li, J.; Wang, W.; Liang, S.-D.; Yao, D.-X. *Scientific Reports* **2018,** 8, (1), 1674.

176. Trzebiatowski, W.; Bryjak, E. *Zeitschrift für Anorganische und Allgemeine Chemie* **1938,** 238, (2 - 3), 255-267.

177. Smith, G.; Wolfe, R. *Journal of Applied Physics* **1962,** 33, (3), 841-846.

178. Long, M.; Gao, A.; Wang, P.; Xia, H.; Ott, C.; Pan, C.; Fu, Y.; Liu, E.; Chen, X.; Lu, W.; Nilges, T.; Xu, J.; Wang, X.; Hu, W.; Miao, F. *Science Advances* **2017,** 3, (6), e1700589.

179. Nie, Y.; Rahman, M.; Wang, D.; Wang, C.; Guo, G. *Scientific Reports* **2015,** 5, 17980.

180. Liu, M.-Y.; Huang, Y.; Chen, Q.-Y.; Cao, C.; He, Y. *Scientific Reports* **2016,** 6, 29114.

181. Yu, W.; Niu, C.-Y.; Zhu, Z.; Wang, X.; Zhang, W.-B. *Journal of Materials Chemistry C* **2016,** 4, (27), 6581-6587.

182. Guo, S.; Zhang, Y.; Ge, Y.; Zhang, S.; Zeng, H.; Zhang, H. *Advanced Materials* **2019,** 31, (39), 1902352.

183. Zhao, N.; Zhu, Y.; Jiang, Q. *Journal of Materials Chemistry C* **2018,** 6, (11), 2854-2861.

184. Ueda, Y.; Duy Khang, N. H.; Yao, K.; Hai, P. N. *Applied Physics Letters* **2017,** 110, (6), 062401.

185. Periwal, P.; Thomsen, J. D.; Reuter, M. C.; Zakharov, D.; Gignac, L.; Booth, T. J.; Hofmann, S.; Ross, F. M. *Microscopy Microanalysis* **2019,** 25, (S2), 1424-1425.

186. Bauer, E. *Reports on Progress in Physics* **1994,** 57, (9), 895-938.

187. Wang, Z.-J.; Weinberg, G.; Zhang, Q.; Lunkenbein, T.; Klein-Hoffmann, A.; Kurnatowska, M.; Plodinec, M.; Li, Q.; Chi, L.; Schloegl, R.; Willinger, M.-G. *ACS Nano* **2015,** 9, (2), 1506-1519.

188. Takahashi, K.; Yamada, K.; Kato, H.; Hibino, H.; Homma, Y. *Surface Science* **2012,** 606, (7), 728-732.

189. Cui, Y.; Fu, Q.; Zhang, H.; Tan, D.; Bao, X. *The Journal of Physical Chemistry C* **2009,** 113, (47), 20365-20370.

190. Cui, Y.; Fu, Q.; Bao, X. *Physical Chemistry Chemical Physics* **2010,** 12, (19), 5053-5057.

191. Loginova, E.; Bartelt, N. C.; Feibelman, P. J.; McCarty, K. F. *New Journal of Physics* **2008,** 10, (9), 093026.

192. Loginova, E.; Bartelt, N.; Feibelman, P.; McCarty, K. *New Journal of Physics* **2009,** 11, (6), 063046.

193. Wofford, J. M.; Nie, S.; McCarty, K. F.; Bartelt, N. C.; Dubon, O. D. *Nano Letters* **2010,** 10, (12), 4890-4896.

194. Sutter, P.; Sadowski, J. T.; Sutter, E. *Physical Review B* **2009,** 80, (24), 245411.

195. Odahara, G.; Otani, S.; Oshima, C.; Suzuki, M.; Yasue, T.; Koshikawa, T. *Surface Science* **2011,** 605, (11-12), 1095-1098.

196. McCarty, K. F.; Feibelman, P. J.; Loginova, E.; Bartelt, N. C. *Carbon* **2009,** 47, (7), 1806-1813.

197. Addou, R.; Dahal, A.; Sutter, P.; Batzill, M. *Applied Physics Letters* **2012,** 100, (2), 021601.

198. Zangwill, A.; Vvedensky, D. D. *Nano Letters* **2011,** 11, (5), 2092-2095.

199. Nie, S.; Wofford, J. M.; Bartelt, N. C.; Dubon, O. D.; McCarty, K. F. *Physical Review B* **2011,** 84, (15), 155425.

200. Hannon, J.; Tromp, R. *Physical Review B* **2008,** 77, (24), 241404.

201. Herrmann, C.; Omelchenko, P.; Kavanagh, K. L. *Surface Science* **2018,** 669, 133-139.

202. Zhang, Y.; Weng, X.; Li, H.; Li, H.; Wei, M.; Xiao, J.; Liu, Z.; Chen, M.; Fu, Q.; Bao, X. *Nano Letters* **2015,** 15, (5), 3616-3623.

203. Algara-Siller, G.; Lehtinen, O.; Wang, F. C.; Nair, R. R.; Kaiser, U.; Wu, H. A.; Geim, A. K.; Grigorieva, I. V. *Nature* **2015,** 519, (7544), 443-445.

204. Locatelli, A.; Bianco, A.; Cocco, D.; Cherifi, S.; Heun, S.; Marsi, M.; Pasqualetto, M.; Bauer, E. *Journal de Physique IV* **2003,** 104, 99-102.

205. Menteş, T. O.; Zamborlini, G.; Sala, A.; Locatelli, A. *Beilstein Journal of Nanotechnology* **2014,** 5, 1873-1886.

206. Horcas, I.; Fernández, R.; Gomez-Rodriguez, J.; Colchero, J.; Gómez-Herrero, J.; Baro, A. *Review of Scientific Instruments* **2007,** 78, (1), 013705.

207. Langreth, D. C.; Mehl, M. J. *Physical Review B* **1983,** 28, (4), 1809-1834.

208. Shan, N.; Zhou, M.; Hanchett, M. K.; Chen, J.; Liu, B. *Molecular Simulation* **2017,** 43, (10-11), 861-885.

209. Dion, M.; Rydberg, H.; Schröder, E.; Langreth, D. C.; Lundqvist, B. I. *Physical Review Letters* **2004,** 92, (24), 246401.

210. Perdew, J. P.; Burke, K.; Ernzerhof, M. *Physical Review Letters* **1996,** 77, (18), 3865.

211. Grimme, S. *Journal of Computational Chemistry* **2006,** 27, (15), 1787-1799.

212. Klimeš, J.; Bowler, D. R.; Michaelides, A. *Physical Review B* **2011,** 83, (19), 195131.

213. Thonhauser, T.; Zuluaga, S.; Arter, C.; Berland, K.; Schröder, E.; Hyldgaard, P. *Physical Review Letters* **2015,** 115, (13), 136402.

214. Langreth, D.; Lundqvist, B. I.; Chakarova-Käck, S. D.; Cooper, V.; Dion, M.; Hyldgaard, P.; Kelkkanen, A.; Kleis, J.; Kong, L.; Li, S. *Journal of Physics: Condensed Matter* **2009,** 21, (8), 084203.

215. Giannozzi, P.; Baroni, S.; Bonini, N.; Calandra, M.; Car, R.; Cavazzoni, C.; Ceresoli, D.; Chiarotti, G. L.; Cococcioni, M.; Dabo, I. *Journal of Physics: Condensed Matter* **2009,** 21, (39), 395502.

216. Giannozzi, P.; Andreussi, O.; Brumme, T.; Bunau, O.; Buongiorno Nardelli, M.; Calandra, M.; Car, R.; Cavazzoni, C.; Ceresoli, D.; Cococcioni, M.; Colonna, N.; Carnimeo, I.; Dal Corso, A.; de Gironcoli, S.; Delugas, P.; DiStasio, R. A.; Ferretti, A.; Floris, A.; Fratesi, G.; Fugallo, G.; Gebauer, R.; Gerstmann, U.; Giustino, F.; Gorni, T.; Jia, J.; Kawamura, M.; Ko, H. Y.; Kokalj, A.; Küçükbenli, E.; Lazzeri, M.; Marsili, M.; Marzari, N.; Mauri, F.; Nguyen, N. L.; Nguyen, H. V.; Otero-de-la-Roza, A.; Paulatto, L.; Poncé, S.; Rocca, D.; Sabatini, R.; Santra, B.; Schlipf, M.; Seitsonen, A. P.; Smogunov, A.; Timrov, I.; Thonhauser, T.; Umari, P.; Vast, N.; Wu, X.; Baroni, S. *Journal of Physics: Condensed Matter* **2017,** 29, (46), 465901.

217. Voter, A. F. In *Introduction to the kinetic Monte Carlo method*, Radiation Effects in Solids, Dordrecht, 2007//, 2007; Sickafus, K. E.; Kotomin, E. A.; Uberuaga, B. P., Eds. Springer Netherlands: Dordrecht, pp 1-23.

218. Seiwatz, R. *Surface Science* **1964,** 2, 473-483.

219. Xie, Z.; Hui, L.; Wang, J.; Zhu, G. a.; Chen, Z.; Li, C. *Computational Materials Science* **2018,** 144, 304-314.

220. Koma, A. *Thin Solid Films* **1992,** 216, (1), 72-76.

221. Ueno, K.; Kuang-Yu, L.; Fujikawa, Y.; Saiki, K.; Koma, A. In *Heteroepitaxy of layered III-VI semiconductor GaSe on hydrogen-terminated Si(111) surfaces*, Extended Abstracts of the 1992 International Conference on Solid State Devices and Materials - SSDM '92, August 26, 1992 - August 28, 1992, Tsukuba, Jpn, 1992; Publ by Business Cent for Acad Soc Japan: Tsukuba, Jpn, pp 680-682.

222. Saiki, K.; Nishita, K.; Ariga, Y.; Koma, A. *Journal of Vacuum Science & Technology A: Vacuum, Surfaces, and Films* **1999,** 17, (5), 2911-2914.

223. Hauch, J. O.; Fonin, M.; May, U.; Calarco, R.; Kittur, H.; Choi, J. M.; Rüdiger, U.; Güntherodt, G. *Advanced Functional Materials* **2001,** 11, (3), 179-185.

224. Arranz, A.; Sánchez-Royo, J.; Avila, J.; Pérez-Dieste, V.; Dumas, P.; Asensio, M. *Physical Review B* **2002,** 65, (7), 075405.

225. Gruyters, M. *Surface Science* **2002,** 515, (1), 53-60.

226. Li, H.; Gao, L.; Li, H.; Wang, G.; Wu, J.; Zhou, Z.; Wang, Z. *Applied Physics Letters* **2013,** 102, (7), 074106.

227. Kiraly, B.; Jacobberger, R. M.; Mannix, A. J.; Campbell, G. P.; Bedzyk, M. J.; Arnold, M. S.; Hersam, M. C.; Guisinger, N. P. *Nano Letters* **2015,** 15, (11), 7414-7420.

228. Deegan, T.; Hughes, G. *Applied Surface Science* **1998,** 123, 66-70.

229. Bodlaki, D.; Yamamoto, H.; Waldeck, D.; Borguet, E. *Surface Science* **2003,** 543, (1), 63-74.

230. Wong, K. T.; Kim, Y.-G.; Soriaga, M. P.; Brunschwig, B. S.; Lewis, N. S. *Journal of the American Chemical Society* **2015,** 137, (28), 9006-9014.

231. Imbihl, R.; Demuth, J.; Himpsel, F.; Marcus, P.; Thompson, W.; Jona, F. *Physical Review B* **1987,** 36, (9), 5037.

232. Su, C.; Tsai, C.-S.; Lin, C.-E.; Chen, K.-H.; Wang, J.-K.; Lin, J.-C. *Surface science* **2000,** 445, (2), 139-150.

233. Sun, S.; Sun, Y.; Liu, Z.; Lee, D.-I.; Pianetta, P. *Applied Physics Letters* **2006,** 89, (23), 231925.

234. Lu, Z. *Applied Physics Letters* **1996,** 68, (4), 520-522.

235. Göthelid, M.; LeLay, G.; Wigren, C.; Björkqvist, M.; Karlsson, U. O. *Surface Science* **1997,** 371, (2-3), 264-276.

236. Boonstra, A.; Van Ruler, J. *Surface Science* **1966,** 4, (2), 141-149.

237. Robey, S.; Bahr, C.; Hussain, Z.; Barton, J.; Leung, K.; Lou, J.-r.; von Wittenau, A. S.; Shirley, D. *Physical Review B* **1987,** 35, (11), 5657.

238. Van Bommel, A.; Meyer, F. *Surface Science* **1967,** 6, (3), 391-394.

239. Citrin, P.; Eisenberger, P.; Rowe, J. *Physical Review Letters* **1982,** 48, (12), 802.

240. Kendelewicz, T.; Woicik, J.; Miyano, K.; Yoshikawa, S.; Pianetta, P.; Spicer, W. *Journal of Vacuum Science Technology A: Vacuum, Surfaces, Films* **1994,** 12, (4), 1843-1847.

241. Kuzmin, M.; Laukkanen, P.; Perälä, R.; Ahola-Tuomi, M.; Väyrynen, I. *Surface Science* **2007,** 601, (3), 837-843.

242. Kim, J. W.; Seo, J. M.; Kim, S. *Surface Science* **1996,** 351, (1-3), L239-L244.

243. Lee, J. Y.; Kang, M.-H. *Physical Review B* **2002,** 66, (23), 233301.

244. Lee, G.; Cho, E.-J.; Park, Y.; Cho, S.; Lee, H.-G. *Surface Science* **2002,** 501, (1), L177-L183.

245. Thonhauser, T.; Cooper, V. R.; Li, S.; Puzder, A.; Hyldgaard, P.; Langreth, D. C. *Physical Review B* **2007,** 76, (12), 125112.

246. Schultz, K.; Seebauer, E. G. *The Journal of Chemical Physics* **1992,** 97, (9), 6958-6967.

247. Tetlow, H.; de Boer, J. P.; Ford, I.; Vvedensky, D.; Coraux, J.; Kantorovich, L. *Physics Reports* **2014,** 542, (3), 195-295.

248. Jacobberger, R. M.; Kiraly, B.; Fortin-Deschenes, M.; Levesque, P. L.; McElhinny, K. M.; Brady, G. J.; Rojas Delgado, R.; Singha Roy, S.; Mannix, A.; Lagally, M. G.; Evans, P. G.;

Desjardins, P.; Martel, R.; Hersam, M. C.; Guisinger, N. P.; Arnold, M. S. *Nature Communications* **2015,** 6, (1), 8006.

249. Mulheran, P. A.; Blackman, J. A. *Philosophical Magazine Letters* **1995,** 72, (1), 55-60.

250. Khang, N. H. D.; Ueda, Y.; Hai, P. N. *Nature Materials* **2018,** 17, (9), 1.

251. Shirokura, T.; Yao, K.; Ueda, Y.; Hai, P. N. *ArXiv:1810.10840.* **2018**.

252. Tersoff, J.; Jesson, D. E.; Tang, W. X. *Science* **2009,** 324, (5924), 236-238.

253. Fornari, R.; Brinciotti, A.; Sentiri, A.; Görög, T.; Curti, M.; Zuccalli, G. *Journal of Applied Physics* **1994,** 75, (5), 2406-2409.

254. Lee, J.-U.; Yoon, D.; Cheong, H. *Nano Letters* **2012,** 12, (9), 4444-4448.

255. Koenig, S. P.; Boddeti, N. G.; Dunn, M. L.; Bunch, J. S. *Nature Nanotechnology* **2011,** 6, (9), 543-546.

256. Ramírez-Jiménez, R.; Álvarez-Fraga, L.; Jimenez-Villacorta, F.; Climent-Pascual, E.; Prieto, C.; de Andrés, A. *Carbon* **2016,** 105, 556-565.

257. Huang, Y.; Wang, X.; Zhang, X.; Chen, X.; Li, B.; Wang, B.; Huang, M.; Zhu, C.; Zhang, X.; Bacsa, W. S.; Ding, F.; Ruoff, R. S. *Physical Review Letters* **2018,** 120, (18), 186104.

258. Jacobs, R. B. *The Journal of Chemical Physics* **1937,** 5, (12), 945-953.

259. Smits, A. *Proceedings of the Royal Netherlands Academy of Arts and Science* **1916,** 18, 992-1007.

260. Liu, X.; Wood, J. D.; Chen, K.-S.; Cho, E.; Hersam, M. C. *The Journal of Physical Chemistry Letters* **2015,** 6, (5), 773-778.

261. Kumar, A.; Telesio, F.; Forti, S.; Al-Temimy, A.; Coletti, C.; Serrano-Ruiz, M.; Caporali, M.; Peruzzini, M.; Beltram, F.; Heun, S. *2D Materials* **2018,** 6, (1), 015005.

262. Luo, W.; Yang, R.; Liu, J.; Zhao, Y.; Zhu, W.; Xia, G. *Nanotechnology* **2017,** 28, (28), 285301.

263. Li, J. H.; Liang, S. H.; Guo, H. B.; Liu, B. X. *Applied Physics Letters* **2005,** 87, (19), 194111.

264. Kong, L.; Enders, A.; Rahman, T. S.; Dowben, P. A. *Journal of Physics: Condensed Matter* **2014,** 26, (44), 443001.

265. Lee, G.; Lee, B.; Kim, J.; Cho, K. *The Journal of Physical Chemistry C* **2009,** 113, (32), 14225-14229.

266. Kozbial, A.; Zhou, F.; Li, Z.; Liu, H.; Li, L. *Accounts of Chemical Research* **2016,** 49, (12), 2765-2773.

267. Kozbial, A.; Li, Z.; Sun, J.; Gong, X.; Zhou, F.; Wang, Y.; Xu, H.; Liu, H.; Li, L. *Carbon* **2014,** 74, 218-225.

268. Munz, M.; Giusca, C. E.; Myers-Ward, R. L.; Gaskill, D. K.; Kazakova, O. *ACS Nano* **2015,** 9, (8), 8401-8411.

269. Hong, G.; Han, Y.; Schutzius, T. M.; Wang, Y.; Pan, Y.; Hu, M.; Jie, J.; Sharma, C. S.; Müller, U.; Poulikakos, D. *Nano Letters* **2016,** 16, (7), 4447-4453.

270. Melios, C.; Giusca, C. E.; Panchal, V.; Kazakova, O. *ArXiv* **2018,** arXiv:.09518.

APPENDIX A β-2D-Sb on graphene/Ge

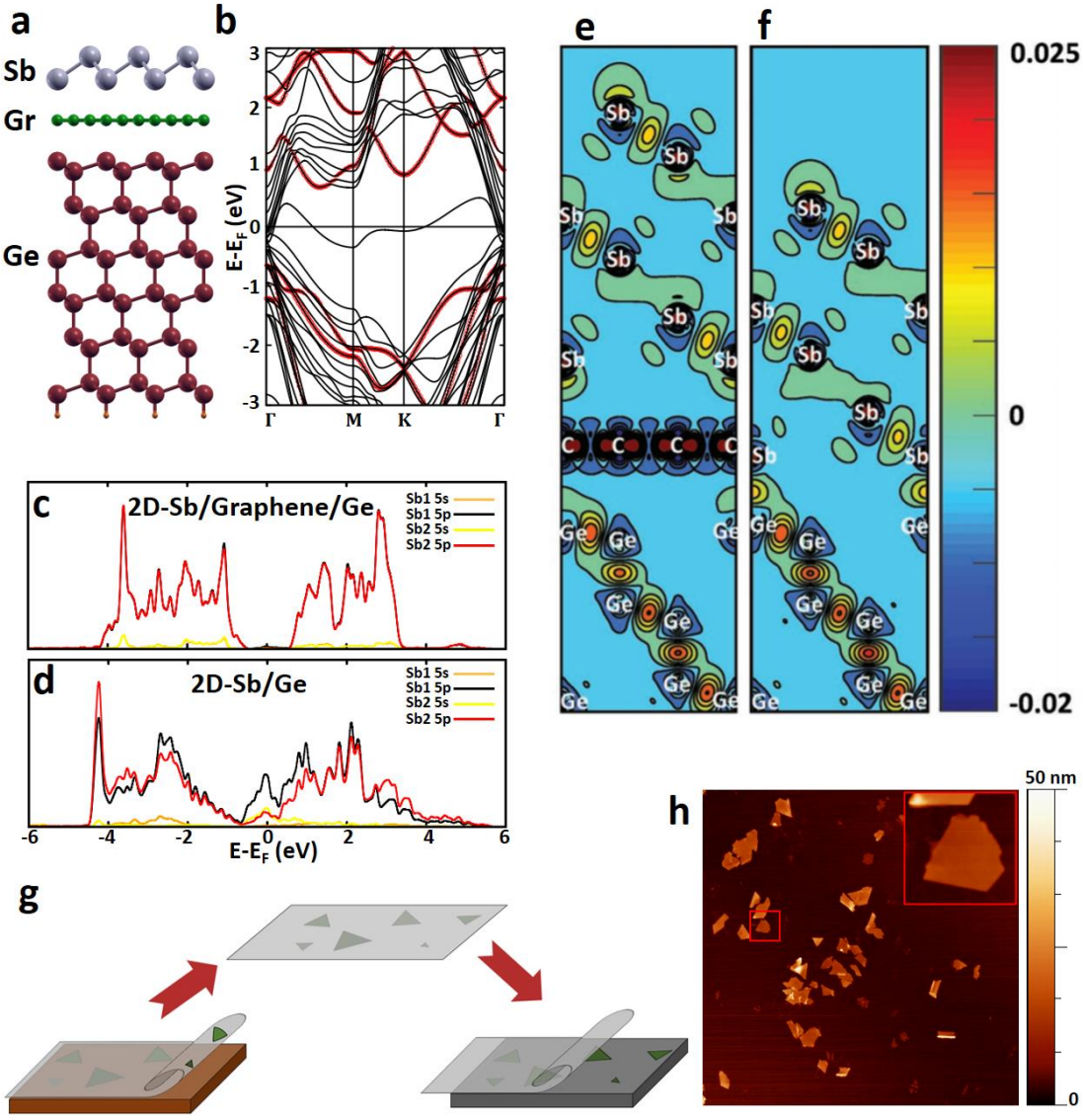

Figure 7.1 Properties of β-2D-Sb on graphene/Ge. a) Schematics of supercell used for DFT calculations (PBE+D2) of β-2D-Sb on graphene/Ge(111). b) Band structure of β-2D-Sb/graphene/Ge(111). The width of the red band is proportional to the projected contribution of Sb orbitals. c) PDOS of β-2D-Sb/graphene/Ge(111). d) PDOS of β-2D-Sb/Ge(111) for comparison. e-f) Charge density minus superposition of atomic charge densities for trilayer β-2D-Sb on graphene/Ge(111) (e) and β-2D-Sb on Ge(111) (f). Color scale is in e^-/a_0^3. g) Schematics of the method used to transfer β-2D-Sb from graphene/Ge to SiO_2. h) AFM image of β-2D-Sb transferred to SiO_2. Adapted from *Fortin-Deschênes, M. et al., Advanced Materials 2019, 31 (21), 1900569* [37].

APPENDIX B GROWTH DYNAMICS OF A SINGLE β-2D-Sb ISLAND

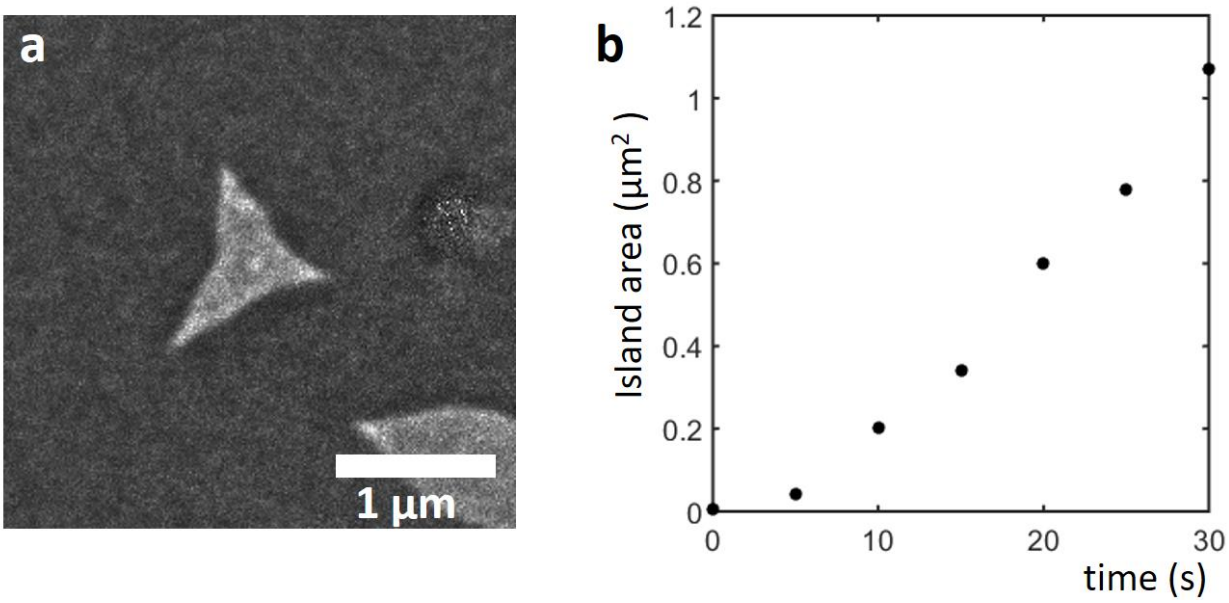

Figure 7.2 Growth dynamics of a single β-2D Sb island. a) Bright-field LEEM (4.3 eV of a β-2D-Sb island growing on graphene/Ge(111) (T=242 °C, F=91nm/min). b) Area of the island as a function of time since nucleation. The early growth stage is superlinear and then the growth rate stabilizes. More details in Chapter 6. Adapted from *Fortin-Deschênes, M. et al., Advanced Materials 2019, 31 (21), 1900569* [37].

APPENDIX C PHASE TRANSFORMATION OF Sb NUCLEI

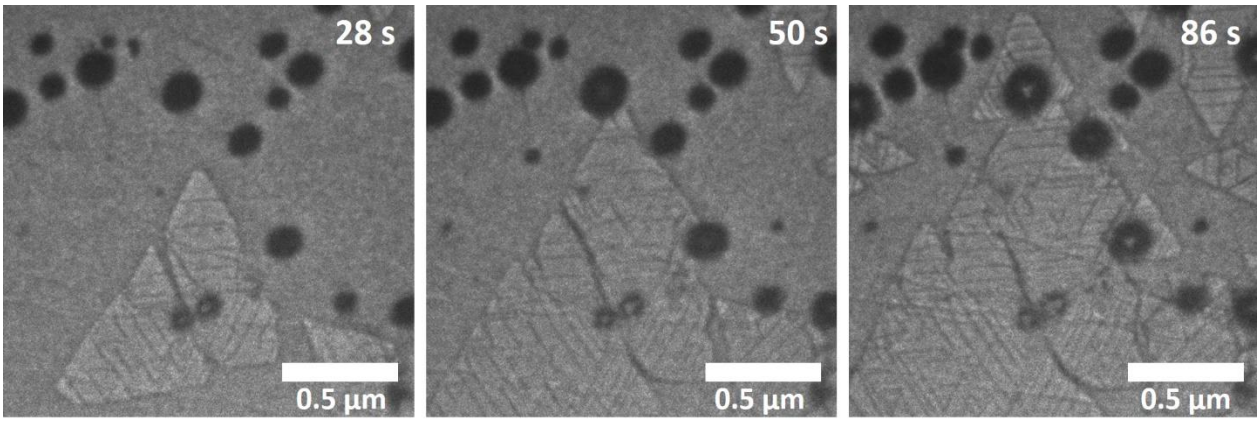

Figure 7.3 Bright-field LEEM snapshots of a β-2D-Sb island with a central 3D nuclei growing on graphene/Ge(110) (F=64 nm/min, T=210 °C). The triangular flat surface of the 3D nuclei can be seen at 50s and 86s. Moreover, we can see that when the branches of the island come in contact with a 3D amorphous island, the latter goes through a phase transition to Sb(111). This can be seen by the formation of a flat triangular surface and the nucleation of a 2D flake with the same crystallographic orientation as the seed island. For instance, look at the tip of the top branch of the island at 50s.

APPENDIX D MBE DEPOSITION OF P ON Nb(110)

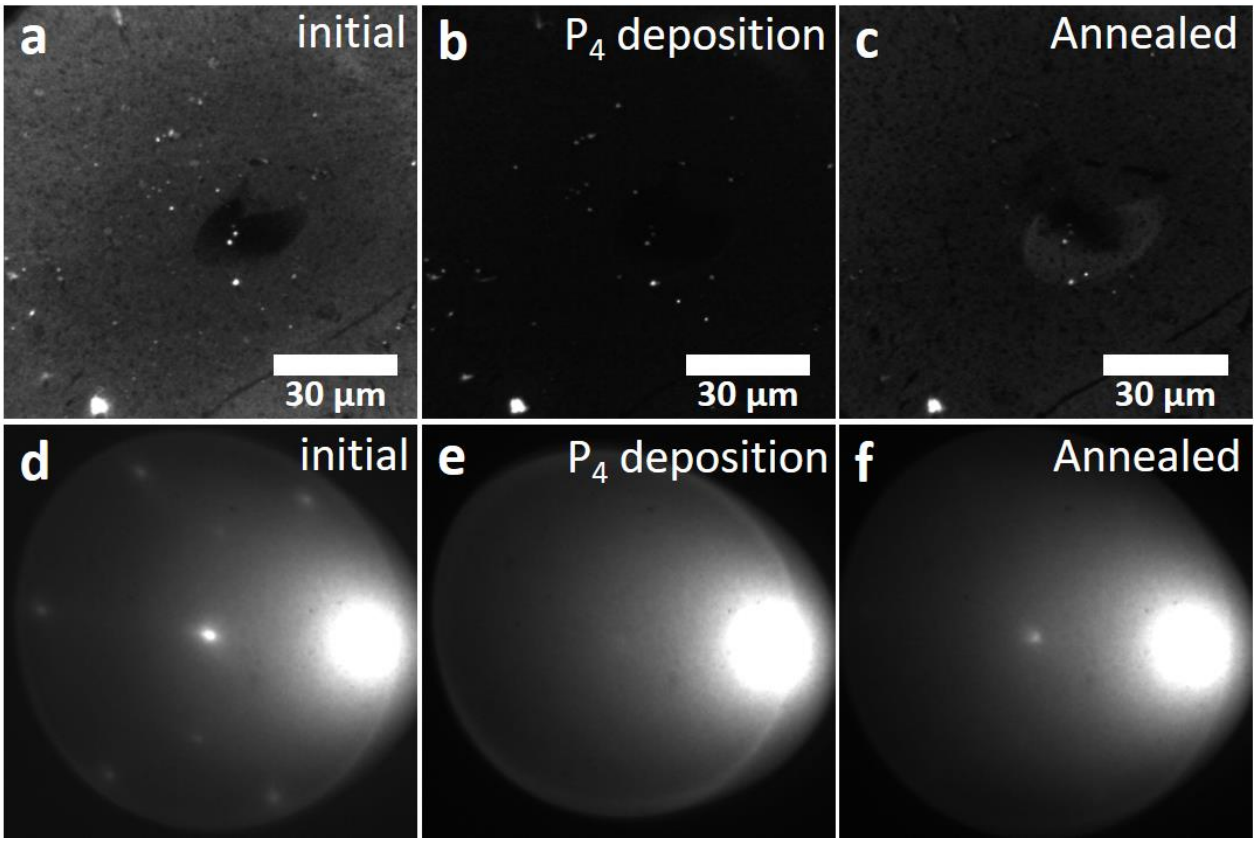

Figure 7.4 (a-c) PEEM images using a short-arc mercury lamp (cutoff hν=4.9 eV) of the deposition of P_4 on Nb(110). The PEEM intensity drops after deposition, which indicates the formation of a film. Annealing leads to a partial desorption of the film. (d-f) LEED patterns (22 eV) of the same deposition process. The Nb(110) LEED disappears after P_4 deposition. The (0,0) spot also disappears, which means that there is no formation of an epitaxial crystalline film.

APPENDIX E α-2D-P

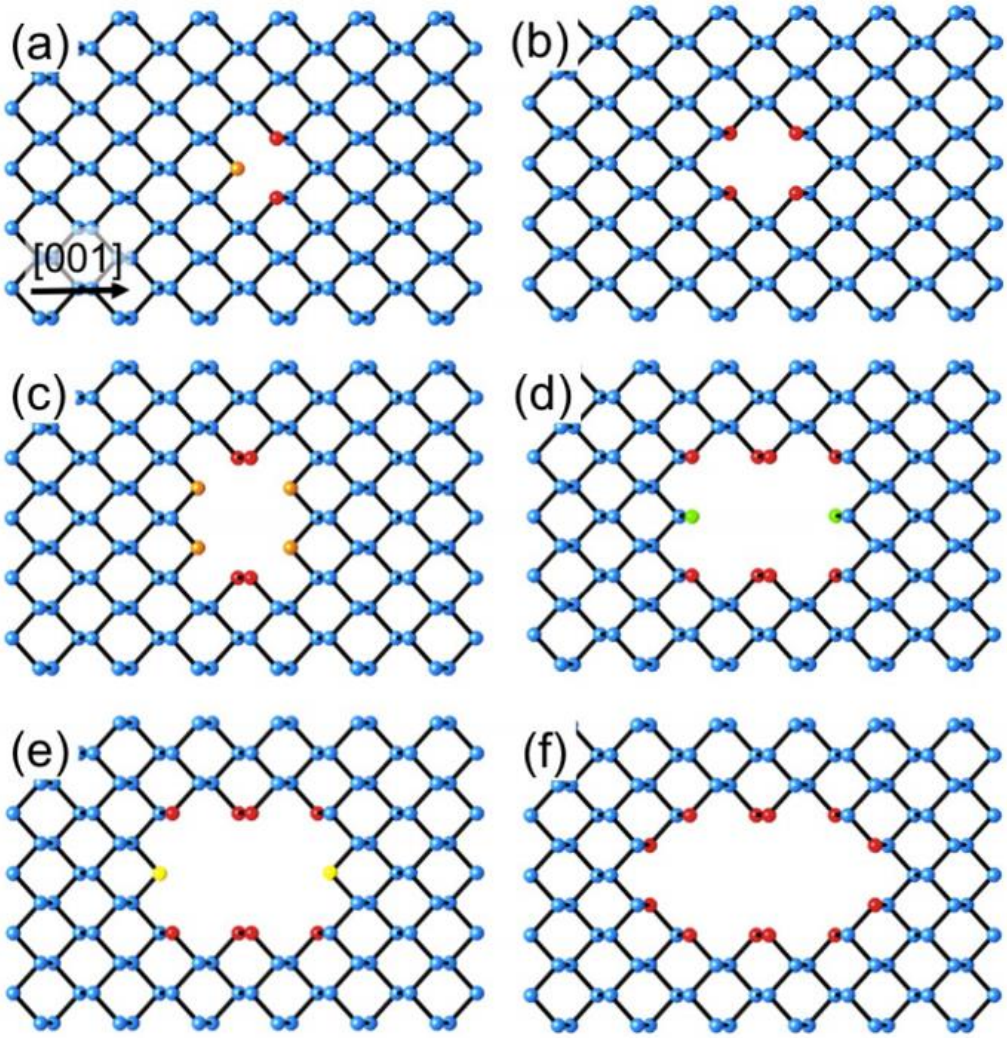

Figure 7.5 α-2D-P sublimation mechanism proposed by Liu et *al*.[260] The mechanism explains the formation of the anisotropic holes by the sublimation of P atoms. In the model, the sublimation starts at a point defect and P atoms are removed in priority according to their number of bonds to the layer. If an atom has 1 bond (green), it desorbs first. If there are two bonds, the atoms desorb in priority is their two bonds are in the plane of the layer (yellow). The atoms with bonds out of the plane of the layer desorb last. Reprinted with permission from *Liu, X. et al, The Journal of Physical Chemistry Letters* ***2015,*** *6, (5), 773-778.* [260] Copyright (2015) American Chemical Society.

APPENDIX F α-2D-P hole coalescence

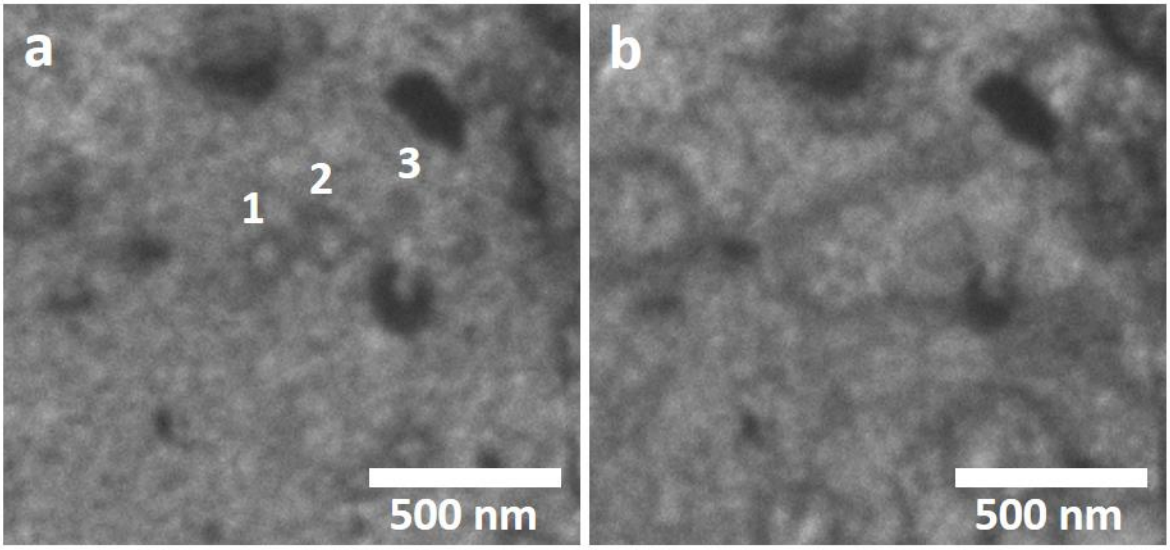

Figure 7.6 Bright-field LEEM images of the formation and coalescence of monolayer deep holes during α-2D-P sublimation. Three holes (labelled 1, 2 and 3) are seen in (a). Their edges appear as dark lines. In (b), the holes coalesce and a continuous surface (without steps) is exposed. This support the hypothesis that the holes are monolayer deep (or at least all of the same depth) since holes of different depths would have left atomic steps at their coalescence.

APPENDIX G LEEM/LEED rotation angle calibration

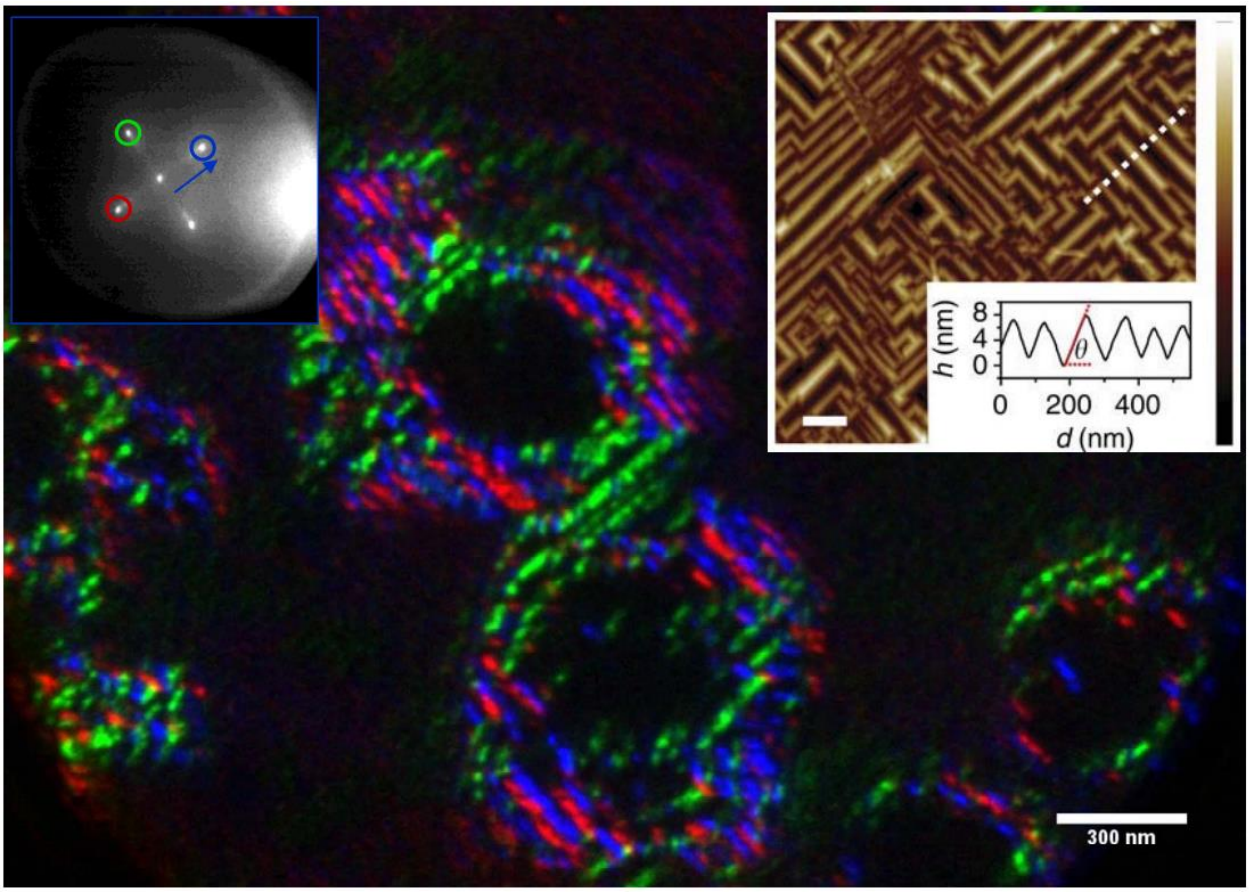

Figure 7.7 Composite dark-field LEEM images of Ge{107} facets on graphene/Ge(001). Inset (top left) shows the corresponding LEED pattern. The LEED spots used for dark-field imaging are circled with the color used to display the LEEM image. Inset (top right): AFM image (scale bar is 200 nm and height colorscale is 11.8 nm) of the nanofacetted graphene/Ge(001) surface. Reproduced with permission from *Fortin-Deschênes et al., The Journal of Physical Chemistry Letters 2016, 7 (9): 1667-1674.* [39] Copyright (2016) American Chemical Society.

APPENDIX H Structure of A7 Sb(110) thin films

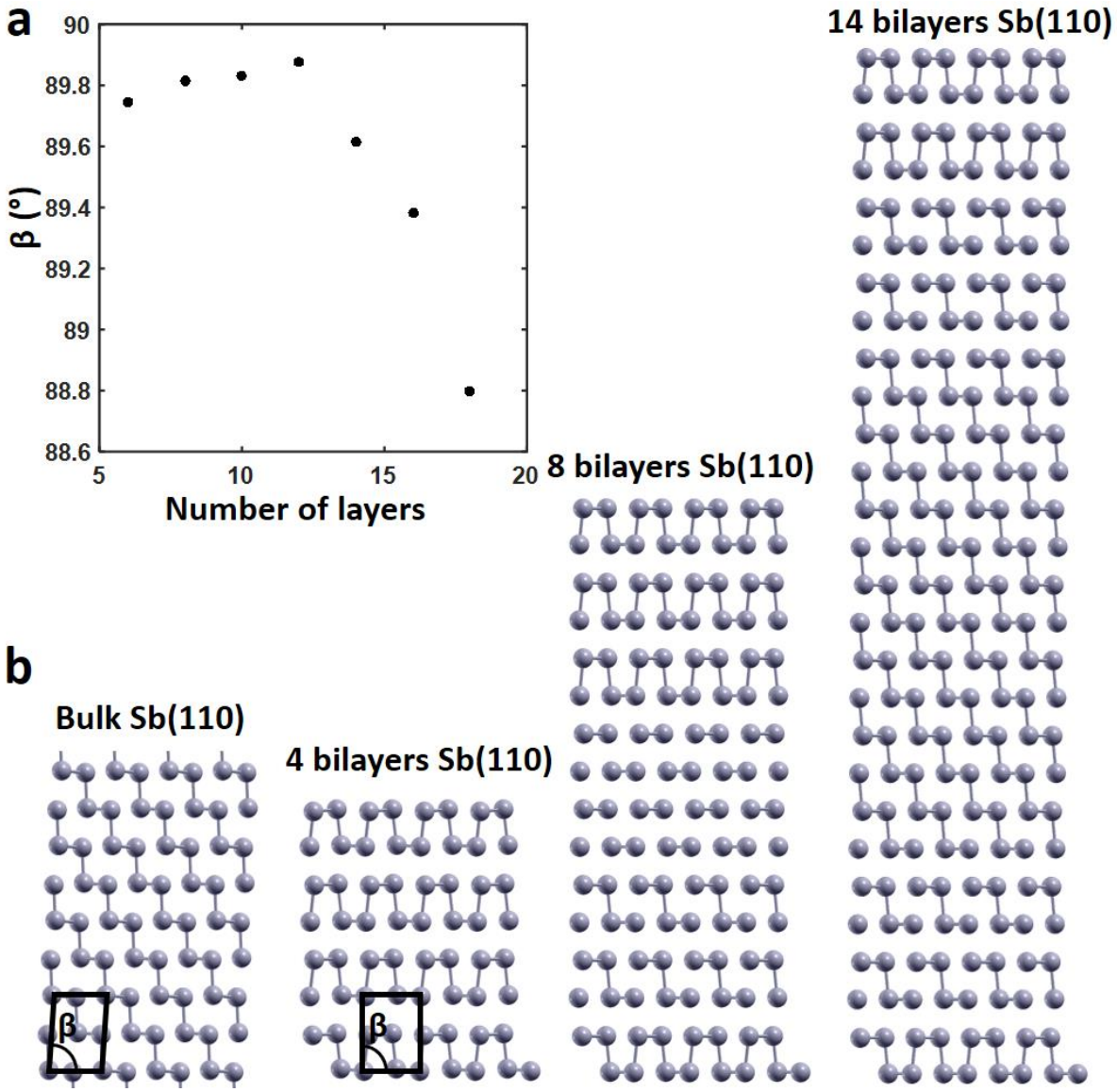

Figure 7.8 DFT (PBE+D2) calculated structure of thin Sb(110) films. Sb(110) films can be represented by a monoclinic supercell. The β angle as a function of the number of layers is shown in (a) (see (b) for the definition of β). In bulk A7 Sb, β=87°. For thin films (below 12 bilayers) β relaxes close to 90° (the deviation from 90° is most likely due to the convergence threshold used in the calculation). The structure of these films (below 12 layers) is almost identical to AA α-2D-Sb. We can also note in (b) that thin films form well-defined bilayers parallel to the (110) surface plane. As the thickness increases, the bilayer structure is progressively lost (especially close to the center of the film) and eventually align with the (111) planes like in bulk A7 Sb.

APPENDIX I STEM of edge nanowires in Sb(110) islands

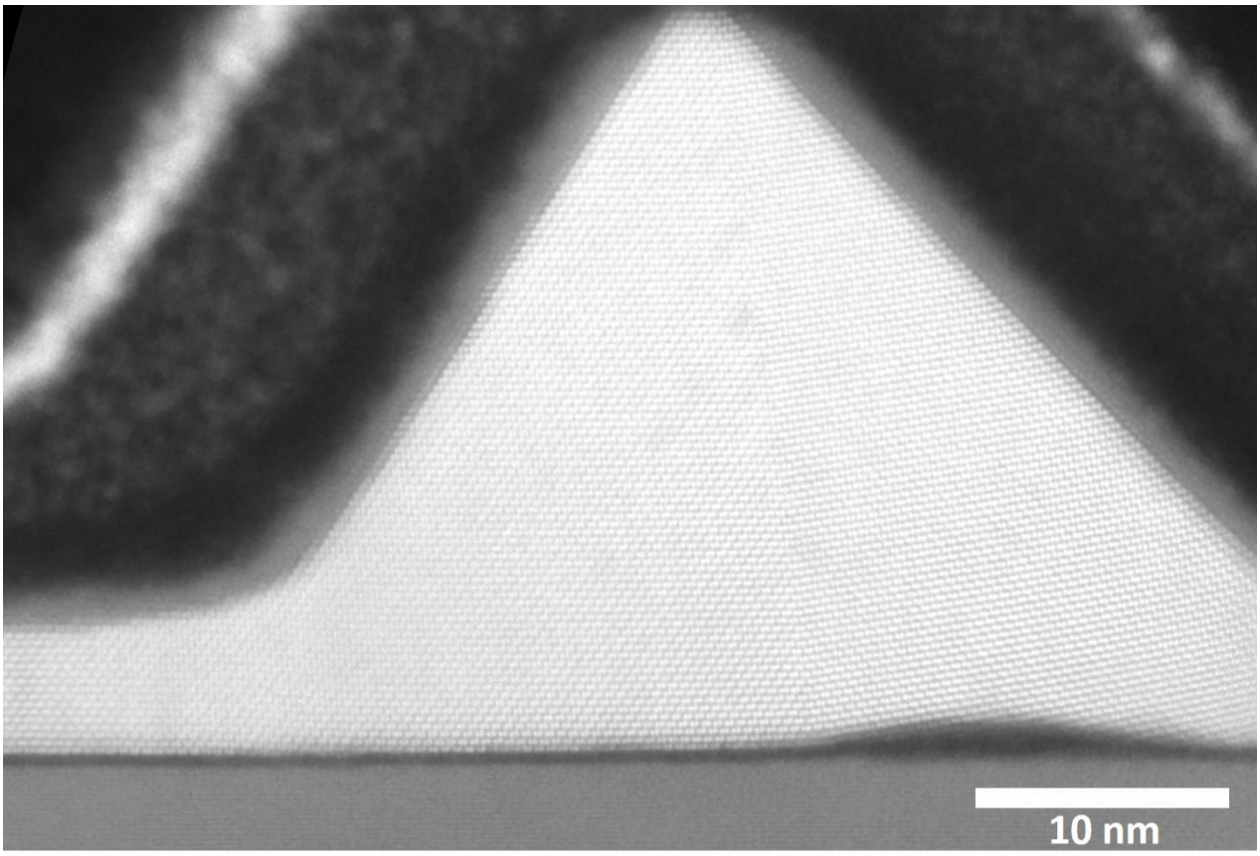

Figure 7.9 Cross-sectional STEM of a NW at the edge of a A7 Sb(110) island (formed by the phase transition of an A17 island during the vdW growth on graphene/Ge). A twin domain is observed at the center of the NW (allowing the orientation of the facets with the (111) planes). In contrast to the data presented in Figure 6.15, there is no rotated grain boundary at the interface between the island and the NW. This is the typical structure of most Sb(110) islands on graphene/Ge observed by STEM.

APPENDIX J AFM of α-2D-Sb and A7 Sb(110)

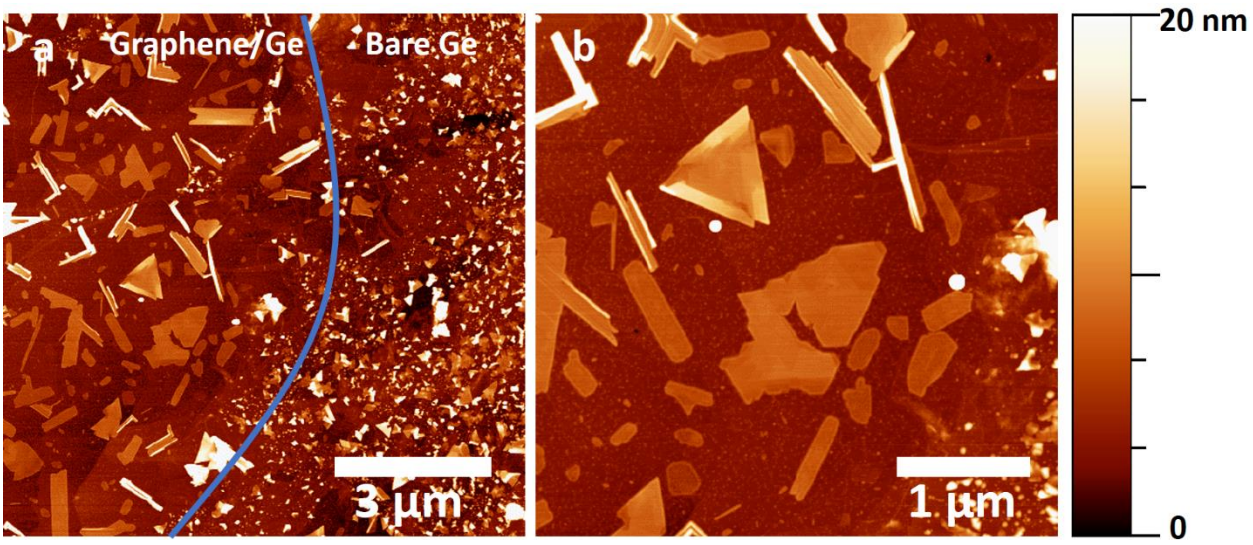

Figure 7.10 AFM images of Sb deposited on graphene/Ge(110) at T=250 °C and F=130 nm/min. The is a hole in the graphene layer on the right side of the blue line in (a), which explains the different growth behavior. A higher magnification image of the same sample is shown in (b). We notice that the flat rectangular islands have thicknesses below 4.5 nm (corresponding to the stability limit of the A17 phase). On the other hand, the nanofacetted rectangular islands (A7 Sb(110)) are typically thicker since the facets form after the phase transition. Adapted from [40].

APPENDIX K Formation of nanoridges after the A17 → A7 transition during the vdW growth of Sb on graphene

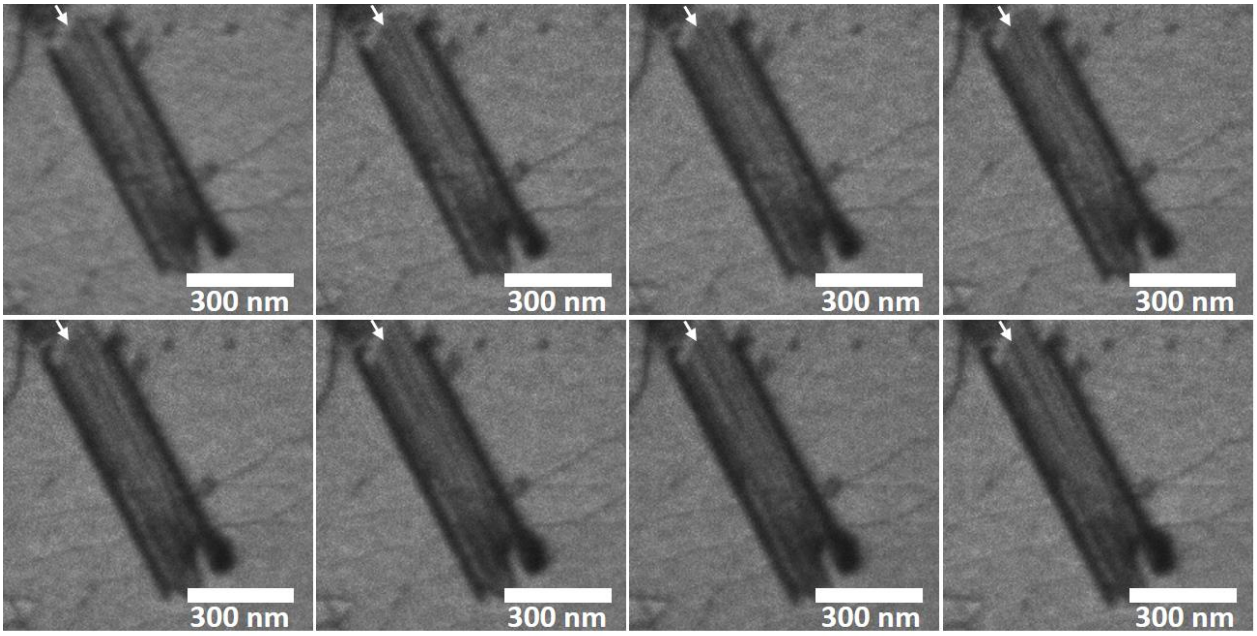

Figure 7.11 Bright-field LEEM snapshots (1 second between frames) showing the formation of nanoridges on a Sb(110) island after the A17 → A7 transition during the deposition on graphene/Ge(110) (F=2.6 nm/min, T=190 °C). The nucleation of a nanoridge at the short edge of the island can be seen (indicated by the white arrow). The nanoridge then grows inward. It is not clear what the contrast means here. The dark line could be the grain boundary between the twin domains the associated facets forming on the island. Adapted from [40].